Defining molecular mechanisms of calcium dysregulation in malignant hyperthermia susceptibility

Rachel Emma Dodds

Submitted in accordance with the requirements for the degree of

Doctor of Philosophy

The University of Leeds
Faculty of Medicine and Health
Leeds Institute of Medical Research at St James's

September, 2019

The candidate confirms that the work submitted is their own and that appropriate credit has been given where reference has been made to the work of others.

Acknowledgements

I would like to express my thanks to my supervisors Prof. Phil Hopkins, Dr. Marie-Anne Shaw and Dr. Jonathan Bilmen, for their insight and encouragement throughout my PhD.

Thank you to Dr. Brian Jackson and Mrs Laura Wilkinson-Hewitt from the Leeds Protein Production Facility for their invaluable help and all of the laughs; Dr. Iain Manfield from the biomolecular interactions facility for his academic insight, suggestions and help with data interpretation; Dr James Ault and Dr Rachel George from the Leeds Mass Spectrometry facility in the Astbury Centre for Structural Molecular Biology for performing mass spectrometry and data analysis; Dr Adam Davison and Mrs Liz Straszynski for performing FACS; and Jodie England for her work towards the p.S1728F CRISPR project.

I am lucky to have worked alongside all members of the MH unit over the past few years. Especially Catherine, for keeping everything running smoothly; Will, for his help with cell culture in the p.D3986E CRISPR project; Vikas, for his help with calcium imaging and Essam and Lois for being there throughout all of the ups and downs.

Thank you to all of my friends, especially Dominique for being on stand-by with her unlimited positivity when I needed it most and Christina because I don't know what I would have done without her by my side since day one.

Thank you to my best friend, my Mum, for her endless reassurance, pep talks and unconditional support that have enabled me to reach my goals.

Finally, thank you to Angelo for his patience and understanding of the sacrifices we have had to make over the past few months, for his unfailing support and for somehow managing to keep this challenging time so happy and silly.

Abstract

Malignant hyperthermia (MH) presents in susceptible individuals following exposure to volatile anaesthetic agents, manifesting as Ca^{2+} dysregulation via aberrant activity of the ryanodine receptor 1 (RYR1) – the major Ca^{2+} release unit of skeletal muscle sarcoplasmic reticulum (SR). Progress in the characterisation of *RYR1* variants identified in MH susceptible individuals has been hindered by characterisation processes that rely on the cloning and heterologous expression of the large, ~15 kb *RYR1* gene. A novel CRISPR-Cas9 based method for variant characterisation was developed to circumvent existing limitations of variant characterisation. The p.D3986E and p.S1728F variants were introduced into C2C12 myoblasts. In addition to the desired integration of the repair template, this resulted in a range of erroneous integrations and undesired editing events. Nonetheless, this work provides a substantial foundation for future development of CRISPR-Cas9 genome editing in the MH field and highlights key areas for future optimisation.

It has been speculated that variants in genes other than the *RYR1* and *CACNA1S* could contribute to MH susceptibility in the proportion of MH cases for which no genetic cause has been ascertained. Next generation sequencing of fifty genes associated with Ca^{2+} handling, performed by the Leeds MH Unit, identified two calsequestrin-1 (CASQ1) variants, p.I138T and p.F186Y, in an MH individual and an exertional heat illness (EHI) individual, respectively. An additional variant, CASQ1 p.E364K was identified in an MHShc individual by colleagues in the Australian population. EHI has significant clinical overlap with MH and MH-associated *RYR1* variants have been detected in EHI patients. CASQ1 is thought to be the major Ca^{2+} binding protein of skeletal muscle SR and a regulator of RYR1 activity. CASQ1 null mice have been shown to exhibit an MH and EHI-like phenotype in response to halothane and heat, respectively. In this project, CASQ1 variants p.F186Y and p.I138T were shown to have reduced Ca^{2+} binding and polymerisation capacities compared CASQ1 WT and CASQ1 p.E364K. These data suggest that the highly conserved CASQ1 p.F186Y and p.I138T variants could act to influence the MH/EHI phenotype.

Table of contents

List of tables

List of figures

List of abbreviations

$^{\bullet}OH$	Hydroxyl radicals
%MR	Percentage maximal response
4-CmC	4-chloro-m-cresol
95% CI	95% confidence interval
AAV	Adeno-associated virus
Ach	Acetylcholine
ACMG	American College of Medical Genetics and Genomics
ADP	Adenosine diphosphate
AID	Alpha-1 interacting domain
AM	Acetoxymethyl ester
ANOVA	Analysis of variance
apoCaM	Calmodulin protein unbound by Ca^{2+}
ATP	Adenosine triphosphate
AUC	Area under the curve
BCA	Bicinchoninic acid assay
BE3	Base editor 3
bGH poly A	Bovine growth hormone poly adenylation signal
bp	Base pair
BR	Broad Range
BSA	Bovine serum albumin
C score	Combined annotation dependent depletion tool score
Ca^{2+}	Calcium ion
Ca^{2+}-CaM	Calmodulin protein bound by Ca^{2+}
CACNA1S	Human alpha-1 subunit of the dihydropyridine receptor gene
CADD	Combined Annotation Dependent Depletion tool
CADT	Custom Assay Design Tool
CALM1	Calmodulin 1 gene
CaM	Calmodulin protein
CaMKII	Calmodulin kinase 2 protein
Cas	CRISPR associated proteins
CASQ1	Human calsequestrin-1 gene
CASQ1	Human calsequestrin-1 protein
Casq1	Mouse calsequestrin-1 gene
Casq2	Mouse calsequestrin-2 protein
CASQ2	Human calsequestrin-2 protein
CASQ2	Human calsequestrin 2 gene
Cav1.1	Alpha-1 subunit of the dihydropyridine receptor
CBh	Chicken beta actin promoter
CCD	Charge-coupled device
CCTOP	CRISPR/Cas9 Target Online Predictor

CDK4	Cyclin dependent kinase 4 protein
cDNA	Complementary DNA
CK	Creatine kinase
CPVT	Catecholaminergic polymorphic ventricular tachycardia
CRISPR	Clustered Regularly Interspaced Short Palindromic Repeats
crRNAs	Precursor CRISPR RNAs
Cryo-EM	Cryogenic electron microscopy
Ct	Cycle threshold
CTP	Cytidine triphosphate
CV	Column volumes
dCas9	Catalytically inactive Cas9
DHPR	Dihydropiridine receptor
DLS	Dynamic light scattering
DMEM	Dulbecco's modified
DMSO	Dimethyl sulfoxide
DNA	Deoxyribonucleic acid
dNTPs	Deoxynucleotides
dRn	Delta Rn
DSB	Double stranded break
DSHB	Developmental studies hybridoma bank
E. coli	*Escherichia coli*
EBV	Epstein Barr Virus
ECC	Excitation contraction coupling
ECCE	Excited coupled calcium entry
ECL	Entactin-collagen-laminin
ECM	Extracellular matrix
EDTA	Ethylenediaminetetraacetic acid
EGTA	Ethylene glycol tetraacetic acid
EHI	Exertional heat illness
EHS	Exertional heat stroke
EMHG	European Malignant Hyperthermia Group
ESI MS	Electrospray ionisation mass spectrometry
ETC	Electron transport chain
ExAC	Exome Aggregation Consortium
FACS	Fluorescence activated cell sorting
FBS	Fetal bovine serum
FITC	Fluorescein isothiocyanate
FKBP12	FK506-binding protein
fps	Frames per second
FSC	Forward scatter
FU	Fluorescence unit
GAPDH	Glyceraldehyde 3-phosphate dehydrogenase protein
GFP	Green fluorescent protein

gnomAD	Genome Aggregation Database
gRNA	Guide RNA
GTP	Guanosine triphosphate
H+	Hydrogen ion
H2O	Water
H2O2	Hydrogen peroxide
HCl	Hydrochloric acid
HDR	Homology directed repair
HEK293 FT	Human embryonic kidney 293 cells with SV40 large T antigen
hFGF	Human fibroblast growth factor
HRP	Horse radish peroxidase
HSV-1	Herpes simplex virus type 1
hTERT	Human telomerase reverse transcriptase protein
IDT	Integrated DNA Technologies
iPSCs	Induced pluripotent stem cells
IPTG	Isopropyl β-D-1-thiogalactopyranoside
IVCT	*In-vitro* contracture test
IVT	*In-vitro* transcription
JP-45	Human JP-45 protein
JSPR1	Human junctional sarcoplasmic reticulum gene
kb	Kilobase
KCl	Potassium chloride
kDa	Kilodalton
L-type	Long-lasting type calcium channels
LB	Lysogeny Broth
LC-MS	Liquid chromatography mass spectrometry
MCU	Mitochondrial Ca^{2+} uniporter
Mg2+	Magnesium ion
MGB	Major groove binder
MH	Malignant hyperthermia
MHN	Malignant hyperthermia normal
MHSc	Malignant hyperthermia susceptible to caffeine
MHSh	Malignant hyperthermia susceptible to halothane
MHShc	Malignant hyperthermia susceptible to caffeine and halothane
MS	Mass spectrometry
MST	Microscale Thermophoresis
MwCO	Molecular weight cut off
MYH1	Myosin heavy chain 1 gene
MYH2	Myosin heavy chain 2 gene
MYH4	Myosin heavy chain 4 gene
MYH7	Myosin heavy chain 7 gene
MyHC-2A	Myosin heavy chain 2A protein

MyHC-2B	Mysoin heavy chain 2B protein
MyHC-2X	Mysoin heavy chain 2X protein
MyHC-β	BETA-myosin heavy chain protein
NAM	Native American Myopathy
NAMHR	North American MH Registry
NEB	New England Biolabs
NFQ	Non-fluorescent quencher
NGS	Next generation sequencing
NHEJ	Non-homologous end joining
NLS	Nuclear localisation signal
nm	Nanometre
NO·	Nitric oxide
NOS	Nitric oxide synthase
nt	Nucleotide
NTD	N terminal domain
O2	Oxygen
O2•−	Superoxide anions
OFP	Orange fluorescent protein
OPPF	Oxford Protein Production Facility
ORAI1	Calcium release-activated calcium channel 1
OXPHOS	Oxidative phosphorylation
P/S	Penicillin-streptomycin
PAGE	Polyacrylamide gel electrophoresis
PAM	Protospacer adjacent motif
PBS	Phosphate buffered saline
PCR	Polymerase chain reaction
PDB	Protein data bank
PEG	Polyethyleneglycol
PES	polyethersulfone
Pi	Inorganic phosphate
PNK	Polynucleotide kinase
POI	Protein of interest
Poly-Phen2	Polymorphism Phenotyping v2
PT	Permeability transition
rpm	Revolutions per minute
RNA	Ribonucleic acid
RNS	Reactive nitrogen species
ROI	Region of interest
ROS	Reactive oxygen species
rSAP	Recombinant shrimp alkaline phosphatase
RYR	Ryanodine receptor protein
RYR1	Human ryanodine receptor 1 gene
RYR1	Human ryanodine receptor 1 protein
Ryr1	Mouse ryanodine receptor 1 gene

Ryr1	Mouse ryanodine receptor 1 protein
RYR2	Human ryanodine receptor 2 protein
RYR2	Human ryanodine receptor 2 gene
S. pyogenes	*Streptococcus pyogenes*
S1	RYR1 transmembrane domain helices 1
S2	RYR1 transmembrane domain helices 2
S3	RYR1 transmembrane domain helices 3
S4	RYR1 transmembrane domain helices 4
S5	RYR1 transmembrane domain helices 5
S6	RYR1 transmembrane domain helices 6
SD	Standard deviation
SDH	Succinate dehydrogenase
SDM	Site directed mutagenesis
SDS	Sodium dodecyl sulfate
SDS-PAGE	Sodium dodecyl sulfate polyacrylamide gel electrophoresis
SEC	Size exclusion chromatography
SEC-MALS	Size exclusion chromatography and multi-angle light scattering
SERCA	Human sarco/endoplasmic reticulum Ca^{2+}-ATPase
shRNA	Short hairpin RNA
SIFT	Sorting Intolerant From Tolerant
siRNA	Short inhibitory RNA
SNP	Single nucleotide polymorphism
SNP	single nucleotide polymorphism
SOC	Super optimal broth with 20mM glucose
SOCE	Store operated calcium entry
SR	Sarcoplasmic reticulum
SSC	Side scatter
ssODN	Single stranded oligonucleotide
STAC3	SH3 And Cysteine Rich Domain 3 gene
STIM1	Stromal interaction molecule 1 protein
STIM1L	Stromal interaction molecule 1 splice variant protein
SV40	Polyomavirus Simian Virus 40
T tubule	Transverse tubule
T7 assay	T7 endonuclease I assay
TAE	Tris-acetic acid-EDTA
TALEN	Tale effector-like endonuclease
TAM	Tubular aggregate myopathy
TBS	Tris-boric acid-EDTA
TBST	Tris buffered saline with tween
TEMED	N,N,N',N'-tetramethylethane-1,2-diamine
TGS	Tris-glycine-SDS
TM1	Transmembrane protein 1
TM2	Transmembrane protein 2

TM3	Transmembrane protein 3
TM4	Transmembrane protein 4
TOF	Time of flight
tracrRNA	Transactivating CRISPR RNA
TRPC	Transient receptor potential-canonical channel
U/L	Units per litre
UPLC	Ultra-performance liquid chromatography
UTP	Uridine triphosphate
v/v	Volume per volume %
VAM	Vacuolar aggregate myopathy
VDAC	Voltage-dependent anion channel
VdW	Van der Waals interactions
VSD	Voltage sensing domain
VUS	Variants of unknown significance
w/v	Weight per volume %
WT	Wild-type
ZFN	Zinc finger nuclease

Chapter 1 - Introduction

1.1 Clinical manifestation of malignant hyperthermia

First described in the 1960s (Denborough and Lovell, 1960), malignant hyperthermia (MH) is a disorder of calcium handling that manifests, in susceptible individuals, following exposure to volatile anaesthetics and/or the muscle relaxant, succinylcholine. Uncontrolled calcium ion (Ca^{2+}) release from the sarcoplasmic reticulum (SR) of skeletal muscle induces a hypermetabolic state leading to hyperthermia, muscle rigidity, acidosis, arrhythmia, increased creatine kinase (CK) levels and rhabdomyolysis (Rosenberg et al., 2015; Jiang et al., 2008). Left untreated, rhabdomyolysis can cause life-threatening hyperkalaemia and with a rise in body temperature, disseminated intravascular coagulation is the usual cause of death (Kim, 2012; Rosenberg et al., 2015). MH reactions are treated with the muscle relaxant, dantrolene. Whilst it has long been known that dantrolene suppresses the release of Ca^{2+} from the SR (Ellis and Bryant, 1972), its mechanism of action was only recently elucidated. Choi et al. (2017) identified that dantrolene increases the affinity of the major Ca^{2+} release unit in SR, the ryanodine receptor 1 (RYR1), to Mg^{2+} which exerts an inhibitory effect on the RYR1. Treatment of MH reactions with dantrolene has reduced the mortality from MH reactions to <5% (Litman and Rosenberg, 2005).

1.2 Epidemiology of MH

Estimates of the incidence of MH vary from 1 in 10,000 to 1 in 250,000 (Halliday, 2003; Ording, 1985) but the prevalence of variants in genes associated with MH may be as high as 1 in 2000 (Monnier et al., 2002); however, these numbers are difficult to ascertain as MH does not usually present on an individual's first exposure to anaesthetics, exposure may be limited to a short duration, reactions may be mild and only a small proportion of the general population are exposed per year (Rosenberg et al., 2015). Interestingly, MH is more prevalent in males than females. Estimates of the

difference in incidence between males and females range from a 2.2:1 ratio to 4:1 in a Japanese study (Strazis and Fox, 1993; Migita et al., 2007). In the North American MH Registry (NAMHR), 78% of MH cases were observed in males (Brandom and Larach, 2002). Between the years of 1990-2010, 68% of MH proband referrals to the Leeds MH unit were male (Gupta and Hopkins, 2017).

1.3 Skeletal muscle calcium homeostasis

1.3.1 Fibre types

Mammalian skeletal muscles are comprised of a mixture of fibre types, allowing them to perform diverse functions from endurance exercise to short, rapid contractions. Whole muscles were initially characterised based on their contractile speed and colour – slow twitch muscles, associated with endurance, appeared red due to high levels of myoglobin and fast twitch muscles, associated with rapid contraction, appeared white (Needham, 1926). Muscle fibre type characterisation transpired as more complex following biochemical advances including histochemical staining for succinate dehydrogenase (SDH), an enzyme involved in oxidative metabolism, and the identification of differential expression of myosin isoforms (Edstrom and Kugelberg, 1968).

There are four major fibre types in adult mammals, type 1, type 2A, type 2B and type 2X. Type 1 fibres are referred to as slow fibres, with high levels of SDH histochemical staining and a reliance upon oxidative metabolism for energy production, resulting in large numbers of mitochondria (Peter et al., 1972). Type 1 fibres express the *MYH7* gene which encodes the beta(β)-myosin heavy chain (MyHC-β) (Stuart et al., 2016). The fast fibres are divided into three major forms, type 2A, 2B and 2X. Type 2A fibres express the *MYH2* gene encoding the myosin heavy chain 2A protein (MyHC-2A) and rely upon both oxidative metabolism and glycolysis for energy production, with intermediate resistance to fatigue (Stuart et al., 2016; Schiaffino and Reggiani, 2011). Type 2B fibres utilise glycolysis only, with low levels of SDH staining, low mitochondrial numbers and low resistance to fatigue (Schiaffino and Reggiaini, 2011). In small mammals, type 2B fibres express the *MYH4* gene

which encodes the myosin heavy chain 2B protein (MyHC-2B) and type 2X fibres (which have fatigue resistance between type 2A and type 2B fibres) express the *MYH1* gene which encodes the myosin heavy chain 2X protein (MyHC-2X) (Schiaffino et al., 1989; Smerdu et al., 1994).

In humans, western blots failed to show MyHC-2B expression in type 2B fibres but did detect MyHC-2X. It is therefore considered that human type 2B fibres are homologous to small mammal type 2X fibres (Hilber et al., 1999). A number of additional 'hybrid' fibre types have been observed in humans including type 1C, 2C and 2AC which express varying levels of MyHC-β and MyHC-2A and type 2AB, which express varying levels of MyHC-2A and MyHC-2X (Scott et al., 2001)

1.3.2 Excitation contraction coupling

Excitation contraction coupling (ECC) begins with the initiation of an action potential that is propagated down invaginations of the sarcolemma into the cell known as transverse tubules (t-tubules) (Figure 1.1) (Sandow, 1952). In the triad regions, where t-tubules are flanked by membranes of the SR, voltage change is detected by the dihydropyridine receptor (DHPR) Ca^{2+} channel (Franzini-Armstrong, 1970; Rios and Brum, 1987). Upon the detection of voltage change, the DHPR undergoes conformational changes that enable its allosteric activation of the RYR1, triggering Ca^{2+} release from the sarcoplasmic reticulum (SR) (Tanabe et al., 1988). Ca^{2+} binds troponin which is associated with tropomyosin on actin filaments. Ca^{2+} binding triggers a conformational change in troponin, altering its interaction with tropomyosin and exposing myosin binding sites on the actin filament. The globular head of myosin, bound to adenosine diphosphate (ADP) and an inorganic phosphate (Pi), binds actin and forms a cross-bridge. The power stroke occurs whereby myosin pulls actin towards the M line and shortens the sarcomere, releasing ADP. Binding of an adenosine triphosphate (ATP) molecule to myosin, and its subsequent hydrolysis to ADP and Pi, releases myosin from actin, enabling it to bind to another site providing Ca^{2+} levels are sufficient (Hopkins, 2006).

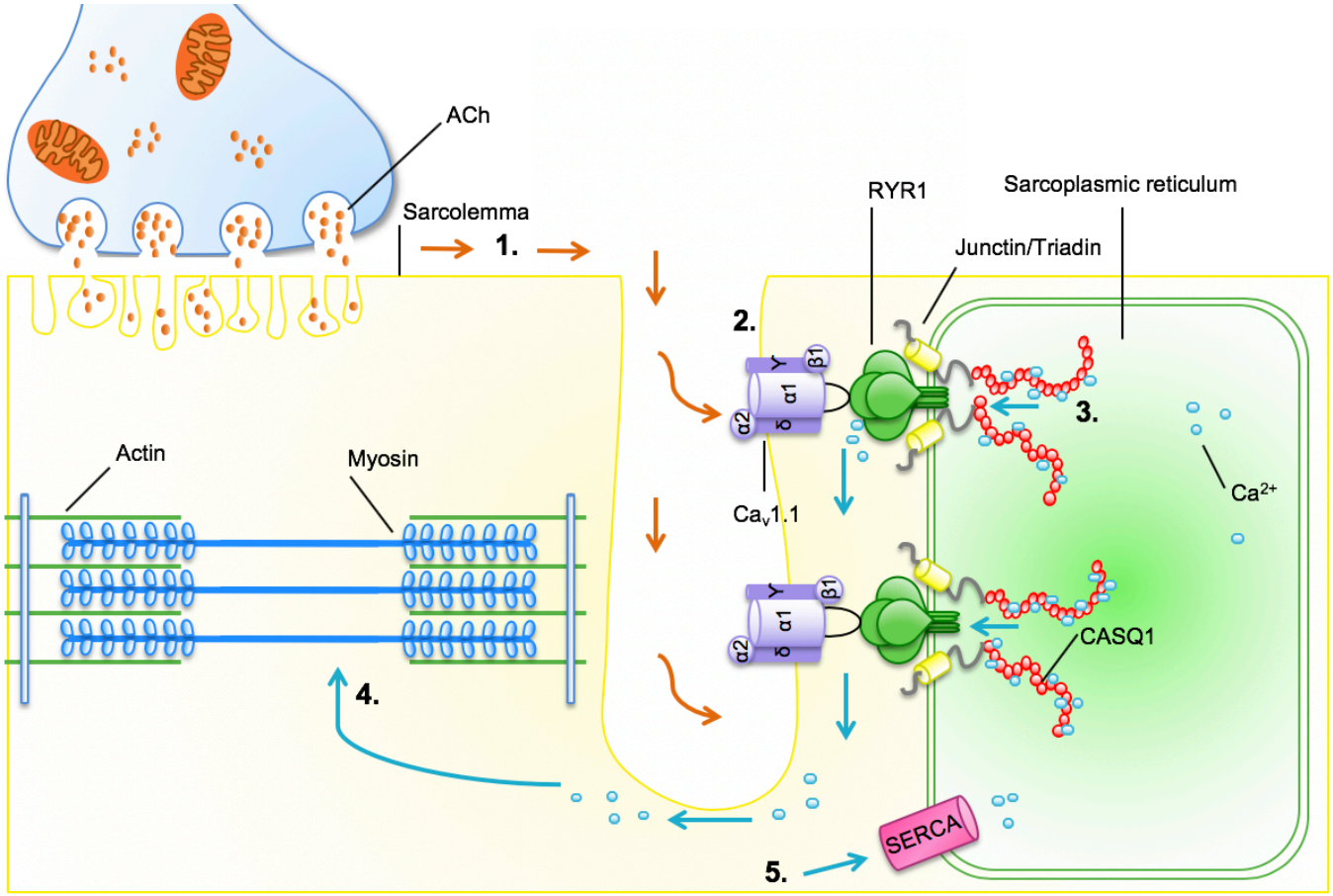

Figure 1.1 – Schematic of the excitation contraction coupling mechanism

1) Action potentials are propagated along the sarcolemma (orange arrows) 2) $Ca_v1.1$ (DHPRs are shown as a single complex rather than a tetrad for simplicity) detects the voltage change and undergoes a conformational change 3) The RYR1 is allosterically activated and Ca^{2+} (blue arrows) released from the SR 4) Ca^{2+} binds troponin, enabling muscle contraction via the interaction of actin and myosin 5) Excess Ca^{2+} from the sarcoplasm is transported into the SR by SERCA.

1.3.2.1 The dihydropyridine receptor

The dihydropyridine receptor (DHPR) is composed of 5 subunits (α1s: 176 kD, α2: 147 kDa, δ: 24 kDa, β1a: 56 kDa and γ: 34 kDa) (Catterall, 2011). The complex is arranged in tetrads that oppose alternate RYR1s on the SR membrane - an arrangement dependent on the presence of the β1a subunit (Schredelseker et al., 2005) (Figure 1.1). Historically, structural resolution of the DHPR has been limited, with progress hindered by its membrane-bound localisation (Hu et al., 2015). Nonetheless, a number of attempts have produced consistent observations with regard to the function of each subunit. To date, the DHPR has been resolved to 15 Å and the α1s subunit to 3.6 Å (Hu et al., 2015; Wu et al., 2016).

The α1s subunit (hereafter referred to as $Ca_v1.1$) is the main component of the DHPR, forming the ion-conducting channel and voltage sensor (Tanabe et al., 1987). It comprises four repeat units (I, II, III and IV), each with six transmembrane domains (S1-S6) (Hu et al., 2015). It has been postulated that, due to DHPR similarity to voltage gated Na^+ and K^+ channels, transmembrane domains S1-S4 are involved in voltage sensing whereas S5-S6 form the ion conducting channel (Samso, 2015). The $Ca_v1.1$ repeat units are connected via linkers known as loops. The I-II loop contains the alpha-1 interacting domain (AID) motif which binds the β1a subunit (Almagor et al., 2012). This interaction is thought to enable the transmission of conformational changes from the voltage-sensing domains (VSDs) to the β1a subunit. The II-III loop physically interacts with the RYR1 (Tanabe et al., 1990), an interaction that has been postulated to occur via β1a docking onto the RYR1, bringing the II-III loop into proximity with its RYR1 interaction site (Hu et al., 2015). Residues 1083-1094 of the III-IV loop interact with the C-terminal domain of $Ca_v1.1$. to realise a globular structure, although the significance of this not fully understood (Wu et al., 2016).

The γ subunit comprises four transmembrane domains (TM1-TM4) with TM2 and TM3 mediating its interaction with S3 and S4 of $Ca_v1.1$ (Wu et al., 2016).

The γ subunit has been shown to act as a Ca^{2+} antagonist, maintaining the integrity of the inactive DHPR state (Andronache et al., 2007).

The α2 and δ subunits are encoded by one gene and are separated by a single disulphide bond. Through its transmembrane domain, the δ subunit tethers α2 to the membrane (Samso, 2015). The role of the α2/δ subunit is not fully elucidated, with proposed functions in excitation-coupled calcium entry (ECCE) and muscle cell development (Gach et al., 2008; Weiss and Ivanova, 2008).

1.3.2.2 Ryanodine receptor 1

The RYR1 is a large, homotetrameric complex that, at ~2.2 megadaltons (MDa), is the largest known ion channel (Lai et al., 1988). It comprises four ~565 kilodalton (kDa) protomers that assemble to form a number of functional domains. Recent advances in the structural resolution of rabbit RYR1 by cryogenic electron microscopy (cyro-EM) have begun to elucidate how the coordinated actions of these domains enable the propagation of conformational signals (Zalk et al., 2015; Efremov et al., 2015; Yan et al., 2015; Samso, 2017). Simplistically, the RYR1 consists of a ligand-sensing sarcoplasmic region and a central domain which relays conformational signals to the pore forming transmembrane domain.

Within the sarcoplasmic region, SPRY domains act as sites of protein-protein interaction. SPRY1 has been shown to bind the RYR1 regulator, FKBP12 (Yan et al., 2015; Yuchi et al., 2015). In some studies, the main functional region of the SPRY2 domain has been shown to bind the $Ca_v1.1$ II-III loop but similar studies using the full length SPRY2 domain failed to corroborate these results; nonetheless, the proximity of the II-III loop to SPRY2 makes this possibility of this interaction plausible (Cui et al., 2009; Lau et al., 2014; Samso, 2017). Helical domains 1 and 2 are highly flexible, suggesting roles in binding and the communication of conformational changes (Yan et al., 2015). The central domain is the only part of the sarcoplasmic region that interacts with the 6-helices transmembrane domain (S1-S6) and this occurs via the cytoplasmic voltage-sensor like domain (VSC) and the C-terminal domain (Yan et al.,

2015). The central domain contains two EF hand domains that act as Ca^{2+} sensors, presumably relaying conformational signals to the VSC that it is in contact with. In addition to this, Van der Waals forces between transmembrane domains and the central domain provide plasticity for relaying conformational signals (Yan et al., 2015). Following allosteric activation of the RYR1, Ca^{2+} is released via the channel into the sarcoplasm, where it initiates contraction of the sarcomere.

1.3.2.2.1 Retrograde RYR1/DHPR signalling

In addition to the orthograde coupling between the DHPR and RYR1 to trigger Ca^{2+} release from the SR, experiments in dyspedic myotubes (those lacking the RYR1) revealed bidirectional signalling between the RYR1 and DHPR. In dyspedic myotubes, L-type Ca^{2+} currents were greatly reduced, an effect reversed by the exogenous expression of the RYR1. Thus, it has been postulated that the RYR1 signals in a retrograde manner to enhance DHPR L-type currents (Nakai et al., 1996).

1.3.3 Calcium reuptake into the SR

Following muscle contraction, the sarcoplasmic/endoplasmic reticulum calcium ATPase (SERCA) hydrolyses ATP to transport Ca^{2+} from the sarcoplasm back into the SR (Figure 1.1). This allows for muscle relaxation as well as the replenishment of SR Ca^{2+} stores for further muscle contraction (Periasamy and Kalyanasundaram, 2006).

1.3.4 Store-operated calcium entry

First described in 2001, store operated calcium entry (SOCE) is the mechanism by which SR Ca^{2+} stores are replenished following depletion (Kurebayashi and Ogawa, 2001). The mechanism by which SOCE occurs and its role in skeletal muscle has been controversial. Initial studies implicated conformational coupling of RYR1 channels with transient receptor potential cation (TRPC) channels; however, sustained SOCE in RYR1 null myotubes showed that the RYR1 is not required for SOCE (Lyfenko and Dirksen, 2008). Further

studies suggested that the combined actions of inositol trisphosphate (IP_3) receptors and TRPC3 channels contributed to SOCE but IP_3 receptors are not enriched in the SR and TRPC3 knockdown experiments failed to show an effect on SOCE (Launikonis et al., 2003; Lee et al., 2006). Following the identification of stromal interaction molecule 1 (STIM1) as a Ca^{2+} sensor in non-excitable cells, it is now largely accepted that SOCE occurs through interactions between STIM1 and the calcium release-activated calcium channel 1 (ORAI1) (Roos et al., 2005). In non-excitable cells, STIM1 exists as a monomer and acts as a Ca^{2+} sensor through an EF hand motif, where depletion of Ca^{2+} and its subsequent dissociation from STIM1 induces conformational changes in STIM1 that trigger its oligomerisation (Stathopulos et al., 2006). STIM1 oligomers are able to translocate to regions of the ER membrane in close contact with the plasma membrane and interact with ORAI1 tetrads, triggering Ca^{2+} influx (Wu et al., 2006). In skeletal muscle cells, STIM1 is pre-localised to the SR membrane regions in close contact with the sarcolemma and it is unclear whether they exist as monomers or oligomers (Stiber et al., 2008). Interestingly, a splice variant of STIM1, STIM1L, is enriched in skeletal muscle cells and is permanently coupled with ORAI1 tetrads on the sarcolemma membrane (Darbellay et al., 2011; Launikonis et al., 2010). This association increases the rate at which SOCE can occur in skeletal muscle cells (Launikonis et al., 2010).

1.3.5 Excitation-coupled calcium entry

Sustained depolarisation of the sarcolemma initiates another extracellular Ca^{2+} entry mechanism known as excitation-coupled calcium entry (ECCE), irrespective of Ca^{2+} store depletion (Cherednichenko et al., 2004). The channel responsible for Ca^{2+} influx via ECCE remains unidentified; however, it is likely that the DHPR at least contributes to Ca^{2+} entry (Bannister et al., 2009)

1.3.6 SH3 and cysteine rich domain 3 protein

SH3 and cysteine rich domain 3 (STAC3), almost exclusively expressed in skeletal muscle, has recently been realised as a player in ECC. Genetic screens in zebrafish have identified a defect in the *STAC3* gene that reduces

Ca^{2+} transients in ECC (Horstick et al., 2013). Further studies have shown that STAC3 is required for the appropriate trafficking of $Ca_v1.1$ to membranes (Nelson et al., 2013). Indeed, fluorescently tagged STAC3 and $Ca_v1.1$ were found to co-localise to the plasma membrane in non-muscle cells which, without STAC3, have poor or no $Ca_v1.1$ expression (Polster et al., 2016).

1.4 RYR1 regulatory proteins

1.4.1 Calsequestrin-1

Calsequestrin-1 (CASQ1) is a ~44 kDa Ca^{2+} binding protein localised to the SR where it acts as a Ca^{2+} buffer and sensor. CASQ1 does not contain an EF-hand domain that is characteristic of other CASQ1 binding proteins (Kumar et al., 2013), but confers its Ca^{2+} binding capacity by numerous acidic glutamate and aspartate residues that are responsible for CASQ1's highly electronegative surface. In the absence of Ca^{2+}, CASQ1 exists as a disordered monomer and undergoes compaction upon Ca^{2+} binding (Sanchez et al., 2012). At low Ca^{2+} levels of ~10 μM, CASQ1 is monomeric and increasing Ca^{2+} to *in vivo* SR levels towards ~1mM triggers CASQ1 polymerisation (Royer and Rios, 2009). CASQ1 consists of three almost identical domains that each comprise a 5-stranded beta sheet and four alpha-helices (Wang et al., 1998). Hydrophobic residues are packed within the CASQ1 core and acidic, Ca^{2+} binding residues populate the exterior (Sanchez et al., 2012). Polymerisation of CASQ1 begins with the self-association of CASQ1 monomers in a front-to-front configuration. The disordered N terminal arm of domain 1 in one monomer is inserted into a groove between beta sheets in domain 2 of the partner monomer (Wang et al., 1998). These dimeric CASQ1 proteins then associate in a back-to-back manner to form linear polymers (Sanchez et al., 2012). Studies have suggested that CASQ1 monomers are able to bind up to 50-80 Ca^{2+} ions; however, the number of acidic residues in the CASQ1 protein sequence do not account for this high capacity binding. Further studies have shown that the polymerisation of CASQ1 induces the formation of clusters of acidic residues, generating additional Ca^{2+} binding sites, accounting for the ability of CASQ1 to bind Ca^{2+} with high capacity (Sanchez et al., 2012). Ca^{2+} binding-induced polymerisation of CASQ1 is dependent on the C-terminal tail which contains a

string of acidic amino acids and ablation of this region abolishes the self-association of CASQ1 monomers (Beard and Dulhunty, 2015). CASQ1 is the only CASQ isoform expressed in fast-twitch muscle fibres; however, in slow twitch fibres, CASQ1 is co-expressed with the cardiac CASQ, calsequestrin 2 (CASQ2).

1.4.1.1 The complex role of CASQ1

CASQ1 had long been considered to function only as Ca^{2+} buffer, providing a store of Ca^{2+} ions for release by the RYR1; however, elucidation of its interactions with a number of SR proteins provided evidence of a complex role in calcium handling. Namely, CASQ1 has been implicated in the regulation of RYR1 activity. Early experiments indicated that addition of CASQ1 to purified heavy SR vesicles within an artificial lipid bilayer activates RYR1s (Kawasaki and Kasai, 1994). Conversely, more recent studies indicate that CASQ1 inhibits native RYR1 channels but activates purified RYR1 channels (Beard et al., 2002). It was postulated that these conflicting reports arose from the requirement of further proteins for CASQ1-mediated regulation that were present only in native preparations. Indeed, it has since been demonstrated that, at low Ca^{2+} levels (~20 μM), CASQ1 inhibits RYR1 activity in the presence of two additional proteins, junctin and triadin (Györke et al., 2004). The interaction of CASQ1 with junctional SR protein 45, JP45, suggests a role for CASQ1 in relaying information regarding Ca^{2+} levels in the SR to $Ca_v1.1$. JP45 is a transmembrane protein that interacts with $Ca_v1.1$ on the sarcolemma and CASQ1 inside of the SR. In mice lacking both JP45 and CASQ1, repeated depolarisation results in a massive Ca^{2+} influx from extracellular stores, suggesting that the JP45 and CASQ1 complex is a negative regulator of ECCE. Furthermore, this Ca^{2+} influx is thought to be via the $Ca_v1.1$ channel, since it is prevented by the known $Ca_v1.1$ blocker, nifedipine (Mosca et al., 2016).

CASQ1 has also been implicated as a component in SOCE. CASQ1 knock-down has been shown to increase SOCE in skeletal muscle fibres, although the mechanism by which this occurs is unclear (Zhao et al., 2010). Experiments in non-muscle cells have shown that CASQ1 colocalises with STIM1, suggestive of binding, preventing STIM1 oligomerisation and its interaction with ORAI1 (Wang et al., 2015).

1.4.1.2 The role of CASQ1 in MH

The implication of CASQ1 in RYR1 regulation and Ca^{2+} handling makes the *CASQ1* gene an interesting candidate for a role in MH. Indeed, mice lacking CASQ1 exhibit an MH-like phenotype in response to halothane exposure (Dainese et al., 2009). Male CASQ1-null mice exposed to 2% halothane had a mortality rate of 80%, compared to 15% for female CASQ1-null mice and 0% for wild-type mice. In addition, an exertional heat-illness (EHI)-like phenotype was observed following exposure to 41^{o}C heat in an environmental chamber. 17 out of 24 CASQ1-null male mice underwent sudden death following heat exposure compared to 1 wild-type male mouse. In contrast, the increased sudden death in female CASQ1-null mice was not significantly different to wildtype. Notably, dantrolene was found to have a protective effect against both halothane and heat exposure. This suggests that variants in the human *CASQ1* gene could also be implicated in EHI, which has considerable clinical overlap with MH (Hopkins et al., 1991; Hopkins, 2007). Interestingly, an increase in voltage-sensitive Ca^{2+} release was observed in CASQ1-null mice, possibly due to loss of CASQ1 inhibition of the RYR1 (Dainese et al., 2009). The observed increase in susceptibility to MH in male mice in this study is mirrored in human MH cases. Whilst the reason behind the increased incidence of MH in males is not entirely understood, recent studies have shown that oestrogens protect against lethal MH-like episodes in CASQ1-null mice. This is an effect perhaps achieved by regulating the activity of enzymes involved in the production of reactive oxygen species (ROS) and reactive nitrogen species (RNS) (Michelucci et al., 2017).

To date, no variants in the *CASQ1* gene have been definitively linked to MH in humans (Lewis et al., 2015). The relevance of *CASQ1* variants identified in MHS individuals will be addressed in this research project.

1.4.2 Junctin and triadin

Junctin and triadin are both embedded in the SR membrane at the triad region, where they interact with the RYR1 and CASQ1 (Figure 1.1). The presence of both proteins has been shown to permit CASQ1-mediated inhibition of the RYR1; however, their individual roles are not fully understood (Gyorke et al.,

2004; Wei et al., 2009). *In-vitro* studies using artificial lipid bilayers have shown that in the absence of CASQ1, both junctin and triadin activate the RYR1 and this occurs at different sites on the RYR1 for each protein, suggesting that they have distinct roles (Wei et al., 2009). Indeed, CASQ1-mediated inhibition of the RYR1 can occur in the presence of junctin alone in artificial bilayers, an effect intensified by low Ca^{2+} levels, suggesting that junctin is the main contributor to CASQ1-mediated RYR1 inhibition (Wei et al., 2009). Furthermore, knockdown of junctin in C2C12 mouse skeletal muscle myotubes resulted in reduced SR Ca^{2+} stores, seemingly consistent with reduced RYR1 inhibition (Wang et al., 2009). Conversely in this study, triadin knockdown resulted in reduced Ca^{2+} release following K^{+} induced depolarisation (Wang et al., 2009).

The generation of triadin and junctin null mice has enabled studies of the structural effects of triadin/junctin ablation on muscle fibres. Triadin null muscle fibres have been shown to lack 'anchors' that connect CASQ1 polymers to the junctional SR membrane, resulting in a disordered and reduced network of CASQ1; however, junctin null fibres had a structural arrangement comparable to wild-type (Boncompagni et al., 2012). This seems to contrast data that has shown junctin alone is able to permit CASQ1-mediated inhibition of the RYR1 (Wei et al., 2009). These discrepancies may be due to the presence of additional proteins in myotubes that are absent from cell-free models.

Functional Ca^{2+} release studies on myotubes derived from triadin/junctin null mouse models have shown that triadin null myotubes have a reduced Ca^{2+} release in response to depolarisation, corroborating observations made in triadin knockdown myotubes (Wang et al., 2009). Ca^{2+} release following caffeine stimulation of junctin null myotubes was comparable to wild-type; however, triadin null myotubes had reduced Ca^{2+} release and reduced sensitivity to caffeine (Boncampagni et al., 2012). In contrast to studies of junctin knockdown in myotubes, junctin-null myotubes did not have reduced SR Ca^{2+} stores but triadin-null myotubes did, which is inkeeping with Ca^{2+} release data. To date, the exact roles of triadin and junctin are not fully understood and conflicting literature surrounding their functions emphasises the complexity of Ca^{2+} handling in skeletal muscle.

1.4.3 FKBP12

FKBP12, sometimes referred to as calstabin 1, is a sarcoplasmic protein constitutively bound to the RYR1 (Samso, 2006). FKBP12 is thought to regulate the RYR1 by stabilising its open and closed states (Gaburjakova et al., 2001). In artificial bilayer studies, the interaction of the RYR1 with the II-III loop of $Ca_v1.1$ increases the RYR1 open probability dramatically, an effect that is not seen upon the removal of FKBP12 (O'Reilly et al., 2002). Interestingly, FKBP12 is proposed to stabilise the closed state of the RYR1 via its interaction with triadin (Eltit et al., 2010). The over-expression of FKBP12 in triadin null myotubes restored SR Ca^{2+} levels and reduced resting sarcoplasmic Ca^{2+} levels; however, it did not restore the abnormal RYR1 sub-conductance states observed, suggesting other proteins may be involved in the FKBP12-mediated closed-state stabilisation of the RYR1 (Eltit et al., 2010).

1.5 Regulation of RYR1 by Mg^{2+}

In addition to protein ligands, small molecules mediate the activity of the RYR1. Mg^{2+} exerts an inhibitory effect on the RYR1 via two mechanisms. Firstly, Mg^{2+} competes with Ca^{2+} for a binding site that triggers activation of the RYR1 and secondly, Mg^{2+} binds to a low-affinity site that inhibits RYR1 activity (Meissner et al., 1986; Laver et al., 1997). Studies have shown that Mg^{2+} inhibition of the RYR1 is reduced in the presence of the C-terminal residues of $Ca_v1.1$ and increases in SR Ca^{2+} may reduce the affinity of Mg^{2+} to activation sites on the RYR1, thus preventing its competition for binding (Haarmann et al., 2005; Laver et al., 2004). Given the potential for a greater role in the regulation of ECC, it has been postulated that Mg^{2+} contributes to the aetiology of MH (Steele and Duke, 2007). Indeed, Mg^{2+} inhibition of Ca^{2+} release is reduced in muscle fibres derived from MHS individuals (Steele and Duke, 2007).

1.6 Mitochondrial function in muscle contraction

The skeletal muscle sarcoplasm is rich in mitochondria that generate ATP required during muscle contraction, primarily by oxidative phosphorylation (OXPHOS). OXPHOS takes place in the mitochondrial inner membrane whereby the electron carrier NADH transfers electrons through a series of electron carriers embedded in the membrane, in a process termed the electron transport chain (ETC). As electrons are transferred, energy is released and is used to drive a proton (H+) gradient across the membrane – the two processes are said to be in coupling. Energy within the H+ gradient is used by ATP synthase, which phosphorylates ADP, converting it to ATP. Having passed through a series of donors and acceptors, electrons combine with O_2 and H+ to form water (Alberts et al., 2008, p. 98-100). The reduction of O_2 to H_2O can lead to the formation of superoxide anions ($O2^{\bullet-}$) and subsequently hydrogen peroxide (H_2O_2), which can form highly reactive oxygen species (ROS) such as hydroxyl radicals ($^{\bullet}OH$) (Görlach et al., 2015). Whilst ROS are required as signalling molecules in normal cellular processes such as cell proliferation and migration, high levels cause damage to DNA and proteins (Martindale and Holbrook, 2002).

1.6.1 Ca^{2+}, ATP and ROS

Ca^{2+} is thought to be transported to the mitochondrial matrix via the voltage-dependent anion channel (VDAC) on the outer membrane and the mitochondrial Ca^{2+} uniporter (MCU) located on the inner membrane (Gincel et al., 2001; Kirichock et al., 2004). It is well established that Ca^{2+} primarily activates OXPHOS in the mitochondria, enabling increased ATP synthesis in response to elevated Ca^{2+} levels (Das and Harris, 1990). In turn, this can lead to increased ROS production due to a higher metabolic rate and increased ETC leakage. In addition to this, elevated Ca^{2+} is also postulated to contribute to mitochondrial dysfunction by potentiating the response of the cell death-associated permeability transition (PT) pore on the outer mitochondrial membrane to ROS (Brookes and Darley-Usmar, 2004).

1.6.2 Reactive nitrogen species

In addition to ROS, reactive nitrogen species (RNS) are a biproduct of OXPHOS. Ca^{2+} has been shown to activate the nitric oxide synthase (NOS) enzyme which catalyses the production of nitric oxide (NO·) (Alderton et al., 2001). Interestingly, NO· has inhibitory effects on a complex within the ETC, complex IV. Inhibition of this complex leads to increased ROS production from another complex, complex III, suggesting a role for NO· in relaying redox signals (Brookes and Darley-Usmar, 2004).

1.6.3 Mitochondrial function in MH

Numerous reports have suggested that mitochondrial structure and function in impaired in MHS muscle. Electron microscopy of muscle samples obtained from mice with the MH RYR1 p.Y522S variant, revealed that a proportion of mitochondria are larger than wild-type, swollen and damaged (Boncompagni et al., 2009). Structural abnormalities are corroborated in studies of MHS human muscle, where the density of some mitochondrial matrices is altered and some mitochondria fragmented (Lavorato et al., 2016). Muscles from mice with the MH RYR1 p.R163C variant have increased levels of ROS, reduced glucose uptake (indicative of reduced OXPHOS) and mitochondrial uncoupling leading to reduced ATP production (Giulivi et al., 2011). ATP production via OXPHOS has also been shown to be reduced in MHS human muscle samples (Thompson et al., 2017). Recently, MHS human muscle samples have been shown to have reduced OXPHOS despite increased mitochondrial mass compared to wild-type. Furthermore, this reduced OXPHOS capacity is thought to be due to a deficiency in complex II of the ETC. Interestingly, complex II is also involved in glycolysis, which could present an area of future research with regard to mitochondrial function in MHS muscle (Chang et al., 2019)

1.6.3.1 Redox modifications of RYR1

The interplay between Ca^{2+} and ROS/RNS is bidirectional, that is, whilst Ca^{2+} is known to affect ROS/RNS production, ROS/RNS also alter Ca^{2+} homeostasis.

The addition of an NO· group to a free thiol group on cysteine residues (S-nitrosylation) occurs primarily when oxygen levels are low and has been implicated in the pathogenesis of the MH RYR1 p.Y522S variant. Y522S mice have increased sensitivity to caffeine and the inhalational anaesthetic, isofluorane. In addition to this, exposure to heat triggers rhabdomyolysis and sudden death (Durham et al., 2008). Ca^{2+} leak from the SR leads to increased RNS production and initiates S-nitrosylation of the RYR1, increasing its activity (Sun et al., 2006). Progressive mitochondrial damage due to elevated Ca^{2+} and RNS ultimately leads to myopathy in Y522S mice (Durham et al., 2008).

As oxygen levels increase, oxidation overtakes nitrosylation as the primary redox modification. S-oxidation activates the RYR1 by enabling the formation of disulphide bonds between RYR1 subunits, thus coordinating their actions (Hamilton and Reid, 2000). Like other forms of regulation of the RYR1, redox modifications are complex, and it is likely that the alteration of these fine-tuned mechanisms in MH could contribute its pathogenesis.

1.7 Genetics of MH

1.8 The *ryanodine receptor 1* gene

The ryanodine receptor 1 gene (*RYR1*), which is ~15 kilobases (kb) and encoded on chromosome 19q, was linked to MH in the 1990s when linkage studies showed the co-segregation of *RYR1* markers with the MH phenotype in an autosomal dominant fashion (Maclennan et al., 1990). To date, over 200 *RYR1* missense variants have been associated with MH and 48 are currently accepted as diagnostic variants by the European Malignant Hyperthermia Group (EMHG), illustrating the allelic heterogeneity of MH. In humans, *RYR1* variants are found in a heterozygous form; however, homozygosity of the p.R614C diagnostic variant has been reported in humans and homozygosity causes an MH-like reaction in pigs in response to halothane, heat and stress (Rueffert et al., 2001; Fujii et al., 1991). Understanding the genetic basis of MH is complex and a single MHS individual may harbour multiple *RYR1* variants (Monnier et al., 2002; Fiszer et al., 2015). Approximately 76% of MH cases in

the UK are attributed to defects in the *RYR1* gene and ~50% of these are attributed to the c.7300G>A p.G2434R variant (Miller et al., 2018; Robinson et al., 2006).

1.9 The *alpha-1 subunit of the dihydropyridine receptor* gene

In addition to the *RYR1*, heterozygous missense variants in the *CACNA1S* gene, encoding the α1 subunit of the DHPR ($Ca_v1.1$) have been explicitly linked to MH. The search for additional MH loci followed the exclusion of *RYR1* linkage to MH in multiple pedigrees (Levitt et al., 1991; Fagerlund et al., 1992; Ruebsam et al., 1993; Iles et al., 1992). A genome-wide linkage study provided evidence of locus linked to MH being located at chromosome 1q, the site of the *CACNA1S* gene (Robinson et al., 1997). To date, *CACNA1S* remains the only gene other than the *RYR1* with accepted MH diagnostic variants (Weiss et al., 2004; Eltit et al., 2012). The p.R1086H and p.R174W variants are found in 1.7% of UK MH cases and in some cases, are found alongside a diagnostic *RYR1* variant, further demonstrating the complexity of elucidating the genetic basis of MH (Miller et al., 2018).

1.9.1 The role of *RYR1/CACNA1S* variants in the pathogenesis of MH

RYR1 variants identified in MHS individuals are gain of function. They cause RYR1 hypersensitivity to agonists, increasing the likelihood of channel activation, an observation first made in p.R615C pigs (Fill et al., 1991; Yang et al., 2003). Experiments using muscle fibres derived from MHS humans and mice, in addition to mouse myotubes expressing *RYR1* variants have shown that sarcoplasmic resting Ca^{2+} levels are higher compared to wild-type (Yang et al., 2007; Feng et al., 2011). This is speculated be the result of a chronic, passive SR Ca^{2+} leak via variant RYR1s.

The mechanism of pathogenesis of the RYR1 p. R163C variant has been extensively studied. The p.R163C variant is the fourth most common variant within the UK population (Miller et al., 2018). Hyperactivity of RYR1 p.R163C channels has been postulated to occur through aberrant post-translational modifications of the cysteine residue or the formation of disulphide bonds that disrupt interactions between intra or inter molecular domains, although this has not been ascertained (Voss et al., 2004; Tung et al., 2010; Feng et al., 2011). Other attempts to explain the hyperactivity of RYR1 variant channels include the disruption of interactions with negative regulators of the RYR1, such as FKBP12, through phosphorylation. Increased phosphorylation of the serine at position 2844 in RYR1 p.R163C channels has been observed; however, western blotting of RYR1 p.R163C sample preparations showed no difference in the amounts of FKBP12 compared to wild-type (Feng et al., 2011). In recent years, multiple Ca^{2+} pathways have been implicated in the pathogenesis of MH. Partial depletion of SR Ca^{2+} stores by leaky RYR1 p.R163C channels leads to an increased level of Ca^{2+} influx via SOCE, an observation previously seen in human MHS muscles (Eltit et al., 2013; Duke et al., 2010). In addition to Ca^{2+}, p.R163C muscle fibres have increased levels of sarcoplasmic Na^{+}, which may occur through the actions of a non-selective Ca^{2+}/Na^{+} channel, thought to be the transient receptor potential channels 3 or 6 (TRPC3/6) on the sarcolemma membrane (Eltit et al. 2013). RYR1 p.R163C myotubes also show increased ECCE which can be suppressed by dantrolene treatment (Cherednichenko et al., 2008)

Whilst the full pathogenic mechanism of *RYR1* variants remains to be elucidated, advances in the resolution of the RYR1 structure are likely to shed light on this complex series of events. Indeed, mapping of MH variants onto structural and functional domains of the RYR1 has been made possible in recent years (Figure 1.2; Yan et al., 2015). The majority of MH variants have been identified in the ligand-sensing N-terminal domain and the flexible helical domain 1; however, this is likely due to DNA sequencing bias.

The $Ca_v1.1$ p. R1086H variant is positioned within the III-IV linker. Residues 1083-1094 of this linker interact with III S6 and form a helix that, when interacting with a helix in the $Ca_v1.1$ C-terminal domain, complete a globular structure (Wu et al., 2016). In myotubes expressing $Ca_v1.1$ R1086H channels, Ca^{2+} release from the SR occurs at a lower voltage than in myotubes expressing wild-type $Ca_v1.1$s and RYR1 R1086H sensitivity to caffeine is increased. This is thought to be due to the dual effect of raised sarcoplasmic Ca^{2+} levels, in addition to the lack of negative regulatory effect thought to be exerted by the DHPR on the RYR1 (Weiss et al., 2004). The role of the DHPR in negatively regulating RYR1 activity is corroborated by studies of the functional effect of the $Ca_v.1.1$ p.R174W variant, which is positioned at a highly conserved gating charge residue in repeat I of the S4 transmembrane domain. Unlike the p. R1086H variant, p. R174W does not cause Ca^{2+} release from the SR to occur at lower voltages; however, its ability to prevent RYR1 Ca^{2+} leak at rest is impaired and RYR1 sensitivity to caffeine is increased (Eltit et al., 2012)

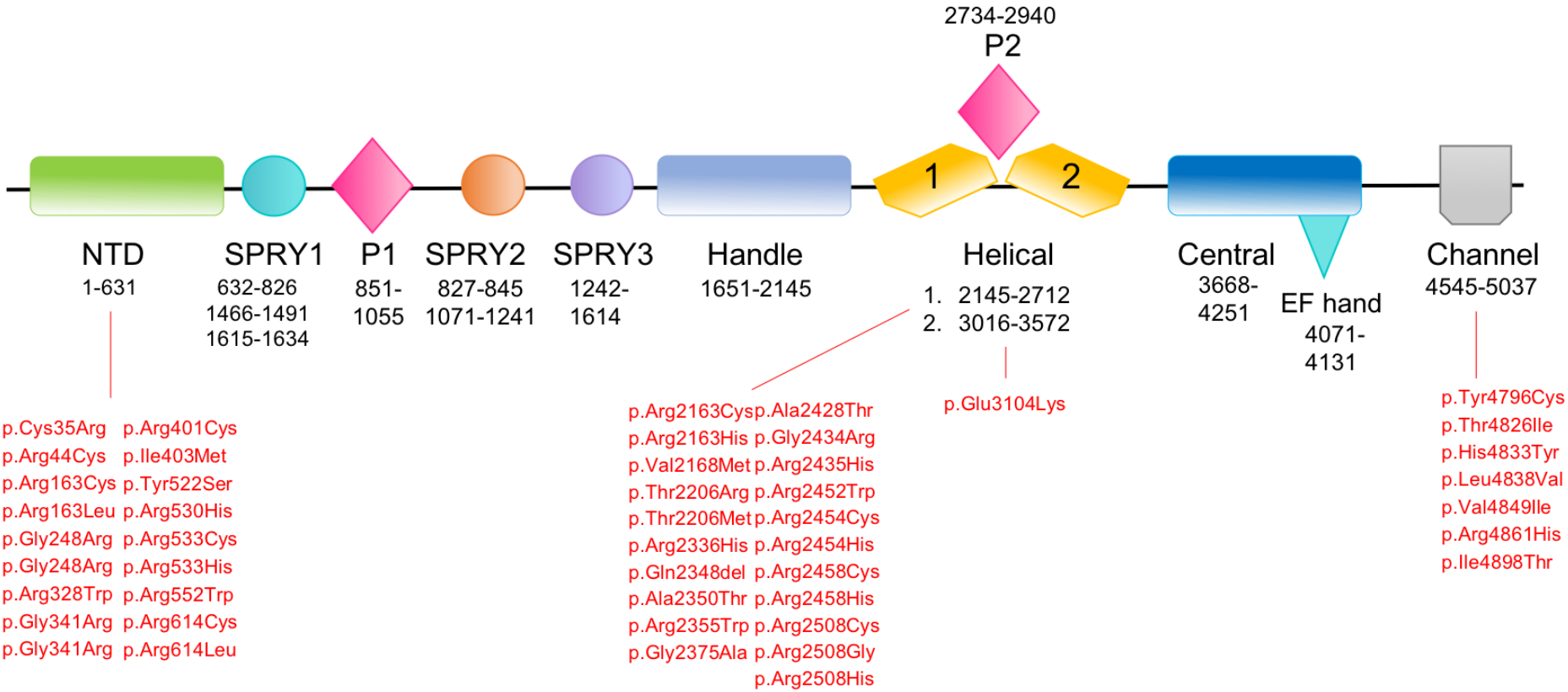

Figure 1.2 – MH variants mapped to RYR1 domains

Major domains of rabbit RYR1 according structures resolved in Yan et al., 2015. Amino acid positions are shown beneath the domain names and MH variants shown in red text. NTD, N-terminal domain. Adapted from Yan et al., 2015.

1.10 *SH3 and cysteine-rich domain-containing protein 3* gene

In recent years, the homozygous p.W284S variant in the *STAC3* gene has been implicated in Native American Myopathy (NAM) (Horstick et al., 2013). NAM, an autosomal recessive disorder, features symptoms including congenital myopathy and skeletal abnormalities, in addition to MH susceptibility (Bailey and Bloch, 1987). Next generation sequencing (NGS) efforts of mainly European Caucasian MH families in recent years have failed to identify any novel, potentially pathogenic *STAC3* variants (Miller et al., 2018). Currently, no *STAC3* variants are accepted as diagnostic MH variants according to the EMHG (available at www.emhg.org, accessed August 2019).

1.11 Role of other genes in MH

Since a proportion of MH cases are not attributed to defects in the *RYR1/CACNA1S/STAC3* genes, variants in genes yet unassociated with MH may be implicated in up to ~25% of MH cases (Miller et al., 2018). Variants in genes encoding gene products that regulate the RYR1, such as CASQ1, are promising candidates for MH susceptibility (Protasi et al., 2009). In an effort to identify MH variants at novel loci, the Leeds MH unit performs NGS of fifty genes associated with calcium handling, in MH families with no diagnostic *RYR1/CACNA1S/STAC3* variant.

1.12 MH link to exertional heat illness

Exertional heat illness (EHI) is a complex disorder arising from interactions between environmental and physiological factor, leading to temperature dysregulation and hypermetabolism (Muldoon et al., 2004). Symptoms of an EHI reaction may be mild, ranging from exhaustion to muscle cramps but severe cases can progress to exertional heat stroke (EHS). EHS is life threatening and symptoms include rhabdomyolysis, tachycardia and hyperthermia, which can lead to multi-organ failure and death (Capacchione and Muldoon, 2009). EHI occurs primarily in young, healthy males performing strenuous exercise in hot environments such as military training exercises; however, it is also more likely to occur in people who are obese, unfit or

suffering a viral infection (Hopkins et al., 1991; Hopkins, 2015). Due to their significant clinical overlap, it has been postulated that there is a link between MH and EHI. A number of reports describe the diagnosis of MH in individuals who had previously had EHI episodes (Hopkins et al., 1991; Thomas and Crowhurst, 2013). More recently, Thomas and Crowhurst (2013) described an EHI episode in an otherwise healthy 25-year-old male running a 10 km race. The proband and a further 5 family members were diagnosed as MHShc. The availability of genetic testing has led to a number of reports in which individuals who have suffered EHI episodes have been found to harbour diagnostic MH variants. For example, in 2001, Tobin et al., published a case study of an anaesthesia-induced MH reaction and subsequent EHI episode whilst playing football in a 12-year-old child. It was later revealed that the child and their father harboured the RYR1 p.R163C variant (Tobin et al., 2001). In more recent years, NGS of individuals who have experienced EHI episodes has revealed a number of rare, potentially pathogenic variants in the *RYR1* and other genes implicated in Ca^{2+} handling that could act to influence susceptibility to EHI; however, the functional significance of these variants remains to be determined (Fiszer et al., 2015).

1.13 Diagnosis of MH

MH susceptibility is diagnosed using the *in vitro* contracture test (IVCT) – an assay based on the increased contractile sensitivity of MH susceptible (MHS) skeletal muscle to caffeine and halothane compared to MH normal (MHN) skeletal muscle (Kalow et al., 1970; Ording et al., 1997). The IVCT protocol is standardised and used as the gold-standard across diagnostic centres within the European Malignant Hyperthermia Group (EMHG). Muscle biopsies from the *vastus medialis* or *vastus lateralis* are maintained in physiological buffer and electrically stimulated to demonstrate viability. A baseline measurement of tension (measured in grams) is taken prior to exposure of the muscle sample to increasing concentrations of caffeine and halothane. An increase in tension of ≥0.2 g from baseline, following exposure to 2% halothane or 2 mM caffeine is deemed a positive response (Figure 1.4). Individuals are characterised as MH

susceptible to halothane and caffeine (MHS_{hc}), MH susceptible to halothane only (MHS_h), MH susceptible to caffeine only (MHS_c) or MHN. Since the IVCT procedure is highly invasive, in recent years, a DNA-level diagnostic approach has been implemented where appropriate but this is limited due to an incomplete understanding of the genetic basis of MH (Figure 1.5; Hopkins et al., 2015).

1.14 Discordancy in MH

The implementation of a DNA-level diagnostic approach is hindered by reports of discordancy between the IVCT phenotype and *RYR1/CACNA1S* genotype. That is, individuals with a positive IVCT phenotype (MHShc or MHSh) and a negative *RYR1/CACNA1S* genotype or individuals with a negative IVCT phenotype and a positive *RYR1/CACNA1S* genotype – the latter of which is less common, likely due to bias as individuals with negative IVCT phenotypes are not routinely offered DNA screening. Discordancy in MH has been widely reported in the past two decades - the G1021A mutation in the *RYR1* gene was shown not to fully co-segregate with MH within families (Adeokun et al., 1997) and MHN individuals were reported to harbour the C1840T mutation (Deufel et al., 1995). Currently, discordancy has been reported in 26.2% of UK MH families (Miller et al., 2018). These observations emphasise the complexity of MH and suggest that multiple variants could act to determine MH susceptibility (Robinson et al., 2000; Robinson et al., 2002). Indeed, a threshold effect has been proposed whereby 'stronger' *RYR1* variants (i.e. those associated with strong IVCT phenotypes) may be sufficient to cause MH susceptibility but 'weaker' *RYR1* variants may only cause MH susceptibility in the presence of other variants (Carpenter et al., 2009). Interestingly, within the UK MH cohort, genotype-phenotype discordancy is distributed equally across *RYR1* variants; however, no discordancy has been observed for the p.R2435H variant which is associated with strong IVCT phenotypes (Miller et al., 2018).

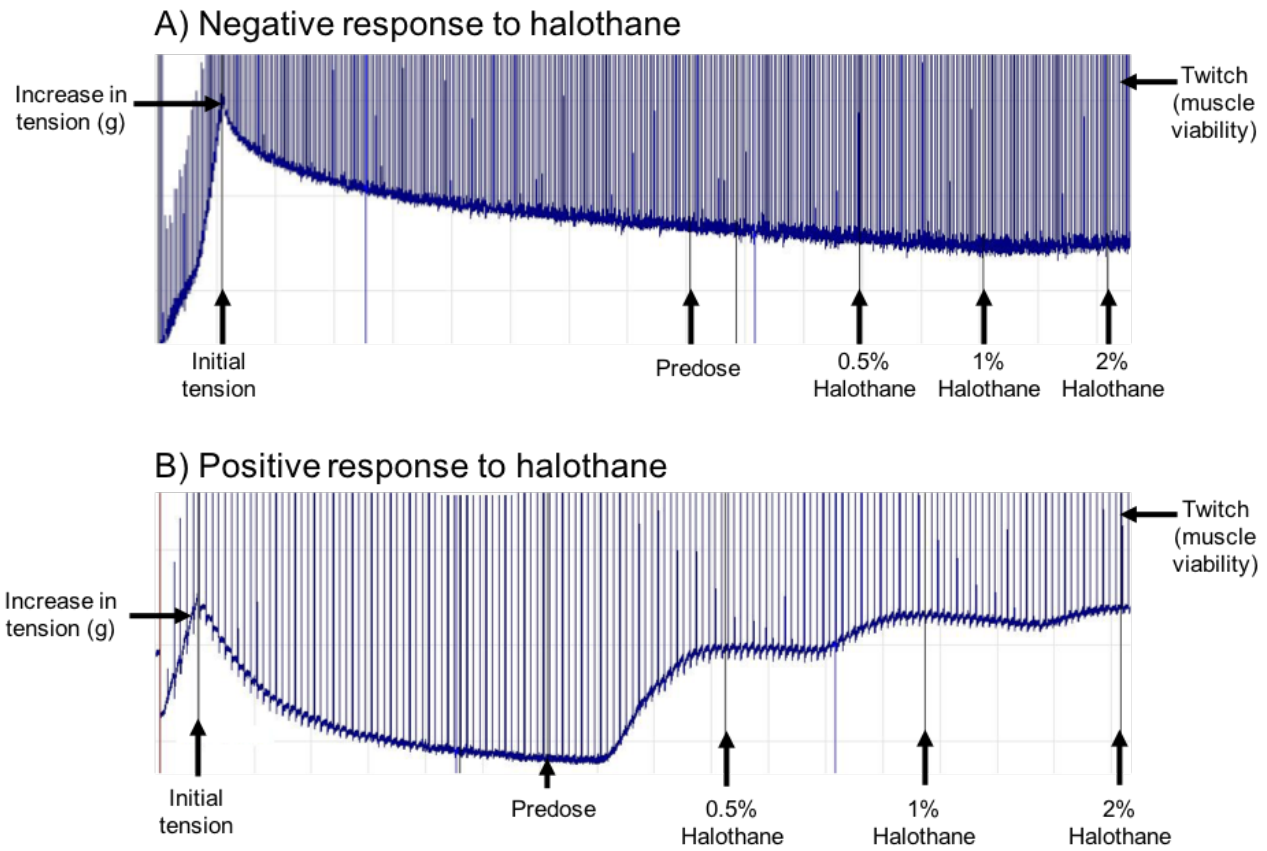

Figure 1.3 – IVCT traces of a negative and positive response to halothane

Representative traces of a negative (A) and positive (B) response to halothane. Electrical stimulation is applied to biopsied muscle samples causing it to twitch, as a measure of viability. An initial tension is applied and the muscle sample allowed to relax prior to application of halothane – the point at which tension is lowest is called the pre-dose and acts as a baseline for measurement of subsequent increases in tension. Halothane is applied incrementally, at 0.5%, 1% and 2% and tension recorded.

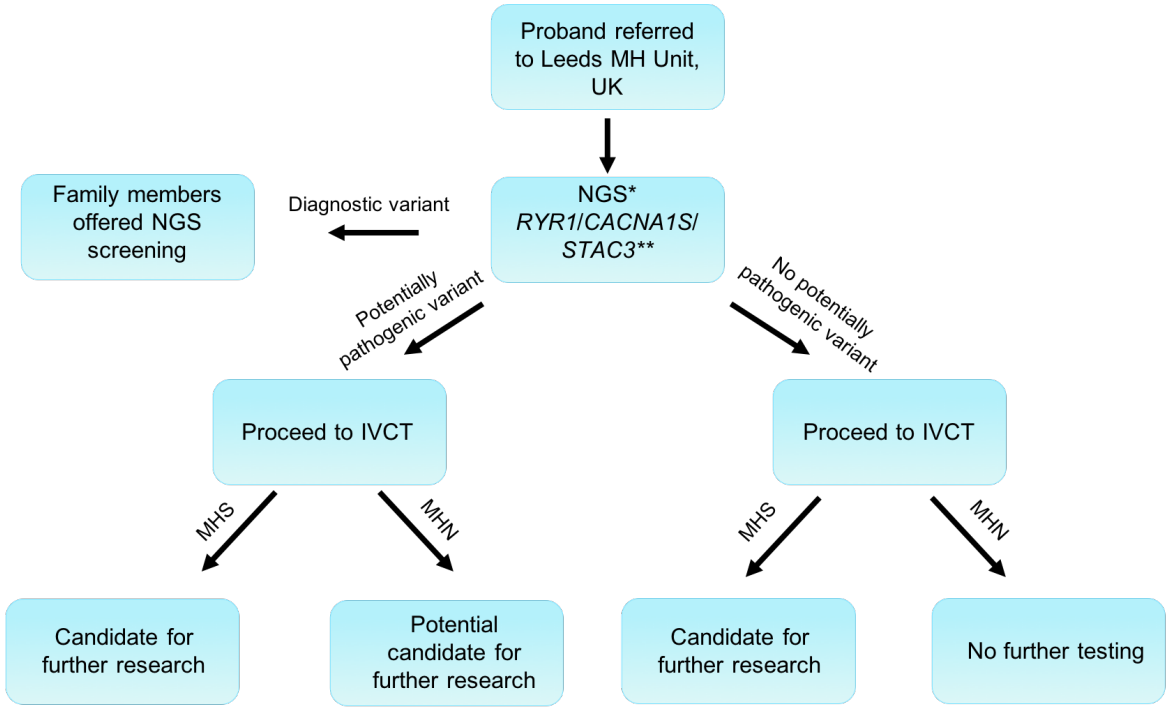

* May proceed directly to IVCT dependent on clinical priorities.
** Genotyping of the *STAC3* p. W284S variant is performed rather than whole coding region sequencing.

Figure 1.4 – Leeds MH unit strategy for the diagnosis and investigation of MH
Suspected probands in the UK are referred to the Leeds MH unit for diagnosis. The Leeds Genetics Laboratory (St James' University Hospital, Leeds) performs NGS of the coding regions of the *RYR1/CACNA1S* genes and genotyping of the STAC3 p. W284S variant. Identification of a diagnostic variant allows for confirmation of MH status without the need for IVCT. If a diagnostic variant is not identified, probands are referred for an IVCT to determine MH status. MHS individuals are candidates for further research.

1.15 Functional characterisation of *RYR1* and *CACNA1S* variants

The development of a genetic diagnostic panel for MH would alleviate the necessity for invasive IVCT diagnosis; however, progress in this field has been hindered in part due to the allelic and genetic heterogeneity of MH – a result of the complex Ca^{2+} handling mechanisms implicated in it. To date, despite the association of over 200 variants in the *RYR1* with MH, only 48 have been added to a diagnostic list of MH variants and only 2 *CACNA1S* variants are diagnostic (EMHG, available at www.emhg.org, accessed August 2019). Furthermore, up to ~25% of MH cases cannot be attributed to defects in the *RYR1* or *CACNA1S* genes (Miller et al., 2018). Past and present methods of variant characterisation will be discussed below, highlighting the need for a novel characterisation process for MH associated variants.

1.15.1 Criteria for the assignment of diagnostic MH variants

The EMHG have published guidelines for the characterisation of variants associated with MH (Hopkins et al., 2015). These guidelines are in line with those set out by the American College of Medical Genetics and Genomics (ACMG; Richards et al., 2015). As such, all variants must be fully described at a genetic and protein level, using the A residue of the ATG start codon as position 1. In addition, the reference sequence used should be cited. The minor allele frequency (MAF) should be ascertained using a population database and in the case of MH, the EMHG anticipates that pathogenic variants will have a MAF of less than 0.001 (0.1%). The EMHG also recommends that the conservation status of a variant across species is reported and the ACMG recommends this is reported along with whether the variant is located in any critical domains (Richards et al., 2015). Previously, it had been a requirement that the variant must have been identified in multiple MH families but since the majority of variants are unique to single families, this criterion has since been removed (Robinson et al., 2006; Miller et al., 2018). The ACMG recommends that *in-silico* tools can be used to aid the interpretation of variants, especially when multiple programmes are used in

parallel; however, these interpretations cannot be used soley to make clinical decisions (Richards et al., 2015). In addition to a full genetic description, the EMHG requires that variants undergo functional characterisation for effects consistent with the pathogenic mechanism of MH (Hopkins et al., 2015).

1.15.2 Methods of characterisation for MH associated variants

1.15.2.1 Primary *ex-vivo* patient samples

IVCT biopsies have provided a convenient means to derive primary myoblasts from patient samples for functional characterisation. Following differentiation into myotubes, cells can be loaded with Ca^{2+} indicating dyes and stimulated with RYR1 agonists such as caffeine to measure Ca^{2+} release from the SR – a mechanism that is perturbed in MHS muscle fibres (Brinkmeier et al., 1999; Wehner et al., 2002). Whilst myotubes offer a balance between physiological relevance (i.e. they express muscle-specific genes and structures) and ease of isolation, primary cells have a limited replicative potential (Hayflick and Moorhead, 1961). Further to this, the contamination of myoblast preparations with fibroblasts means that repeated pre-plating procedures are required to obtain a pure myoblast population, increasing the passage number of the cells further (Chowdhury et al., 2015). Whilst there has been limited success in immortalising human myoblasts through retroviral-mediated delivery of human telomerase reverse transcriptase (hTERT) and cyclin dependent kinase 4 (CDK4) (Mamchaoui et al., 2011), replication of this procedure in our group has proved challenging and there are no reports of the use of immortalised human myoblasts for the characterisation of variants in MH. To overcome issues with the immortalisation of human myoblasts, some groups have isolated B-lymphocytes, which express the RYR1 but not all functional components of the ECC mechanism, from patient blood samples and immortalised them with Epstein-Barr virus (EBV) prior to Ca^{2+} release studies (Girard et al., 2001; Sei et al., 2002).

Despite this, the main limitation of using any primary patient samples is the unknown genetic background of the patient. That is, the presence of additional

unknown variants may alter Ca^{2+} handling making it difficult to determine that the observed effect is attributed to the variant in question. Ultimately, this provides only corroboration of MH status previously determined by IVCT. In efforts to address concerns regarding genetic background, it has been recommended that functional characterisation in this manner must be performed on multiple MH families; however, it has been postulated that high-risk MH haplotypes exist which could ultimately lead to functional characterisation of the incorrect variant (Carpenter et al., 2009). Furthermore, since the majority of MH variants are unique to individual families, a large proportion of variants could not be characterised this way (Miller et al., 2018).

1.15.2.2 Heterologous *RYR1* expression in HEK293 cells and dyspedic myotubes

The predominant system for functional characterisation of MH associated variants is the heterologous expression of variant rabbit or human *RYR1* cDNAs in human embryonic kidney (HEK293) cells that inherently lack RYR1 expression (Nakai et al., 1996). Tong et al., (1997) introduced this method for the functional characterisation of 15 variants associated with MH. Following site-directed mutagenesis of an *RYR1* construct, it is transiently transfected into HEK293 cells and Ca^{2+} release in response to RYR1 agonists is measured (Tong et al., 1999a; Lynch et al., 1999). In contrast to the use of primary myoblasts derived from *ex-vivo* patient samples, the HEK293 system offers a constant genetic background meaning that differences in Ca^{2+} release can be attributed to the variant present in the cDNA. Nonetheless, the HEK293 system does not come without limitations. Firstly, most site directed mutagenesis protocols rely on the amplification of the entire plasmid which is problematic for large vectors. Indeed, the *RYR1* coding sequence alone is ~15 kb. To overcome this, subcloning of fragments of the *RYR1* coding sequence is required which can prove time consuming and laborious (Merritt et al., 2017). Dramatic reductions in transfection efficiencies are observed with large vectors, making confirmation of heterologous RYR1 expression by western blotting challenging and data obtained from Ca^{2+} release studies highly variable between cells (Kreiss et al., 1999; Merritt et al., 2017). Another point of contention when using HEK293 cells is that they do not express ECC

machinery such as the DHPR, nor do they form muscle-specific structures such as triad regions or SR that ensures efficient Ca^{2+} storage, release and reuptake.

Dyspedic 1B5 skeletal myotubes, those that lack RYR1 channels, provide an appealing means to overcome the limitations associated with primary samples and HEK293 cells. Indeed, a number of MH variants have been characterised whereby modified type 1 herpes simplex virus (HSV-1) vectors were co-transfected alongside a vector encoding the *RYR1* variant, enabling the study of RYR1 channels in the presence of muscle-specific structures and the ECC machinery (Yang et al., 2003). Despite this, heterologous expression of RYR1s in any cell type requires the mutagenesis and transfection or transduction of the large *RYR1* cDNA. Ultimately, a novel variant characterisation process that allows for the study of variants in a muscle cell line and circumvents issues with laborious cloning and transfection of the *RYR1* gene is needed to overcome the bottleneck associated with *RYR1* variant characterisation. The development of such a pipeline will extend the availability of DNA-level diagnostics in MH and allow for an individualised, stratified medicines approach to anaesthesia.

1.16 CRISPR-Cas9 as a functional characterisation system

1.16.1 History of engineered nucleases

The ability to introduce mutations at any location in any genome has been a long sought-after objective. In the 1990s, the development of zinc finger nucleases (ZFNs) saw introduction of double stranded breaks (DSBs) at targeted DNA sequences (Kim and Chandrasegaran, 1994). The DNA-binding ZF domains, that each recognise a 3 base pair (bp) sequence, are assembled together to produce a large complex with specific DNA targeting capacities (Klug and Rhodes, 1987). Following designation of the target DNA sequence, fusion to a modified, recognition-inactive *Fok* I endonuclease enables cleavage of both DNA strands (Kim and Chandrasegaran, 1996). DSBs can be repaired by two major mechanisms, non-homologous end joining (NHEJ) and homology directed repair (HDR) (reviewed in Gupta and Musunuru, 2014). NHEJ results in the incorporation of random insertions or the deletion of bases flanking the cleavage site, leading to knockout of the targeted gene through frameshift or the insertion of a stop codon. HDR enables the introduction of specific mutations via the presence of a repair template that has the mutation to be introduced flanked by several bases of homology to the sequence flanking the cleavage site (Figure 1.5). Despite the widespread use of ZFNs, their use presents two major limitations. Firstly, the engineering and assembly of ZF domains has proved challenging, typically taking months to complete (Gupta and Musunuru, 2014). Secondly, since ZFNs target 3 bp, sequence specificity may be limited. More recently, a class of nucleases known as transcription activator-like effector nucleases (TALENs) have been utilised. TALENs comprise an array of repeat amino acids, of which just two confer specificity to a single nucleotide, expanding the scope for sequence specificity engineering compared to ZFNs (Bogdanove and Voytas, 2011). Furthermore, since just two amino acid residues determine nucleotide specificity, engineering TALENs is less time consuming and laborious. Nonetheless, the use of TALENs is limited by their large size. With a coding sequence of ~3 kb (compared to 1 kb for ZFNs), their delivery into cell lines has proved challenging (Gupta and Musunuru, 2014). In addition, the preferred method of delivery into cell lines is

using viruses; however, the tandem array present in TALENs is prone to recombination in viral vectors (Holkers et al., 2013).

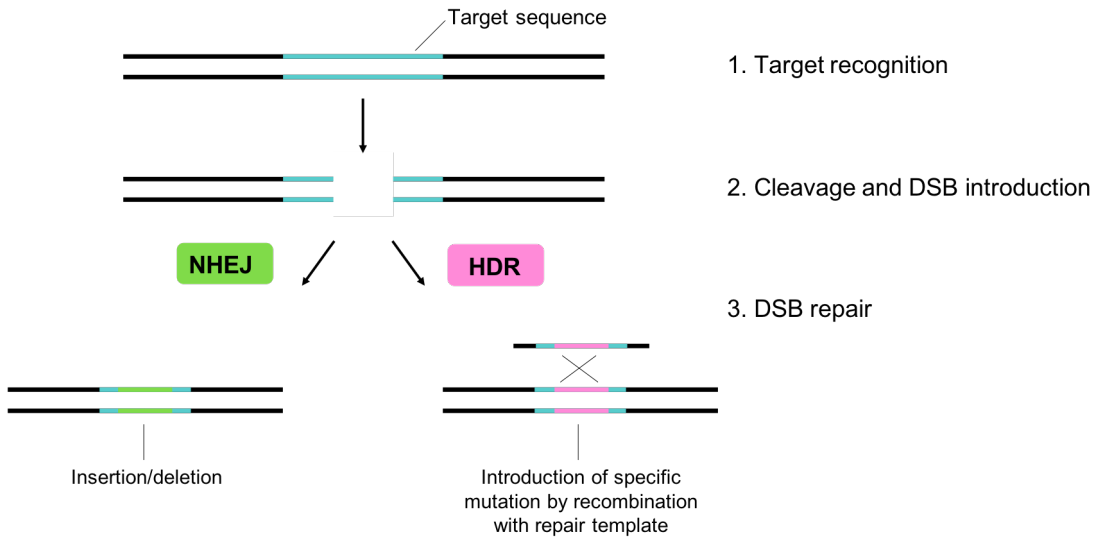

Figure 1.5 – Double stranded break repair outcomes

Following target recognition (1) and cleavage of the target site by a nuclease (2), DSBs can be repaired by two main mechanisms – NHEJ and HDR (3). NHEJ results in the insertion of random nucleotides or deletion of the sequences flanking the cleavage site. HDR requires a repair template which contains a specific mutation to be introduced flanked by homology to the regions encompassing the cleavage site. Homologous recombination between the genome and the repair template results in the introduction of the desired mutation.

1.16.2 CRISPR-Cas system

1.16.2.1 The CRISPR-Cas9 type II system

In 2013, the exploitation of a bacterial acquired immunity system revolutionised genome editing (Cong et al., 2013; Ran et al., 2013a). The Clustered Regularly Interspaced Short Palindromic Repeats (CRISPR) array and its CRISPR associated proteins (Cas) comprise an RNA-guided mechanism by which invading bacteriophage DNA is cleaved to prevent re-infection (Mojica et al., 1993; Mojica et al., 2005; Jansen et al., 2002; Figure 1.6). CRISPR systems are divided into two main categories – type I systems which require the actions of multiple Cas proteins and type II systems which rely only upon

the activity of the Cas9 nuclease (Brouns et al., 2008; Jinek et al., 2012). The most widely characterised and implemented system is the *Streptococcus pyogenes* (*S. pyogenes*) type II system which will be described here. Sections of the invading DNA called protospacers lie immediately upstream of the protospacer adjacent motif (PAM). The PAM consists of a dinucleotide repeat (NGG – where N is any nucleotide) and acts as a recognition sequence for Cas9 (Bolotin et al., 2005). Following infection, protospacers are incorporated into the CRISPR array in the bacterial genome - a cluster of repeats that lie downstream of the *Cas* genes. Following incorporation of the protospacers into the CRISPR array, the CRISPR locus is transcribed, producing immature, precursor CRISPR RNAs (crRNAs). These long RNAs are cleaved into their mature form that comprise a single protospacer sequence. Following re-infection of the bacterial cell, the crRNAs form a duplex with a small RNA unique to the type II system – the transactivating CRISPR RNA (tracrRNA) (Deltcheva et al., 2011). The RNA duplex binds Cas9 and guides it to the invading DNA where the crRNA binds to its complementary sequence and Cas9 introduces a double stranded break. The mechanism by which Cas9 recognises the PAM and cleaves DNA is partially understood. Cas9 has two nuclease domains – HNH and RuvC. The HNH domain cleaves the DNA strand that is complementary to the crRNA sequence and the RuvC domain cleaves the opposite strand (Jinek et al., 2012; Gasiunas et al., 2012). Importantly, the recognition of the PAM sequence is critical to the ability of Cas9 to cleave. It is postulated that PAM recognition triggers a conformational change in the Cas9-RNA complex into an active form, enabling the formation of an R-loop (Nishimasu et al., 2014)

The CRISPR-Cas9 system provides a programmable, sequence specific genome editing tool. For exploitation in mammalian cells, the system requires only the Cas9 nuclease, a short RNA sequence comprising the target sequence (which must lie upstream of a PAM) and a tracrRNA which can be fused to the sequence specific guide RNA (gRNA) (Jinek et al., 2012). Unlike ZFNs and TALENs, the sequence specificity of the CRISPR-Cas9 system is conferred by a short RNA sequence and does not require protein engineering. Thus, the system is more rapidly programmable.

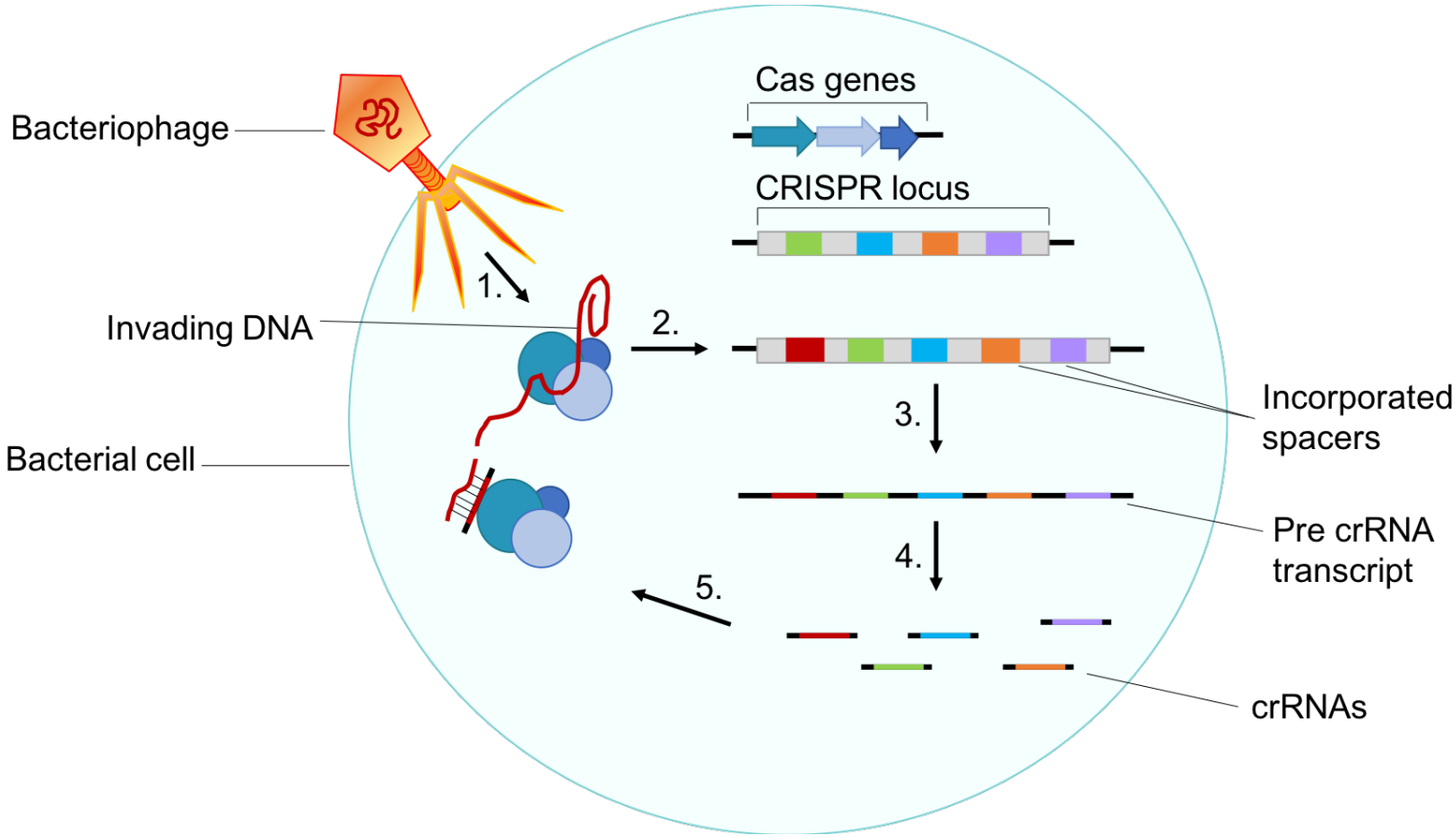

Figure 1.6 – CRISPR-Cas mechanism

Invading bacteriophage DNA enters the cell (1) and is incorporated into the CRISPR array through association with Cas proteins (2). Following transcription of the CRISPR locus, a pre crRNA transcript is formed (3) which is cleaved by Cas genes into mature crRNAs (4). Following reinfection, the crRNAs are able to associate with the Cas genes and guide a Cas nuclease to the invading DNA through base pair complementarity. Here, the crRNA binds its complementary site and a Cas nuclease introduces a double-stranded break (5).

1.17 Thesis aims

This thesis aims to investigate the molecular mechanisms of calcium dysregulation in malignant hyperthermia susceptibility. This will be achieved through developing a novel CRISPR-Cas9 pipeline for the introduction MH-associated *RYR1* variants into a skeletal myoblast cell line, overcoming the existing limitations of variant characterisation. Since a growing body of evidence suggests a role of *CASQ1* in conferring MH susceptibility, this thesis also aims to develop systems for the characterisation of human *CASQ1* variants identified in patients referred to the Leeds MH unit, through the generation of a *Casq1* knockout C2C12 cell line and characterisation of the Ca^{2+} binding and polymerisation capacities of three CASQ1 variant proteins using *in-vitro* biochemical assays. This work will contribute to the understanding of the mechanisms underlying calcium dysregulation in MH and ultimately, provide a biologically relevant characterisation process of MH-associated variants that broadens the availability of DNA diagnostics in MH.

1.18 Thesis objectives

1.18.1 Develop a novel characterisation process of *RYR1* variants identified in MHS individuals

The main objective of this thesis is to develop a novel characterisation pipeline for rare, missense *RYR1* variants identified in MHS individuals. Candidate variants will be selected from data generated through NGS of fifty genes associated with calcium handling, already performed by the Leeds MH unit. CRISPR-Cas9 genome editing will be used to engineer candidate variants into immortalised human myoblasts and C2C12 mouse myoblasts. The functional effects of these variants on Ca^{2+} release from the SR will be investigated by fluorescence Ca^{2+} imaging upon stimulation of Ca^{2+} release by caffeine.

1.18.2 Investigate the functional and biochemical effects of *CASQ1* variants identified in MHS individuals

CRISPR-Cas9 genome editing will be used to knockout out of expression of the endogenous *Casq1* gene in C2C12 mouse myoblasts and the consequence of *Casq1* ablation determined by Ca^{2+} imaging. This cell line will provide a vehicle for the re-introduction of human *CASQ1* cDNAs encoding variants of interest in the future, for the determination of the functional effect of the variants on Ca^{2+} release. In addition, wild-type human *CASQ1* and cDNAs encoding three pre-selected *CASQ1* variants will be cloned into expression vectors, for heterologous protein expression and purification in *Escherichia coli* (*E. coli)*. The effect of the variants on CASQ1 polymerisation and Ca^{2+} binding will be investigated using a range of biochemical and biophysical techniques.

Chapter 2 - Materials and Methods

2.1 General cell culture methods

2.1.1 Immortalised human myoblast culture

Immortalised human myoblasts (Mouley group, Institut de Myologie, Paris) were cultured in growth medium consisting of Hams-F10 (Gibco®) supplemented with 20% (v/v) heat inactivated fetal bovine serum (FBS; Gibco®),1X penicillin/streptomycin (50 units/ml penicillin, 50 µg/ml streptomycin), and human fibroblast growth factor (hFGF) to a final concentration of 2.5 ng/ml. The human immortalised myoblasts were, for some experiments, cultured in PromoCell Skeletal Muscle Growth Medium supplemented with 25% (v/v) fetal calf serum, 50 µg/ml bovine fetuin, 10 ng/ml human epidermal growth factor (hEGF), 1 ng/ml hFGF, 10 µg/ml insulin and 0.4 µg/ml dexamethasone (PromoCell). Where each growth media was used is clearly indicated in section 3.2. Tissue culture flasks were coated in entactin-laminin-collagen (ECL) cell attachment matrix (Merck Millipore). A 20 µg/ml stock solution of ECL was made in serum-free Hams-F10 media) and added to culture vessels to a final concentration of 5 µg per cm^2 by incubation at 37°C for 1 hour prior to plating. Cells were incubated at 37°C with 5% CO_2.

2.1.2 C2C12 mouse myoblast culture

C2C12 mouse myoblasts were cultured in growth medium consisting of DMEM GlutaMAX™ high glucose, high pyruvate media (Gibco®) supplemented with 10% (v/v) heat inactivated FBS (Gibco®) and 1X penicillin/streptomycin. Cells were incubated at 37°C with 5% CO_2.

2.1.3 HEK293 FT culture

HEK293 FT cells were cultured in growth medium consisting of DMEM GlutaMAX™ high glucose, high pyruvate media (Gibco®) supplemented with 10% (v/v) FBS, 1X penicillin/streptomycin and 500 µg/ml Geneticin™ for maintenance of cells transformed with the SV40 enhancer. Cells were incubated at 37°C with 5% CO_2.

2.1.4 Cell passage

To passage, media was aspirated and 4ml 0.25% trypsin-EDTA (Gibco®) added to the cells in a T-75 flask prior to incubation at 37°C for ~4 min (trypsin volumes were appropriately scaled for different culture vessels). The detached cells were added to 20ml phosphate buffered saline (PBS; Gibco®), centrifuged at 400 x *g* for 6 min and the cell pellet resuspended in warm growth media.

2.1.5 Cryostorage of cell lines

Cells were pelleted as described in 2.1.4 and resuspended in 900 µl growth media. The cells were transferred to a 2 ml cryovial containing 100 µl dimethyl sulfoxide (DMSO) and mixed by inversion. The cells were cooled slowly by transfer to a freezing container and placed in the -80°C freezer. After at least 24 hours in the -80°C freezer, cells were transferred to liquid nitrogen storage at ~ -200°C.

2.1.6 Myoblast differentiation

Aliquots of Extracellular Matrix (ECM) Gel from Engelbreth-Holm-Swarm murine sarcoma (Sigma) were thawed on ice overnight and diluted 1:1 in serum-free DMEM. Black, clear bottom 96-well plates (Greiner) and pipette tips were pre-chilled at -20°C and 30 µl of the diluted gel added to the desired wells in a chilled 96-well plate. The plate was placed on a rocking device for 30 min at room temperature to ensure an even layer of the gel was dispersed on the well surface. The plate was then incubated at 37°C, 5% CO_2 for 1 hour.

Myoblasts were plated on ECM gel-coated wells at 2 x 10^4 cells per well of a black, clear bottom 96-well plate (Greiner) in growth media. The following day, when cells had reached ~90% confluency, growth media was aspirated and replaced with 200 µl differentiation media. Differentiation media consisted of DMEM GlutaMAX™ high glucose, high pyruvate media (Gibco®) supplemented with 2% (v/v) horse serum (Sigma), 1 µM insulin (Sigma) and 1X

penicillin/streptomycin, was added to myoblasts and changed every other day for 5-6 days.

2.1.7 Cell counting and cell viability analysis

Cells were detached, pelleted and resuspended, as described previously, in 1ml media. Ten µl of trypan blue (Gibco®) was added to 10 µl cells and 10 µl of the mixture loaded onto a haemocytometer for counting.

2.1.8 Fluorescence activated cell sorting

Transfected cells were detached, pelleted and resuspended at ~1.5 x 10^6/ml in growth media, as described previously. Resuspended cells were filtered through a 70 µm cell strainer and transferred to FBS-coated 5 ml polypropylene fluorescent activated cell sorting (FACS) tubes. To prevent cell aggregation, FACS tubes were and kept on ice prior to cell sorting. FACS was performed using the BD Influx™ Cell Sorter (BD Biosciences) and was provided as a service by Dr Adam Davison and Mrs Liz Straszynski at Leeds Institute of Medical Research at St James' Hospital (Leeds, UK). Gates were drawn to exclude non-viable cells from the sort. For all cell sorts, a non-transfected control population of cells was provided to enable the determination gating boundaries for the OFP/GFP-expressing cells. OFP-expressing cells were detected using the 561 nm laser and 585/30 bandpass filter. GFP-expressing cells were detected using the 488 nm laser and 530/40 bandpass filter. Cells were collected in 1 ml growth media or a 1:1 ratio of conditioned media to growth media to a final volume of 200 µl for cell sorting into an ECL-coated 96 well plate.

2.2 General DNA methods

2.2.1 DNA extraction from mammalian cells

Cell pellets were resuspended in lysis buffer (25 mM ethylenediaminetetraacetic acid (EDTA) and 2% (w/v) sodium dodecyl sulfate (SDS)) at 1ml per 1 x 10^6 cells and agitated by pipetting up and down. One third volume of 10 M ammonium acetate was added and the sample mixed by inversion. The samples were centrifuged at 3200 *x g* for 15 min and the supernatant transferred to a clean Falcon tube. For large samples (>1 ml), 1 volume of 100% isopropanol was added. For smaller samples, 2.5 volumes of cold 100% ethanol was added. For isopropanol precipitation, the sample was mixed by inversion until DNA was visible. For ethanol precipitation, the sample was incubated overnight at -20^{o}C. Precipitated DNA was pelleted by centrifugation at 3200 *x g* for 15 min. The supernatant was discarded and the cell pellet washed in 70% (v/v) ethanol for a total of 2 washes. The pellet was left to air dry for 10 min at room temperature before being resuspended in nuclease-free water (Ambion) and quantified using the NanoDrop™ 1000 spectrophotometer (ThermoFisher).

Where contaminants were present, indicated by 260/230 and 260/280 ratios, samples were further purified by adding an equal volume of phenol:chloroform:isoamyl alcohol (24:25:1) and mixing thoroughly to form an emulsion. The sample was separated by centrifugation at 13,200 *x* g for 5 min. The aqueous layer was transferred to a clean tube and an equal volume of chloroform added. The sample was mixed and centrifuged at 13,200 *x g* for 5 min. The aqueous layer was transferred to a new tube and 0.1 volumes of 3 M sodium acetate (pH 5.2) was added. DNA was precipitated and resuspended as described previously.

2.2.2 PCR

Primers for PCR were designed using Primer Blast (Ye et al., 2012) and commercially synthesised by Integrated DNA Technologies (IDT). Lyophilised primers were resuspended to 10 µM in nuclease-free water. Where PCR

products were used in Gibson cloning applications, the Q5® hot start high-fidelity polymerase (NEB) was used in a 50 µl reaction comprising 1X Q5® reaction buffer (NEB), 0.2 mM dNTPs, 0.2 µM forward primer, 0.2 µM reverse primer, 10-200 ng template DNA, 1 unit Q5® hot start high fidelity DNA polymerase and nuclease-free water to 50 µl. For all other PCR applications, DreamTaq polymerase (ThermoFisher) was used in a 50 µl reaction. The composition of the reaction was the same as described previously, but with 1.25 units DreamTaq polymerase. For difficult to amplify PCR reactions, DMSO was added to a final concentration of 5%.

To visualise PCR products, 2 µl 6X purple gel loading dye (NEB; 1X components: 2.5% (w/v) Ficoll®-400, 10 mM EDTA, 3.3 mM Tris-HCl, 0.08% (w/v) SDS, 0.02% (w/v) Dye 1 and 0.0008% (w/v) Dye 2) was added to 10 µl PCR product. 10 µl sample was loaded onto a 1% (w/v) agarose gel made with 1X Tris-acetate-EDTA (TAE) buffer (40 mM Tris, 20 mM acetic acid and 1 mM EDTA) containing 0.5 µg/ml ethidium bromide. PCR products were separated by gel electrophoresis at 120 V for 40 min. Gels were visualised using ultraviolet (UV) light in the UGenius gel imaging system (Syngene).

2.2.3 Direct PCR

2.2.3.1 Mammalian cells

Cells were trypsinised and 10 µl of the detached cells transferred to a PCR tube containing 15 µl nuclease-free water. Cells were centrifuged at 4000 *x g* for 6 min, the supernatant discarded and the cells resuspended in 200 µl nuclease-free water. Cells were heated at 99^{o}C for 10 min before adding proteinase K to a final concentration of 200 µg/ml and the reaction incubated at 56^{o}C for 30 min. Proteinase K was inactivated by incubation at 96^{o}C for 10 min and the reaction cooled on ice for 5 min. 2.5 µl of the cell lysate was added to a 50 µl PCR.

2.2.3.2 Bacterial colonies

A PCR was set up as described in 2.2.2. A sterile pipette tip was used to pick a single bacterial colony on an agar plate and the pipette tip swirled into the PCR mixture.

2.2.4 PCR product purification

Where necessary, PCR products were purified using AMPureXP beads (Beckman Coulter) according to manufacturer's instructions. PCR products were pooled and 1.8 volumes of room-temperature beads added and mixed by pipetting up and down 10 times. The mixture was incubated at room temperature for 10 min to allow for binding of DNA to the beads before transfer to a magnetic rack for 5 min to separate the beads from solution. The supernatant was removed and the DNA-bound beads washed with 800 µl 70% (v/v) ethanol for a total of two washes. The DNA-bound beads were allowed to air dry at room temperature for 10 min before being removed from the magnetic rack and resuspended in 40 µl nuclease-free water. The reaction was transferred to a magnetic stand for 5 min to separate the beads from the solution and the solution carefully transferred to a new tube.

2.2.5 Restriction digest

Restriction digest reactions comprised 0.5-1 µg plasmid DNA, 1 µl of each restriction enzyme and the corresponding buffer to a final concentration of 1X and made up to 20 µl with nuclease-free water. FastDigest enzymes (ThermoFisher) and High-Fidelity HF® enzymes (NEB) were incubated at 37^{o}C for 10 min and inactivated at 80^{o}C for 20 min (unless manufacturer recommended alternative temperatures). Ten µl of the sample was loaded onto a 1% (w/v) agarose gel made with 1X TAE buffer containing 0.5 µg/ml ethidium bromide. The gel was electrophoresed at 120 V for 40 min to 1 hour and the products visualised using the UV UGenius gel imaging system (Syngene).

2.2.6 Sanger sequencing

Where Sanger sequencing was performed at the Leeds Institute of Medical Research at St James' University Hospital, unincorporated dNTPs and primers were removed by incubating 2 µl Illustra^{TM} ExoProStar^{TM} (GE Healthcare) with 5 µl PCR product for 30 min at 37^{o}C and then for 15 min at 80^{o}C for deactivation. Cycle sequencing was performed using 1 µl BigDye^{TM} Terminator (Applied Biosystems) , 1 µl half BD^{TM} reagent (Merck Millipore), 1 µl of primer to a final concentration of 3.2 µM, 2 µl sample and was made up to 10 µl with nuclease-free water. The DNA template was denatured at 96^{o}C for 5 min prior to 30 cycles of 96^{o}C for 30 seconds, 68^{o}C for 20 seconds and 60^{o}C for 4 min. The resultant products were precipitated in ethanol as described previously and air-dried at room temperature for 20 min. The air-dried pellets were stored at -20^{o}C. At least one hour prior to Sanger sequencing, pellets were resuspended in 10 µl Hi-Di Formamide (Applied Biosystems). Sanger sequencing was provided as a service at Leeds Institute of Medical Research at St James' University Hospital (Leeds, UK) using the ABI3130xl Genetic Analyser (Applied Biosystems). Where sequencing was outsourced, un-purified PCR products and 3.2 µM primers were sent by post to SourceBioscience (Cambridge, UK) for clean-up and Sanger sequencing. Sanger sequencing reads were analysed using 4Peaks software (Nucleobytes).

2.3 General bacterial methods

2.3.1 Transformation

Escherichia.coli (*E. coli*) cells were thawed on ice for 15 min prior to transformation. Two µl of the DNA product was added to 50 µl of cells and mixed gently by flicking the bottom of the tube. The tube was incubated on ice for 30 min. The cells were heat shocked at 42^{o}C for 45 seconds using a heated block or water bath and incubated on ice for 2 min. Five-hundred µl Super Optimal broth with Catabolic repressor (SOC) medium (Invitrogen^{TM}; 2% tryptone, 0.5% yeast extract, 10 mM NaCl, 2.5 mM KCl, 10 mM MgCl2, 10 mM MgSO4, and 20 mM glucose) was added to the cells and the mixture incubated at 37^{o}C with shaking at 200 rpm for 1 hour. Depending on the expected

transformation efficiency, between 100 µl and 500 µl of the transformation reaction was plated on a Lysogeny Broth (LB) agar (Invitrogen; 1% (w/v) SELECT peptone 140, 0.5.% (w/v) SELECT yeast extract, 0.5% (w/v) NaCl, 1.2% (w/v) SELECT agar) plate containing ampicillin at 100 µg/ml.

For XL10-gold® ultracompetent cells, (Agilent) cells were thawed on ice for 20-30 min. Four µl beta-mercaptoethanol was added to 100 µl cells and the mixture incubated on ice for 10 min, swirling periodically. The cells were heat shocked at 42^{o}C for 30 seconds using a heated block and incubated on ice for 2 min. Five-hundred µl SOC medium was added to the cells and the mixture incubated at 37^{o}C with shaking at 200 rpm for 1 hour. The entire transformation reaction was plated onto an LB agar plate containing ampicillin at 100 µg/ml, 40 µl 100 mM IPTG and 120 µl 20 mg/ml X-gal spread onto the surface of the plate.

2.3.2 Bacterial culture for plasmid prep

Following transformation, single colonies were picked from LB agar plates using a pipette tip and the tip transferred to 5 ml LB media (1% (w/v) SELECT peptone 140, 0.5% (w/v) SELECT yeast extract, 0.5% (w/v) NaCl) containing the appropriate antibiotic(s) concentration in Falcon tubes. Overnight cultures or starter cultures for utilisation in downstream maxi-preps were grown at 37^{o}C with shaking at 200 rpm.

2.3.3 Plasmid mini prep

5ml overnight cultures were pelleted by centrifugation at 4000 *x g* for 10 min at 4^{o}C. Plasmid isolation was performed using the QIAGEN QIAprep® spin miniprep kit according to manufacturer's instructions. The pellet was resuspended in 250 µl Buffer P1 (50 mM Tris-HCl pH 8.0, 10 mM EDTA, 100 µg/ml RNaseA) by vortexing and transferred to a microcentrifuge tube. Cells were lysed by the addition of 250 µl Buffer P2 (200 mM NaOH, 1% SDS) and the tube inverted multiple times to mix. The lysis solution was neutralised by adding 350 µl Buffer N3 (4.2 M Gu-HCl, 0.9 M potassium acetate pH 4.8) and

mixed immediately by inversion. The solution was centrifuged at maximum speed in a table-top centrifuge for 10 min. The resultant supernatant was applied to a QIAprep 2.0 spin column, centrifuged for 60 seconds and the flow-through discarded. Any trace nuclease activity was removed by the addition of 500 µl Buffer PB (5 M Guanidine-HCl, 30% v/v isopropanol) to the spin column and centrifugation at maximum speed for 60 seconds. The flow-through was discarded and 750 µl Buffer PE (10 mM Tris-HCl pH 7.5, 80% v/v ethanol) was applied to the spin column to remove contaminants. The flow through was discarded and the spin column centrifuged for 60 seconds to remove any residual Buffer PE. Finally, spin columns were placed into clean microcentrifuge tubes and 50 µl nuclease-free water was added to the spin column. The spin column was left to stand at room temperature for 5 min prior to centrifugation for 1 min to elute the plasmid DNA. Plasmid DNA was quantified using the NanoDrop^{TM} 1000 spectrophotometer.

2.3.4 Plasmid maxi prep

Maxi prep cultures were generated by using 200 µl of starter culture to inoculate 200 ml of LB media containing 100 µg/ml ampicillin. The culture was incubated overnight at 37^{o}C with shaking at 200 rpm. Plasmid isolation was performed using the QIAGEN-Tip 500 plasmid maxi kit or QIAGEN HiSpeed plasmid maxi kit according to manufacturer's instructions. Plasmid DNA was resuspended in TE buffer (QIAGEN; 10 mM Tris·Cl, pH 8.01 mM EDTA) and quantified using the NanoDrop^{TM} 1000 spectrophotometer.

2.3.5 Establishment of glycerol stocks

Glycerol stocks were established for long term storage of plasmids. 500 µl overnight culture was added to 500 µl 50% (v/v) glycerol and vortexed briefly to mix. The stocks were stored at -80^{o}C.

2.4 *In-silico* pathogenicity prediction methods

2.4.1 Pathogenicity prediction tools

Three tools were used to predict pathogenicity of the selected MH-associated VUS. Sorting Intolerant From Tolerant (SIFT) predicts whether a missense variant will affect protein function based on the conservation of the residue or the conservation of the class of amino acid at that position, that is, its charge state and polarity (Ng and Henikoff, 2003; Sim et al., 2012). SIFT scores were generated using SIFT 4G (2018) available at https://sift.bii.a-star.edu.sg/sift4g/. Polymorphism Phenotyping 2 (PolyPhen-2) predicts whether a missense variant is likely to be damaging based on its predicted effect on protein structure and function (Adzhubei et al., 2010). PolyPhen2 scores were generated using PolyPhen-2 v2 (2018) available at http://genetics.bwh.harvard.edu/pph2/. The combined annotation dependent depletion tool (CADD) combines 63 *in-silico* pathogenicity prediction annotations to compute a CADD score (C score) (Kircher et al., 2014). C scores were generated using CADD v1.4 (2018) available at https://cadd.gs.washington.edu/score.

2.4.2 Conservation analysis

The entire human RYR1 amino acid sequence (P21817.3) and human CASQ1 amino acid sequence (NP_001222.3) were entered into The ConSurf Server (Ashkenazy et al., 2016; Celniker et al., 2013; Asheknazy et al., 2010; Berezin et al., 2004) available at http://consurf.tau.ac.il. CSI-BLAST (Angermuller et al., 2012) was used to search for homologues in the UniRef90 database (Suzek et al., 2015) and MAFFT L-INS-i version 7.392 (Katoh et al., 2002; Katoh and Standley, 2013) was used to create a multiple sequence alignment using the Bayesian calculation method. To limit the analysis to RYR1 homologues and CASQ1 homologues (excluding other RYR/CASQ isoforms), ConSurf was programmed to search only for sequences with >70% homology to the human RYR1 sequence and >50% homology to the human CASQ1 sequence.

2.4.3 PyMOL mutagenesis

The rabbit RYR1 (PDB ID: 3J8H; Yan et al., 2015) human CASQ1 (PDB ID: 5CRD; Lewis et al., 2015) protein structures were opened in PyMOL Molecular Graphics System version 2.0 (Schrödinger, LLC). Sequences were displayed and the residue of interest was selected. From the action panel, polar contacts to any atom excluding the solvent were found and displayed. From the wizard panel, mutagenesis was selected and the desired residue substitution introduced. Polar contacts to any atom excluding the solvent were re-selected with the substituted residue.

2.5 CRISPR-Cas9 methods

Unique sequences designed for gRNAs and HDR templates are reported as results in sections 3.2.4, 4.2.4 and 5.2.2. As such, specific oligonucleotide sequences of gRNAs (with and without appended overhangs for pSpCas9(BB)-2A-GFP and pGCS cloning), gRNA specific primers for *in-vitro* gRNA synthesis, and HDR templates are detailed there.

2.5.1 gRNA design and off-target prediction

2.5.1.1 *RYR1/Ryr1* gRNA design for human immortalised myoblasts and C2C12 myoblasts

A 100 bp sequence flanking the base to be edited (human *RYR1* reference sequence: NG_008866.1; mouse *Ryr1* reference sequence: NC_000073.6; was entered into CRISPR/Cas9 Target Online Predictor (CCTOP; Stemmer et al., 2015) available at https://crispr.cos.uni-heidelberg.de/. CCTOP was programmed to search for gRNAs in the GRCh38 and GRCm38/mm10 genomes using the *Streptococcus pyogenes* (*S. pyogenes*) PAM of NGG (where N is any nucleotide), that were 20 nt in length and unique sequences in the genome. CCTOP ranks gRNAs based on the number and location (i.e. whether they are located in introns, exons or intergenic regions) of predicted off-target sites. The top three ranked gRNA sequences that had Cas9 cut sites within 30 bp of the base to be edited were selected for testing of gene-editing in the appropriate cell line. Within CCTOP, an efficacy prediction was made by CRISPRater (Labuhn et al., 2017) based on the analysis of molecular features

associated with highly active gRNAs such as PAM-distal GC content. The gRNAs with efficacy values <0.56 are deemed low efficacy, gRNAs with efficacy values ≥0.56 but ≤0.74 are deemed medium efficacy and gRNAs with efficacy values >0.74 are deemed high efficacy

The same 100 bp sequence was entered into CRISPOR (Haeussler et al., 2016) available at http://crispor.tefor.net/ to confirm the off-target predictions made by CCTOP and identify any others. CRISPOR was programmed to search for gRNAs and associated off-targets using the same parameters as CCTOP (20 bp gRNA and the NGG PAM). Following gRNA selection, the top 10 predicted off-target sites from each tool were selected for primer design (Table 2.1) and subsequent Sanger sequencing in the resultant cell lines.

Table 2.1 – Primers used to sequence Ryr1 p.D3986E and p.S1728F off-target sites

Where multiple primer sets were tested, the underlined primer sequences show the primer set that generated successful PCR amplification and Sanger sequencing reads.

Variant and off target site	Forward primer 5'-3'	Reverse primer 5'-3'
p.D3986E; Ptpn14	CCCTAATGTCACACTCCGCT	GCGTGACAATCACGATCCCT
p.D3986E; Bcat1	TGTGCAACCATGAGAGCCTG	AGCACACACTTGCTGACCTT
p.D3986E; RP23-267G12.1	TTTGCAGGGTAGCTGGTCAA	AGCTGTGGTCAGGCAAATCT
p.D3986E; Med23	TGCTTTTTGAGATGGGTCTTGC	AAAGACGGGGTGACTCACAC
p.D3986E; Nrros	ATAGGCAAGGTTGAGACGCC	CCTGTGGAACCATTCCCTCC
p.D3986E; Gm4889-Dusp4	TTTTCAGGGCTGATTGGCAC	ACTGCTTACTCCCACTTGCC
p.D3986E; Gm23796-Gm23831	TGTGGAGGTGAGTCTCTGCT	CACCCAAGTCCAGACTGAGC
p.D3986E; Zmiz1	TCCCCTTGTTAGGAGGCAGA	ACAGACACACGGAGAACGAC
p.D3986E; Pabpc6-Qk	GCCATCCTACCAGAACCCTG	AGAGGAAGCAGCAGTTTGCT
p.D3986E; Optn	AGTCCATCTCAGGGACGACA	TCCAGATTCTTTGCCGTGGT
p.D3986E; Gm3898	1 TGGCAGAACGATTGAGCAGA	1 GGGATCTTGTGTGGAACCCA
	2 GACCACGTGTATGGCTCCAA	2 TCTGTAACCACACCTGGGGA
	3 GCTGTTGTATCTTCGGCTGC	3 TGGGTAGCAGGTGCTCAGTA
p.D3986E; Rreb1	1 ATCCTTCCAACGGTCAAGGC	1 CAAGGACCTGATGGGCTACC
	2 GGACCAGAGCCTCAGACTTC	2 CTGATGGGCTACCCTCTGTG
p.D3986E; Nkx6	1 GTAGACACCTGCAGACGAGG	1 GTCCTCTCGCTTTCCCGTAG
	2 GCCCGAAGTAGACACCTGC	2 CTGCCTTCTCTCTGACCGC
p.D3986E; 6030407O03Rik	1 AGAGCCTCTGCAAATTCCGA	1 GGCTCTGTAAGAGGGAAGCC
	2 AGAAGCCACACCGCTGTTAT	2 GGTCCTGTGAAGACACCTGG
p.D3986E; Smtnl2-Ggt6	1 TGGTTGCACAGATGAACACT	1 CTGGAGGGGGAAGGAACAAC
	2 CCACCTGGAGGCAAAGTAGG	2 TGAGTAGGCAGCAGGTAATGG
	3 GCACCTCTAAAATCTGTCAGGGA	3 GAGGGGGAAGGAACAACGAA
	4 GTGAAGAACGTTGCCTGATTGA	4 GGAAGGAACAACGAAGCCC
p.S1728F; Zhx2	ACATCAGTGTGACGGGCATT	TGGAAGCAAGGATGAACGCT
p.S1728F; Rpgrip1l	AAAAGGCAGAGTGGGCACAT	GGGCAAGGAAGAGTGTGGTT

p.S1728F; Cenph	GCAAAGGCCATTGGACACAG	TAGCAAAGCAACTCGGCTCA
p.S1728F; Ptprs	1 CCTGTTGTCCCTGTGGTCC	1 CGCCATCATCAAGTACACGG
	2 CTGTTGTCCCTGTGGTCCG	2 CTTCCCGCAGATCTTGGGC
p.S1728F; 2310022B05Rik	CAGGGTCACTGCATTCCACT	CTTCCTACCGCTGAGAGCAG
p.S1728F; Adcy1	AGCCTGGACAGACCCTACAT	GCAGACTGAGGCTCAAGGAG
p.S1728F; Dusp26	GGAGTGAGCAGATCCGCTAC	GGTCTTGGGGCTCTTCACTC
p.S1728F; Gm5464	CAATGGAGGGGTGATCGTCC	TAGATCTGCAAGCGCCACAA
p.S1728F; A930001A20Rik-Gm9733	GAGCTCTTTGACCTGACCCC	AAGCCTCACAACATGCAGGT
p.S1728F; Tnfrsf25	GGACATAGCCCCTCAGCTTC	TAGGTCGCCGGTGAAGACTA
p.S1728F; Gm12604-Mllt3	ATTAGCTCTTCCACGTGGGC	CCCAAAGCAATGCCTCTGAC
p.S1728F; Gm23892-Gm25382	GAGGTTGGAAGGGGAAAGCA	AGGCTGGCAGTTCAAAGTCC
p.S1728F; Aqp9-Aldh1a2	GCCCACAAGATTCCCCCTTT	GACCTTTTGCCCTGCTTGTG
p.S1728F; Gm25665-Gm24469	CCCTTAGCCACATGATTGCC	CCTCACCTCACTGTGTCACC
p.S1728F; Hmcn2	GAGATGGGCACCGTGAAGAA	GCTCTGAGCTGTGTCTCCAG
p.S1728F; Scara5	CACCTCTTCCACAGTGTCCC	GGAGTCACTCTGCTGTCCTG

2.5.1.2 *Casq1* knockout in mouse C2C12 myoblasts

The *Casq1* knock out gRNA sequences were designed as described for the *RYR1/Ryr1* gRNAs; however, a 450 bp sequence beginning at base 1 of exon 1 in the mouse Casq1 coding sequence (NM_009813.2) was entered into CCTOP and CRISPOR for gRNA design and off-target prediction. Two of the top gRNA sequences were selected for testing in C2C12 myoblasts. Following gRNA selection, all of the off-target sites were selected for primer design (Table 2.2) and Sanger sequencing in the resultant cell lines.

Table 2.2 – Primers used to sequence *Casq1* off-target sites

Where multiple primer sets were tested, the underlined primer sequences show the primer set that generated successful PCR amplification and Sanger sequencing reads.

Off-target site	Forward primer 5'-3'	Reverse primer 5'-3'
Gm24444	CCCCCGATGGAAGAAAAGCA	GATAGAGGCAGAGGCAGCAA
Dpep	AAGGGGTCCCGGAGTGC	GATTCCAGGCAGTAGGTCCC
Col15A	CACTGGATGGATGCCTTGGT	GAGCCTTATGTAACCCGCGA
Serpin	TGATTCCCCCTCTCCCCTTT	AACCTCATATGTACTACAAAGTCCT
pGap	TGTCCCTGCTGGAATTGCTT	TGGAGAGATGAGCCCACTGA
	AATCTCTCCTGTTCCTGCCC	CCAGCCTCTTTAGTCCAGCT
Gypc	GAGGCATCAAGAGTTTTCGAA	CCTAGTGCCACTGTTATAGCCT

The gRNA sequences for human *RYR1*-targetting gRNAs are detailed in 3.2.4, the gRNA sequences for mouse *Ryr1*-targetting gRNAs are detailed in 4.2.4, the gRNA sequences for mouse *Casq1*-targetting gRNAs are detailed in 5.2.2.

2.5.2 HDR repair template design for *RYR1/Ryr1* variant introduction

HDR repair templates were designed manually from genomic DNA reference sequences (NG_008866.1; NC_000073.6). The HDR arms were designed as 160 nt single stranded oligonucleotides (ssODNs), with 80 nt of complementarity to the sequences flanking the cut site. Silent mutations were introduced within either the PAM or seed region of the gRNA to prevent re-cleavage following incorporation of the HDR template. The ssODNs were commercially synthesised by Integrated DNA Technologies (IDT). HDR template sequences are detailed in 3.2.5 and 4.2.5.

2.5.3 Cloning of gRNAs into pSpCas9(BB)-2A-GFP

Cloning of gRNAs into the pSpCas9(BB)-2A-GFP vector (Figure 2.1) was performed as described in Ran et al., 2013a. The pSpCas9(BB)-2A-GFP vector was a gift from Feng Zhang (Addgene #48138). The desired gRNA

sequences were synthesised as single stranded HPLC purified oligonucleotidies by IDT.

Overhangs complementary to the resulting overhangs following digestion of pSpCas9(BB)-2A-GP with FastDigest™ *Bbs*I (ThermoFisher) were added to the 5' of the forward and reverse gRNA sequences (Figure 2.2). The appended sequences on the forward and reverse gRNA sequences were 5'-CACC-3' and 5'-ACCC-3', respectively. The forward and reverse single stranded DNA oligonucleotides comprising the gRNA sequences were resuspended in nuclease-free water (Ambion) to a final concentration of 100 µM. The forward and reverse oligonucleotides were phosphorylated and annealed in a reaction comprising each oligonucleotide at a final concentration of 10 µM, 1X T4 ligation buffer (NEB), 10 units of T4 polynucleotide kinase (NEB) and nuclease-free water to a final volume of 10 µl. In a thermocycler, the reaction was incubated at 37°C for 30 min, 95°C for 5 min and ramped down to 25°C at a rate of 5°C per min. The phosphorylated and annealed oligonucleotides were diluted 1:200 and added to a simultaneous digestion-ligation reaction consisting of 100 ng of pSpCas9(BB)-2A-GFP, 2 µl diluted oligonucleotides, 1X tango buffer (ThermoFisher; 33 mM Tris-acetate pH 7.9, 10 mM magnesium acetate, 66 mM potassium acetate, 0.1 mg/ml bovine serum albumin (BSA), dithiothreitol (DTT) to a final concentration of 0.5 mM, ATP to a final concentration of 0.5 mM, 1 µl FastDigest *Bbs*I (ThermoFisher), 1500 units of T7 DNA ligase (NEB) and nuclease-free water to a final volume of 20 µl. The reaction was incubated at 37°C for 5 min followed by 21°C for 5 min for a total of 6 cycles.

The reaction was incubated with PlasmidSafe ATP-dependent DNase (Epicentre) to remove remaining linear DNA. Two µl of the product was transformed into OneShot® chemically competent Stbl3™ cells (Invitrogen™), as described in 2.3.1. Four colonies per vector were picked and plasmid was isolated by mini prep as described in 2.3.3.

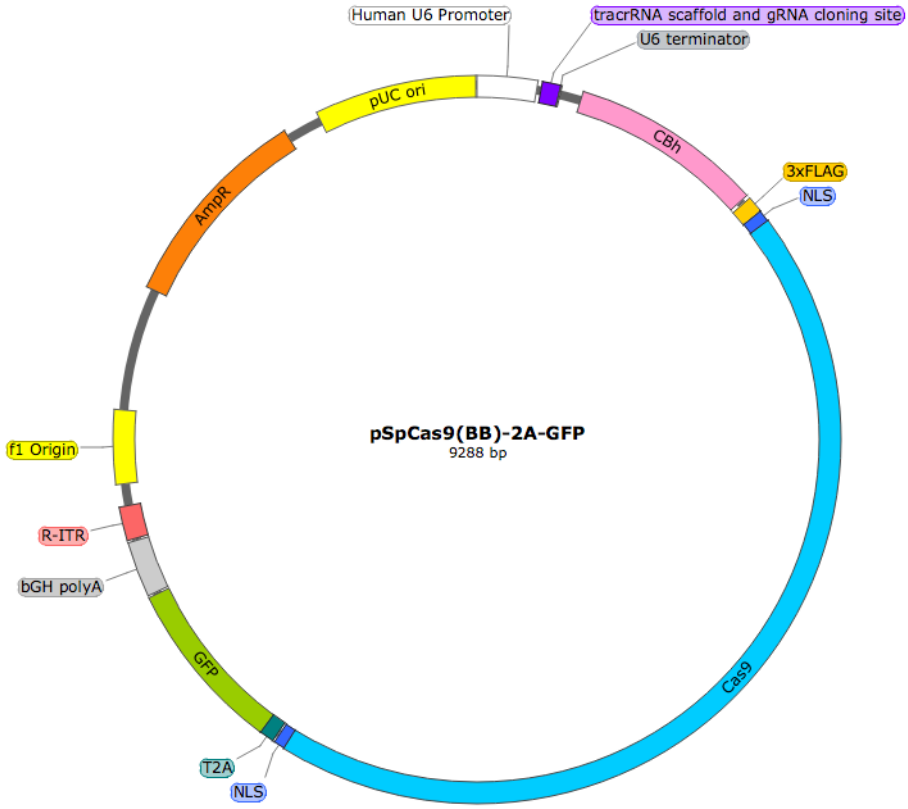

Figure 2.1 – Vector map of pSpCas9(BB)-2A-GFP

The pSpCas9(BB)-2A-GFP vector was purchased from Addgene (Addgene code PX458) where it had been deposited by Feng Zhang. Following the pUC origin of replication, the vector encodes the human U6 promoter for transcription of the tracrRNA-gRNA fusion. The Cas9 gene, flanked by two nuclear localisation signals (NLS), a 5' 3x FLAG peptide and a 3' T2A self cleaving peptide sequence, is transcribed by the hybrid chicken β-actin promoter (CBh). Downstream of the T2A cleavage site is the GFP coding sequence, the bovine growth hormone (bGH) poly A signal for transcript stability and an inverted terminal repeat which is required for packaging if generating adeno-associated virus (AAV). Vector maps were taken from Addgene (www.addgene.org/48138; accessed August 2019) and modified in SnapGene®.

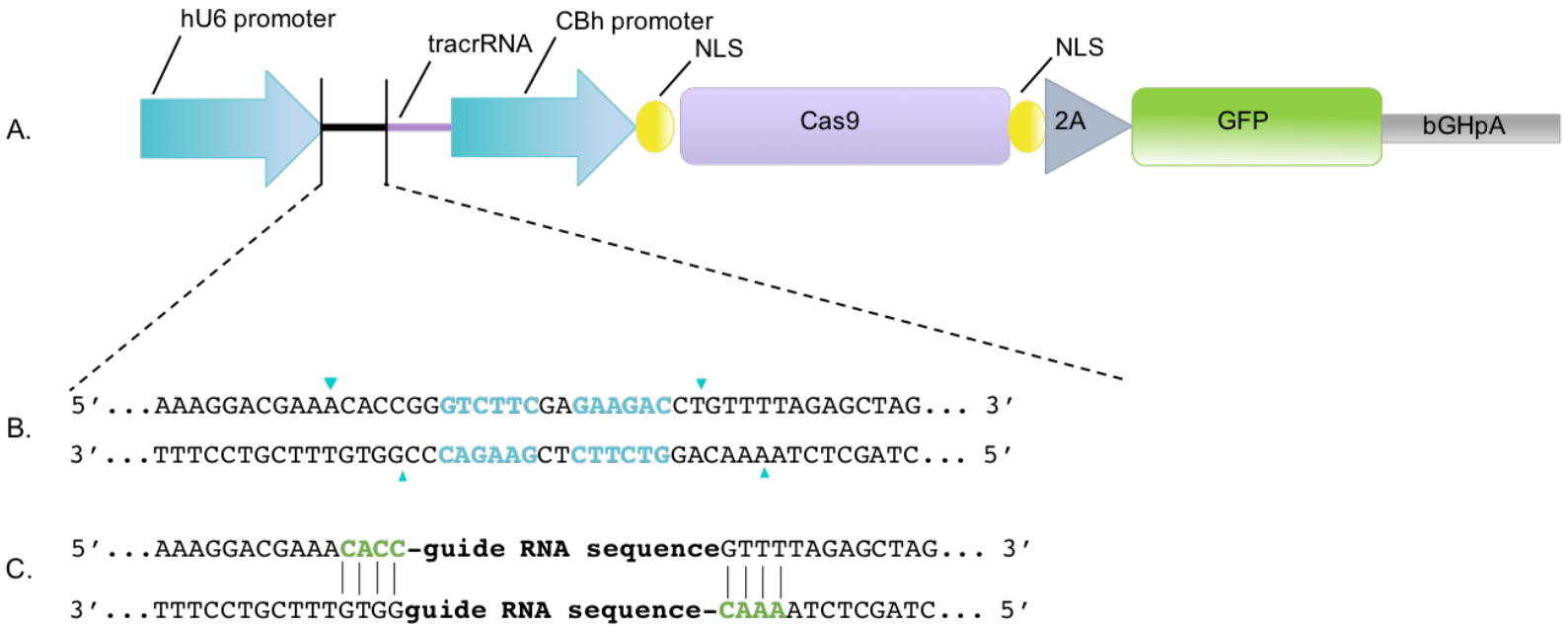

Figure 2.2 – Cloning into pSpCas9(BB)-2A-GFP

In pSpCas9(BB)-2A-GFP (Panel A), there are two *Bbs*I sites within close proximity. Digestion with *Bbs*I in these vectors leads to the excision of a small fragment of DNA and yields a bottom strand overhang of 3' GTGG 5' and a top strand overhang of 5' GTTT 3 (Panel B)'. Appendage of 5' CACC 3' to the 5' top strand gRNA and 5' AAAC 3' to the 5' of the bottom strand gRNA facilitates cloning into both vectors (Panel C). Adapted from www.addgene.org/crispr/zhang; accessed August 2019.

2.5.4 Cloning of gRNAs into pGCS

The GeneArt™ genomic cleavage selection kit (Invitrogen™) was used to select for cells that had successfully been transfected with Cas9 nuclease and *in-vitro* transcribed gRNAs. Oligonucleotides were designed that contained the gRNA sequence and the PAM sequence. To the top strand oligonucleotide, a 5' AATT overhang was appended and to the bottom strand oligo, a 5' CTAG overhand was appended. These overhangs are complementary to the overhang sequence on the linearised pGCS vector (Figure 2.3). Oligonucleotide sequences were synthesised by IDT and are detailed in 3.2.4.

The oligonucleotides were annealed and ligated into pGCS according to manufacturer's instructions. To anneal the oligonucleotides, each oligonucleotide to a final concentration of 5 µM, 1X ligation buffer (ThermoFisher; 50 mM Tris-Hcl, pH 7.6, 10 mM $MgCl_2$, 1 mM ATP, 1 mM DTT and 5% w/v polyethylene glycol (PEG) and nuclease-free water to 20 µl were added to a PCR tube and heated at 95°C for 5 min. The reaction was ramped down from 95°C to 85°C at a rate of -2°C/second and then from 85°C to 25°C at a rate of -0.1°C per second to anneal the forward and reverse oligonucleotides. The double-stranded oligonucleotides were diluted to 50 nM in nuclease-free water. A ligation reaction was performed by mixing 1X ligation buffer (ThermoFisher), 30 ng linearised pGCS, double stranded oligonucleotides to a final concentration of 5 nM, 1 unit T4 DNA ligase (ThermoFisher) and nuclease-free water to 20 µl. The reaction was incubated for 2 hours at room temperature and transformed into OneShot™ chemically competent Stbl3™ cells as described in 2.3.1. Single colonies were picked and used to inoculate 5 ml cultures of LB broth containing 100 µg/ml ampicillin. After ~ 8 hours of growth, samples of the cultures were taken and later used to as starter cultures for maxiprep, described in 2.3.4. The remaining sample was further incubated for up to 24 hours and used to isolate plasmid DNA by miniprep, described in 2.3.3.

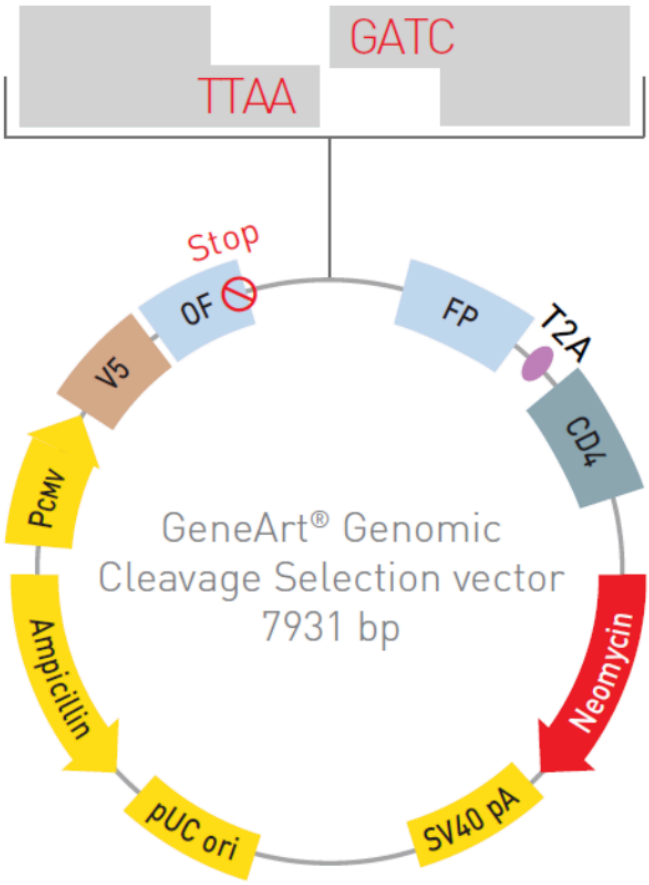

Figure 2.3 – Vector map of the GeneArt® Genomic Cleavage Selection vector, pGCS

The pGCS vector is provided linearised with the overhangs shown above the vector map. The vector contains a pUC origin of replication (ori). The cytomegalovirus promoter transcribes the V5 epitope, the OFP sequences for FACS-based selection, the CD4 coding sequence which can be used for bead-based enrichment or fluorescent labelling with an anti-CD4 fluorescently labelled antibody. A T2A cleavage site separates the OFP and CD4 sequences. Neomycin coding sequence allows for selection of the vector in mammalian cells while ampicillin allows for selection in bacterial cells. A polyomavirus simian virus 40 (SV40) polyadenylation signal terminates transcription. Vector map was taken from the User Guide: GeneArt® Genomic Cleavage Selection Kit (Life Technologies, 2015). Available at http://tools.thermofisher.com/content/sfs/manuals/GeneArt_Genomic_Cleavage_Selection_Kit_UG.pdf (Accessed August 2019).

2.5.5 *In-vitro* transcription of gRNAs

The GeneArt™ gRNA synthesis kit (Invitrogen™) was used to generate gRNAs from DNA templates according to manufacturer's instructions. Briefly, a forward primer (containing a region of complementarity to the T7 promoter

sequence and a 5' portion of the gRNA specific sequence) and primer 2 (with a region of complementarity to the tracrRNA and the 3' gRNA sequence that partially overlaps with the gRNA specific sequence on the forward primer) were designed (exact sequences are detailed in 3.2.4) and commercially synthesised as PAGE-purified single stranded DNA oligonucleotides by IDT. Primers were added to a PCR containing the tracr fragment sequence, the T7 forward primer and the tracr reverse primer. This yielded a ~ 100 bp PCR product which was used as the DNA template for *in-vitro* transcription (IVT) of the gRNA-tracr RNA sequence. The IVT reaction comprised 6 µl of the DNA template, 160 mM nucleoside-triphosphate (NTP) mix, 1X TranscriptAid™ reaction buffer and 2 µl TranscriptAid™ enzyme mix containing the T7 RNA polymerase made to 20 µl with nuclease-free water. The reaction was incubated at 37°C for 3 hours. The DNA template was removed by DNAse I digestion at 37°C for 15 min and the RNA purified using the gRNA clean up kit GeneJET™ RNA purification micro columns (Invitrogen™) according to manufacturer's instructions.

2.5.6 RNA agarose gel electrophoresis

1 µl sample was diluted in 4 µl nuclease-free water and mixed with RNA loading dye to a final concentration of 1X (NEB; 47.5% formamide, 0.01% SDS, 0.01% bromophenol blue, 0.005% xylene cyanol, 0.5mM EDTA). The sample was heated at 99°C for 10 min before electrophoresis on a 1% agarose-TAE gel at 100V for 1 hour.

2.5.7 RNA quantification

In-vitro transcribed RNA was diluted 1:10 and quantified using the QuBit® Broad Range (BR) RNA assay kit (ThermoFisher) according to manufacturer's instructions. Prior to starting, the kit was allowed to reach room temperature. Working solution was prepared by diluting the Qubit® RNA BR reagent (200X concentrate in DMSO) 1:200 in Qubit® RNA BR buffer, 190 µl working solution was added to 10 µl of Qubit® standard 1 (0 ng/µl in TE buffer) and Qubit® standard 2 (100 ng/µl in TE buffer) and mixed by vortexing. RNA samples were diluted 1:10 in nuclease-free water and 199 µl working solution added to 1 µl RNA sample. All tubes were incubated at room temperature for 2 min. On

the Qubit® fluorometer 2.0, RNA broad range was selected as the assay type. The tube containing Qubit® standard 1 was inserted into the sample chamber and the fluorescence read. This was repeated with Qubit® standard 2, followed by the RNA samples. The stock concentration of the RNA samples was calculated using the 'Calculate Stock Conc' function on the fluorometer and the value multiplied by 10 to account for the original 1:10 dilution.

2.5.8 Transfection of pSpCas9(BB)-2A-GFP and HDR templates

Plating densities and Lipofectamine™ 3000 reagent (Life Technologies) volumes for each cell line are shown in Table 2.3. Immediately prior to transfection, cells were plated in a 6-well plate in 1 ml growth media. Lipofectamine® 3000 reagent was diluted in 125 µl Opti-MEM media (Gibco®). Plasmid DNA, p3000 reagent at 2 µl/µg plasmid DNA and, where needed, a total of 5 µl of the 10 µM HDR template stock, were diluted in 125 µl Opti-MEM media and the mixture added to the diluted Lipofectamine mixture. Lipid:DNA complexes were incubated at room temperature for 15 minutes before being added drop-wise to the cells. Cells were incubated at 37°C with 5% CO_2 for 24 hours prior to FACS/viability analysis. Following 24 hours incubation, transfection efficiencies were estimated using the cell counting tool on the Evos™ FL Imaging System (ThermoFisher). Cells within 12 4mm^2 grids were counted and averages taken.

Table 2.3 – Volumes used for Lipofectamine™ 3000 transfection of human immortalised myoblasts and C2C12 myoblasts

All cell densities and volumes are for transfection in one well of a 6-well plate.

	Human immortalised myoblasts	C2C12 myoblasts
Plating density	~1.5 x 10^5	~2.5 x 10^5
Lipofectamine™ 3000	3.75 µl	7.5 µl
P3000 reagent	5 µl	10 µl
Plasmid DNA	2.5 µg	5 µg

2.5.9 Transfection of pGCS, Cas9 protein and HDR templates

Cells were plated at 1.5 x 10^5 cells per well in a 6-well plate immediately prior to transfection. 6.25 µg Cas9 nuclease (ThermoFisher), 1.2 µg gRNA, 2.5 µg pGCS (ThermoFisher), 12.5 µl Lipofectamine™ Cas9 plus™ reagent and, where needed, a total of 5 µl of a 10 µM stock of HDR templates were diluted in 125 µl Opti-MEM. 7.5 µl Lipofectamine™ CRISPRMAX™ reagent was diluted in 125 µl. The diluted complexes were mixed 1:1 and incubated at room temperate for 10 min before being added drop-wise to cells. Cells were incubated at 37°C with 5% CO_2 for 24 hours prior to FACS/viability analysis.

2.5.10 T7 endonuclease I assay

A T7 endonuclease 1 assay (T7 assay) was performed to estimate gene-editing efficiencies (Figure 2.4). PCR was performed to amplify a region surrounding the predicted Cas9 cut site (primer sequences for amplification are shown in Table 2.4). The PCR products were purified using Agencourt AMPureXP beads (Beckman Coulter). Purified products were quantified using the Nanodrop 1000. 600 ng DNA, 2 µl NEBuffer 2 and nuclease-free water to a final volume of 19.25 µl was added to a PCR tube. DNA was denatured by incubation for 5 min at 95°C and renatured by ramping down to 85°C at -2°C/sec, followed by ramp down to 25°C at -0.1°C/sec, 0.25 µl T7 endonuclease I was added and incubated at 37°C for 5 min. The reaction was terminated by adding EDTA to a final concentration of 2.5 mM, 20 µl of the reaction separated by electrophoresis on a 1% agarose-TAE gel as described in 2.2.2.

Table 2.4 – Primer sequences for amplification of the gRNA region for T7 assay

Editing event	Forward primer 5'-3'	Reverse primer 5'-3'	Size (bp)
p.D3986E human	GAGCAGGGCAAGAGGAACTT	CTCGGGTGACAAACTGACCA	388
p.D3986E mouse	ACTGGTATTACTCGGGCAAGG	CAATTCAGAAGGGGTTTGGGC	449
p.S1728F mouse	CTACAGCGCTTCCACTCACA	CCAACATTCTCAGCGCCTTG	475
Casq1 knockout mouse	CCCAGAAGGTGTCGTCCTTG	GCTCTTAAGCTAGCCCCCAC	1005

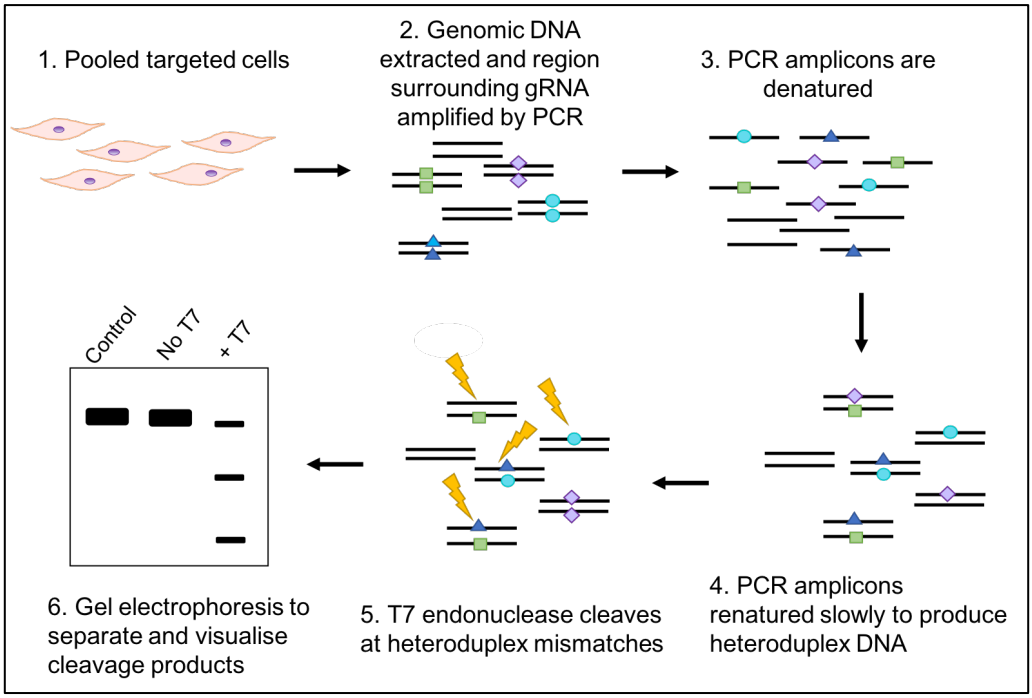

Figure 2.4 – Schematic of T7 endonuclease 1 assay
Transfected cells are enriched by FACS/antibiotic selection and pooled. 2. Genomic DNA is extracted from these cells and a PCR performed to amplify a region (500 bp – 1 kb) around the Cas9 cut site. This results in the amplification of a multitude of editing events. 3. PCR amplicons are denatured. 4. PCR amplicons are renatured slowly, using a ramp-down protocol, to encourage the formation of heteroduplex DNA. That is, PCR amplicons containing different editing events are encouraged to anneal. 5. The renatured amplicons are incubated with the T7 enzyme which recognises the mismatched editing events and cleaves at the heteroduplex DNA. 6. Gel electrophoresis of the T7 assay is performed and cleavage products produced by the T7 enzyme are revealed. Expected sizes of cleavage products can be calculated from the number of bases into the amplicon the cut site lies.

2.5.11 TaqMan™ genotyping

Custom TaqMan™ genotyping assays were designed using the ThermoFisher Custom Assay Design Tool (CADT) to detect the presence of the D3986E and S1728F variants in C2C12 myoblasts. The custom assays were designed to avoid the silent mutations introduced into the PAM/seed regions of the HDR templates, allowing for allele-specific detection of the variant of interest. To confer single-base specificity, genotyping assays comprise two allele-specific probes each bound to either VIC™ or FAM™ reporter dyes. The probes also contain a 3' minor groove binder (MGB) that stabilises binding and a non-fluorescent quencher (NFQ) that quenches fluorescence of the probes whilst in solution, reducing background signal. Binding of the probe to the complementary template sequence allows *Taq* polymerisation and the 5' nuclease activity of the *Taq* polymerase degrades the probe sequence, enabling separation of the reporter dye from the quencher and subsequent fluorescence emission. As such, the end-point levels of fluorescence of each dye indicates the genotype of the sample. The assay ID for the D3986E genotyping assay was ANNKVVX and the assay ID for the S1728F genotyping assay was ANYMNZR. Primer and probe sequences are shown in Table 2.5. Each genotyping reaction contained 20 ng DNA, 1X TaqMan™ universal master mix, 0.25 µl of the assay and was made up to 10 µl with nuclease-free water. Real-time PCR was performed using the QuantStudio 3 Real-Time PCR System (Applied Biosystems) and data was analysed in the Genotyping Module on the ThermoFisher cloud.

Table 2.5 – Custom TaqMan™ genotyping assay primer and probe sequences

	p.D3986E	p.S1728F
Forward primer	CCGGAAACCAGCAGAGTCT	TCAGCATCCACCTCGAAAGC
Reverse primer	ATCATCATGTGCGCGAACAC	GGTCTCCGGCGTGAGT
Wild-type probe	ACCACGGCATCCCA	AGAGAGCATGGAGCGAC
Variant probe	ACCACGGCCTCCCA	AGAGCATGAAGCGAC

2.5.12 TA cloning

TA cloning was performed using the pGEM®-T vector system (Promega). Primers were designed to amplify a ~500 bp region around the Cas9 cut site by PCR (Table 2.6) and PCR products were purified using AMPureXP beads as described in 2.2.4. Purified PCR products were phosphorylated by incubation of approximately 3 µg DNA with 1X T4 polynucleotide kinase (PNK) buffer (NEB; 70 mM Tris-HCl pH 7.6, 10 mM $MgCl_2$, 5mM DTT), 1 mM ATP and 10 units of T4 PNK (NEB). The reaction was incubated at 37°C for 30 min and enzymes inactivated at 65°C for 20 min. The linearised pGEM®-T vector was dephosphorylated to prevent self-ligation using recombinant Shrimp Alkaline Phosphatase (rSAP; NEB). The vector was incubated with 1X CutSmart® buffer (NEB; 50 mM potassium acetate, 20 mM Tris-acetate, 10 mM magnesium acetate, 100 µg/ml BSA, pH 7.9) and 1 unit of rSAP per 1 µg plasmid DNA. Reaction volumes were made to 20 µl with nuclease-free water. The reaction was incubated at 37°C for 30 min and enzymes inactivated by incubation at 65°C for 20 min. Phosphorylated PCR products and dephosphorylated pGEM®-T vector were incubated at a 5:1 molar ratio with 1X rapid ligation buffer (Promega; 30 mM Tris-HCl pH 7.8, 10 mM $MgCl_2$, 10 mM DTT, 1 mM ATP, 10% w/v PEG), 5 units T4 DNA ligase (Promega) per 100 ng vector and made to 20 µl in nuclease-free water. Ligation reactions were incubated overnight at 4°C. Following incubation, the reactions were immediately transformed into OneShot® TOP10 chemically competent *E. coli* cells (Invitrogen™) as described in 2.3.1. Transformation reactions were plated on LB agar plates with ampicillin at 100 µg/ml and 40 µl 100mM IPTG and 120 µl 20 mg/ml X-gal spread onto the surface of the plate. White colonies were picked and used to inoculate miniprep cultures and plasmid DNA isolated as described in 2.3.3. Isolated plasmid DNA was subjected to Sanger sequencing as described in 2.2.6. A summary of the number of TA clones picked per cell line used in this project is provided in Table 2.7.

Table 2.6 – Primers used for amplification of templates for TA cloning

Editing event	Forward primer 5'-3'	Reverse primer 5'-3'	Size (bp)
p.D3986E mouse	ACTGGTATTACTCGGGCAAGG	CAATTCAGAAGGGGTTTGGGC	449
p.S1728F mouse	CTACAGCGCTTCCACTCACA	CCAACATTCTCAGCGCCTTG	475
Casq1 knockout mouse	GAGAGCTACCGACAGGATGGG	TAGCCCCCACCCTCAGACTC	330

Table 2.7 – Number of TA clones processed for sequencing for each cell line

Cell line	No. TA clones
Ryr1 p.D3986E 8G6	28
Ryr1 p.D3986E 2G7	17
Ryr1 p.D3986E 9H12	18
Ryr1 p.D3986E 1E6	27
Ryr1 p.D3986E 1C5	27
Ryr1 p.D3986E 10G5	27
Ryr1 p.S1728F 6F12	10
Ryr1 p.S1728F 6B4	10
Casq1 knockout 8E10	18
Casq1 knockout 3B9	20
Casq1 knockout 7E5	19

2.6 Calcium release assay methods

2.6.1 Preparation of imaging buffer

A 10X concentrated stock of imaging buffer (1X components: 10 mM HEPES pH 7.4, 133 mM NaCl, 5 mM KCl, 1 mM $MgCl_2$, 2 mM $CaCl_2$, 5.5 mM glucose) was prepared without glucose, $CaCl_2$ and $MgCl_2$ and was stored at 4^{o}C. The 1X imaging buffer was prepared on the day of imaging or the evening before (stored at 4^{o}C overnight) with glucose, $CaCl_2$ and $MgCl_2$ added and the solution corrected to pH 7.4. Imaging buffer was pre-warmed to 37^{o}C prior to cell loading and Ca^{2+} imaging.

2.6.2 Cell loading with Fluo-8 AM and Pluronic® F-127

Pluronic® F-127 (Sigma) was used to improve cell loading by facilitating the dispersal of the acetoxymethyl ester (AM) group on Fluo-8 AM. The AM esters render ion indicators membrane permeable by neutralising their negative charge. A Pluronic® F-127 stock solution was prepared by dissolving Pluronic® F-127 in DMSO to a final concentration of 20% (w/v) at 40^{o}C with shaking at 200 rpm for at least 30 minutes. Once dissolved, the Pluronic® F-127 stock solution was stored at room temperature. Stock solutions of Fluo-8 AM (Abcam, UK) were prepared in DMSO to a final concentration of 10 mM. 5 µl aliquots of the stock Fluo-8 AM solution were stored at -20^{o}C.

Myotubes were differentiated for 5-6 days in black, clear-bottom 96-well plates coated with ECM Gel from Engelbreth-Holm-Swarm murine sarcoma (Sigma) as described in 2.1.6. Differentiation media was removed and the cells washed twice with 200 µl imaging buffer pre-warmed to 37^{o}C. To generate a working dye solution, the 20% (w/v) stock of Pluronic® F-127 was mixed 1:1 with 10 mM Fluo-8 AM and diluted in imaging buffer to give a final concentration of 0.04% (v/v) Pluronic® F-127 and 10 µM Fluo-8 AM. 80 µl of the working dye solution was added to each well and incubated for 30 min at 37^{o}C, 5% CO_2. Following loading, cells were washed twice with imaging buffer and allowed to equilibrate at room temperature for 20 min in the dark.

2.6.3 Preparation of the caffeine series for Ca^{2+} imaging

Whilst cells were equilibrating at room temperature for 20 min, a caffeine series was prepared in imaging buffer to final concentrations of 0.1 mM, 1 mM, 3 mM, 5 mM, 10 mM and 20 mM.

2.6.4 Fluorescence microscopy Ca^{2+} imaging data acquisition

Caffeine solutions were loaded onto a multivalve perfusion system connected to a Nikon TE2000 inverted microscope for the measure of caffeine-induced Ca^{2+} transients. Myotubes in 96-well plates that had been loaded with Fluo-8 AM were transferred to the stage of the microscope.

The multivalve perfusion system (Automate Scientific Inc.) comprised 8 x 35 ml syringes that were computer controlled using the ValveBank controller (Automate Scientific Inc.), allowing for the automated opening and closing of stop valves located at the bottom of the syringes. One syringe was reserved for imaging buffer and a faulty stop valve on one of the syringes prevented its use, hence 6 caffeine concentrations were used. Pressure at 1 pound per square inch (psi) was applied to the syringes using the Bambi BB24V air compressor (Air Supplies™). Each syringe was connected to a single inflow port via Tygon® plastic tubing that enabled the delivery of solutions to a myotubes in a well of a 96-well plate (Figure 2.5). Previous experiments performed by Dr Xiaochen Liu showed that at 1 psi, solutions were delivered at a rate of 100 µl per second. Solutions were removed from the well into a waste container using an outflow port connected to a vacuum pump. For dose response experiments, a program was created using the ValveBank controller whereby myotubes were perfused with imaging buffer for 10 seconds, caffeine at the desired concentration for 10 seconds and imaging buffer for a further 10 seconds. Myotubes were allowed to recover for approximately 60 seconds prior to the next application of caffeine to allow replenishment of SR Ca^{2+} stores and avoid cell death. A single dose-response experiment, defined by the application of all 6 caffeine concentrations, was performed per well.

Caffeine-induced Ca^{2+} transients were detected using the Nikon TE2000 inverted microscope and a 40x oil immersion objective. Fluo-8 AM was excited at 494 nm using the X-cite 120 metal halide arc lamp (EXFO) and a 480/20 nm excitation filter. Emission was filtered using a 540/40 nm emission filter. The intensity of the light source was adjusted to the lowest level possible whilst allowing detection of a robust fluorescent signal, to avoid cell damage. The data were collected using an intensified charge-coupled device (CCD) camera at 20 frames per second (fps). Piper Control™ Acquisition Software (Stanford Photonics) was used to draw regions of interest (ROIs) around myotubes.

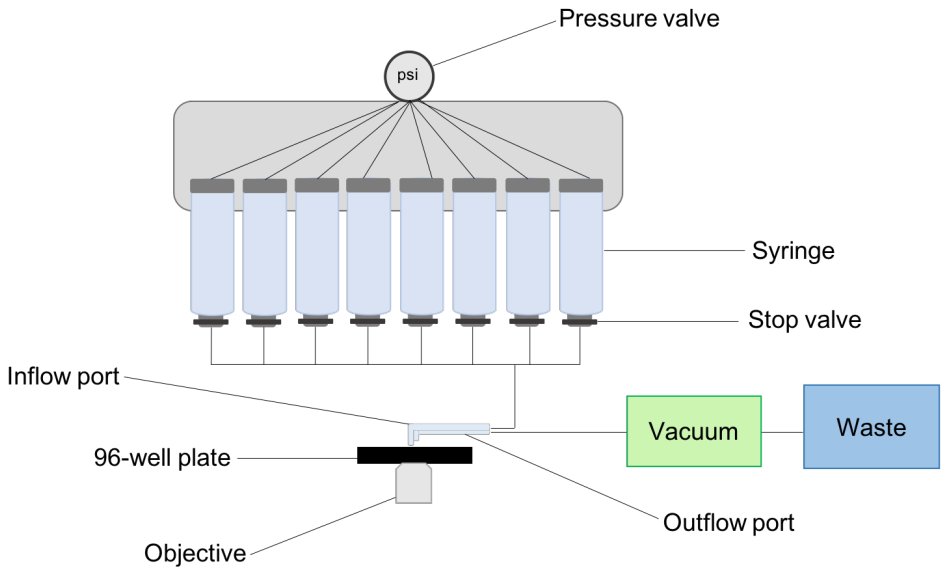

Figure 2.5 – Schematic of the multivalve perfusion system for live-cell Ca^{2+} imaging

The multivalve perfusion system comprised 8 syringes under pressure of 1 psi. Six of the syringes contained caffeine solutions and one contained imaging buffer. One of the syringes was faulty and unable to be used. Stop valves located at the bottom of the syringes were controlled by the ValveBank automated controller. As such, syringes were automatically opened and closed, allowing the automated delivery of solutions to the cells via tubing and the inflow port. The outflow port removed excess liquid using a vacuum pump into a waste container.

2.6.5 Imaging schedule, exclusion criteria and n numbers

Due to differences in cell growth and myoblast differentiation, Ca^{2+} imaging was not always able to be performed for all genotypes being compared on the same day. The days on which the data were collected for each genotype is summarised in Table 2.8. Myotubes were removed from the analysis if they did not show a dose dependent increase in fluorescence in response to caffeine. Furthermore, cells that did not show a response following 3 mM caffeine perfusion were also removed. Finally, myotubes with particularly low (<50) or high (>600) baseline fluorescence units (FUs) were excluded from the analysis. The total n numbers for each genotype are summarised in Table 2.9.

Table 2.8 – Data collection for all cell lines

An X indicates where data were collected.

Experiment	WT	3E1	8G6	10G5	3B9	8E10	7E5	5F2
1	X		X	X				
2	X				X		X	
3			X	X				
4	X			X	X			
5					X	X	X	
6						X	X	X
7			X			X		
8			X				X	
9								X
10		X					X	X
11						X	X	
12								
13		X	X					
14								X
15					X			
16					X			

Table 2.9 – Total n numbers for all cell lines

Total n numbers included in the analysis following application of exclusion criteria.

Cell line	n
WT	45
3E1	33
8G6	44
10G5	46
3B9	59
8E10	55
7E5	49

2.6.6 Fluorescence microscopy imaging data analysis

The raw fluorescence values of each pixel within a ROI were averaged and imported into Prism 8 (GraphPad) for analysis. Half maximal effective concentration (EC_{50}) values were generated from two separate analyses - area under the curve (AUC) measurements and peak height measurements.

For both analyses, baseline measurements for each caffeine-induced peak were calculated by averaging fluorescence values for 20 frames (1 second) prior to caffeine application. The built-in AUC analysis function on Prism 8 was used to calculate the total area of each peak (AUC analysis) and the maximum peak fluorescence value (peak height analysis). Peaks were ignored that were less than 10% of the distance from baseline to maximum fluorescence. For peak height analysis, the change in fluorescence from baseline was calculated by subtracting the baseline measurement from the maximum peak measurement. For both analyses, AUC measurements and peak height measurements were normalised to the maximum response of that myotube at 20 mM caffeine. The resultant values were plotted against caffeine concentration on a logarithmic scale and a non-linear regression analysis performed to derive EC_{50} values. EC_{50} values are expressed as the mean of all myotubes for each genotype (standard deviation; 95% confidence interval). Statistical analysis was performed to determine whether the EC_{50} values differed between genotypes using a one-way analysis of variance (ANOVA) followed by Tukey's post hoc test for multiple pair-wise comparisons, correcting for multiple testing. EC_{50} values were considered significantly different when $p<0.05$.

2.7 Western blot methods for Casq1, myosin and GAPDH detection

2.7.1 Mammalian whole cell lysate preparation

C2C12 cells and CASQ1 knockout C2C12 derivatives were differentiated for 6 days as described in 2.1.6. Cells were pelleted as described in 2.1.4 and resuspended in an appropriate volume of ice cold RIPA buffer (ThermoFisher; 25 mM Tris-HCl pH 7.6, 150 mM NaCl, 1% (v/v) NP-40, 1% (w/v) sodium deoxycholate and 0.1% (w/v) SDS). The resuspended cells were incubated on

ice for 15 min. Lysates were clarified by centrifugation at 13,000 *x g* for 30 min at 4°C. The supernatant was transferred to a clean tube for quantification. Lysates were stored at -20°C.

2.7.2 BCA assay

Cell lysates were diluted 1:10 and quantified using the detergent-compatible Pierce™ protein BCA assay kit (ThermoFisher) according to manufacturer's instructions. A series of BSA (provided at 2 mg/ml in 0.9% saline and 0.05% sodium azide) standards were prepared in RIPA buffer ranging from 2000 µg/ml to 0 µg/ml. Twenty-five µl of each standard was transferred to a well of a 96-well plate for a total of 2 replicates. Twenty-five µl of each lysate sample was transferred to a well of the same 96-well plate for a total of 2 replicates. 200 µl of working reagent, consisting of a 50:1 ratio of reagent A (sodium carbonate, sodium bicarbonate, bicinchoninic acid and sodium tartrate in 0.1M sodium hydroxide) to reagent B (containing 4% cupric sulfate) was added to each standard and each sample. The plate was incubated at 37°C for 30 min and absorbance at 540 nm measured using the SpectraMax plate reader (Molecular Devices). Averaged blank values were subtracted from all standard and sample measurements. The blank-corrected standard measurements were plotted against their concentration in µg/ml and a linear trendline fitted to the graph to generate a calibration curve. This was used to calculate the concentrations of the unknown samples.

2.7.3 SDS-PAGE

For western blots, where visualisation of CASQ1 (~42 kDa), GAPDH (~ 25 kDa) and myosin heavy chain (~ 223 kDa) was needed, precast Mini-PROTEAN TGX™ 8-16% gradient gels were purchased from BioRad. In the first lane of each gel, 10 µl prestained colour protein standard (NEB) was loaded. Samples were heated to 95°C for 5 min with an equal volume of 2X protein loading dye (2% (w/v) SDS, 10% (v/v) glycerol, 5% (v/v) beta-mercaptoethanol, 60 mM Tris-HCl pH 6.8, 0.1 % (w/v) bromophenol blue) prior to loading. Fifty µg total protein was loaded per lane. Electrophoresis was performed in Tris-glycine SDS buffer (250 mM Tris pH 8.3, 1.92 M glycine and 1% (w/v) SDS) at 180 V for 1 hour.

2.7.4 Western blot

Following SDS-PAGE, proteins were transferred onto 0.45 µm mini PVDF membranes using the Trans-Blot® Turbo™ transfer system (BioRad). The Trans-Blot® Turbo™ ready-to-assemble transfer kit was used according to manufacturer's instructions. Briefly, filter paper stacks were equilibrated in 1X transfer buffer (BioRad; 25 mM Tris-HCl pH 8.3, 192 mM glycine, 20% (v/v) methanol) and PVDF membranes were equilibrated in 100% ethanol for 2-3 min. The stack was assembled in the following order: filter paper stack, membrane, gel and filter paper stack. Proteins were transferred at 2.5 A for 30 min. The PVDF membrane was placed in 5% skimmed milk powder in Tris-buffered saline with 0.1% Tween® (Sigma) (TBST; 25 mM Tris-HCl pH 7.5, 0.15 M NaCl, 0.1% w/v Tween®20) for 1 hour at room temperature before being washed with TBST for a total of 3 washes, each lasting 5 minutes. Antibodies were diluted in 1% skimmed milk powder in TBS according to Table 2.10. For re-probing with the GAPDH loading control, membranes were washed 3 times in TBST, blocked and re-probed. Primary antibodies were incubated with the membrane overnight at 4^{o}C and secondary antibodies incubated for 1 hr at room temperature, washing between the use of each antibody. To visualise proteins by enhanced chemiluminescence, the membrane was incubated for 5 min with SuperSignal West Femto Maximum Sensitivity Substrate (ThermoFisher) and images captured using the Gel Doc™ XR+ Gel Documentation System (BioRad).

Table 2.10 – Antibodies used and working dilutions

Antibodies were used to detect proteins within C2C12 myotube lysates.

Antibody	Host species	Supplier	Working dilution	Expected band (kDa)
Anti-casq1 EPR15227(B)	Rabbit (IgG)	Abcam (ab191564)	1:2000	50
MF-20 anti-myosin heavy chain	Mouse (IgG2b)	Deposited to the DSHB by D.A. Fischman.	0.5 ug/ml	220
Anti-GAPDH	Mouse (IgG2b)	Abcam (ab9484)	1:2000	37
Anti-rabbit IgG (HRP)	Goat	Abcam (ab6721)	1:2000	N/A
Anti-mouse IgG (HRP)	Rabbit	ThermoFisher (A16160)	1:2000	N/A

2.8 Heterologous CASQ1 expression and purification methods

2.8.1 Cloning into pOPINF

The expression vector, pOPINF (a gift from Ray Owens; Addgene #26042) was used for heterologous expression of human *CASQ1* wild-type, *CASQ1* E364K, *CASQ1* F186Y and *CASQ1* I138T (Figure 2.6). This vector incorporates an N-terminal hexa-histidine tag followed by a 3C cleavage site onto translated proteins. The pOPINF vectors containing the *CASQ1* cDNAs without the 34 amino acid signal peptide, were assembled by Gibson assembly, as described in the Oxford Protein Production Facility (OPPF) manual (Gibson et al., 2009; OPPF pOPIN vector suite, 2016). The pOPINF vector was linearised in a restriction digest reaction consisting of 10 µl pOPINF vector (200 ng/µl), 1 µl *Kpn*I-HF® (NEB), 1 µl *Hind*III-HF® (NEB), 2 µl 10X Green CutSmart Buffer (NEB) and nuclease-free water to a final volume of 20 µl. The reaction was incubated at 37^{o}C for 30 min and the enzymes inactivated by heating at 80^{o}C for 20 min. Five µl of the reaction was electrophoresed for 40 min at 120 V as described in 2.2.2 .

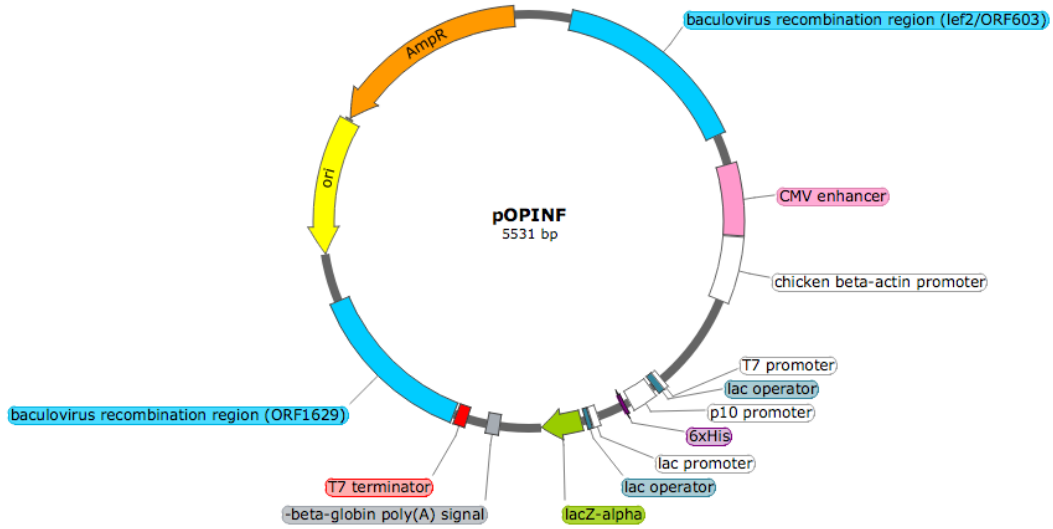

Figure 2.6 – Vector map of pOPINF

The pOPINF vector was developed by the Oxford Protein Production Facility (Oxford, UK) and deposited on Addgene (#26042). The vector allows for heterologous protein expression in insect cells (via baculovirus recombination regions and the p10 promoter), mammalian cells (via the cytomegalovirus enhancer and chicken beta actin promoter) and bacterial cells (via the T7 promoter). The lac operator allows for IPTG induction and ampicillin allows for the selection of transformed *E. coli* clones. A beta-globin poly(A) signal is located downstream of the POI cDNA sequence for mRNA stabilisation and the T7 terminator terminates transcription. Proteins expressed from pOPINF contain an N-terminal hexa-histidine tag (6xHis tag). Vector maps were taken from Addgene (www.addgene.org/26042; accessed August 2019) and modified in SnapGene®.

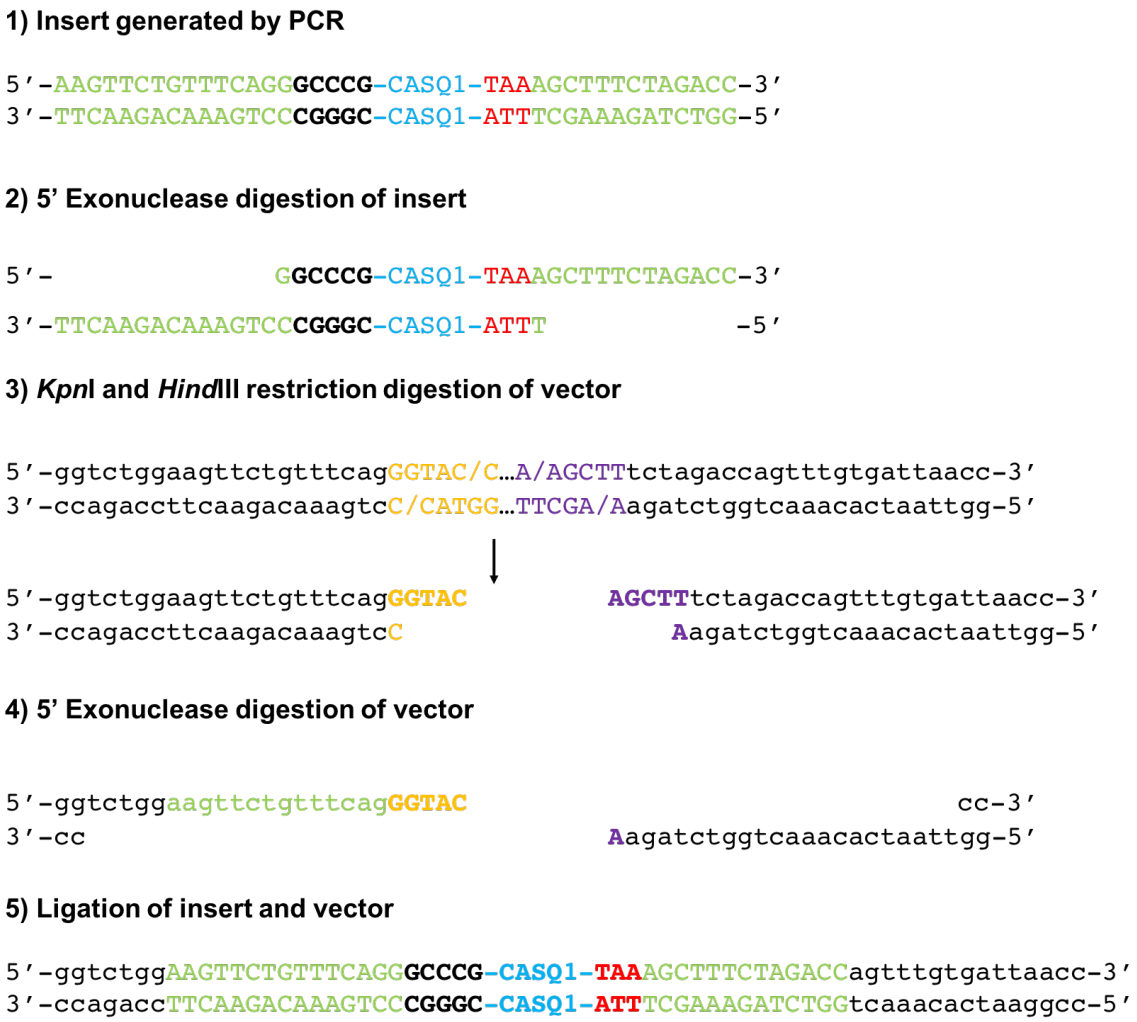

Figure 2.7 – pOPINF Gibson assembly schematic

Primers with appendages complementary to the pOPINF vector (green) were used to amplify the CASQ1 coding region (blue) without the N-terminal signal peptide. Bases were added to complete the 3C cleavage site (bold text) and a stop codon was added to the reverse primer (red). 2) the PCR product was digested with a 5' exonuclease to generate large overhangs. 3) The pOPINF vector was digested with *Kpn*I (yellow) and *Hind*III (purple) restriction enzymes to linearise the vector. 4) The linearised vector was digested with 5' exonuclease prior to ligation with the digested insert (5).

The *CASQ1* cDNAs without the signal peptide were amplified by PCR from vectors already containing the cDNAs. A 21-22 nt sequence was appended to the 5' of the forward primer consisting of 15 nt complementarity to the pOPINF vector and a 5 nt sequence which completed the 3C cleavage site. An 18 nt sequence was appended to the 5' of the reverse primer consisting of 15 nt

complementarity to the pOPINF vector and a 3 nt stop codon. A ligation reaction was assembled consisting of 1 µl digested pOPINF vector (~200 ng), 600 ng purified insert, 10 µl 2X Gibson assembly master mix (NEB) and nuclease-free water to a final volume of 20 µl. The ligation reaction was incubated at 50°C for 1 hour and immediately transformed into XL10-gold® cells (Agilent) as described in 2.3.1. Four white colonies per vector were picked and plasmid was isolated by mini prep as described in 2.3.3. To confirm successful cloning, a series of overlapping sequencing primers spanning the entire CASQ1 insert within the pOPINF backbone were designed and Sanger sequencing was outsourced to Source Bioscience (Cambridge, UK). The Sanger sequencing chromatograms were analysed using 4Peaks software and assembled manually.

Table 2.11 – pOPINF-*CASQ1* assembly primers

Green text shows the sequences complementary to pOPINF. Bold black text shows the sequence added to complete the 3C cleavage site. Red text shows the stop codon sequence. Blue text shows the primer sequence complementary to the *CASQ1* cDNA.

Primer name	Sequence 5'-3'
pOPINF_CASQ1_ Forward	AAGTTCTGTTTCAGG**GCCCG**CAGGAAGGGCTGGACTTCCCTG
pOPINF_CASQ1_ Reverse	CTGGTCTAGAAAGCTTTAGTCATCATCATCATCGTCATC

2.8.2 Induction of his-tagged CASQ1 expression

The pOPINF-*CASQ1* vectors were transformed into BL21(DE3) Rosetta™ *E. coli* cells (Novagen®) as described in 2.3.1. Single colonies were picked using a sterile toothpick and used to inoculate 100 ml LB media containing the ampicillin at 100 µg/ml and chloramphenicol at 25 µg/ml. The 100 ml culture was incubated overnight at 37°C with shaking at 200 rpm. The following day, the 100 ml culture was used to inoculate 1 L LB media containing the appropriate antibiotics. The 1 L culture was grown for ~4 hours at 37°C with shaking at 200 rpm until the optical density at 600 nm (OD_{600}) reached 0.4-0.6. IPTG was added to a final concentration of 0.4 mM and the culture incubated overnight at 18°C.

2.8.3 Preparation of lysates protein purification

Cultures were decanted into 1 L containers and centrifuged at 7,500 *x g* for 15 min at 4°C. The supernatant was removed and pellets resuspended on ice in 40 ml resuspension buffer (0.01M phosphate buffered saline (PBS; 0.01M phosphate buffer, 0.0027M KCl, 0.137M NaCl; pH 7.4; tablets were purchased from Fisher Bioreagents) with 0.1% (v/v) Triton® X-100 (Fisher Bioreagents), 200 µg/ml lysozyme from chicken egg white (Sigma) and one tablet of cOmplete™ EDTA-free, *EASYpack*, protease inhibitor cocktail tablets (Roche)). The cells were lysed by sonication on ice using the Fisherbrand™ Model 120 Sonic Dismembrator (Fisher Scientific). Lysates were clarified by centrifugation at 25,000 *x g* for 30 min at 4°C followed by filtration through a 0.22 µM syringe-driven filter. Clarified lysates were kept on ice here onwards.

2.8.4 Nickel affinity chromatography

Nickel affinity chromatography was performed using an AKTA Pure FPLC system (GE Healthcare) and HisTrap™ HP 1 ml columns (GE Healthcare). All buffers used on the AKTA system were filtered through a vacuum driven 0.22 µM filter (Nalgene) and degassed. The AKTA system and column were pre-equilibrated with low salt wash buffer (50 mM Tris-HCl pH 7.6, 300 mM NaCl, 20 mM imidazole, 5% (v/v) glycerol, 0.075% (v/v) beta-mercaptoethanol) for 5

column volumes (CV). Samples were loaded onto the column using a sample pump at a rate of 1 ml/min. The column was washed with 5 CV of low salt wash buffer, high salt wash buffer (50 mM Tris-HCl pH 7.6, 500 mM NaCl, 20 mM imidazole, 5% (v/v) glycerol, 0.075% (v/v) beta-mercaptoethanol) and then low salt wash buffer again. Bound protein was eluted using a linear gradient from 0% elution buffer (50 mM Tris-HCl pH 7.6, 300 mM NaCl, 300 mM imidazole, 5% glycerol (v/v), 0.075% (v/v) beta-mercaptoethanol) to 70% elution buffer over 15 CV and elution monitored by absorbance at 280 nm. Elution at 70% elution buffer was maintained for 5 CV before a step to 100% elution buffer was applied for a further 5 CV to remove remaining protein bound to the column. Flow-through from sample application and washes were collected in Falcon tubes and eluate was collected in 1 ml fractions in a 96-well deep well plate. Fractions that displayed a peak of absorbance at 280 nm were analysed by SDS-PAGE along with the pellet, flow through and washes. Columns were stored in 20% ethanol.

2.8.5 SDS-PAGE for confirmation human CASQ1 purification

To determine the masses of proteins within the eluted fractions that showed a peak of absorbance at 280 nm, SDS-PAGE was performed. SDS-PAGE gels comprised of 12% acrylamide resolving gels with a 5% acrylamide stacking layer were prepared using the BioRad mini-PROTEAN apparatus. 10 ml resolving gels were prepared by mixing 3.3 ml distilled, deionised water (ddH_2O), 4 ml 30% (w/v) acrylamide-bis solution (19:1) (Severn Biotech), 2.5 ml 1.5 M Tris pH 8.8, 100 µl 10% (w/v) ammonium persulfate, 100 µl 10% (w/v) SDS and 4 µl N,N,N',N'-tetramethylethane-1,2-diamine (TEMED). A layer of water saturated butanol was added to the top of the resolving gel and the gel left to set for 30 min. The water saturated butanol was removed and 5 ml 5% stacking gel prepared by mixing 3.4 ml ddH_2O, 830 µl 30% (w/v) acrylamide-bis (19:1), 630 µl 1M Tris pH 6.8, 50 µl 10% (w/v) ammonium persulfate, 50 µl 10% (w/v) SDS and 5 µl TEMED. The stacking gel was layered on top of the resolving gel and a comb inserted. The stacking gel was left to set for 20 min. Electrophoresis was performed as described in 2.7.3.

2.8.6 Coomassie staining

Gels were incubated with InstantBlue™ Coomassie protein stain (Expedeon) for 30 min and images were captured using the G:BOX Chemi XX6/XX9 imager (Syngene). Densitometry was performed using ImageJ software to determine the percentage purity of purified CASQ1 protein fractions.

2.8.7 Protein concentration

Purified protein samples were concentrated using Pierce™ protein concentrators with a polyethersulfone (PES) membrane and 10 kDa molecular weight cut off (MwCO) (ThermoFisher). Samples were pipetted into the upper chamber and centrifuged at 4000 *x g* at 4°C in 5 minute increments until the desired concentration had been achieved.

2.8.8 Preparative size exclusion chromatography

Samples prepared by nickel affinity chromatography were further purified by preparative size exclusion chromatography using an AKTA Pure FPLC system (GE Healthcare) and a HiLoad 26/600 Superdex 200 prep grade (pg) column (GE Healthcare). Buffer exchange was performed prior to preparative size exclusion chromatography (SEC) using Sephadex G-25 PD-10 desalting columns (GE Healthcare) according to manufacturer's instructions. Briefly, columns were equilibrated with 25 ml of SEC buffer (10 mM HEPES pH 7.5, 500 mM NaCl), 2.5 ml protein sample was loaded onto the column and the flow through discarded before protein was eluted with 3.5 ml SEC buffer and collected in a bijou container. The HiLoad 26/600 Superdex 200 pg column SEC column was pre-equilibrated with 1 CV SEC buffer at a rate of 1 ml/min. Samples were loaded onto the column manually by injecting into a 5 ml sample loop using a syringe. Isocratic elution was performed at a rate of 2 ml/min and elution was monitored by absorbance at 280 nm. The first 64 ml of eluate was discarded and the remaining eluate collected in 2 ml fractions in a 96-well deep well plate. Fractions that displayed a peak in absorbance at 280 nm were analysed by SDS-PAGE. Fractions containing purified CASQ1 were pooled

and concentrated as described in 2.8.7 and then buffer exchanged into experimental buffer (10 mM HEPES pH 7.5, 300 mM KCl).

2.8.9 Protein quantification

Purified CASQ1 was quantified using the Qubit™ protein assay kit and Qubit™ 3.0 fluorometer (Invitrogen™) according to manufacturer's instructions. Briefly, the fluorescent dye was diluted 1:200 in protein assay buffer to prepare the working solution. Pre-made BSA standards were diluted 1:20 in working solution used to plot a calibration curve. Protein samples were diluted 1:100 in working solution and concentration derived from the calibration.

2.8.10 Protein storage

Purified proteins in experimental buffer were snap frozen using liquid nitrogen and stored in 50 µl aliquots at -80°C.

2.9 Biomolecular interactions methods

2.9.1 Mass spectrometry

All mass spectrometry was performed as a service by the Mass Spectrometry facility in the Astbury Centre for Structural and Molecular Biology, by Dr James Ault and Dr Rachel George. Briefly, samples for protein identification by peptide mass fingerprinting were submitted as 10 µg protein on an SDS-PAGE gel stained with InstantBlue™ Coomassie stain (Expedeon). Proteins extracted from the gel were subject to tryptic digestion and peptides separated by liquid chromatography using the ACQUITY M-Class UPLC system prior to tandem mass spectrometry (MS/MS). Data were processed with PEAKS Studio (Bioinformatic Solutions Inc, Waterloo, Ontario, Canada) and searched against a Uniprot database for CASQ1.

Samples for native and denatured mass spectrometry were supplied at 10 µM-20 µM in experimental buffer, with or without 1 mM $CaCl_2$. Denatured samples were separated by liquid chromatography as described previously and the eluant directed into the Xevo QToF G2-XA mass spectrometer via a Z-spray

electrospray source. MS was operated in positive TOF mode. Data were analysed using MassLynx v4.1 (Waters). For native mass spectrometry, CASQ1 proteins were provided in experimental buffer with or without 1 mM $CaCl_2$. Native samples without Ca^{2+} were buffer exchanged into 200 mM ammonium acetate using Zeba™ spin 7K MWCO columns (ThermoFisher). Native samples with calcium were buffer exchanged into 200 mM ammonium acetate with 1 mM calcium acetate. For samples with EGTA, EGTA was added to experimental buffer at 1 mM by dialysis overnight at 4°C using Slide-A-Lyzer™ 10 MwCO cassettes (ThermoFisher) prior to dialysis back into experimental buffer. Native MS was performed using either the ESI-MS Synapt G2 high definition mass spectrometer (Waters) and data analysed in MassLynx v4.1 (Waters) or the Q-Exactive Plus mass spectrometer (ThermoFisher) and data analysed in UniDec v2.7.1 (Marty et al., 2015).

2.9.2 Microscale thermophoresis

Purified proteins were diluted to 20 uM in PBS and incubated for 1 hour at room temperature with a 4.5X molar excess of fluorescein isothiocyanate (FITC). Excess dye was removed using NAP-5 columns (GE Healtchare) according to manufacturer's instructions and the labelled proteins eluted into 10 mM HEPES pH 7.5, 150 mM NaCl. To confirm sufficient labelling, samples of each protein were diluted 10- to 320-fold with 2-fold iterations in between and transferred to NT.115 standard treated capillaries (NanoTemper Technologies) and each dilution scanned for fluorescence with blue LED at 15% power using the Monolith NT.115 (NanoTemper Technologies). LED power was decreased if fluorescence values were greater than 1500 fluorescence units (FUs) for all dilutions. The optimal dilution was chosen for the experiment based on what one would provide sufficient FUs following subsequent 2-fold dilution in a $CaCl_2$ titration. A 2-fold $CaCl_2$ titration ranging from 200 mM to ~6 uM was prepared in 10 mM HEPES pH 7.5, 150 mM NaCl, mixed 1:1 with labelled protein (final concentration of the $CaCl_2$ gradient 100 mM – 5 uM), and allowed to equilibrate for 10 min at room temperature. A protein sample diluted 1:1 in experimental buffer with no $CaCl_2$ as a control. MST was performed at MST intensity 20, 40 and 80%. Fluorescence values from two experiments averaged and plotted against $CaCl_2$ concentration in GraphPad Prism.

2.9.3 Dynamic light scattering

CASQ1 proteins at 0.5 mg/ml in experimental buffer were prepared in 2 x 250 µl aliquots per protein. 1 M $CaCl_2$ was prepared in experimental buffer and 2.5 µl added to the 250 µl protein aliquots to generate a final concentration of 10 mM $CaCl_2$. Samples with Ca^{2+} were allowed to equilibrate at room temperature for 10 min. Due to practical limitations, all samples were prepared at the same time and incubated on ice prior to experiments. The 250 µl samples were injected into the Wyatt miniDawn Treos® system attached to the WyattQELS module for DLS measurements at 135^{o}. Baselines were measured before and after sample injection for 5 min, using filtered (0.22 µm) experimental buffer that was kept on ice. After each sample, the flow cell was washed with 1 ml 1M nitric acid followed by ddH_2O prior to re-equilibration with 2 ml experimental buffer. Correlation curves were analysed using the ASTRA® 6.0.3 software by regularisation, using a 3 minute sample window.

Chapter 3 - CRISPR-Cas9 mediated knock in of the RYR1 p.D3986E variant in human immortalised myoblasts

3.1 Introduction

3.1.1 Complications of existing characterisation methodologies

Despite the association of >200 *RYR1* variants with MH, since the implementation of the EMHG guidelines for variant characterisation, only 48 have been functionally characterised (EMHG, available at www.emhg.org, accessed August 2019). Functional characterisation is currently performed, predominantly, by two imperfect methods – primary patient myoblast or B-lymphocyte isolation and heterologous rabbit or human RYR1 expression in HEK293 cells. Primary myoblasts have limited replicative potential and despite some success, predominantly from the Institut de Myologie in Paris, France (Zhu et al., 2007; Mamchaoui et al., 2011), myoblast immortalisation has proved a challenge in the field. Indeed, to date, no MH variants have been functionally characterised in human immortalised myoblasts and attempts in our group to generate human immortalised myoblasts that retain their ability to proliferate and differentiate have been with limited success (Vikas Kaura, pers. comms). B-lymphocytes from patient blood samples can be immortalised with relative ease and express the RYR1; however, they do not express other ECC apparatus (Levano et al., 2009; Girard et al., 2001). Furthermore, the unknown genetic background of patient samples means that it is difficult to ascertain that any observed effect on Ca^{2+} release is attributed to the variant in question. The HEK293 system is plagued by the need for laborious site directed mutagenesis and sub-cloning to introduce the variant of interest, followed by the inefficient transfection of large constructs into cells (Kreiss et al., 1999). Indeed, the *RYR1* coding sequence is ~15 kb in length. Fundamental physiological differences between HEK293 cells and myotubes has made obtaining consistent resting Ca^{2+} data difficult (Tong et al., 1999b). Despite these discrepancies, variants characterised in both HEK293 cells and myotubes thus far appear to show consistent results with regard to sensitivity to caffeine, halothane and 4-chloro-m-cresol (4-CmC; Yang et al., 2003). In contrast, challenges with existing methods of functional characterisation are highlighted by numerous conflicting reports of functional relevance following

characterisation in HEK293 cells and B-lymphocytes. Expression of the RYR1 p.R2336H variant in HEK293 cells showed that the p.R2336H variant had a significantly lowered EC_{50} to caffeine compared to wild-type RYR1 (Merritt et al., 2017). In contrast, characterisation of the same variant in B-lymphocytes did not show a significant difference in response to caffeine compared to wild-type, but did show a significant abnormal Ca^{2+} response following perfusion with 4-CmC (Levano et al., 2009). Merritt et al., (2017) also showed increased sensitivity of the p.V4849I variant to caffeine in HEK293 cells; however, characterisation in B-lymphocytes showed no difference compared to wild-type in response to either caffeine or 4-CmC (Ducreux et al., 2006).

3.1.2 Selection of the p.D3986E variant

The p.D3986E variant is an aspartate (D) to glutamate (E) substitution at position 3986 in the RYR1 coding sequence (P21817.3) resulting from a C>G transition at cDNA position 11958 (c.11958C>G; NM_000540.2), changing the amino acid codon from GAC to GAG. Within the rabbit RYR1 structure, the p.D3986 residue is located in the central domain – the only cytoplasmic structure that interacts with the channel domain (Yan et al., 2015).

The p.D3986E variant was selected for introduction into immortalised human myoblasts due to its identification in MHShc/MHSh individuals in multiple families. The p.D3986E variant has been identified in 6 MH families referred to the Leeds MH unit (Table 3.1). Across these families, p.D3986E has been identified in a total of 7 MHShc individuals, 3 MHSh individuals and no MHN individuals (Table 3.1). Discordancy was detected in one family, whereby an MHSh individual did not harbour the p.D3986E variant, suggesting that an undetected variant in another gene could influence the MH response in addition to the p.D3986E variant; however, no further variants were identified in the 4 MHShc individuals that were subject to NGS of 50 genes associated with Ca^{2+} handling. The p.D3986E variant is rare, with no occurrences in the Exome Aggregation Consortium (ExAC, 2019; Lek et al., 2016) or the Genome Aggregation Database (gnomAD, 2019; Karczewski et al., 2019). Analysis of the relative strength of contracture during IVCT of 22 variants associated with MH (including some diagnostic variants) showed that samples harbouring the

p.D3986E variant produced significantly stronger contractures in response to caffeine during IVCT compared to the most common UK MH variant, p.G2434R and probands harbouring p.D3986E variant had significantly increased creatine kinase (CK) levels (suggestive of increased Ca^{2+} turnover in normal conditions); however, probands did not have an increased onset time to a clinical reaction nor did p.D3986E samples produce significantly increased responses to halothane (Carpenter et al., 2009). The power of this study to draw phenotype-genotype associations with the p.D3986E variant is likely limited by the small sample size of 2. The Leeds MH Unit has shown no significant difference in the EC_{50} to caffeine in HEK293 cells expressing the p.D3986E variant compared HEK293 cells expressing wild-type RYR1 (Merritt et al., 2017). In HEK293 cells, the p.D3986E variant did have a significantly reduced EC_{10} compared to wild-type, but this is unlikely to account for the strong IVCT reaction observed in individuals harbouring the variant. Functional characterisation of a p.D3986E B-lymphocyte cell line showed a significantly increased sensitivity to 4-CmC compared to wild-type controls (sensitivity to caffeine was not measured; Gonsalves, 2014). Furthermore, CK levels in the p.D3986E B-lymphocyte cell line were significantly higher (1,271 units per litre (U/L)) than both the wild-type control (78 U/L) and the diagnostic variant p.R614C positive control (194 U/L), corroborating observations made by Carpenter et al. (2009). Nonetheless, it is important to emphasise that the studies in B-lymphocytes were performed on samples derived from a single individual and thus the results may not reflect genuine differences attributed to the p.D3986E variant (Gonsalves, 2014). Further exploration of the effect of the p.D3986E variant in a myoblast cell line is necessary to provide clarification of its role in MH.

Table 3.1 – Prevalence of p.D3986E variant in Leeds MH Unit referrals

The 6 MH families in which the p.D3986E variant has been detected have been anonymised and assigned codes from D1-D6 (column 1). Since not all family members have been subject to DNA sequencing, the genetic analysis column refers to the number of family members who have had their DNA sequenced to determine the presence of the p.D3986E variant. The p.D3986E + column refers to the number of family members determined to harbour the p.D3986E variant after DNA sequencing was performed.

	No. MHShc			No. MHSh			No. MHN		
Family	**Total MHShc**	**Genetic analysis**	**p.D3986E +**	**Total MHSh**	**Genetic analysis**	**p.D3986E +**	**Total MHN**	**Genetic analysis**	**p.D3986E +**
D1	1	1	1	1	1	0	1	1	0
D2	3	3	3	1	1	1	3	3	0
D3	8	1	1	2	0	-	9	0	-
D4	7	1	1	1	0	-	4	0	-
D5	1	1	1	2	2	2	0	-	-
D6	1	1	0	0	0	0	-	-	-

3.1.3 Chapter aims and strategy

This primary aim of this chapter is to develop a novel, robust CRISPR-Cas9 methodology by which MH-associated variants of unknown significance (VUS) can be introduced into a human immortalised myoblast cell line and to explore the feasibility of this strategy for MH variant characterisation. In addition, *in-silico* tools will be used to gain insight into the potential pathogenicity of the p.D3986E variant.

Establishment of a CRISPR-Cas9 pipeline for the introduction of MH-associated VUS will overcome existing issues with variant characterisation by providing a constant genetic background, overcoming issues with the limited proliferative capacity of primary cells and providing characterisation in a physiologically relevant environment with all components of the ECC machinery expressed and muscle-specific structures such as the SR. Previous attempts at functional characterisation of the p.D3986E variant in HEK293 cells affords the opportunity to determine the consistency in caffeine dose-response data between the HEK293 system and CRISPR-Cas9 system in myotubes. Due to difficulties in generating an immortalised human myoblast line in our group, the cell line for editing was obtained from the Institut de Myologie courtesy of Prof. Vincent Mouly (Paris, France) from a male patient undergoing surgery for hip fracture with no known muscle disorders (Anne Bigot, pers. comms.).

Two CRISPR-Cas9 strategies will be employed in this chapter (Figure 3.1). In recent years, dramatic increases in gene-editing efficiency and on-target activity have been observed using purified Cas9 protein in complex with the gRNA:tracrRNA fusion (Dewari et al., 2018; Mason et al., 2018; Xu et al., 2018). Thus, commercially available Cas9 will be co-transfected alongside the gRNA:tracrRNA fusion, HDR templates and a commercially available vector to detect functionality of the transfected reagents (pGCS) (Figure 3.1; panel A). The pGCS vector contains two partially overlapping orange fluorescent protein (OFP) coding sequences separated by a cloning site for the gRNA and PAM. Following introduction of all reagents into target cells, Cas9 is able to cleave not only target cell DNA but also the gRNA sequence in pGCS. Introduction of a double-stranded break in pGCS allows for recombination between the overlapping partial OFP sequences, restoring full OFP expression which can

be detected by fluorescent activated cell sorting (FACS). In addition, the more widely-used plasmid-based system will be executed in parallel (Ran et al., 2013a). The pSpCas9(BB)-2A-GFP vector encodes Cas9, the tracrRNA, a cloning site for the gRNA and the green fluorescent protein (GFP) coding sequence for selection of transfected cells. The vector will be transfected alongside HDR templates to incorporate p.D3986E (Figure 3.1; panel B). For the introduction of base changes by HDR, it is recommended that the Cas9 cut site lies as close to the base to be changed as possible – ideally 0-20 bp away (Ran et al., 2013a). Since gene-editing could produce undesired editing events such as the incorporation of random indels at the Cas9 cut site (Peng et al., 2015) or aberrant incorporation of the HDR template (Boel et al., 2018), the isolation of polyclonal cells for use in determining the effect of the p.D3986E variant is not appropriate. As such, transfected cells will be FACS-sorted into single cells and propagated to obtain a monoclonal cell line which will be validated by genotyping and Sanger sequencing.

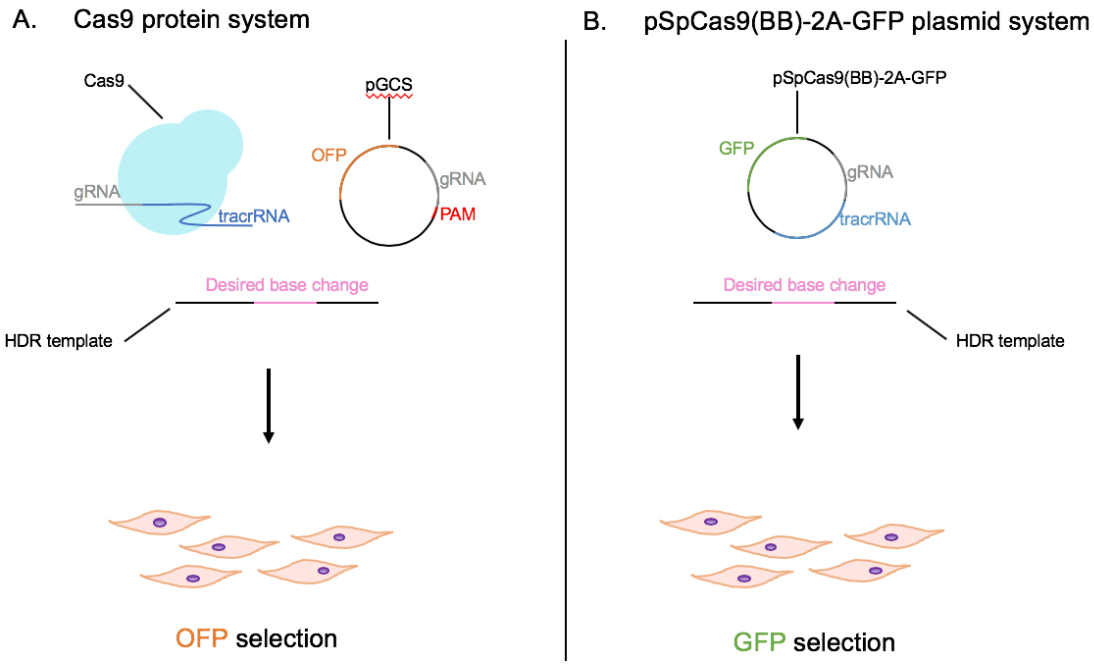

Figure 3.1 – CRISPR-Cas9 strategy for p.D3986E introduction into human immortalised myoblasts

Commercially supplied purified Cas9 protein will be transfected into human immortalised myoblasts alongside the gRNA:tracrRNA fusion, pGCS containing the gRNA sequence and PAM and the HDR templates (panel A). Transfected cells, and those in which gene-editing has occurred can be selected by OFP expression. In a parallel strategy, the pSpCas9(BB)-2A-GFP vector which encodes Cas9, GFP, tracrRNA and a cloning site for the gRNA will be transfected into human immortalised myoblasts alongside the HDR template (panel B). Transfected cells can be selected by GFP expression.

3.2 Results

3.2.1 p.D3986E *in-silico* pathogenicity prediction

A number of bioinformatics tools were used to predict the pathogenicity of the p.D3986E missense variant. Using Sorting Intolerant From Tolerant (SIFT), the p.D3986E variant was predicted to be 'damaging' with a SIFT score of 0.03 – where a score of 0 is damaging and a score of 1 is tolerated (SIFT 4G, 2018; Ng and Henikoff, 2003; Sim et al., 2012). Using PolyPhen-2, the p.D3986E variant was determined to be 'probably damaging' with a score of 0.999 – where a score of 1 is damaging and a score of 0 is benign (PolyPhen-2 v2, 2018; Adzhubei et al., 2010). Finally, the combined annotation dependent depletion (CADD) tool generated a CADD score (C-score) of 24.1, indicating

that it is in the top 1% of predicted deleterious variants (CADD v1.4, 2018; Kircher et al., 2014).

3.2.2 p.D3986E residue conservation and *in-silico* mutagenesis

ConSurf (Ashkenazy et al., 2016; Celniker et al., 2013; Asheknazy et al., 2010; Berezin et al., 2004) was used to identify highly conserved regions within the human RYR1 protein and create a multiple sequence alignment (MSA). The search returned 75 results and the 40 are shown for reference in a random order (Figure 3.2). At position 3986 (accession number P21817.3), the D residue is highly conserved with a ConSurf conservation score of 8, where ConSurf scores from 1-9. The residue is predicted to be exposed on the folded protein and have a functional role. Of all the homologues included in the search, 74 had a D residue at position 3986. Furthermore, the sequence surrounding the p.D3986E residue appears highly conserved across homologues. The mutagenesis wizard on PyMOL Molecular Graphics System version 2.0 (Schrödinger, LLC) was used to investigate the effect of the D to E substitution on local hydrogen bonding and Van der Waals (VdW) interactions using the rabbit RYR1 structure (PDB: 3J8H; Yan et al., 2015; Figure 3.3). The substitution is shown in its PyMOL-assigned most likely rotamer formation based on the prevalence of the rotamer found in proteins within the PyMOL library (21%). A number of mild (green discs) and severe (red discs) VdW clashes occur in this rotamer conformation and all other 18 potential conformations.

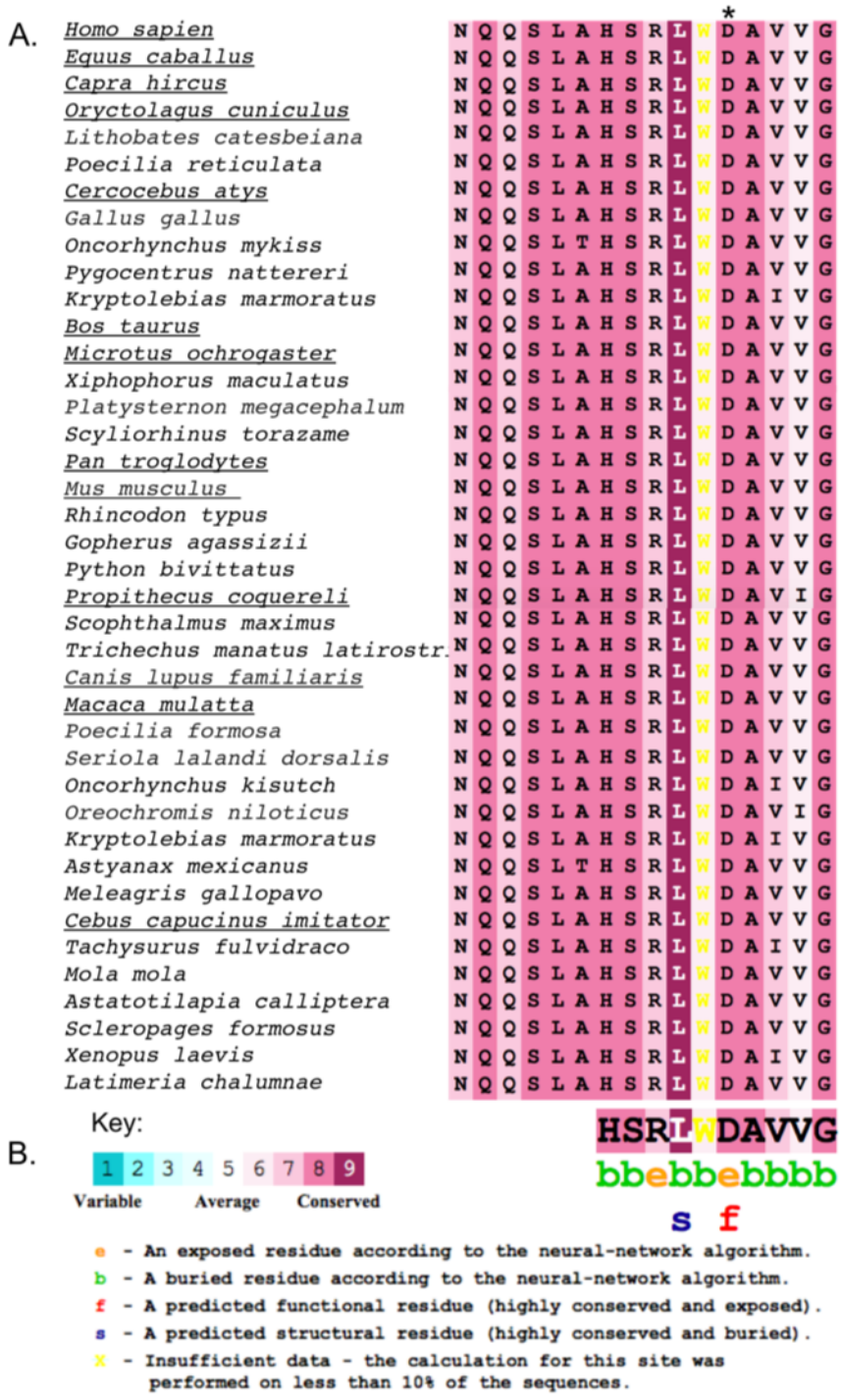

Figure 3.2 – Multiple sequence alignment of p.D3986E residue across 40 RYR1 homologues

CSI-BLAST was used to search for homologues with at least 70% homology to the human RYR1 protein and MAFTT was used to create a multiple sequence alignment. ConSurf was used to determine and colour code the conservation of residues across homologues. The region surrounding the p.D3986E residue is shown in panel A. Predictions made regarding the exposure and role of the residue are shown in panel B. Mammalian species are indicated by underlining and an asterisk highlights the residue of interest.

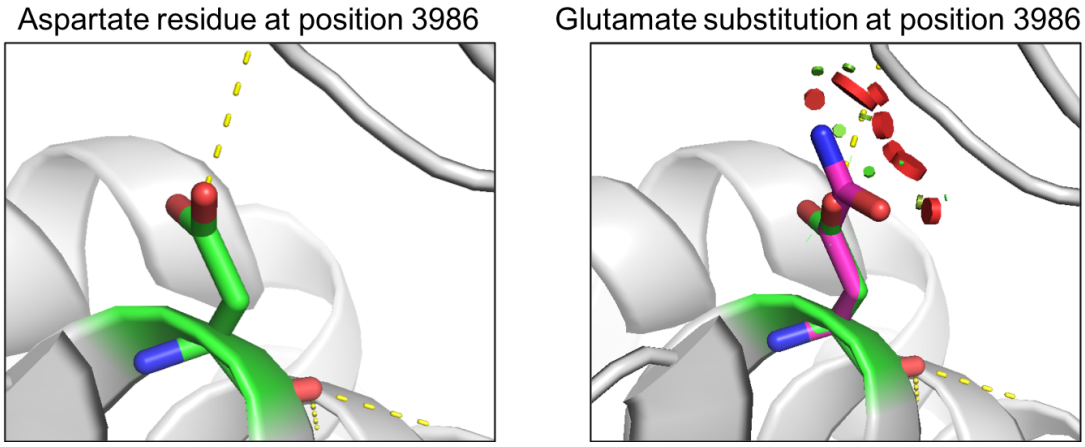

Figure 3.3 – PyMOL mutagenesis of rabbit RYR1 p.D3986E resiude

The mutagenesis tool on PyMOL was used to model the effect of the p.D3986E variant on hydrogen bonding and VdW interactions, within the rabbit RYR1 structure (Protein data bank (PDB ID: 3J8H). The ancestral residue is shown in green and the variant is in pink. Hydrogen bonds are shown by yellow dashes and VdW clashes are shown by green (less severe) and red (more severe) disks.

3.2.3 Cell line validation

Prior to genome-editing, DNA was extracted from the human immortalised myoblasts used in this project and primers were designed to amplify regions around all diagnostic MH variants that had been functionally characterised at the time this work was performed. Sanger sequencing was performed on the regions around each variant to confirm the absence of them in the cell line. Indeed, no variants were detected.

3.2.4 gRNA design

For the introduction of the p.D3986E variant, all gRNAs were designed using CCTOP (Stemmer et al. 2015) and off-targets predicted by CCTOP were confirmed using CRISPOR (Haeussler et al., 2016). Within CCTOP, CRISPRater generates a predicted efficacy score (Labuhn et al., 2017). The gRNAs with efficacy values <0.56 are deemed low efficacy, gRNAs with efficacy values ≥0.56 but ≤0.74 are deemed medium efficacy and gRNAs with efficacy values >0.74 are deemed high efficacy. Inputting a 100 bp sequence flanking the base to be edited returned 14 gRNA results. Within the top 5 ranked gRNAs, three were of medium to high quality and were deemed

suitable distances away from the desired based change (Table 3.2). The first human p.D3986E-targeting gRNA (Hs_D3986E_gRNA1) had a cut site 8 bp from the desired base change. Hs_D3986E_gRNA1 had an efficacy score of 0.82 and 8 off-targets of which 1 was exonic, 5 were intronic and 2 were intergenic. Hs_D3986E_gRNA2, with a cut site 9 bp from the target, had an efficacy score of 0.76 and 27 off-targets of which 2 were exonic, 15 were intronic and 10 were intergenic. Hs_D3986E_gRNA3, with a cut site 20 bp from the target, had an efficacy score of 0.68 and 43 off-targets of which none were exonic, 12 were intronic and 31 were intergenic. Hs_D3986E_gRNA1 and 2 target the coding strand whereas Hs_D3986E_gRNA 3 targets the non-coding strand.

Table 3.2 – Human p.D3986E-targeting gRNA sequences and their PAM

gRNA name	Sequence	PAM
Hs_D3986E_gRNA1	CCTGGCGCACAGTCGCCTAT	GGG
Hs_D3986E_gRNA2	GCCTGGCGCACAGTCGCCTA	TGG
Hs_D3986E_gRNA3	TCATGTGGGCGAACACGTGC	AGG

The gRNAs were commercially synthesised as single-stranded oligonucleotides with appropriate overhangs to facilitate *in-vitro* transcription (Table 3.3), cloning into pGCS (Table 3.4) and cloning into pSpCas9(BB)-2A-GFP (Table 3.5). To confirm that there were no single nucleotide polymorphisms (SNPs) within the intended gRNA region in the target cells, DNA was extracted from human immortalised myoblasts by salting-out and used as a PCR template to amplify a 400 bp region around the intended gRNA site. The resultant amplicons were prepared for Sanger sequencing. No SNPs were identified within any of the intended gRNA sequences (Figure 3.4).

Table 3.3 – Human RYR1 p.D3986E-targeting gRNA primer sequences for *in-vitro* transcription

Sequences in black text show the partial gRNA sequence (primer 1 is a partial forward sequence and primer 2 is a partial reverse complement sequence). Sequences in green text show the T7 promoter sequence to enable *in-vitro* transcription and sequences in blue text show the partial tracrRNA sequence.

Primer name	Primer 1 5'-3'	Primer 2 5'-3'
Hs_D3986E_IVT_gRNA1	TAATACGACTCACTATAGCCTGGCGCACAGTCGC	TTCTAGCTCTAAAACATAGGCGACTGTGCGCCAG
Hs_D3986E_IVT_gRNA2	TAATACGACTCACTATAGGCCTGGCGCACAGTCG	TTCTAGCTCTAAAACTAGGCGACTGTGCGCCAGG
Hs_D3986E_IVT_gRNA3	TAATACGACTCACTATAGTCATGTGGGCGAACAC	TTCTAGCTCTAAAACGCACGTGTTCGCCCACATG

Table 3.4 – Human RYR1 p.D3986E-targeting gRNA sequences for cloning into pGCS

Sequences in black text show the gRNA sequences and their complements, with PAM sequences shown in orange. Sequences in green text show the overhangs to facilitate cloning into linearised pGCS.

Oligonucleotide name	Forward sequence 5'-3'	Reverse sequence 5'-3'
Hs_D3986E_pGCS_gRNA1	AATTCCTGGCGCACAGTCGCCTATGGG	CTAGCCCATAGGCGACTGTGCGCCAGG
Hs_D3986E_pGCS_gRNA2	AATTGCCTGGCGCACAGTCGCCTAGGG	CTAGCCCTAGGCGACTGTGCGCCAGGC
Hs_D3986E_pGCS_gRNA3	AATTTCATGTGGGCGAACACGTGCGGG	CTAGCCCGCACGTGTTCGCCCACATGA

Table 3.5 – Human RYR1 p.D3986E-targeting gRNA sequences for cloning into pSpCas9(BB)-2A-GFP

Sequences in black show the gRNAs and their complements. Sequences in green show the overhangs needed to facilitate cloning into linearised pSpCas9(BB)-2A-GFP and blue text shows the additional G residue added to gRNA sequences of which the first base is not G. This additional G base facilitates transcription from the U6 promoter present on the pSpCas9(BB)-2A-GFP vector.

Oligonucleotide name	Forward sequence 5'-3'	Reverse sequence 5'-3'
Hs_D3986E_pSp_gRNA1	CACCgCCTGGCGCACAGTCGCCTAT	AAACATAGGCGACTGTGCGCCAGGc
Hs_D3986E_pSp_gRNA2	CACCGCCTGGCGCACAGTCGCCTA	AAACTAGGCGACTGTGCGCCAGGC
Hs_D3986E_pSp_gRNA3	CACCgTCATGTGGGCGAACACGTGC	AAACGCACGTGTTCGCCCACATGAc

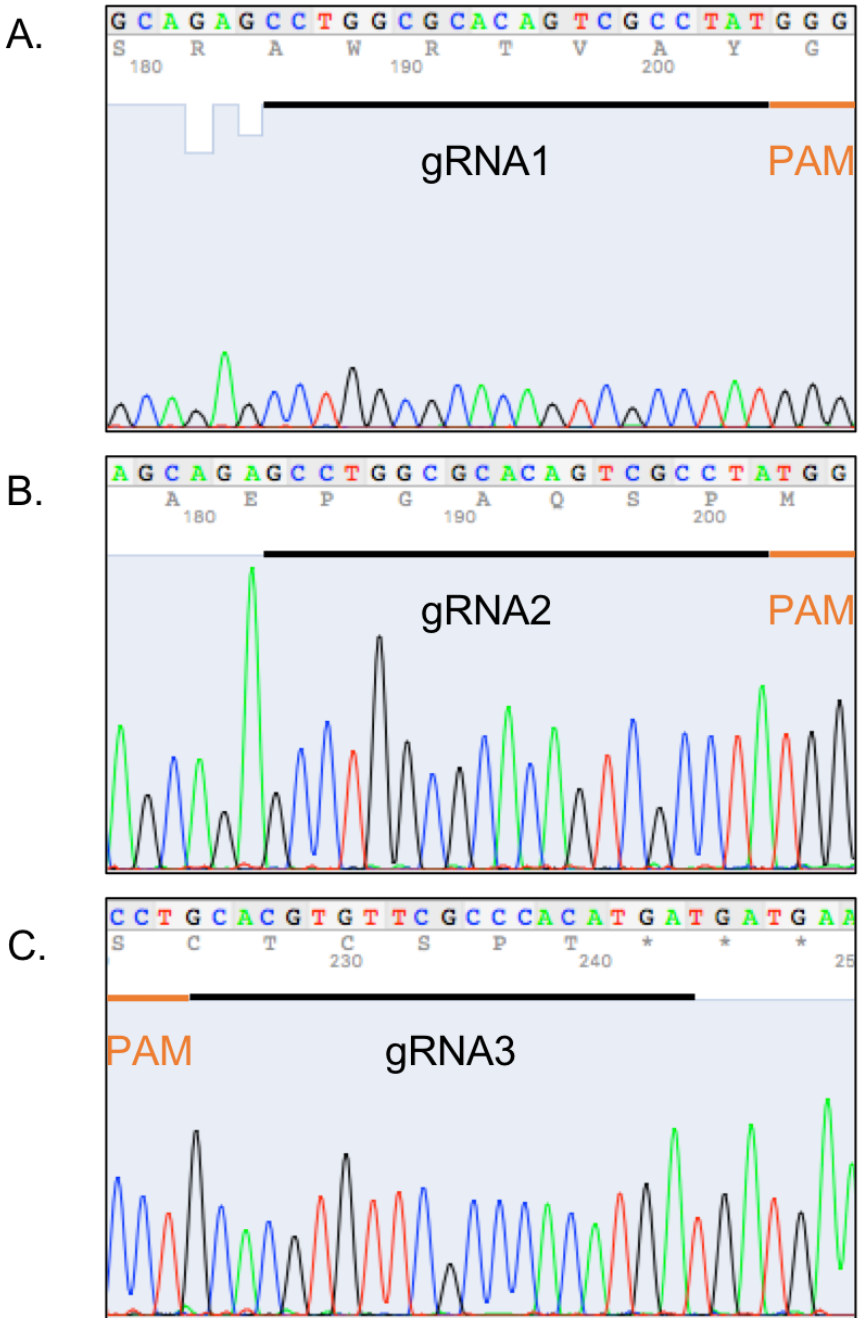

Figure 3.4 – Human p.D3986E-targeting gRNA sequences in the human immortalised myoblast genome

Sanger sequencing was performed to confirm the presence or absence of SNPs within the intended gRNA regions. The gRNA sequences for Hs_D3986E_gRNA1, 2 and 3 (panels A, B and C, respectively) are indicated and their PAMs labelled in orange. Note that Hs_D3986E_gRNA3 targets the reverse strand but the sequence shown is the forward, coding strand. Sequencing chromatograms were viewed in 4Peaks software (Nucleobytes).

3.2.5 HDR template design

Following confirmation that the gRNA regions were free of SNPs, the genomic human RYR1 reference sequence, NG_008866.1, was retrieved and used to manually design HDR templates that would introduce the variant of interest. HDR templates were designed as single stranded oligonucleotides that had 80 base pairs of homology to the target sequence flanking the Cas9 cut site (Table 3.6). For Hs_D3986E_gRNA3, a silent mutation in the PAM site was introduced to prevent re-cleavage following successful incorporation of the HDR arms. For Hs_D3986E_gRNA1 and Hs_D3986E_gRNA2, it was not possible to introduce a silent mutation in the PAM without affecting the amino acid coding sequence, so a number of silent mutations were added to the 12 nt seed region of the gRNA (Figure 3.5). To facilitate the production of heterozygotes following transfection, two HDR templates were designed per gRNA – one which contained the edited p.D3986E variant plus the PAM/seed region silent mutations and one which contained the wild-type D3986 residue plus the PAM/seed region silent mutations.

Table 3.6 – Human RYR1 p.D3986E-targeting HDR template sequences

HDR template sequences used to introduce the RYR1 p.D3986E variant into human immortalised myoblasts. The gRNA sequences are shown in orange and edited bases in purple. PAMs are shown in green and the base to be changed is shown in red. The Cas9 cut site is indicated by a /.

HDR template	Sequence 5'-3'
Hs_D3986E_ HDR_gRNA1	GATTCCCTTCCCCCCCACACGGCACTCTGCCTCCCAGGGTCCCTGCACCGGGAACCAGCAGAGCCTGGCGCACTCCAGGT/ TGTGGGAGGCAGTGGTGGGATTCCTGCACGTGTTCGCCCACATGATGATGAAGCTCGCTCAGGTTCGAGCCCCTCTGGTC
Hs_D3986E_ HDR_gRNA2	GGATTCCCTTCCCCCCCACACGGCACTCTGCCTCCCAGGGTCCCTGCACCGGGAACCAGCAGAGCCTGGCGCACTCCAGG/ TTGTGGGAGGCAGTGGTGGGATTCCTGCACGTGTTCGCCCACATGATGATGAAGCTCGCTCAGGTTCGAGCCCCTCTGGT
Hs_D3986E_ HDR_gRNA3	GCCTCCCAGGGTCCCTGCACCGGGAACCAGCAGAGCCTGGCGCACAGTCGCCTATGGGAGGCAGTGGTGGGATTTCTGCA/ CGTGTTCGCCCACATGATGATGAAGCTCGCTCAGGTTCGAGCCCCTCTGGTCTCCATCCACCTGCTTCCGGGCGTCCCCC

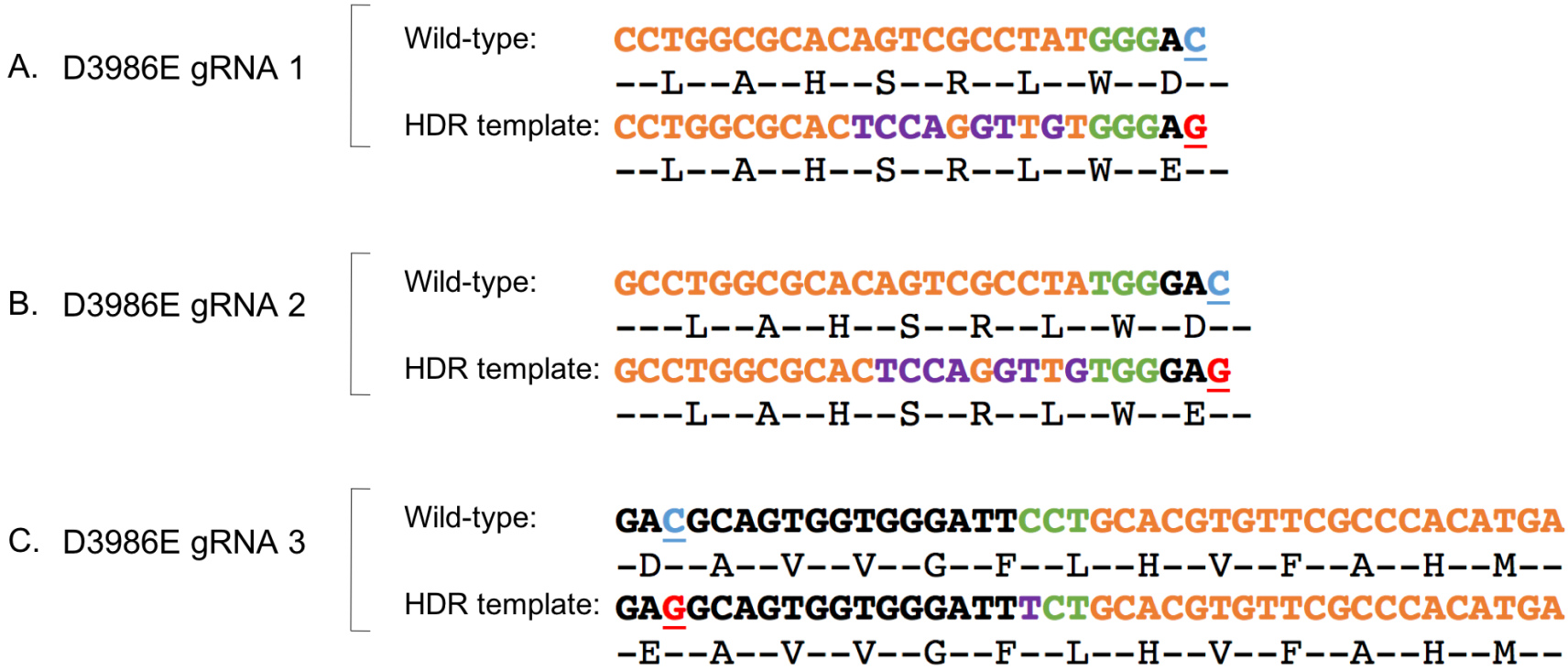

Figure 3.5 – Human *RYR1* p.D3986E-targeting HDR templates

HDR arms were designed to include 80 bp of homology upstream and downstream of the Cas9 cut site. HDR templates were modified from the original target sequence to prevent re-cleavage by Cas9 following insertion into the genome, by introducing silent mutations into either the PAM sequence (panel C) or the seed region (panels A and B). The gRNA sequences are shown in orange text, PAMs in green text, the base to be edited in blue text, the edited base in red and the silent mutations in purple. Beneath the DNA sequences are the amino acid single letter codes.

3.2.6 Preparation of reagents for use in Cas9 protein system

For the introduction of purified Cas9 in complex with the gRNA:tracrRNA duplex and pGCS, the gRNA:tracrRNA fusion was produced by *in-vitro* transcription (IVT) and the gRNA sequences (including their PAMs) were cloned into pGCS.

3.2.6.1 *In-vitro* transcription of gRNAs

Using the Precision gRNA synthesis kit (Invitrogen™), the gRNA:tracrRNA fusion DNA template for IVT was produced by PCR using primers shown in Table 3.3. Primer 1 contained a region of complementarity to the T7 promoter sequence and a 5' portion of the gRNA specific sequence. Primer 2 had a region of complementarity to the tracrRNA and the 3' gRNA sequence that partially overlaps with the gRNA specific sequence on the forward primer (Figure 3.6). Incubation of each primer in a PCR with the company-provided universal T7 primer, tracrRNA sequence and tracrRNA reverse primer would yield a full DNA template for gRNA synthesis.

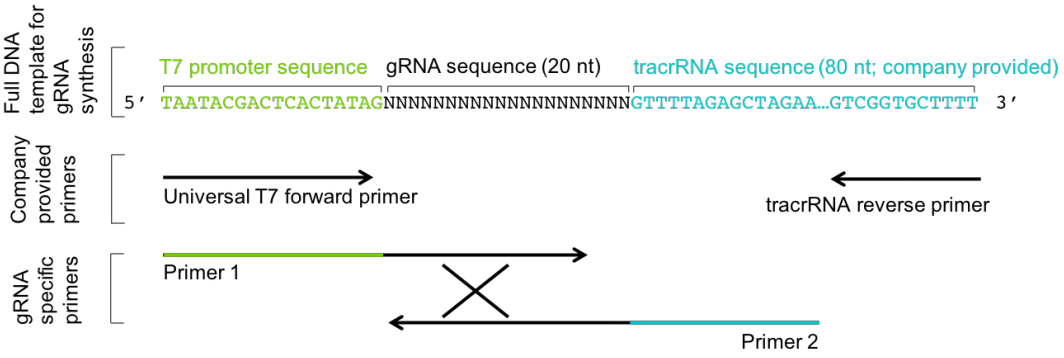

Figure 3.6 – PCR assembly schematic of the T7 promoter:gRNA:tracrRNA fusion

Primer 1 was designed to include 16 nt of the gRNA sequence with the T7 promoter sequence appended to the 5'. Primer 2 was designed to include 19 nt of the reverse complement gRNA sequence and 15 nt of the reverse complement tracrRNA sequence. Adapted from Thermo Fisher Scientific, 2016. Available at: https://tools.thermofisher.com/content/sfs/manuals/geneart_precision_gRNA_synthesis_kit_man.pdf (accessed April 2017).

Successful assembly of the PCR template was determined by agarose gel electrophoresis of the resultant DNA fragment, to confirm its size. Indeed, a ~120 bp product was formed comprising the 18 nt T7 promoter sequence, 20 nt gRNA sequence and 80 nt tracrRNA sequence (Figure 3.7).

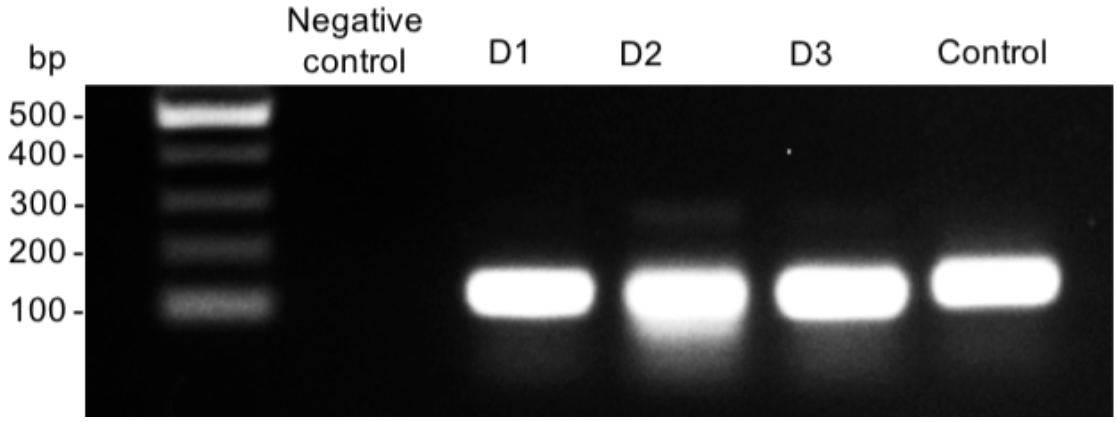

Figure 3.7 – Confirmation of IVT template assembly

IVT template assembly was confirmed by agarose gel electrophoresis on a 1% TAE-agarose gel. Lane 1 contains the 100 bp plus ladder (NEB), lane 2 contains the entire PCR reaction minus the gRNA specific primers, lanes 3, 4 and 5 contain the Hs_D3986E_IVT_gRNA 1, 2 and 3 reactions, respectively. Lane 6 contains the reaction using company-provided positive control primers.

Following confirmation of the correct template assembly, the templates were added to an IVT reaction containing NTPs and the T7 RNA polymerase and incubated at 37^{o}C for 3 hours to synthesise the gRNA:tracrRNA fusion. Successful production of each gRNA:tracrRNA fusion by IVT was confirmed by RNA agarose gel electrophoresis of the resultant products (Figure 3.8). Indeed, a 100 nt band corresponding to the gRNA:tracrRNA fusion was observed in all samples. The RNA was purified from the reaction using an RNA-binding spin column in preparation for complex formation with Cas9 and transfection into human immortalised myoblasts.

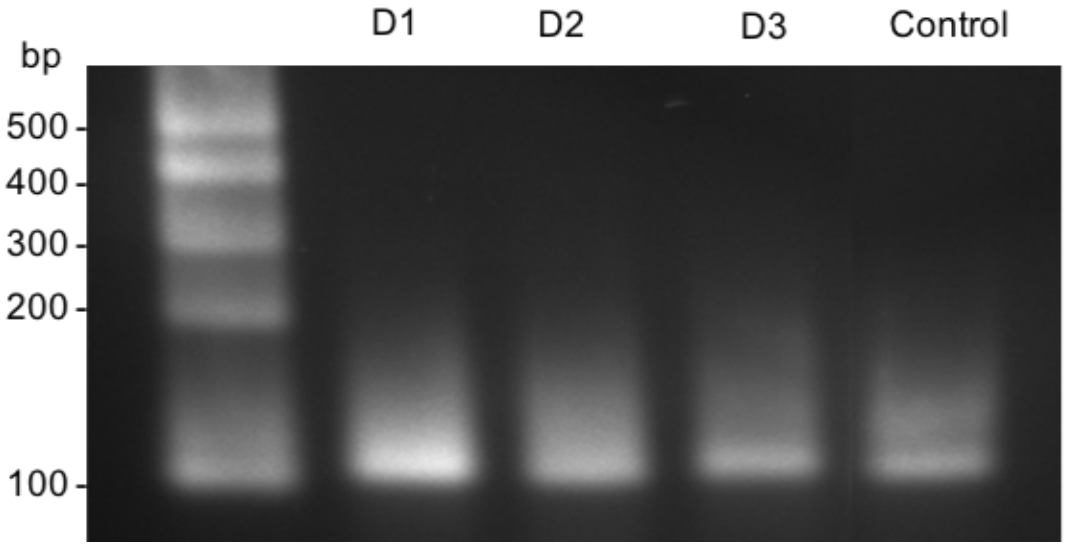

Figure 3.8 – Confirmation of IVT RNA product assembly

RNA generation by IVT was confirmed by electrophoresis on a 1% TAE-agarose gel. Lane 1 shows the Century^{TM}-Plus RNA marker (Ambion), lanes 2, 3 and 4 show IVT reaction products from incubation with the Hs_D3986E_IVT_gRNA1, 2 and 3 templates, respectively. Lane 5 shows the IVT reaction products from incubation with the template made using company-provided positive control primers.

3.2.6.2 Cloning into pGCS

Oligonucleotides containing the gRNAs were designed to include overhangs to facilitate ligation into the pre-linearised pGCS vector (Table 3.4). The forward and reverse oligonucleotides were annealed and incubated with pre-linearised pGCS in a ligation reaction. Ligation reactions were transformed into OneShot^{TM} chemically competent Stbl3^{TM} cells (Invitrogen^{TM}) and plated onto LB agar plates containing ampicillin at 100 µg/ml. 5 single colonies per gRNA were picked and used to inoculate LB media for plasmid isolation by miniprep. Isolated DNA was prepared for Sanger sequencing to confirm successful cloning (Figure 3.9). All of the selected colonies contained the desired insertion.

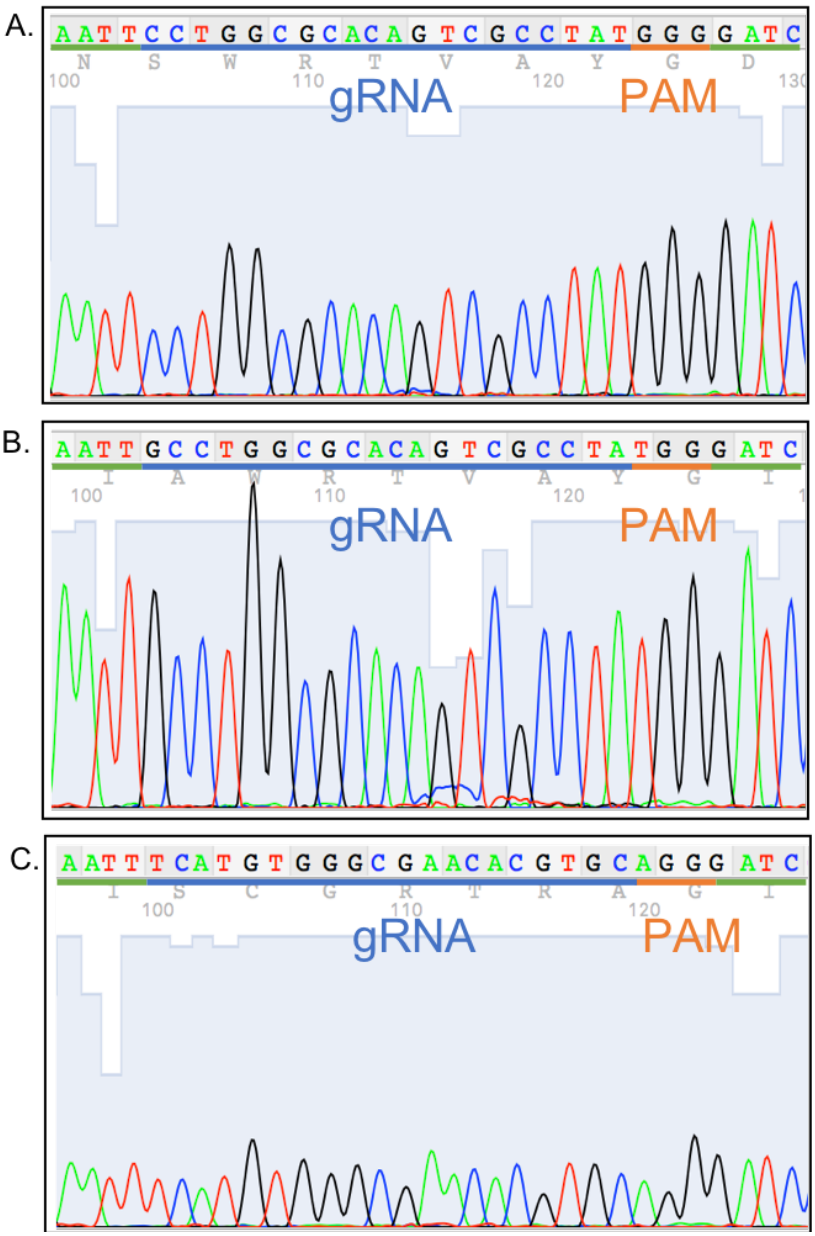

Figure 3.9 – Sanger sequencing traces of human RYR1 p.D3986E-targeting gRNAs in PGCS

Following plasmid isolation, Sanger sequencing was used to confirm the insertion of Hs_D3986E_gRNA, 1 (panel A), 2 (panel B) and 3 (panel C) into pGCS. The pGCS overhangs are shown in green, gRNA sequences in blue and the PAM is in orange. Sequencing chromatograms were viewed in 4Peaks software (Nucleobytes).

3.2.7 Preparation of reagents or use in pSpCas9(BB)-2A-GFP plasmid system

3.2.7.1 Cloning into pSpCas9(BB)-2A-GFP

Prior to cloning, a restriction digest using *Bbs*I and *Age*I was used to confirm plasmid integrity and expected size and digestion products. As expected, digestion with *Bbs*I and *Age*I resulted in the generation of 2 fragments of ~8 kb and ~1 kb. Digestion of pSpCas9(BB)-2A-GFP with *Bbs*I, results in the generation of overhangs. The forward and reverse gRNA sequences designed with complementary overhangs to facilitate cloning into pSpCas9(BB)-2A-GFP (Table 3.5) were annealed to form double stranded DNA. The duplexes were incubated with digested pSpCas9(BB)-2A-GFP in a ligation reaction before treatment with PlasmidSafe ATP-dependent DNase (Epicentre) to remove any residual linearised DNA that could affect transformation efficiency. Ligation reactions were transformed into OneShot™ chemically competent Stbl3™ cells (Invitrogen™) and colonies allowed to grow on LB agar plates containing ampicillin. Four single colonies were picked per gRNA and used to inoculate 5 ml LB broth for miniprep cultures and for use as starter cultures for maxipreps at a later date, as described previously. Isolated plasmid DNA was screened for gRNA insertions by digestion with *Bbs*I and *Age*I – insertion of the gRNA removes the *Age*I restriction site, thus the digest produces only a single band in successfully cloned plasmids. For all gRNAs, restriction digest showed that 100% of the clones analysed contained the insert (Figure 3.10). One colony per gRNA was selected for Sanger sequencing confirmation of the insertion (Figure 3.11). The desired insertion was confirmed for each of the gRNAs.

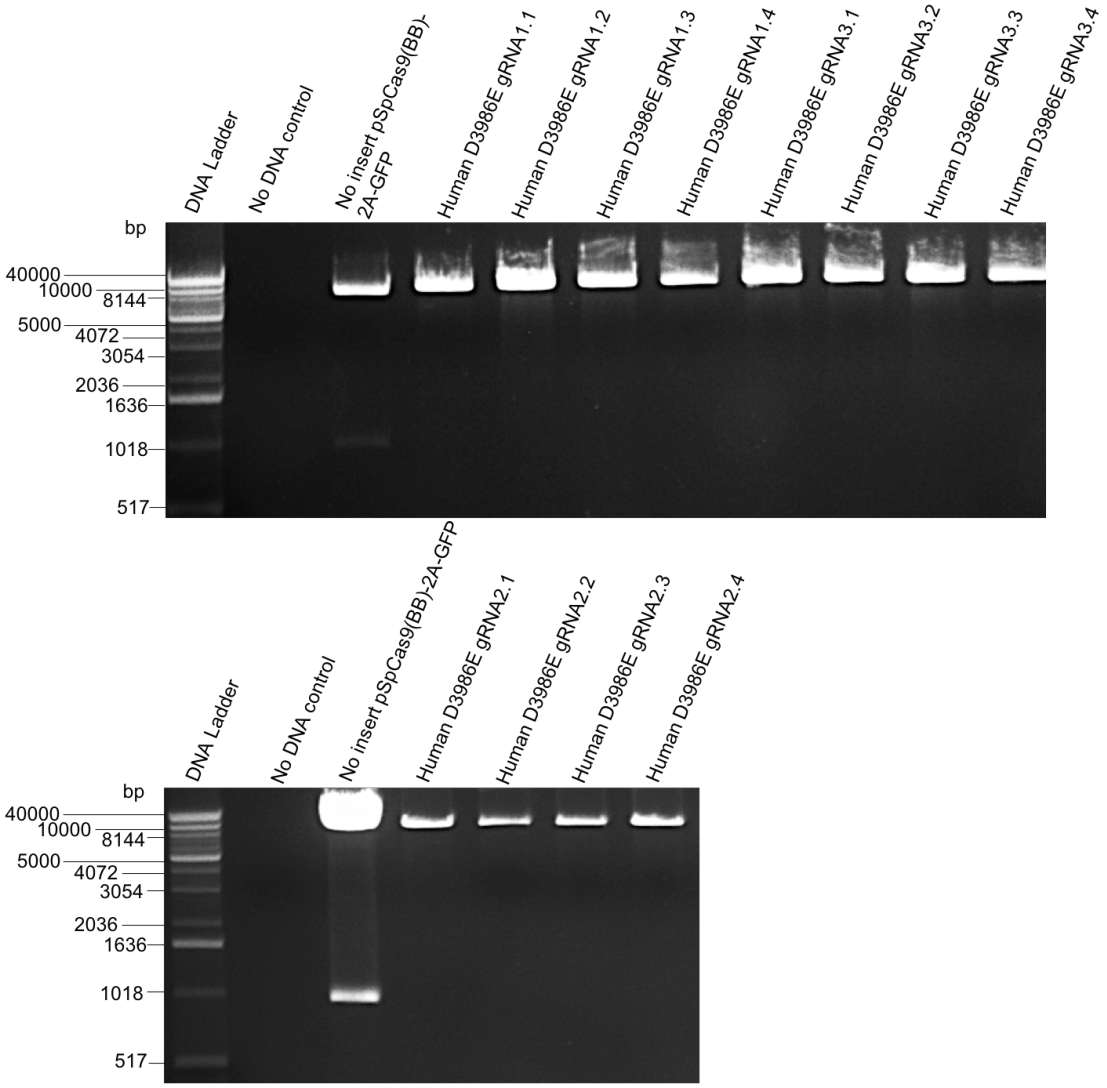

Figure 3.10 - Restriction digest screening of pSpCas9(BB)-2A-GFP clones containing gRNAs

Plasmid DNA was prepared by miniprep from 4 single colonies per gRNA and 500-1000 ng added to a restriction digest with FastDigest *Bbs*I and *Age*I (Thermo Scientific). The entire reaction was loaded onto a 1% TAE-agarose gel for electrophoresis. For each image, lanes 1, 2 and 3 show the 1 kb Plus Extension DNA Ladder (Invitrogen™), a no DNA negative control and a no insert pSpCas9(BB)-2A-GFP control, respectively. Subsequent lanes show the pSpCas9(BB)-2A-GFP vector with the gRNA inserts.

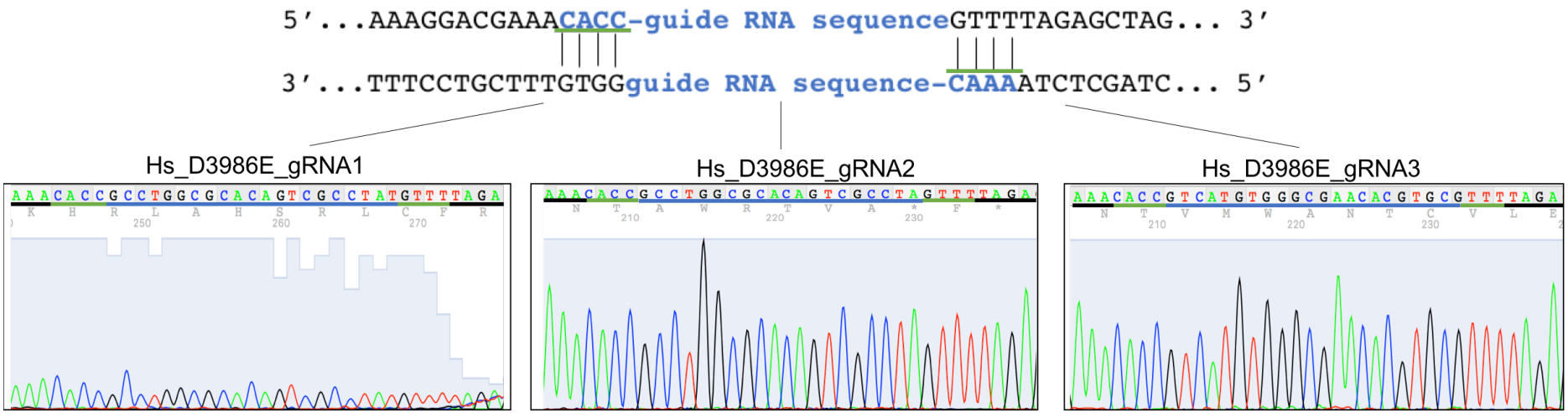

Figure 3.11 - Sanger sequencing traces of human RYR1 p.D3986E-targeting gRNAs in pSpCas9(BB)-2A-GFP

Sanger sequencing was used to confirm the insertion of Hs_D3986E_gRNA1, 2 and 3 into pSpCas9(BB)-2A-GFP. The gRNA sequences are shown in blue and pSpCas9(BB)-2A-GFP overhangs are in green, with additional pSpCas9(BB)-2A-GFP sequence flanking the insertions shown in black. Sequencing chromatograms were viewed in 4Peaks software (Nucleobytes).

3.2.8 Determining gene-editing capacity of gRNAs

The T7 endonuclease I assay (T7 assay) detects and cleaves at mismatches in heteroduplex DNA caused by gene editing. Due to their rapid growth and ease of transfection, human embryonic kidney (HEK)293 FT cells were plated in 6-well plates and used to perform the T7 assay. The pSpCas9(BB)-2A-GFP system was used to detect gene-editing due to the simplicity of transfection, relative ease of plasmid regeneration and cost effectiveness compared to the commercially supplied purified Cas9 protein. The HEK293 FT cells were transfected with the pSpCas9(BB)-2A-GFP plasmids containing each gRNA using the Lipofectamine3000^{TM} transfection reagent. Importantly, no HDR templates were transfected alongside the plasmids at this stage. Twenty four hours following transfection, GFP-expressing (i.e. transfected) cells were enriched by FACS using a 488 nm blue laser and 530/40 bandpass filter. Gates were drawn to exclude non-viable cells from the sort. Cell viability was determined using the forward and side scatter profiles whereby non-viable cells tend to have lower forward scatter measurements (as a measure of size) and higher side scatter measurements (as a measure of granularity). The transfected HEK293 FT cells had an overall viability of 95.94%, comparable to 96.57% for non-transfected HEK293 FT cells (Figure 3.12; panels A and B). As expected, non-transfected cells showed low fluorescence values between 10^0 and 10^1. In contrast, the fluorescence values of transfected HEK293 FT cells are more broadly distributed across the fluorescence intensity spectrum, up to 10^4, indicating that GFP was being expressed in the transfected cells. Using the non-transfected cells as a reference, gates were drawn to define and collect the proportion of cells with GFP expression – this was 51.02% of the total population (Figure 3.12; panels C and D).

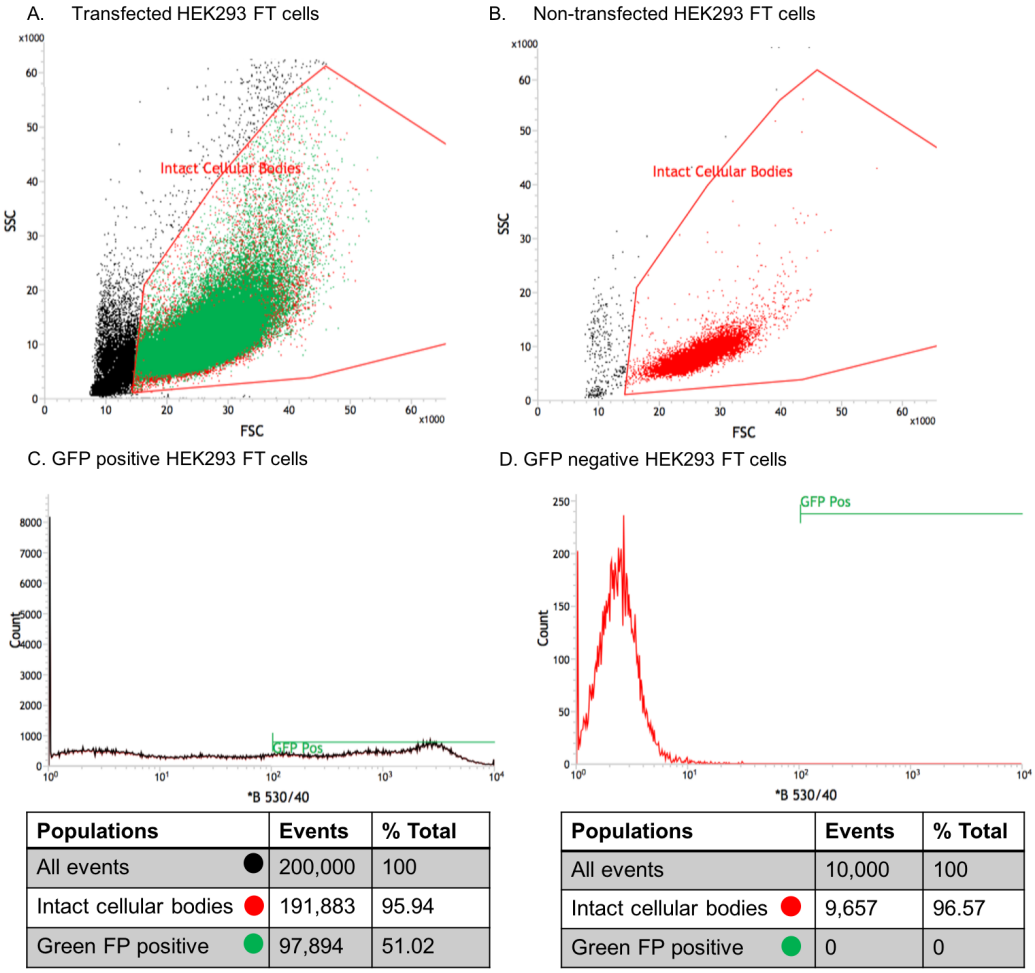

Populations	Events	% Total
All events	200,000	100
Intact cellular bodies	191,883	95.94
Green FP positive	97,894	51.02

Populations	Events	% Total
All events	10,000	100
Intact cellular bodies	9,657	96.57
Green FP positive	0	0

Figure 3.12 – FACS traces for HEK293 FT cells transfected with the pSpCas9(BB)-2A-GFP plasmid

Transfected HEK293 Cells were incubated for 24 hours at 37°C, 5% CO_2 prior to FACS. Panels A and B show the side scatter profile (SSC; X axis) and forward scatter profile (FSC; Y axis) of HEK293 FT cells transfected with pSpCas9(BB)-2A-GFP and non-transfected HEK293 FT cells, respectively. Panels C and D show the cell count (Y axis) and fluorescence intensity count in arbitrary units (X axis) of GFP positive HEK293 FT cells and non-transfected HEK293 FT cells, respectively. Non-transfected cells were used as a control to assist the drawing of GFP positive gates in the transfected sample. The number of events corresponds to the number of cells detected by the laser and is usually measured between 10,000-200,000 cells dependent on the sample size, to give a snapshot of the profile of the cells.

For each gRNA, the GFP-expressing cells were pooled and genomic DNA extracted. A 388 bp region around the gRNA cut site was amplified by PCR and purified using AMPureXP magnetic beads (Beckman Coulter™). The purified PCR product was denatured by heating and slowly reannealed, to encourage the formation of heteroduplex DNA. The heteroduplex products were incubated with T7 endonuclease I and separated by agarose gel electrophoresis (Figure 3.13). Successful gene-editing by the gRNA-Cas9 complex is indicated by the presence of cleavage products derived from the 388 bp amplicon. The size of the expected cleavage products was determined by the location of the Cas9 cut site within the amplicon. Indeed, the T7 assay from HEK293 FT cells transfected with Hs_D3986E_gRNA 1, 2 and 3 yielded products corresponding to ~157 bp and 231 bp, 156 bp and 232 bp and 129 bp and 259 bp, respectively. Furthermore, no cleavage products arose from the T7 assay from non-transfected cells.

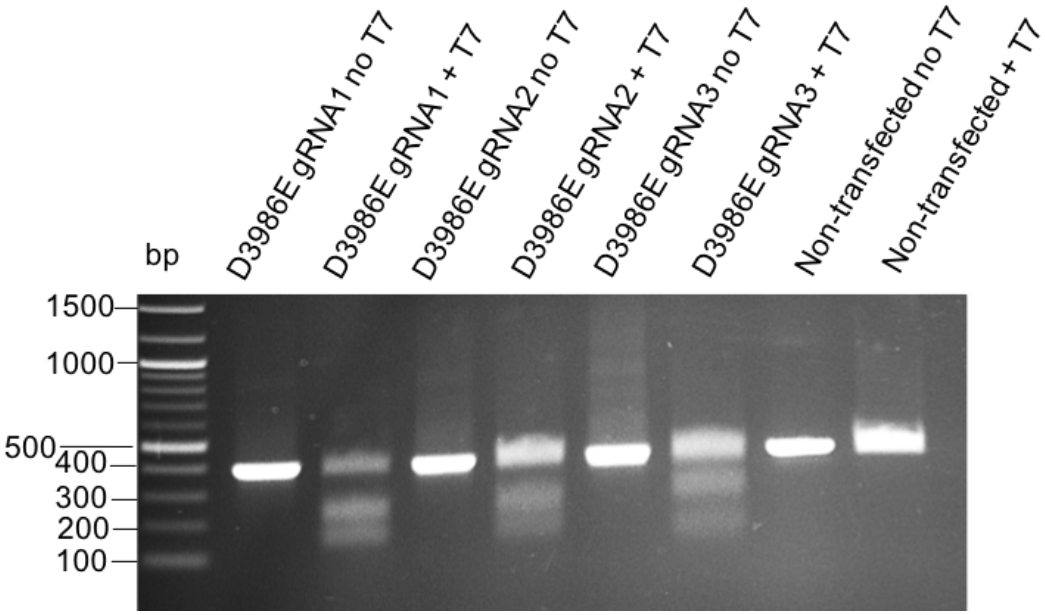

Figure 3.13 – T7 assay to determine gene editing capacity of Hs_D3996E_gRNA 1, 2 and 3 in HEK293 FT cells.

Products from T7 assay were separated by gel electrophoresis on a 1% TAE-agarose gel. Lane 1 shows the 100 bp DNA ladder (NEB), lane 2 shows the T7 assay from cells transfected with the Hs_D3986E_gRNA1 plasmid without the T7 enzyme, lane 3 shows the T7 assay from cells transfected with the Hs_D3986E_gRNA1 plasmid with the T7 enzyme, lane 4 shows the T7 assay from cells transfected with the Hs_D3986E_gRNA2 plasmid without the T7 enzyme, lane 5 shows the T7 assay from cells transfected with the Hs_D3986E_gRNA2 plasmid with the T7 enzyme, lane 6 shows the T7 assay from cells transfected with the Hs_D3986E_gRNA3 plasmid without the T7 enzyme, Lane 7 shows the T7 assay from cells transfected with the Hs_D3986E_gRNA3 plasmid with the T7 enzyme, lane 8 shows the T7 assay from non-transfected cells without the T7 enzyme and lane 9 shows the T7 assay from non-transfected cells with the T7 enzyme.

ImageJ was used to quantify the relative intensity (which is proportional to DNA quantity) of each band by 2D densitometry. The percentage of product cleaved for Hs_D3986E_gRNA1, 2 and 3 was 62.6%, 31.5% and 23.0%, respectively. Gene-editing efficiency was calculated using Equation 1, where the fraction cleaved is the sum of the cleaved fragments divided by the sum of all fragments (Guschin et al., 2010).

Equation 1.

$$\%\ \boldsymbol{gene\ modification} = \mathbf{100} \times \left(\mathbf{1} - (\mathbf{1} - \boldsymbol{fraction\ cleaved})^{\mathbf{1}/\mathbf{2}}\right)$$

The percentage gene modifications of Hs_D3986E_gRNA1, 2 and 3 were 39.2%, 17% and 12.3%, respectively. Since Hs_D3986E_gRNA1 had the highest predicted gene-editing efficiency and had the shortest distance between the base to be edited and the Cas9 cut site, this gRNA was selected for future work.

3.2.9 Transfection of human immortalised myoblasts

Following the determination that all gRNAs induced gene-editing in HEK293 FT cells, progress was made towards implementing both the Cas9 protein system and pSpCas9(BB)-2A-GFP plasmid system in human immortalised myoblasts.

3.2.9.1 Transfecting Cas9, pGCS and gRNA:tracrRNA

Prior to full transfection of the Cas9:tracrRNA:gRNA complex alongside pGCS, human immortalised myoblasts were treated with Lipofectamine™CRISPRMAX™ reagent to determine whether any cell toxicity could be observed from the lipid reagent. Human immortalised myoblasts were plated in 6-well plates and treated with the reagent for 24 hours in triplicate. Following treatment, images were captured of the cells to observe cell morphology using the EVOS™ FL microscope (Figure 3.14). Cell viability was estimated by trypan blue staining and counting using a haematocytometer; the estimated cell viability before treatment was 98.6% and 95.5% following treatment, suggesting that there is no significant detrimental effect on the use of CRISPRMAX™ reagent on human immortalised myoblast viability. Both before and after treatment, cells appeared spindle-like in shape, characteristic of healthy human myoblasts and adhered to the surface of the cell culture flask (Figure 3.14).

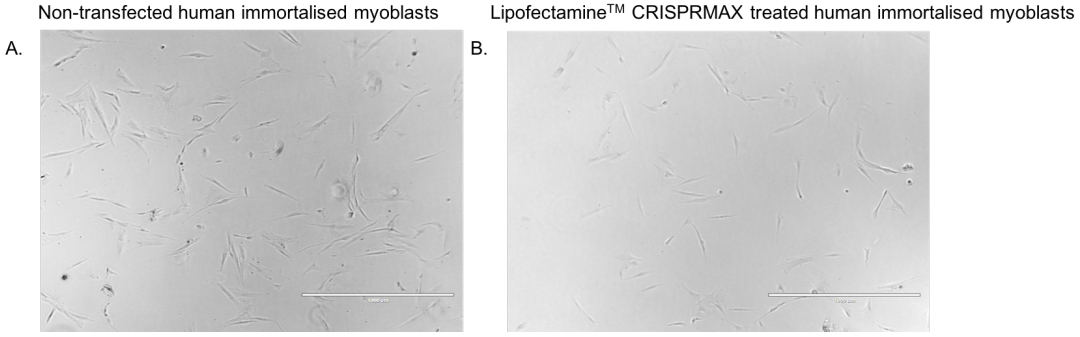

Figure 3.14 – Human immortalised myoblasts treated with CRISPRMAX™ reagent

Human immortalised myoblasts were plated at 1.5 x 10^5 cells per well in a 6-well plate with 1 ml growth media. 3 wells were maintained in growth media (panel A) and 3 were treated with 250 µl OptiMEM media, 7.5 µl CRISPRMAX™ and 5 µl Cas9 plus reagent (panel B). Cells were incubated for 24 hours at 37°C, 5% CO_2 prior to analysis. Images were captured using the EVOS™ FL microscope using the x10 objective. The scale bar shows 1000 µM.

Following confirmation that the CRISPRMAX™ reagent was not detrimental to cell viability, a full transfection of Cas9, pGCS, the tracrRNA:gRNA fusion and the HDR templates was performed in triplicate. Human immortalised myoblasts were plated in 6-well plates and transfected with all reagents using CRISPRMAX™ transfection reagent. Following incubation for 24 hours, a marked increase in cell death was observed, with 78.5% of the cells rounded in shape and detached from the surface of the plate (Figure 3.15). Despite this, the remaining cells were obtained for FACS to confirm OFP expression and separate transfected cells from non-transfected cells into a single cell per well in a 96-well plate for cell line propagation (Figure 3.16). In total, FACS for bulk OFP enrichment was attempted 4 times and single-cell collection was attempted 2 times. FACS was performed using a 561 nm laser and 585/30 bandpass filter. Gates were drawn to exclude non-viable cells from the sort as described previously. Despite significant cell death following transfection, the mean viability of the remaining cells was 88.46% (cf. 95.94% for HEK293 FT plasmid transfection) and for non-transfected cells the mean viability was 97.752%. The mean proportion of OFP positive cells within the population was 26.0%.

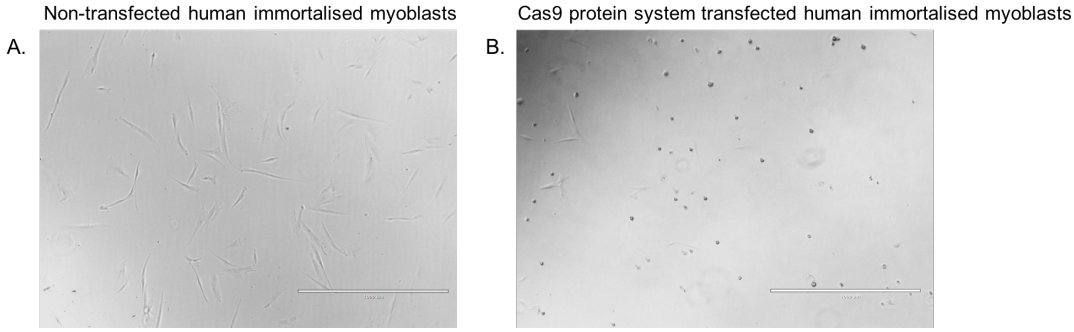

Figure 3.15 – Human immortalised myoblasts following full transfection of Cas9, gRNA:tracrRNA, pGCS and HDR templates

Human immortalised myoblasts were plated at 1.5 x 10^5 cells per well in a 6 well plate with 1 ml growth media (2 full 6-well plates were used per transfection). 250 µl OptiMEM media, 7.5 µl CRISPRMAX™, 12.5 µl Cas9 plus reagent, 1.2 µg gRNA:tracrRNA, 6.25 µg Cas9, 2.5 µg pGCS and 5 µl of 10 µM HDR templates were added to 3 wells and incubated for 24 hours at 37°C, 5% CO_2. Images were captured using the EVOS™ FL microscope using the x10 objective. The scale bar shows 1000 µM.

A. Transfected human immortalised myoblasts B. Non-transfected human immortalised myoblasts

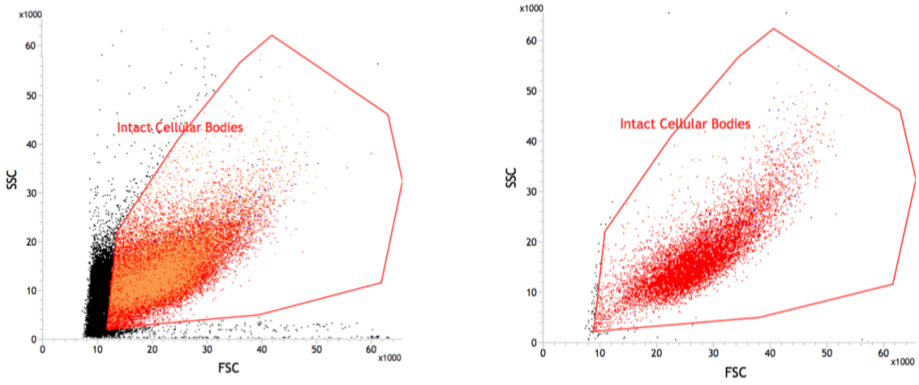

C. OFP positive human immortalised myoblasts D. Non-transfected human immortalised myoblasts

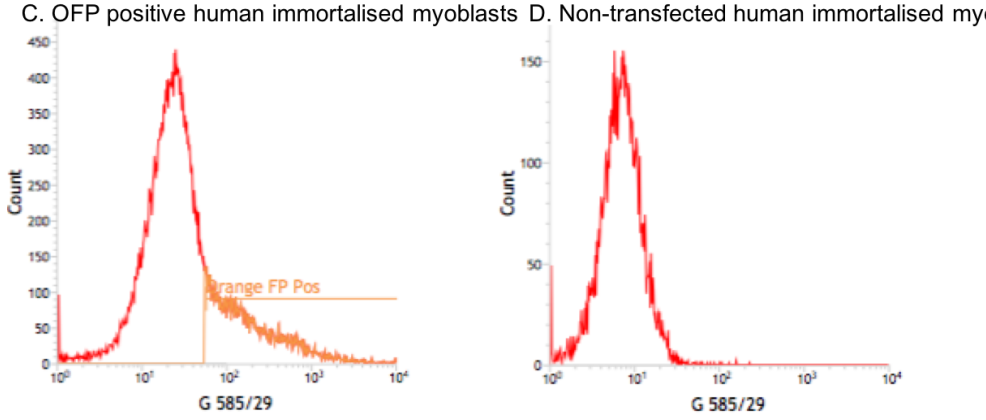

Populations	Events	% Total
All events	52,832	100.00
Intact cellular bodies	41,668	78.87
Orange FP positive	9,879	18.70

Populations	Events	% Total
All events	10,000	100.00
Intact cellular bodies	9,907	99.07
Orange FP positive	-	-

Figure 3.16 – FACS traces of human immortalised myoblasts following transfection with Cas9, tracrRNA:gRNA, pGCS and HDR templates.

Transfected human immortalised myoblasts (between doubling number 51 and 60) were incubated for 24 hours at 37°C, 5% CO_2 prior to FACS. Panels A and B show the side scatter (SSC; X axis) and forward scatter (FSC; Y axis) profiles for transfected and non-transfected cells, respectively. Panels C and D show the cell counts (X axis) and fluorescence intensity in arbitrary units (Y axis) for OFP positive and OFP negative cells, respectively. The number of events corresponds to the number of cells detected by the laser and is usually measured between 10,000-200,000 cells dependent on the sample size, to give a snapshot of the profile of the cells. A representative trace of a bulk cell collection FACS sort has been shown for reference; however, bulk enrichment was attempted 4 times and single cell collection was attempted twice.

Promising levels of OFP expression were achieved in human immortalised myoblasts transfected with all components of the Cas9 protein system, indicating that the system was functional and gene-editing had occurred;

however, cells isolated for both single cell propagation and bulk cell storage failed to survive. For the optimisation of bulk cell collection, collection media was provided in different ratios of conditioned:fresh media – 0:1, 1:1, 1:2 and 1:4 and cells were added to ECL-coated flasks. Despite this, cells failed to attach to the surface of the plate. For single cell collection, two ratios of conditioned:fresh media were used – 1:1 and 1:2 and 96-well plates were coated with ECL. Unfortunately, no single cells appeared to show signs of growth. Since transfection of the Cas9 protein system resulted in significant cell death, the pSpCas9(BB)-2A-GFP system was implemented and optimised in an attempt to limit cell death following transfection and encourage cell survival following FACS.

3.2.9.2 Transfecting pSpCas9(BB)-2A-GFP

To ensure that the Lipofectamine™ 3000 reagent did not have obvious cytotoxic effects on human immortalised myoblasts, the cells were plated in 6-well plates and treated with the reagent for 24 hours in triplicate. Images were captured and cell viabilities estimated as described previously. The estimated cell viabilities of non-treated cells and treated cells were 98.6% and 97.7%, respectively. Both before and after treatment, cells remained spindle-like in shape and adhered to the surface of the cell culture flask (Figure 3.17). Thus, like the CRISPRMAX™ reagent, Lipofectamine 3000™ did not appear to have any significant effect on cell viability.

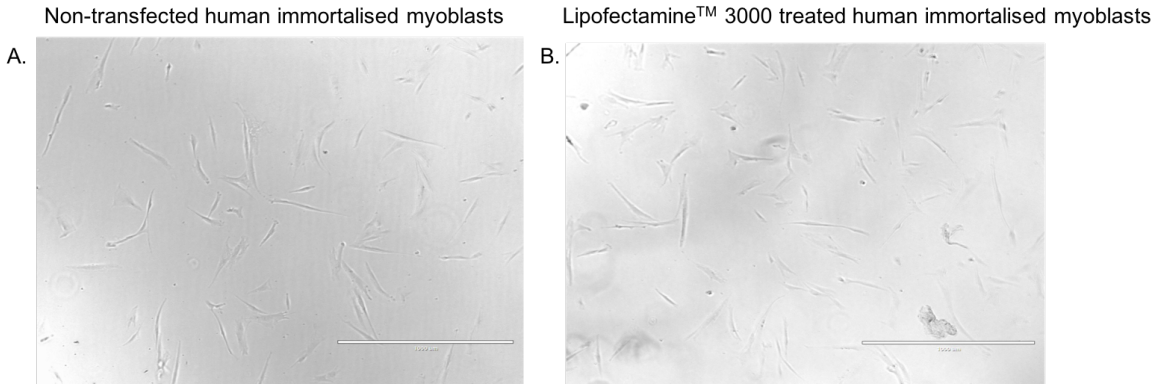

Figure 3.17 – Human immortalised myoblasts following treatment with Lipofectamine™ 3000 reagent

Human immortalised myoblasts were plated at 1.5 x 10^5 cells per well with 1 ml growth media in a 6-well plate. 250 µl OptiMEM media, 7.5 µl Lipofectamine™ 3000 and 5 µl p3000 reagent were added to the cells and incubated overnight at 37°C, 5% CO_2. Images were captured using the EVOS™ FL microscope using the x40 objective. The scale bar shows 1000 µM.

3.2.9.2.1 Viability of human immortalised myoblasts following transfection of pSpCas9(BB)-2A-GFP

Following the determination that Lipofectamine™ 3000 does not cause any obvious cell toxicity, the transfection of pSpCas9(BB)-2A-GFP containing Hs_D3986E_gRNA1 alongside HDR templates was performed. To determine optimal conditions for the transfection, a range of DNA:Lipofectamine™ 3000 ratios and volumes were tested in triplicate. Transfection efficiency was estimated by counting the proportion of GFP expressing cells within a given area using the EVOS™ FL counting tool. The estimated transfection efficiencies of cells transfected with 0.5 µg DNA and 0.75 µl Lipofectamine™ 3000 (1:1.5 ratio; Figure 3.18 panel A), 0.5 µg DNA and 1.5 µl Lipofectamine™ 3000 (1:3 ratio; Figure 3.18 panel B), 1 µg DNA and 0.75 µl Lipofectamine™ 3000 (1.3:1 ratio, Figure 3.18 panel C) and 1 µg DNA and 1.5 µl Lipofectamine™ 3000 (1:1.5 ratio; Figure 3.18 panel D) were 2.5%, 4.8%, 7.1% and 7.7%, respectively).

With all Lipofectamine™ 3000 doses, cell death was observed with cells forming ball-shaped structures (as opposed to healthy spindle-like myoblasts) that detached from the surface of the plate (Figure 3.18). The average estimated viabilities of cells transfected with 0.5 µg DNA and 0.75 µl

Lipofectamine™ 3000 (1:1.5 ratio; Figure 3.18 panel A), 0.5 µg DNA and 1.5 µl Lipofectamine™ 3000 (1:3 ratio; Figure 3.18 panel B), 1 µg DNA and 0.75 µl Lipofectamine™ 3000 (1.3:1 ratio, Figure 3.18 panel C) and 1 µg DNA and 1.5 µl Lipofectamine™ 3000 (1:1.5 ratio; Figure 3.18 panel D) were 81.1%, 64.7%, 68.1% and 60.11%, respectively. The estimated viability of non-transfected cells was 84.7%.

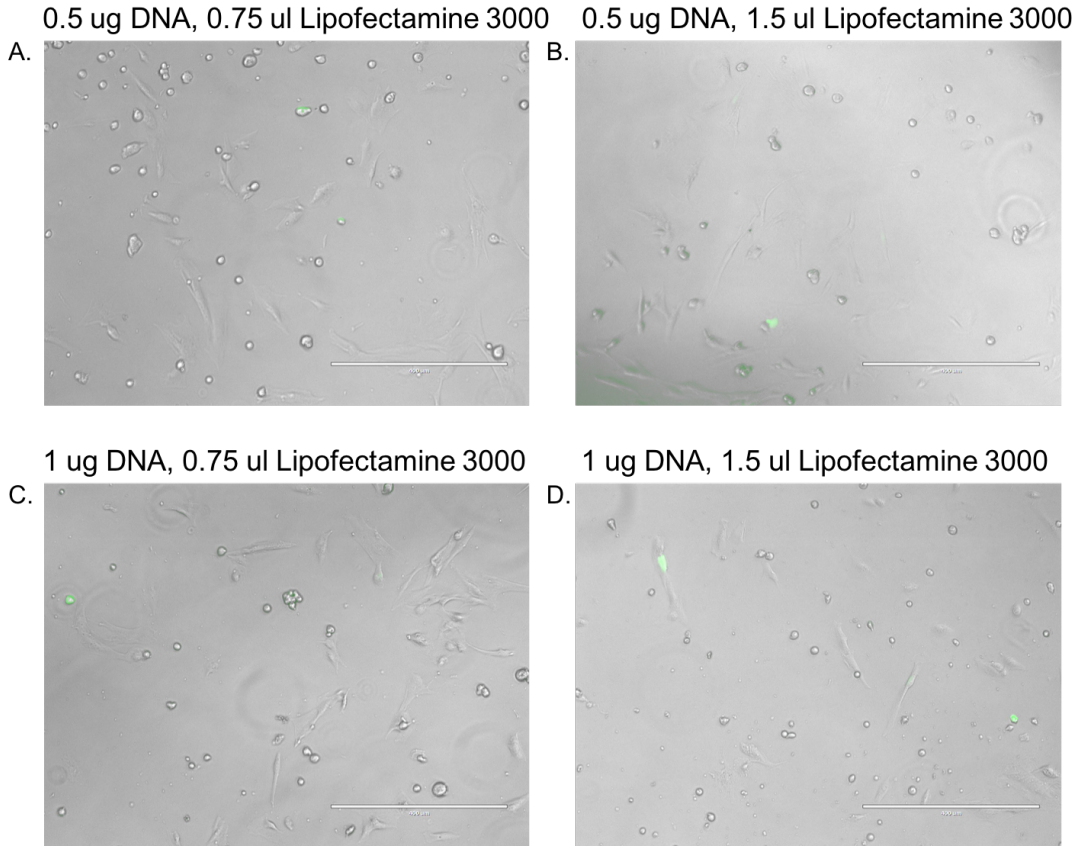

Figure 3.18 - Human immortalised myoblasts transfected with pSpCas9(BB)-2A-GFP

Human immortalised myoblasts were plated at 3 x 10^4 cells per well in a 24-well plate and treated with a range of DNA:Lipofectamine™ 3000 ratios and volumes - with 0.5 µg DNA and 0.75 µl Lipofectamine™ 3000 (panel A), 0.5 µg DNA and 1.5 µl Lipofectamine™ 3000 (panel B), 1 µg DNA and 0.75 µl Lipofectamine™ 3000 (panel C) and 1 µg DNA and 1.5 µl Lipofectamine™ 3000 (panel D). 2 µl p3000 reagent was added per µg of DNA. Lipid complexes were incubated at room temperature for 20 min before being added dropwise to cells. Cells were incubated for 24 hours at 37°C, 5% CO_2 prior to image capture using the EVOS™ FL microscope with a x40 objective. The scale bar shows 400 µM.

The conditions resulting in the highest cell viability (0.5 µg, 0.75 µl Lipofectamine 3000) were selected for future use in transfections. FACS was performed using the 488 nm blue laser and 530/40 bandpass filter to isolate GFP-expressing cells and sort into single cells per well of 96-well plates. Unlike the Cas9 protein system, GFP expression using the pSpCas9(BB)-2A-GFP plasmid system is not necessarily indicative of gene-editing and acts as a marker of transfection only. Gates were drawn as described previously to exclude non-viable cells from the sort and to enrich GFP positive cells. A representative trace of human immortalised myoblasts transfected with Hs_D3986E_gRNA1 prior to single cell sorting is shown for reference (Figure 3.19); however, bulk GFP-cell enrichment and single-cell collection were each attempted twice. In this instance, the percentage of GFP positive cells in the sample was 5.68%. Of the cells that remained following detachment from the surface of the plate after transfection, the viability was 96.15%. The viability of non-transfected cells was 97.44%. Across repeated sorts, the percentage of GFP positive cells varied with a mean of 7.11% (range 1.42%-15.31%). The mean viability of transfected cells was 97.54% and the mean viability of non-transfected cells was 97.0%. Despite encouraging viabilities of the remaining cells following transfection, similarly to human immortalised myoblasts transfected with the Cas9 protein system, FACS-sorted cells failed to propagate following collection in filtered conditioned media:fresh media at a ratio of 0:1 or 1:1.

The immortalised human myoblasts used in this project were routinely cultured in Hams-F10 Nutrient Mix (Gibco™) supplemented with 20% FBS and 2.5 ng/ml as per routine myoblast culture protocols (Rezniczek et al., 2016); however, since the use of PromoCell Skeletal Muscle Growth media has been reported elsewhere (Lattanzi et al., 2017), a batch of human immortalised myoblasts were cultured in this media and subject to transfection and FACS for bulk cell enrichment as described previously. No clear improvements in cell viability, transfection efficiency or cell survival were observed. After gating, non-transfected cells had a viability of 76.32% and cells transfected with Hs_D3986E_gRNA1 had a cell viability of 84.17%. The proportion of GFP-positive cells after gating was 5.49%. Whilst the cell viabilities were lower here

than in previous sorts, it cannot be determined whether this is due to a change in media since transfection and FACS in PromoCell Skeletal Muscle media was performed once. Unfortunately, FACS-sorted cells did not survive bulk cell enrichment following collection in a 1:1 ratio of conditioned:fresh PromoCell Skeletal Muscle Growth media.

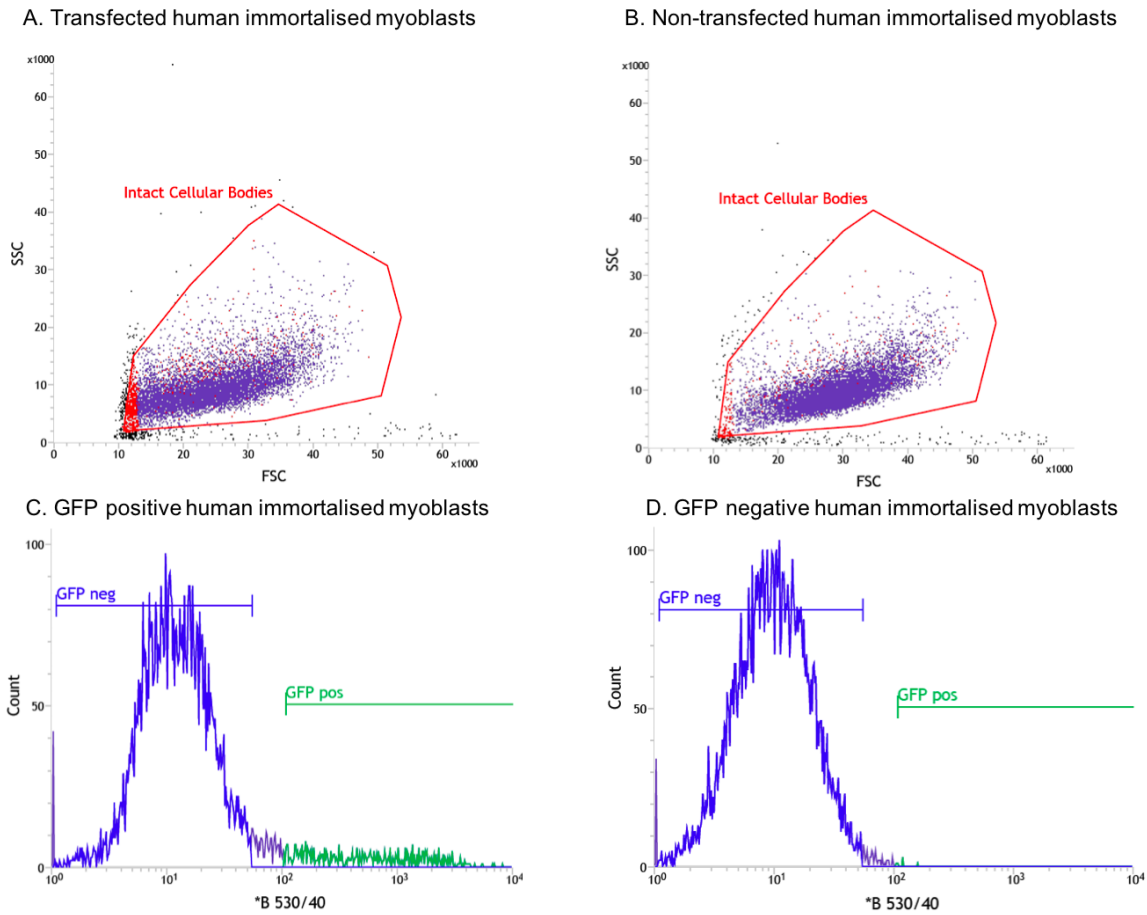

Populations	Events	% Total
All events	10,000	100
Intact cellular bodies	9,615	96.15
Green FP positive	568	5.68
Green FP negative	7,460	74.6
Single cells	8,323	83.23

Populations	Events	% Total
All events	10,000	100.00
Intact cellular bodies	9,744	97.44
Green FP positive	7	0.07
Green FP negative	9,123	91.23
Single cells	9,236	92.36

Figure 3.19 – FACS traces of human immortalised myoblasts transfected with pSpCas9(BB)-2A-GFP

Transfected human immortalised myoblasts (between doubling number 51 and 60) were incubated for 24 hours at 37°C, 5% CO_2 prior to FACS. Panels A and B show the side scatter (SSC; X axis) and forward scatter (FSC; Y axis) profiles for transfected and non-transfected cells, respectively. Panels C and D show the cell counts (X axis) and fluorescence intensity in arbitrary units (Y axis) for GFP positive and GFP negative cells, respectively. The number of events corresponds to the number of cells detected by the laser and is usually measured between 10,000-200,000 cells dependent on the sample size, to give a snapshot of the profile of the cells. A representative trace of a cell population prior to single cell sorting has been shown for reference. In total, bulk cell enrichment was attempted 2 times in Hams-F10 media and once in PromoCell Skeletal Muscle media. Single cell collection was attempted 2 times in Hams-F10 media.

3.3 Discussion and future directions

The results presented in this chapter demonstrate significant progress towards implementing CRISPR-Cas9 in human immortalised myoblasts for a novel method of functional characterisation of MH-associated VUS, namely, p.D3986E.

CRISPR-Cas9 genome-editing was selected for use in this project as it overcomes the requirement for the laborious site directed mutagenesis, cloning and transfection of large *RYR1* constructs that has been considered a bottleneck in MH-associated VUS characterisation. Furthermore, it allows functional characterisation to take place in the context of a muscle cell with a constant genetic background, where ECC machinery is expressed following differentiation into myotubes (Park et al., 1998). For targeting of the human p.D3986E variant, medium to high quality gRNAs targeting the region of interest were designed with relative ease. Using CCTOP, a search for gRNAs with the sequence flanking 50 bp either side of the base to be edited returned 14 gRNAs (Stemmer et al., 2015). The gRNAs for use were selected based on their ranking by CCTOP (determined by the number and location of off-targets and efficacy score) and proximity to the desired base change, since increased gene editing efficiencies are observed when the base to be edited is located as close as possible to the Cas9 cleavage site (Ran et al., 2013a). In this case, the requirement of a PAM did not hinder the design of gRNAs, since the NGG dinucleotide repeat was located frequently within the region of interest; however, it is important to consider that gRNAs targeting in such close proximity to the base to be edited may not be possible for all MH associated VUS. Indeed, on average, GG dinucleotide repeats are located every 42 bp in the human genome (Scherer, 2008).

For Hs_D3986E_gRNA1 and 2, it was not possible to introduce a silent mutation in the PAM to prevent re-cleavage following incorporation into the genome. The final G base of the PAM for Hs_D3986E_gRNA1 (GGG, encoding glycine) was also the first base of the GAC codon to be edited. The alternative codons for glycine are GGA, GGC and GGT. Mutation of the final G

base in the glycine codon to A, C or T would have changed the aspartate codon at position 3986 to AAC (asparagine), CAC (histidine) or TAC (tyrosine), respectively. For Hs_D3986E_gRNA2, the PAM was TGG, the only codon that encodes tryptophan so could not be mutated silently. In both cases, it was possible to introduce silent mutations in the 10-12 nt 'seed region' proximal to the PAM, which is essential for sequence specific targeting of Cas9 (Wu et al., 2014). In most cases, the presence of just two mismatches within the seed region abolishes Cas9 activity so the inability to silently mutate the PAM in other MH-associated VUS targeting gRNAs is unlikely to hinder gRNA/HDR template design (Anderson et al., 2015). Since all MH diagnostic variants and VUS are found in the heterozygous form (with the exception of STAC3 p.W284S variant), generation of both homozygote cells and heterozygote cells would be optimal for functional studies. To facilitate this, HDR arms containing both the edited base and wild-type base were designed for introduction into human immortalised myoblasts. Another method for the generation of heterozygotes is optimisation of the cut-to-mutation distance. For the introduction of Alzheimer's disease associated point mutations, a cut-to-mutation distance of 23 nt produced ~50% heterozygotes compared to 100% homozygotes with a cut-to-mutation distance of 2 nt (Paquet et al., 2016).

Off-target activity is a major concern in any CRISPR-Cas9 genome-editing experiment. Hs_D3986E_gRNA 1, 2 and 3 were predicted to have 8, 27 and 43 off-targets, respectively. For comparison, the lowest ranking p.D3986E-targeting gRNA generated by CCTOP had 205 off-targets. Since no edited human immortalised myoblast lines were obtained, it is not possible to comment on the off-target activity of the specific gRNAs designed in this chapter; however, high-throughput screening of 380 gRNAs showed that 96% do not function when they contain 2 mismatches to the target. Since all gRNAs designed in this chapter had at least 2 mismatches and, in most cases, 4 mismatches to the *in-silico* predicted off-target sites, it is likely that the gRNAs function with specificity to the desired target (Anderson et al., 2015). MiSeq deep sequencing performed on iPSC-derived myogenic cell lines edited in the *DMPK* gene to correct myotonic dystrophy defects showed 0 to 0.3% off-target activity at the two most probable off-target sites (as predicted using the

Optimised CRISPR Design Tool formerly available at http://crispr.mit.edu) (Dastidar et al., 2018). Despite this, it is important to consider that off-target activity may occur at locations other than those predicted by computational algorithms and ultimately, genome-wide profiling is necessary to rule out all off-target activity (Tsai et al., 2015).

Two strategies to introduce the p.D3986E into human immortalised myoblasts were implemented in this chapter. At the time of starting the work, significantly more literature was available utilising the pSpCas9(BB)-2A-GFP system; however, an emerging body of evidence indicated that increased gene-editing efficiencies and reduced off-target activities were achieved with the Cas9 protein system in conjunction with a purified gRNA:tracrRNA fusion (Ran et al., 2013a; Dewari et al., 2018; Mason et al., 2018; Xu et al., 2018). The human immortalised myoblasts used in this chapter were sensitive to both plasmid and protein transfection, with the protein system resulting in the largest reductions in cell viability following transfection. Nonetheless, sufficient numbers of cells survived for use in FACS and both systems resulted in moderate transfection efficiencies determined by FACS of ~7% for the plasmid system and ~26% for the protein system which are comparable to myoblast transfection efficiencies reported in the literature (Jackson et al., 2013).

Alternatives to fluorescence were available for the selection of transfected/edited cells. The pSpCas9(BB)-2A-GFP was available with a puromycin resistance marker rather than GFP (Addgene plasmid PX459, deposited by Feng Zhang) and the pGCS vector contains partial overlapping sequences for the CD4 gene in addition to the OFP coding sequence, allowing enrichment of edited cells using Dynabeads® CD4 antibody conjugated magnetic beads (Invitrogen™). Fluorescence-based enrichment was deemed optimal for several reasons. Firstly, selection by FACS retains lower passage numbers in transfected cells, since antibiotic selection would need to be performed over several days. Secondly, FACS allows for the automated sorting of single cells into wells of a 96-well plate for the propagation of monoclonal cell populations. An alternative procedure for the isolation of single cells in cell populations that are sensitive to FACS is to perform a limiting

dilution of enriched cells. Whilst this method would overcome issues associated with FACS, it is important to consider that results generated elsewhere in this project suggest that myoblast propagation from single cells is inefficient, with only a proportion showing growth (sections 4.2 and 5.2). As such, a vast number of dilutions may need to be performed to obtain sufficient number of cell lines for screening. Nonetheless, it is a promising alternative to FACS that should be explored for future development of CRISPR-Cas9 in human immortalised myoblasts.

The reasons for lack of cell survival following FACS observed in this chapter are undetermined, since average cell viabilities of cells subjected to FACS were relatively high for both systems and HEK293 FT cells consistently survived FACS. Since FACS involves the movement of cells through narrow tubing under pressure and the application of an electric charge to the cells prior to collection, it is likely that the process is inherently damaging to more sensitive cell types (Herzenberg et al., 1976).

CRISPR-Cas9 genome-editing has previously been performed on human immortalised myoblasts obtained from the Institut de Myologie (Paris, France). The CRISPR-Cas9 system was used to correct mutations associated with Duchenne muscular dystrophy (DMD), namely the targeted deletion of duplicated exon 2 in the *DMD* gene and myotonic dystrophy type 1 (DM1) by the targeted deletion of $(CTG{\cdot}CAG)_n$-repeats in the *DMPK* gene (Ousterout et al., 2015; Lattanzi et al., 2017; Van Agtmaal et al., 2017). Unlike the work presented in this chapter, none of these studies used HDR templates to introduce a specific variant but delivered gRNAs to induce a knock-out by NHEJ. Lattanzi et al., (2017) used lentiviral vectors to transduce myoblasts with higher efficiencies than lipid-based transfections. Van Agtmaal et al., (2017) used nucleofection to introduce purified Cas9 protein alongside a gRNA:tracrRNA fusion RNA inot the cells and FACS was performed to enrich GFP-expressing cells two days post transfection (cf. 24 hours as used in this chapter). Ousterout et al., (2015) utilised a plasmid-based system to introduce the gRNA:tracrRNA and Cas9 into cells by electroporation followed by enrichment of GFP-expressing cells using FACS. The exploitation of the

CRISPR-Cas9 system for the correction of disease-causing mutations provides a promising insight into feasibility of using CRISPR-Cas9 to introduce MH-associated VUS into human immortalised myoblasts. Nonetheless, the work presented here shows that genetic manipulation of human myoblasts remains difficult and optimisation of the CRISPR-Cas9 pipeline is required.

As illustrated in this chapter, the Cas9 protein system is more laborious than the pSpCas9(BB)-2A-GFP system, requiring the cloning of gRNAs into pGCS and the generation of gRNAs by IVT and their subsequent purification. Another practical consideration is that the Cas9 protein reagents used in this chapter were all commercially supplied meaning that unlike the pSpCas9(BB)-2A-GFP plasmid, they were not easily nor cost-effectively regenerated. The ease of regeneration of the pSpCas9(BB)-2A-GFP plasmid was the reason for its use in the T7 assay in HEK293 cells and HEK293 cells were chosen for use due to their rapid growth and ease of transfection. The T7 assay determined gene editing efficiencies of Hs_D3986E_gRNA1, 2 and 3 to be 39.2%, 17% and 12.3%, respectively. These values show the same hierarchy in efficiency as the efficacy prediction by the *in-silico* CRISPRater tool which for Hs_D3986E_gRNA1, 2 and 3 were 82, 76 and 68, respectively, potentially allowing a single gRNA to be designed in the future if CRISPRater efficacy predictions are supported by more functional work. Since no edited cell lines were obtained, the accuracy or sensitivity of the T7 assay in this case cannot be commented on.

3.3.1 *In-silico* investigations of p.D3986E pathogenicity

Whilst the determination of functional significance of the p.D3986E variant in myotubes was beyond the scope of this chapter, *in-silico* pathogenicity tools and investigation of the levels of conservation across species of the residue have provided insight into the potential pathogenicity of the variant.

Three *in-silico* predictors of pathogenicity were used in this chapter because they each use different parameters to predict the effect of a variant. In a study addressing the sensitivity and specificity of these tools for prediction of MH-associated variant pathogenicity, SIFT identified three diagnostic MH *RYR1* variants as ‘tolerated’ and PolyPhen-2 identified one as ‘benign’; however, both

tools correctly identified all true negatives when common sequence variants were tested. CADD identified all diagnostic MH *RYR1* variants as being potentially pathogenic but predicted half of the common *RYR1* sequence variants tested to be potentially pathogenic using a user-defined cut-off score of 15 (Schiemann and Stowell, 2016). Whilst this study clearly demonstrates bioinformatic data cannot be relied upon alone for determination of functional significance, it can at least provide a screening tool for MH-associated VUS in combination with segregation data and MAF. In this chapter, SIFT, PolyPhen-2 and CADD all identified p.D3986E as potentially pathogenic or an equivalent annotation. SIFT predicts makes predictions on a protein level whereby residue conservation and amino acid class are considered (Ng and Henikoff, 2003; Sim et al., 2012). The transition from D to E results in the addition of a CH_2 group to the amino acid side chain but the amino acid retains its acidic property. The SIFT tool classified p.D3986E as damaging, despite the relatively mild D to E substitution. Indeed, a number of functionally characterised MH variants result from amino acid changes that do not affect the charged state or polarity such as p.R530H and p.V4849I (EMHG, available at www.emhg.org, accessed August 2019).

Across all homologues analysed, the p.D3986 residue was highly conserved, suggesting that it could have an important structural or functional role. Using ConSurf, p.D3986 was predicted to be an exposed residue and therefore likely to have a functional role. Indeed, exploration of the rabbit RYR1 3D structure using PyMOL (Schrödinger, LLC) indicated that the p.D3986 was exposed on the surface of the protein (Yan et al., 2015). Such advances in resolving the rabbit RYR1 structure have revealed that the p.D3986 residue is located within the central domain of RYR1 – the only cytoplasmic domain that interacts with the channel domain and forms part of the activation module, presumably relaying conformational signals between the ligand sending cytoplasmic domain and pore forming channel domain (Yan et al., 2015; des Georges et al., 2016). Using the PyMOL mutagenesis wizard, mutagenesis of D to E does not disrupt normal hydrogen bonding but does result in the generation of VdW clashes in all possible rotamer conformations. VdW clashes occur when VdW radii overlap and produce repulsion effects. Since VdW clashes are not

physically allowed, the p.D3986E would likely result in an alteration in local protein structure at this position; however, *in-silico* mutagenesis does not allow one to determine whether this alteration in structure would be tolerated or not. Nonetheless, the co-segregation of the p.D3986E variant with the MH phenotype in multiple MH families referred to the Leeds MH Unit, in conjunction with bioinformatic data, make p.D3986E a promising candidate for a role in MH. Previous studies in our group have shown that HEK293 cells expressing p.D3986E RYR1 channels do not have a significantly reduced EC_{50} to caffeine compared to wild-type RYR1 channels (Merritt et al., 2017). It is possible that an effect of p.D3986E depends upon the expression of other ECC apparatus that are absent in HEK293 cells or depends upon the presence of an additional variant that has not been yet been identified; however, without functional data for p.D3986E in myotubes, its role remains to be elucidated and this will be addressed in Chapter 4.

3.3.2 Future directions

In the first experiments of their kind in the Leeds MH Unit and the wider MH field, this chapter has provided significant insight into the development of a CRISPR-Cas9 methodology for the introduction of MH-associated VUS into human immortalised myoblasts and highlighted some key considerations to be made for future use which are detailed below.

3.3.2.1 Selection of the cell line for genome-editing

One of the major benefits of using CRISPR-Cas9 to introduce MH-associated VUS is that it is performed in a single cell line with a constant genetic background. The work presented in this chapter has highlighted the importance of using a robust cell line for editing. Whilst optimisation of several factors could improve the survival of the human immortalised myoblasts used here, alternative cell types should be considered for future work. A growing number of reports detail the use of induced pluripotent stem cells (iPSCs) programmed into myogenic lines (Dastidar et al., 2018; Young et al., 2016); however, to the best of my knowledge iPSCs have not been used in the wider

MH field and are likely to require optimisation of differentiation protocols that would hinder immediate progress in the functional characterisation of MH-associated VUS. Alternative cell types include primary mouse cells, immortalised mouse cells and C2C12 cells – an immortal mouse myoblast cell line generated from the serial passage of cells derived from C3H mouse muscle (Yaffe and Saxel, 1977).

3.3.2.2 Consideration of the feasibility of the Cas9 protein system in its current form

The pSpCas9(BB)-2A-GFP plasmid system is easily regenerated and comprises a single cloning step followed by transfection of a single plasmid. In contrast, the Cas9 protein system is more laborious, requiring the IVT, purification and quantification of gRNAs and cloning into pGCS, followed by the transfection of Cas9, the gRNA and pGCS into cells. The Cas9 protein used in this chapter was commercially supplied (GeneArt Platinum Cas9 Nuclease, Invitrogen^{TM}), limiting its ease of regeneration. For future work using the Cas9 protein system, in-house heterologous expression and purification of Cas9 would be advantageous.

3.3.2.3 FACS alternatives

Alternative strategies that circumvent the need for FACS sorting such as the use of a pSpCas9(BB)-2A vector encoding puromycin would enable enrichment of transfected cells by puromycin selection and single cell isolation by limiting dilution; however, as mentioned previously, the feasibility of performing limiting dilutions to obtain sufficient cell lines for screening would need to be explored.

Chapter 4 – Exploration of the utility of CRISPR-Cas9 in the functional characterisation of MH-associated variants in C2C12 myoblasts

4.1 Introduction

Previous attempts to introduce the RYR1 p.D3986E variant into human immortalised myoblasts highlighted challenges in the utilisation of CRISPR-Cas9 genome editing to introduce MH-associated variants for downstream functional characterisation. To address the difficulties that were associated with the use of human immortalised myoblasts, CRISPR-Cas9 gene-editing will be performed using C2C12 mouse myoblasts for the introduction of the RYR1 p.D3986E and p.S1728F variants. The C2C12 myoblast line is a subclone of cells generated by the isolation of satellite cells following repeated crush injury of C3H mouse thigh muscle (Yaffe and Saxel, 1977; Blau et al., 1983). C2C12 cells are not bound by the limited replicative potential associated with primary cells and they form multinucleated myotubes following cell culture in conditions that promote differentiation. As such, they have been used extensively in the study myogenesis. For example, recently, a small interfering RNA (siRNA) screen of 100 genes previously uncharacterised with regard to their function in myogenesis, revealed 13 novel genes implicated in differentiation, providing candidates for further *in-vivo* studies (Alwan et al., 2017). In another study, the *Stac3* gene, which has recently been implicated in MH, was shown to act as a negative regulator of C2C12 cell differentiation (Ge et al., 2014). As such, studies in C2C12 cells have contributed to our understanding of the complex mechanisms governing myogenesis that will, ultimately, facilitate the development of regenerative medicine approaches to the treatment of myopathies.

The same characteristics that have validated C2C12 cells for the study of myogenesis also make them a promising candidate for use in MH-associated VUS characterisation via CRISPR-Cas9 genome editing. The majority of reports of CRISPR-Cas9 genome editing in C2C12 cells are in the context of

NHEJ. Xu et al., (2016) performed proof-of-principle in-frame deletion of *DMD* gene exons 21-23 to overcome a pathogenic nonsense mutation in exon 23, prior to post-natal editing in the *mdx* DMD mouse model, Wang et al., (2017) used CRISPR-Cas9 to explore the effect of MyoD ablation in C2C12 cells and Kim et al., (2019) used CRISPR-Cas9 to knockout the STIM2β splice variant in C2C12 cells that revealed a role for STIM2β in myogenesis. To date, C2C12 cells have not been utilised in the characterisation of MH-associated VUS since they express the *Ryr1* following differentiation and current strategies rely on heterologous expression of variant *Ryr1* cDNAs into *Ryr1* null cells e.g. dyspedic myotubes or more commonly, HEK293 cells.

4.1.1 Selection of the p.S1728F variant

Whilst it is important to emphasise that any results observed in mouse cells may not directly recapitulate the response in human cells, the mouse RYR1 protein and human RYR1 protein share 96% homology at the amino acid level. The human RYR1 variant p.S1728F comprises a serine (S) to phenylalanine (F) substitution resulting from a C to T variant at cDNA position 5183, changing the codon from TCC to TTC. Both the amino acid residue and codon are conserved in the mouse genome. In contrast, the p.D3986E variant that results from a GAC to GAG codon change in humans results from a GAT to GAG alteration in the mouse genome, whilst the D residue is conserved at an amino acid level.

The p.S1728F variant was selected for characterisation due to its enrichment in in MHShc/MHSh individuals across multiple MH families. In total, p.S1728F has been identified in 12 MHShc individuals and 15 MHSh individuals across 8 families referred to the Leeds MH unit (Table 4.1). Discordance was observed in one family (family S5), with the variant being detected in one MHN individual and one MHSh individual not harbouring the variant. No further variants were detected in the 9 MHShc/MHSh individuals referred for NGS of 50 genes associated with Ca^{2+} handling. The p.S1728F variant is rare, with a MAF of 0.000004064 in the gnomAD browser (gnomAD, 2019; Karczewski et al., 2019).

Recent advances in the resolution of the rabbit RYR1 structure by cryo-EM revealed that the p.S1728F variant lies within the handle domain, which in conjunction with the central and helical domains, provides a scaffold for the ligand binding and the propagation of conformational signals (Yan et al., 2015). Analysis of the relative contracture strength in samples derived from patients harbouring specific MH-associated variants revealed individuals harbouring the p.S1728F variant produced weak contractures upon IVCT compared to the most common variant in the UK population, p.G2434R. The p.S1728F variant has not been characterised using the HEK293 system; however, one study has shown increased sensitivity of a B-lymphocyte cell line containing the p.S1728F variant to 4-CmC compared to wild-type controls, in addition to increased resting Ca^{2+} (Gonsalves, 2014). These experiments were performed on a cell line obtained from a single individual and the contribution of genetic background to the results is unknown.

Table 4.1 – Prevalence of the p.S1728F variant in the Leeds MH Unit referrals

The 8 MH families in which the p.S1728F variant has been detected have been anonymised and assigned codes from S1-S8 (column 1). Since not all family members have been subject to DNA sequencing, the genetic analysis column refers to the number of family members who have had their DNA sequenced to determine the presence of the p.S1728F variant. The p.S1728F + column refers to the number of family members determined to harbour the p.S1728F variant after DNA sequencing was performed.

	No. MHShc			No. MHSh			No. MHN		
Family	**Total MHShc**	**Genetic analysis**	**p.S1728F +**	**Total MHSh**	**Genetic analysis**	**p.S1728F +**	**Total MHN**	**Genetic analysis**	**p.S1728F +**
S1	4	1	1	6	4	4	13	0	-
S2	1	1	1	2	2	2	3	0	-
S3	8	4	4	4	2	2	4	0	-
S4	0	-	-	1	1	1	0	-	-
S5	6	3	3	4	4	3	4	3	1
S6	2	2	2	1	1	1	3	0	-
S7	1	1	1	2	0	-	4	0	-
S8	1	0	-	4	2	2	5	0	-

4.1.2 Chapter aims and strategy

The primary aim of this chapter is to introduce the RYR1 p.D3986E and p.S1728F variants into C2C12 myoblasts and determine the sensitivity of the resultant cell lines to caffeine by Ca^{2+} imaging. In addition, the karyotype of C2C12 cells will be confirmed and *in-silico* tools will be used to gain insight into the potential pathogenicity of the p.S1728F variant.

Since traditional HDR is inefficient and resultant cell lines can contain a number of NHEJ events, recent developments in CRISPR-Cas9 gene-editing technologies will be explored as alternatives to traditional HDR for the introduction of MH-associated VUS (Ran et al., 2013a; Liu et al., 2019). In particular, an analysis of the feasibility of using cytidine deaminase base editors for the introduction of MH-associated VUS will be conducted. Cytidine deaminase base editors are comprised of a Cas9 nuclease that is inactive in one of its catalytic domains, resulting in the introduction of single stranded DNA breaks (Cas9 D10A) fused to a cytidine deaminase and uracil glycosylase inhibitor (BE3) (Komor et al., 2016). The Cas9 D10A-BE3 system enables the introduction of C>T base substitutions when gRNAs are designed to target the forward strand, and the introduction of G>A substitutions when gRNAs are designed to target the reverse strand. As such, the potential for using this tool will be analysed for all MH-associated VUS identified in at least one family that occur due to a C>T or G>A substitution. Importantly, the bases to be edited must be located within positions 1-8 bp of the PAM-distal end of the gRNA, with maximum base editing efficiencies observed within positions 4-8 bp (Komor et al., 2016). Since the p.D3986E variant is a result of a G>T substitution, it is not amenable to Cas9 D10A-BE3 editing and traditional HDR will be performed for this variant. For the introduction of variants by traditional HDR, the plasmid system (pSpCas9(BB)-2A-GFP encoding gRNAs) will be used. In contrast to the purified Cas9 protein system detailed in Chapter 3, the plasmid system boasts the benefit easy regeneration of the vector, increased tolerance for transfection of a single plasmid compared to the components of the purified Cas9 protein system and encouraging plasmid transfection efficiencies of up to 60% for C2C12 cells reported in the literature (Balci and Dinçer, 2009).

Development of a robust CRISPR-Cas9 gene-editing platform in the widely used C2C12 cell line will overcome limitations of the existing characterisation methodologies for MH-associated VUS and will address the challenges identified in using CRISPR-Cas9 gene-editing on immortalised human myoblasts.

4.2 Results

4.2.1 p.S1728F *in-silico* pathogenicity prediction, conservation analysis and mutagenesis

The following *in-silico* pathogenicity predictions were made for p.D3986E in Chapter 3, section 3.2.1. Three bioinformatics tools were used to predict the pathogenicity of the p.S1728F variant. The p.S1728F variant was predicted to be 'tolerated' by SIFT with a score of 0.2 – where a score of 0 is damaging and a score of 1 is tolerated (SIFT 6.2.1, 2019; Ng and Henikoff, 2003; Sim et al., 2012). Conversely, PolyPhen-2 categorised the p.S1728F variant as 'possibly damaging' with a score of 0.756 – where a score of 1 is damaging and a score of 0 is benign (PolyPhen-2 v2, 2019; Adzhubei et al., 2010). The CADD tool generated a CADD score (C-score) of 24, indicating that it is in the top 1% of predicted deleterious variants (CADD v1.4, 2019; Kircher et al., 2014).

ConSurf (Ashkenazy et al., 2016; Celniker et al., 2013; Asheknazy et al., 2010; Berezin et al., 2004) was used to investigate the conservation of the RYR1 p.S1728F residue (sequence accession number P21817.3) across RYR1 homologues. This returned 75 results, of which the first 40 are shown for reference to show a sample of the results (Figure 4.1). The p.S1728F residue was predicted to be exposed; however, no functional or structural prediction was made by ConSurf. The p.S1728F residue was not highly conserved across all homologues analysed, with a ConSurf score of 1 meaning that the residue is 'variable'. Across all homologues, 37.736% had a serine residue at position 1728, 26.415% had a glycine residue, 18.868% had a methionine, 13.208% had a threonine and both alanine and leucine accounted for the 1728 residue in 1.887% of sequences. Despite this, the p.S1728F residue was

conserved in all mammalian RYR1 protein sequences. The conservation of the sequence surrounding p.S1728F varied, with some residues (p.R1728) being highly conserved and some (p.S1725) being variable. None of the homologues analysed have an F residue at position 1728. The PyMOL Molecular Graphics System version 2.0 mutagenesis wizard (Schrödinger, LLC) was used to explore the effect of the S to F substitution on local hydrogen bonding and VdW interactions using the rabbit RYR1 structure (PDB: 3J8H; Yan et al., 2015; Figure 4.2). Substitution of the S residue to F generated four potential rotamer conformations, all of which showed varying degrees of VdW clashes. The most likely rotamer conformation (57% probability) showed mild VdW clashes (green disks; Figure 4.2; Panel B), as did the third rotamer conformation (11.0%; Figure 4.2, Panel D). In contrast, the second and fourth rotamer conformations (29.8% and 1.3%, respectively) showed severe VdW clashes (red disks; Figure 4.2, panels C and E).

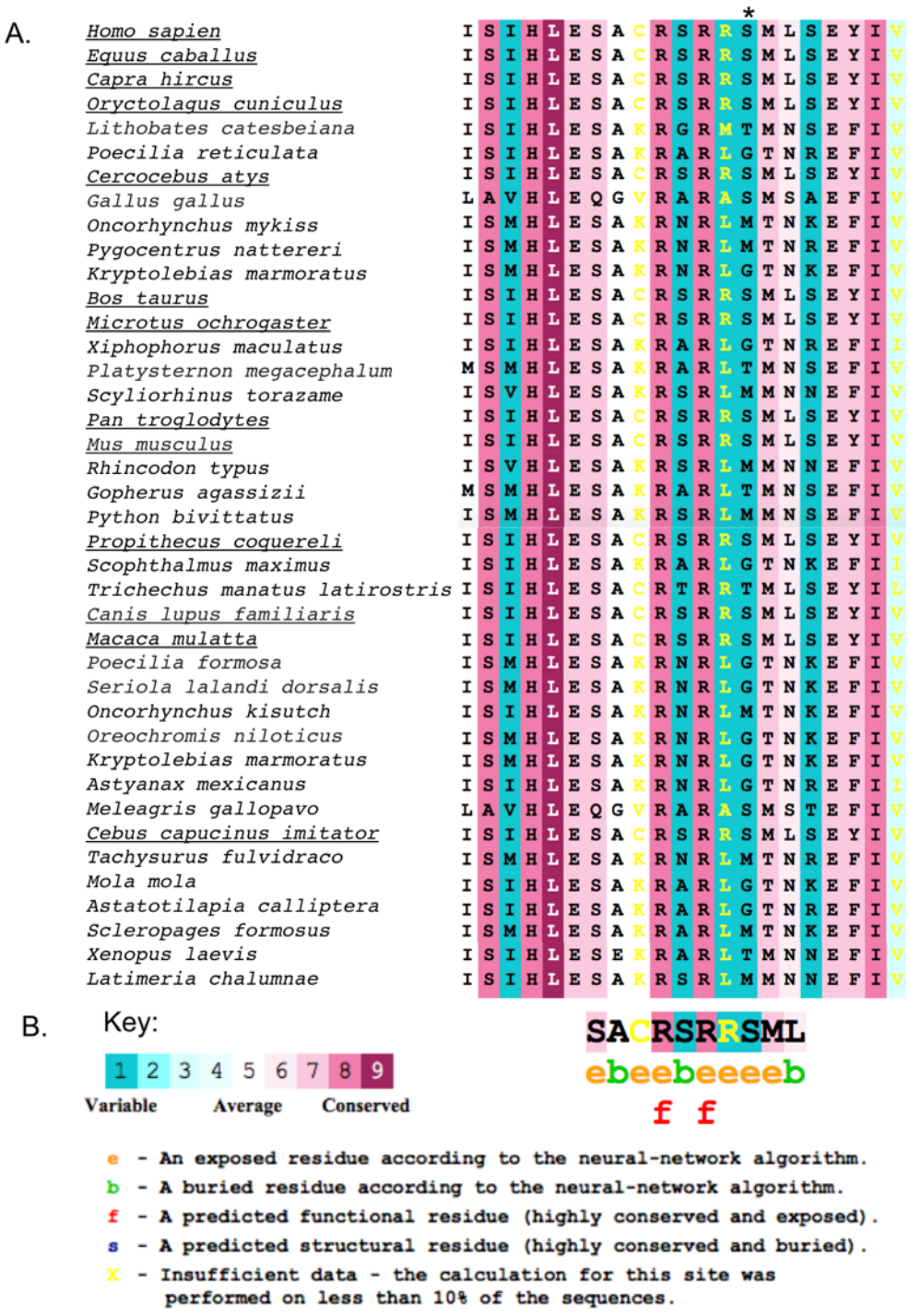

Figure 4.1 – Multiple sequence alignment of the p.S1728 residue across 40 RYR1 homologues

CSI-BLAST was used to search for homologues with at least 70% homology to the human RYR1 protein and MAFTT was used to create a multiple sequence alignment. ConSurf was used to determine and colour code the conservation of residues across homologues. The region surrounding the p.S1728 residue is shown here in panel A. Predictions made regarding the exposure and role of the residue are shown in panel B. Mammalian species are indicated by underlining and an asterisk highlights the residue of interest.

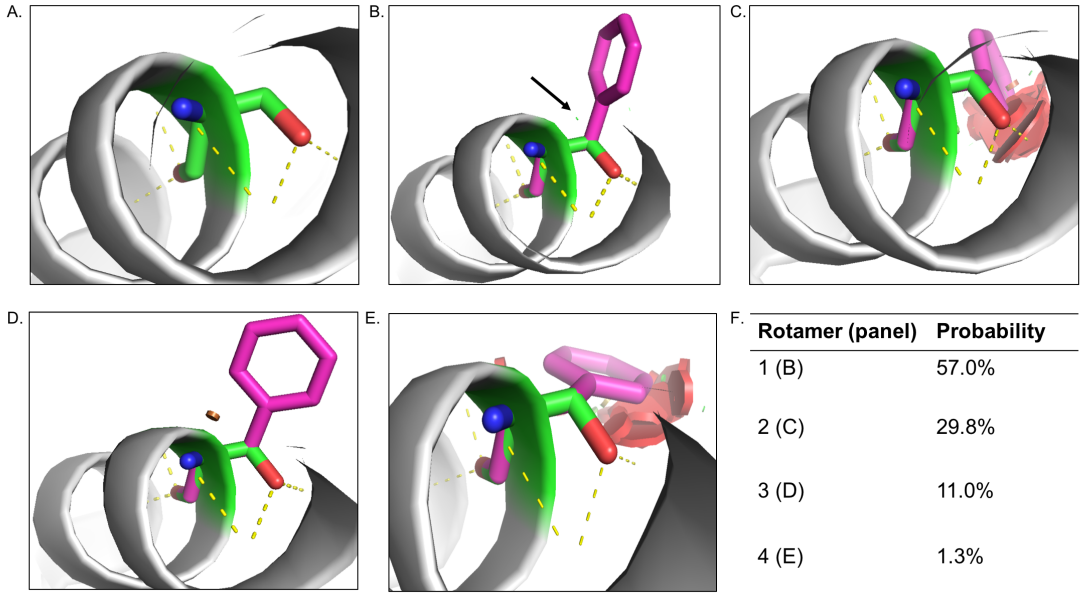

Rotamer (panel)	Probability
1 (B)	57.0%
2 (C)	29.8%
3 (D)	11.0%
4 (E)	1.3%

Figure 4.2 – PyMOL mutagenesis of rabbit RYR1 p.S1728F residue

The mutagenesis tool on PyMOL was used to model the effect of the p.S1728F variant on hydrogen bonding and VdW interactions, within the rabbit RYR1 structure (PDB: 3J8H). The ancestral residue is shown in green and the variant residue is in pink. Hydrogen bonds are shown by yellow dashes and VdW clashes are shown by green (less severe) and red (more severe) disks. Black arrows are used to highlight VdW clashes that are difficult to see. Panel A shows the S residue at position 1728 and panels B, C, D and E show each rotamer conformation in order of decreasing probability of occurrence. Panel F shows the probabilities of occurrence of each rotamer conformation.

4.2.2 Exploration of the use of the cytidine deaminase vector for MH-associated VUS

Developments in genome-editing technologies at the time of these experiments were investigated as potential alternatives to traditional HDR for the introduction of point mutations; namely Cas9 D10A-BE3 (Komor et al., 2016). Since p.D3986E results from a G>T variant, the use of Cas9 D10A-BE3 was not possible. To design potential gRNAs Cas9 D10A-BE3-mediated base editing of the p.S1728F variant, a region around the variant was entered into CCTOP (Stemmer et al., 2015) and gRNAs 20 nt in length, with at least 4 mismatches to any other sequence in the mouse (GRCm38/mm10) genome. Only one gRNA result was returned that targeted the forward strand and thus would produce C>T variants. The variant to be edited lay 12 bp downstream of

the PAM, thus it did not meet the positional criteria for C>T editing (Figure 4.3); as such, a traditional HDR strategy was implemented for the introduction of p.S1728F. In fact, out of all MH-associated VUS that occur as a result of a C>T or G>A variant and are found in more than one family (a total of 19), only 5 produced gRNAs that could potentially edit the variant of interest (Table 4.2). Of the 14 variants for which no gRNAs were designed, 5 were excluded due to codon differences between human and mouse that prevented substitution of the correct amino acid (Table 4.2). The arginine residue of p.R177C is comprised of the codon CGC, whilst in mouse the codon is CGA. Thus, editing of the C base would result in AGA which also encodes arginine. The threonine residue of p.T214M is comprised of the codon ACG but in mouse, it is comprised of the codon ACT. Editing of the C base would result in the formation of ATT which encodes isoleucine, not methionine. The arginine residue of p.R1469W is comprised of CGG but in mouse the codon is AGG, thus there is no C base available for editing. The arginine residue of p.R2676W is comprised of CGG but in mouse the codon is CGC. Editing of the C bases in this instance could produce either TGT, TGC or CGT which encode cysteine (TGT and TGC) and arginine (CGT). Finally, the threonine residue in p.T3711M is encoded by ACG but in mouse the codon is ACT. Editing of the C base at this position would result in the formation of ATT, which also encodes threonine. The remaining variants failed to produce gRNAs where the base to be edited was within positions 1-8 bp of the PAM-distal site (Table 4.2).

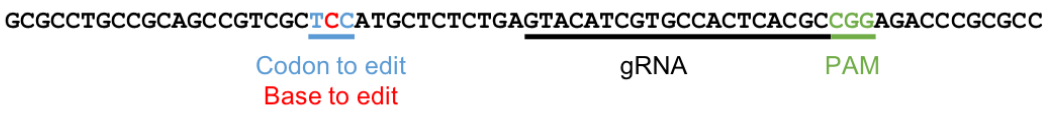

Figure 4.3 – gRNA design for cytidine deaminase-mediated editing of the p.S1728F variant

CCTOP (Stemmer et al., 2015) was used to design gRNAs using the mouse (Mm10) genome for targeting of the p.S1728F variant with Cas9 D10A-BE3. The p.S1728 codon is shown in blue with the base to be edited in red. The PAM sequence is shown in green.

Table 4.2 – Potential for genome-editing using cytidine deaminase Cas9 across MH-associated VUS

All MH-associated VUS that occur due to a C>T or G>A variant that were found in at least two independent families were included for an analysis of the utility of Cas9 D10A-BE3. The base to be edited is underlined. No. IF refers to the number of independent families the variant has been identified in.

Variant	Human codon	Mouse codon	No. IF	Result
p.R177C	CGC	CGA	10	Excluded
p.T214M	ACG	ACT	4	Excluded
p.R1469W	CGG	AGG	2	Excluded
p.S1728F	TCC	TCC	9	No suitable gRNAs
p.P1787L	CCT	CCA	8	No suitable gRNAs
p.E2362K	GAG	GAG	2	No suitable gRNAs
p.V2627M	GTG	GTG	5	Potential gRNAs
p.R2676W	CGG	CGC	3	Excluded
p.R3051H	CGC	CGC	2	No suitable gRNAs
p.R3366H	CGT	CGT	2	Potential gRNAs
p.R3539H	CGT	CGC	7	No suitable gRNAs
p.T3711M	ACG	ACT	3	Excluded
p.R3772Q	CGG	CGG	6	No suitable gRNAs
p.R3903Q	CGG	CGG	2	No suitable gRNAs
p.A4295V	GCG	GCG	4	Potential gRNAs
p.G4638D	GGC	GGC	3	Potential gRNAs
p.R4737Q	CGG	CGG	7	No suitable gRNAs
p.R4893Q	CGG	CGG	3	Potential gRNAs
p.P4973L	CCG	CCA	3	No suitable gRNAs

The five variants potentially amenable to cytidine deaminase editing were p.V2627M, p.R3366H, p.A4295V, p.G4638N and p.R4893Q which produced 1, 3, 3, 1 and 1 potential gRNAs, respectively (Figure 4.4). All of the gRNAs for p.V2627M, p.A4295V, p.G4638N and p.R4893Q contained additional C residues within positions 1-8 in the PAM-distal gRNA region and would likely be subject to deamination resulting in the introduction of undesired amino acid changes (Table 4.3). Two gRNAs targeting p.R3366H, gRNAs 2 and 3, did contain an additional C base within the 1-8 bp PAM-distal region; however, substitution of a C>T in these cases did not alter the original amino acid, leucine. Thus, whilst Cas9 D10A-BE3 could be used to base-edit p.R3366H, its scope for use as a tool to characterise MH-associated VUS in murine cells was limited. Since the use of cytidine deaminase Cas9 was not feasible for the introduction of the two candidate variants in this project, p.S1728F and p.D3986E, traditional HDR was used to introduce these variants into C2C12 myoblasts.

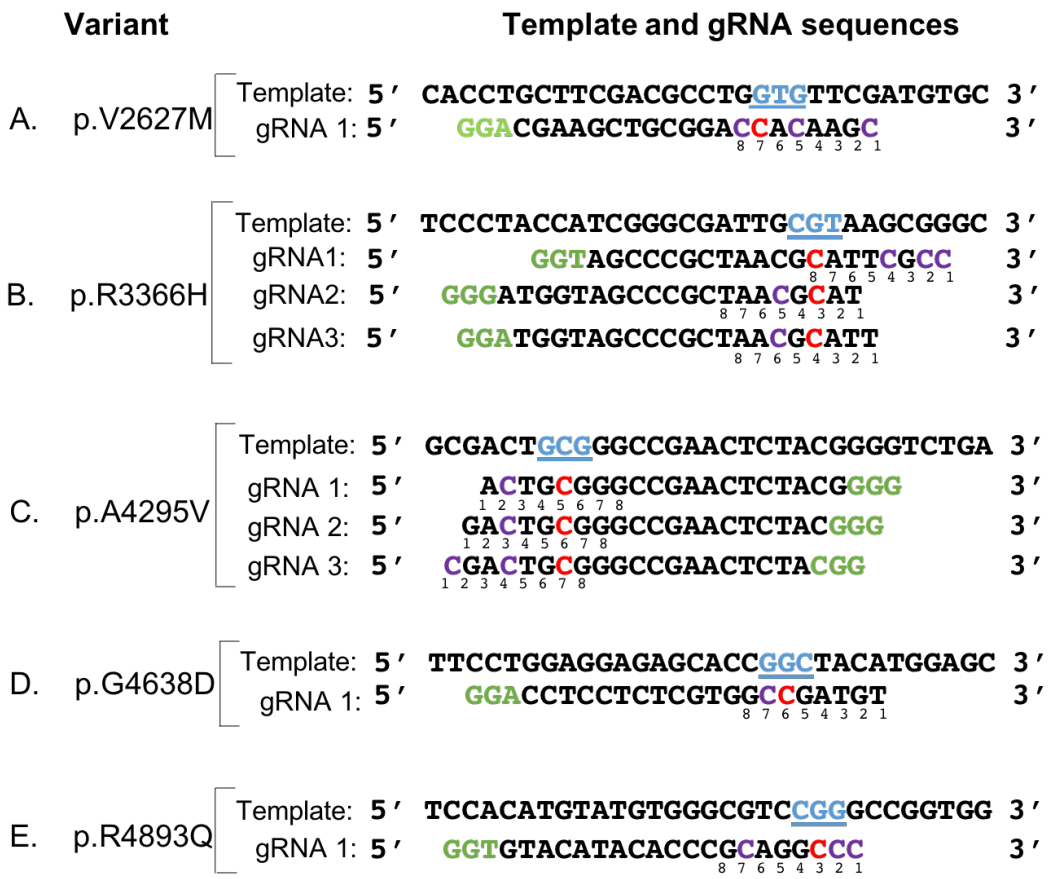

Figure 4.4 – gRNAs designed for base-editing with Cas9 D10A-BE3

CCTOP was used to design gRNAs for the introduction of MH-associated variants that result from a C>T or G>A variant – p.V2627M (A), p.R3366H (B), p.A4295V (C), p.G4638D (D) and p.R4893Q (E). The codon to be edited is shown in blue, with the base to be edited shown in red. The PAM is shown in green and additional C residues with the potential for editing shown in purple. Numbers beneath the PAM-distal end of the gRNA sequence show the position of the bases within the 1-8 bp PAM-distal region.

Table 4.3 – Potential variant substitution for gRNAs designed for use with Cas9 D10A-BE3

The base position refers to the position of the base within the 1-8 bp PAM distal end.

Variant and gRNA	Base position	Codon	Amino acid
p.V2627M gRNA 1	1	GAT>AAT	ASP>ASN
	5	GTG>GTA	VAL>VAL
	5 and 7	GTG>ATA	VAL>ILE
	7	GTG>ATG	VAL>MET*
	8	CTG>CTA	LEU>LEU
p.R3366H gRNA1	1	CGG>CGA	ARG>ARG
	2	CGG>CAG	ARG>GLN
	1 and 2	CGG>CAA	ARG>GLN
	4	AAG>AAA	LYS>LYS
	8	CGT>CAT	ARG>HIS*
p.R3366H gRNA2	3	CGT>CAT	ARG>HIS*
	5	TTG>TTA	LEU>LEU
p.R3366H gRNA3	4	CGT>CAT	ARG>HIS*
	6	TTG>TTA	LEU>LEU
p.A4295V gRNA1	2	ACT>ATT	THR>ILE
	5	GCG>GTG	ALA>VAL*
p.A4295V gRNA2	3	ACT>ATT	THR>ILE
	6	GCG>GTG	ALA>VAL*
p.A4295V gRNA3	1	GCG>GTG	ALA>VAL
	4	ACT>ATT	THR>ILE
	7	GCG>GTG	ALA>VAL*
p.G4638D gRNA 1	6	GGC>GAC	GLY>ASP*
	7	GGC>AGC	GLY>SER
	6 and 7	GGC>AAC	GLY>ASN
p.R4893Q gRNA 1	1	GCC>ACC	ALA>THR
	2	CGG>CGA	ARG>ARG
	2 and 3	CGG>CAA	ARG>GLN*
	3	CGG>CAG	ARG>GLN*
	7	GTC>ATC	VAL>ILE

* Intended variant substitution

4.2.3 C2C12 cell line karyotyping

Due to conflicting reports in the literature regarding the ploidy of C2C12 cells, (Hardeman et al., 1988; Fischer et al., 2016), cells at passage number 11 (cells resuscitated from liquid nitrogen storage were labelled as passage 0 at the outset of this project) were outsourced for karyotyping by Cell Guidance Systems (Cambridge, UK). Three populations of karyotypes were identified, with C2C12s appearing predominantly tetraploid (Figure 4.5). The mouse *Ryr1* gene is located on chromosome 7, of which there are three copies in all karyotypes. The first karyotype, hereafter referred to as karyotype A (Figure 4.5; panel A) had 81 chromosomes in total. Karyotype A had four copies of chromosomes 1, 2, 4 (with one chr.4 showing additional material notated as add(4)), 5, 6, 8, 11, 12, 14, 17, 19 and X. Three copies of chromosomes 7, 9, 13, 16 and 18 were identified and five copies of chromosome 15 were identified. In addition, three marker chromosomes of unknown origin were detected (Figure 4.5; panel A). The second karyotype identified, hereafter referred to as karyotype B (Figure 4.5; panel B), had 80 chromosomes in total. Four copies of chromosomes 1, 2, 3, 4, 5, 6 (with 2 derivatives of chromosome 6 and 15, notated as der (6;15)), 8, 9, 16, 17, 19 and X were identified. Three copies of chromosomes 7, 12, 13, 14 and 18 were identified within karyotype B and five copies of chromosomes 11 and 15 (with one der(15;15)) were identified. Finally, six copies of chromosome 10 were identified within karyotype B and an additional marker chromosome of unknown origin was detected (Figure 4.5; Panel B). The third karyotype, hereafter referred to as karyotype C (Figure 4.5; panel C) had 83 chromosomes in total. Four copies of chromosomes 1, 3, 4, 5, 6, 8, 9, 10, 11, 13, 16, 17, 18, 19 and X were identified. Three copies of chromosomes 7 and 14 were identified, five copies of chromosomes 2 and 12 were identified and six copies of chromosome 15 were identified. Finally, an additional marker chromosome was detected, the origin of which is unknown (Figure 4.5; Panel C).

A.

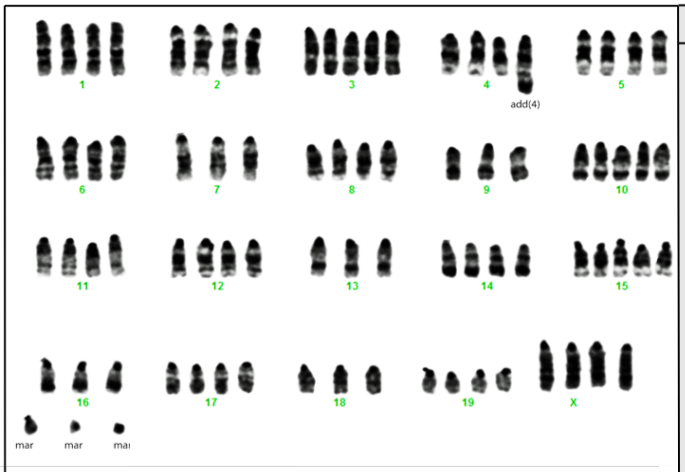

Chr.	Copy no.	Chr.	Copy no.
1	4	11	4
2	4	12	4
3	5	13	3
4	4	14	4
5	4	15	5
6	4	16	3
7	3	17	4
8	4	18	3
9	3	19	4
10	5	X	4

B.

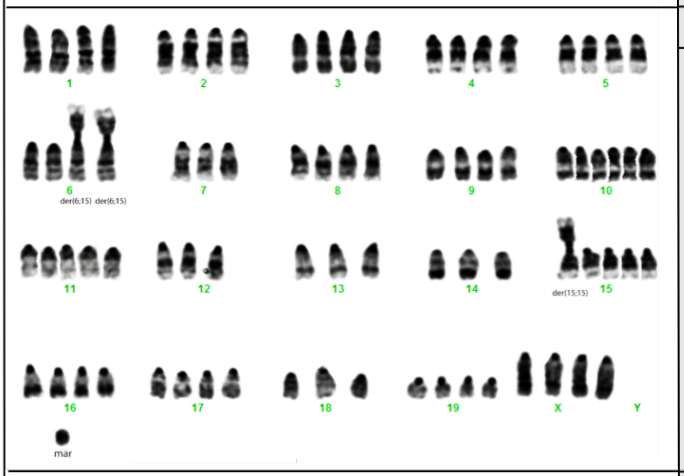

Chr.	Copy no.	Chr.	Copy no.
1	4	11	5
2	4	12	3
3	4	13	3
4	4	14	3
5	4	15	5
6	4	16	4
7	3	17	4
8	4	18	3
9	4	19	4
10	6	X	4

C.

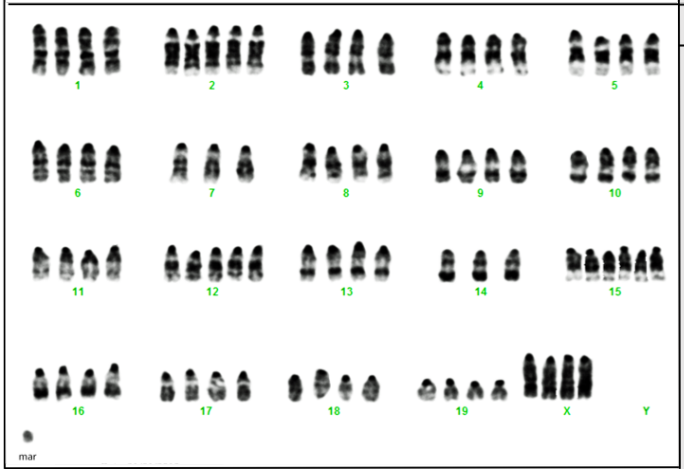

Chr.	Copy no.	Chr.	Copy no.
1	4	11	4
2	5	12	5
3	4	13	4
4	4	14	3
5	4	15	6
6	4	16	4
7	3	17	4
8	4	18	4
9	4	19	4
10	4	X	4

Figure 4.5 – C2C12 cell karyotyping

C2C12 cells at passage number 11 were outsourced to Cell Guidance Systems (Cambridge, UK) for karyotyping. The three populations identified are shown in panels A, B and C. Chromosome number is depicted in green text beneath chromosome images. A tabular summary of chromosomal copy number is provided to the right of each karyotype image.

4.2.4 gRNA design

Three gRNAs were designed per variant for testing in C2C12 myoblasts (Ran et al., 2013a). The gRNAs were designed using CCTOP (Stemmer et al., 2015). Within CCTOP, an extension called CRISPRater (Labuhn et al., 2017) was used to predict the efficacy of the gRNAs. Using the *Mus musculus* (GRCm38/mm10) genome, CCTOP was used to search for gRNAs 20 nt in length and upstream of an *S. pyogenes* PAM (NGG). For p.D3986E-targetting gRNAs, inputting a sequence of 101 bp with 50 bp flanking both upstream and downstream of the base to be edited returned 13 gRNA results. The top 3 gRNAs (ranked on number of off-targets, distribution of mismatches to off-targets and location of off-targets i.e. whether they are exonic, intronic or intergenic) were selected for use in this chapter.

The first gRNA, named Mm_D3986E_gRNA1 (Table 4.4) had a cut site 21 bp from the desired base change, an efficacy score of 0.68 (deemed medium efficacy) and 11 off-targets, of which 1 was exonic, 4 were intronic and 6 were intergenic. The second gRNA, Mm_D3986E_gRNA2 (Table 4.4) had a cut site 8 bp away from the desired base change, a high efficacy score of 0.82 and 42 off-targets, of which 3 were exonic, 15 were intronic and 24 were intergenic. The third gRNA, Mm_D3986E_gRNA3 (Table 4.4) had a cut site 6 bp away from the desired base change, a medium efficacy score of 0.69 and 41 off-targets, of which 6 were exonic, 16 were intronic and 19 were intergenic Mm_D3986E_gRNA1 targets the reverse DNA strand, whereas Mm_D3986E_gRNA2 and 3 target the forward strand. An additional gRNA design tool, CRISPOR v4.4 was used to confirm predicted off-targets and identify those that had not been predicted by CCTOP (Haeussler et al., 2016). CRISPOR predicted 31 off-targets for Mm_D3986E_gRNA, including the 11 were identified by CCTOP. Mm_D3986E_gRNA 2 was predicted to have 63 off-targets by CRISPOR, including the 42 predicted by CCTOP and Mm_D3986E_gRNA3 was predicted to have 56 off-targets by CRISPOR, including the 41 predicted by CCTOP.

For the p.S1728F-targetting gRNAs, inputting a 101 bp sequence with 50 bp flanking the base to be edited into CCTOP returned 8 results. The first gRNA, Mm_S1728F_gRNA1 had a cut site 24 bp away from the base to be edited, a high efficacy score of 0.75 and 26 off-targets, of which none were exonic, 9 were intronic and 17 were intergenic. The second gRNA, Mm_S1728F_gRNA2 had a cut site 13 bp from the base to be edited, a high efficacy score of 0.79 and 29 off-targets, of which 15 were exonic, 10 were intronic and 4 were intergenic. The third gRNA, Mm_S1728F_gRNA3 had a cut site 9 bp from the base to be edited, a high efficacy score of 0.79 and 54 off-targets, of which 6 were exonic, 25 intronic and 23 intergenic. All p.S1728F-targetting gRNAs target the reverse strand. As described for p.D3986E-targeting gRNAs, CRISPOR was used to confirm and identify additional potential off-target sites not predicted by CCTOP. For Mm_S1728F_gRNA1, CRISPOR predicted 60 off-target sites including the 26 identified by CCTOP. For Mm_S1728F_gRNA2, CRISPOR predicted 66 off-target sites including the 29 predicted by CCTOP. Finally, for Mm_S1728F_gRNA3, CRISPOR predicted 166 off-target sites, including the 54 predicted by CCTOP.

Table 4.4 - Mouse *Ryr1* p.D3986E and p.S1728F-targeting gRNA sequences and their PAM

gRNA	Sequence	PAM
Mm_D3986E_gRNA1	TCATGTGCGCGAACACGTGC	AGG
Mm_D3986E_gRNA2	TCTGGCGCACAGTCGCCTCT	GGG
Mm_D3986E_gRNA3	CGCCTCTGGGATGCCGTGGT	GGG
Mm_S1728F_gRNA1	GGCTGCGGCAGGCGCTTTCG	AGG
Mm_S1728F_gRNA2	CATGGAGCGACGGCTGCGGC	AGG
Mm_S1728F_gRNA3	AGAGCATGGAGCGACGGCTG	CGG

Prior to gRNA synthesis, DNA was extracted from C2C12 myoblasts and a 400 bp region around each gRNA of interest was amplified by PCR and processed for Sanger sequencing, to confirm that no SNPs were located within the gRNA sequence that could affect targeting. Indeed, all gRNA sites in the C2C12 genome were wild-type (Figure 4.6).

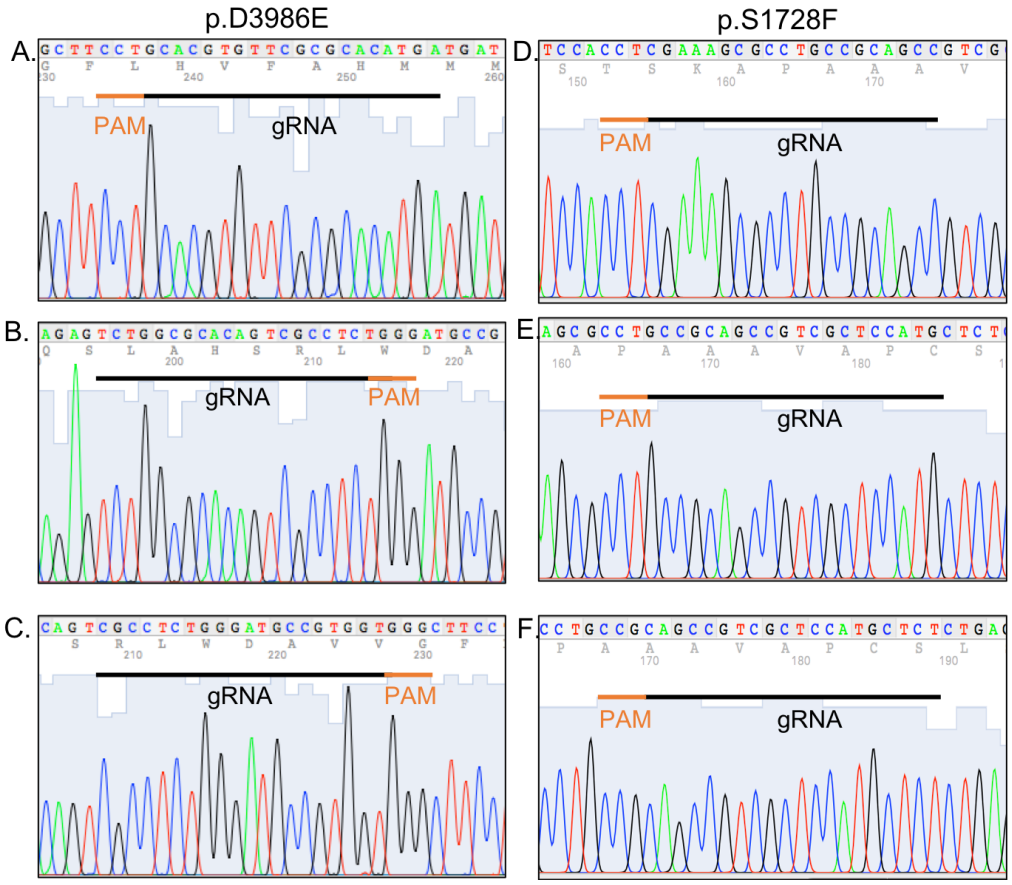

Figure 4.6 – Sanger sequencing traces of p.D3986E and p.S1728F gRNAs in C2C12 myoblasts

Sanger sequencing was performed to exclude the possibility of SNPs being present within the intended gRNA sequences. Traces for p.D3986E gRNAs 1 (A), 2 (B) and 3 (C) and p.S1728F gRNAs 1 (D), 2 (E) and 3 (F) are shown in 4Peaks software (Nucleobytes, Amsterdam, Netherlands). gRNA sequences are underlined in black and the PAM is underlined in orange.

Following confirmation that all intended gRNA sequences were free of SNPs in C2C12 myoblasts, gRNAs and their reverse complements were outsourced for synthesis as HPLC-purified single stranded oligonucleotides by Integrated DNA Technologies (IDT). For gRNAs that did not have a G as the first base, an additional G nucleotide was added to facilitate transcription from the hU6 promoter. To facilitate cloning into pSpCas9(BB)-2A-GFP, a 5'-CACC overhang was added to the forward sequence and a 5'-AAAC overhang was added to the reverse sequence (Table 4.5; Table 4.6).

Table 4.5 – Mouse *Ryr1* p.D3986E- targeting gRNAs for cloning into pSpCas9(BB)-2A-GFP

Sequences in black text show the gRNAs and their complements. Sequences in green text show the overhangs to facilitate cloning into pSpCas9(BB)-2A-GFP and the additional G nucleotide to enhance transcription from the U6 promoter is shown in blue text.

gRNA name	Forward sequence 5'-3'	Reverse sequence 5'-3'
Mm_ D3986E_gRNA1	CACCgTCATGTGCGCGAACACGTGC	AAACGCACGTGTTCGCGCACATGAc
Mm_D3986E_gRNA2	CACCgTCTGGCGCACAGTCGCCTCT	AAACAGAGGCGACTGTGCGCCAGAc
Mm_D3986E_gRNA3	CACCgCGCCTCTGGGATGCCGTGGT	AAACACCACGGCATCCCAGAGGCGc

Table 4.6 – Mouse *Ryr1* p.S1728F-targeting gRNAs for cloning into pSpCas9(BB)-2A-GFP

Sequences in black text show the gRNAs and their complements. Sequences in green text show the overhangs to facilitate cloning into pSpCas9(BB)-2A-GFP and the additional G nucleotide to enhance transcription from the U6 promoter is shown in blue text.

gRNA name	Forward sequence 5'-3'	Reverse sequence 5'-3'
Mm_S1728F_gRNA1	CACCGGCTGCGGCAGGCGCTTTCG	AAACCGAAAGCGCCTGCCGCAGCC
Mm_S1728F_gRNA2	CACCgCATGGAGCGACGGCTGCGGC	AAACGCCGCAGCCGTCGCTCCATGc
Mm_S1728F_gRNA3	CACCgAGAGCATGGAGCGACGGCTG	AAACCAGCCGTCGCTCCATGCTCTc

4.2.5 HDR template design

HDR templates were designed as described previously (3.2.5), with single stranded oligonucleotides containing 80 bp homology to the sequence flanking the gRNA cut site. To prevent re-cleavage of the gRNA if successfully incorporated into the C2C12 genome, silent mutations were introduced either into the PAM or 12 nt gRNA seed region. For Mm_D3986E_gRNA1, the PAM sequence spanned 2 amino acid codons – TTC (phenylalanine, F) and CTG (leucine, L). Substituting the C base of the TTC codon to produce TTT removed the PAM site without altering the amino acid (Figure 4.7; panel A). For Mm_D3986E_gRNA2, it was not possible to introduce a silent mutation into the PAM sequence; however, 8 silent mutations were able to be introduced into the 12 nt PAM seed region (Figure 4.7; panel B). Introduction of a silent mutation within the PAM of Mm_D3986E_gRNA3 was also not possible and only 2 silent mutations were able to be introduced within the 12 nt seed region. Since reports show that up to 2 mismatches within the seed region may be tolerated (Hsu et al., 2013), 2 additional silent mutations were introduced towards the PAM-distal end of Mm_D3986E_gRNA3 in an attempt to further prevent re-cleavage (Figure 4.7; panel C). For all of the p.S1728F-targetting gRNAs, introduction of a silent mutation in the PAM was possible. For Mm_S1728F_gRNA1, the PAM was comprised of 2 amino acids codons, CAC (histidine, H) and CTC (leucine, L). Substitution of the CAC codon for CAT abolished the PAM site without altering the histidine residue (Figure 4.8; panel A). For Mm_S1728F_gRNA2, the PAM spanned 2 amino acid codons, GCC (alanine, A) and TGC (cysteine, C). Substitution of GCC for GCA removes the PAM site but does not alter the alanine residue at that position (Figure 4.8; panel A). The PAM of Mm_S1728F_gRNA3 also spanned two amino acid codons, TGC (cysteine, C) and CGC (arginine, R). Substitution of the TGC codon for TGT removed the PAM site without affecting the cysteine residue at that position (Figure 4.8; panel C).

Table 4.7 – HDR template sequences for mouse *Ryr1* p.D3986E and p.S1728F-targeting gRNAs.

Single stranded HDR template sequences were used to introduce the RYR1 p.D3986E and RYR1 p.S1728F variants into C2C12 myoblasts. The gRNA sequences are shown in orange and edited bases in purple. PAMs are shown in green and the base to be changed is shown in red. The Cas9 cut site is indicated by a /.

HDR template	Sequence 5'-3'
Mm_D3986E_HDR_gRNA1	GTTCCCCAGGGACCCTGCACCGGAAACCAGCAGAGTCTGGCGCACAGTCGCCTCTGGGAGGCCGTGGTGGGCTTTCTGCA/CGTGTTCGCGCAC ATGATGATGAAGCTGGCTCAGGTTTGAGTTCGTCTGAGAACAGCTCTTTCCCTCCAGCCATCCCCTA
Mm_D3986E_HDR_gRNA2	CTCCTGCTGAGGCTTCAGGCCACCCTTTGTTCCCCAGGGACCCTGCACCGGAAACCAGCAGAGTCTGGCGCATTCAAGAT/TATGGGAGGCCGT GGTGGGCTTCCTGCACGTGTTCGCGCACATGATGATGAAGCTGGCTCAGGTTTGAGTTCGTCTGAGA
Mm_D3986E_HDR_gRNA3	TTCAGGCCACCCTTTGTTCCCCAGGGACCCTGCACCGGAAACCAGCAGAGTCTGGCGCACAGTAGACTATGGGAGGCAGT/AGTGGGCTTCCTG CACGTGTTCGCGCACATGATGATGAAGCTGGCTCAGGTTTGAGTTCGTCTGAGAACAGCTCTTTCCC
Mm_S1728F_HDR_gRNA1	TTGCATGCGCTGGAGGATGCGCGCTTGCCAGGTCCTCTGCGAGCAGGCTACTACGACCTCCTCATCAGCATCCATCTCGA/AAGCGCCTGCCGC AGCCGTCGCTTCATGCTCTCTGAGTACATCGTGCCACTCACGCCGGAGACCCGCGCCATCACGCTTT
Mm_S1728F_HDR_gRNA2	GGAGGATGCGCGCTTGCCAGGTCCTCTGCGAGCAGGCTACTACGACCTCCTCATCAGCATCCACCTCGAAAGCGCATGCC/GCAGCCGTCGCTT CATGCTCTCTGAGTACATCGTGCCACTCACGCCGGAGACCCGCGCCATCACGCTTTTCCCACCTGGG
Mm_S1728F_HDR_gRNA3	GATGCGCGCTTGCCAGGTCCTCTGCGAGCAGGCTACTACGACCTCCTCATCAGCATCCACCTCGAAAGCGCCTGTCGCAG/CCGTCGCTTCATG CTCTCTGAGTACATCGTGCCACTCACGCCGGAGACCCGCGCCATCACGCTTTTCCCACCTGGGCGAA

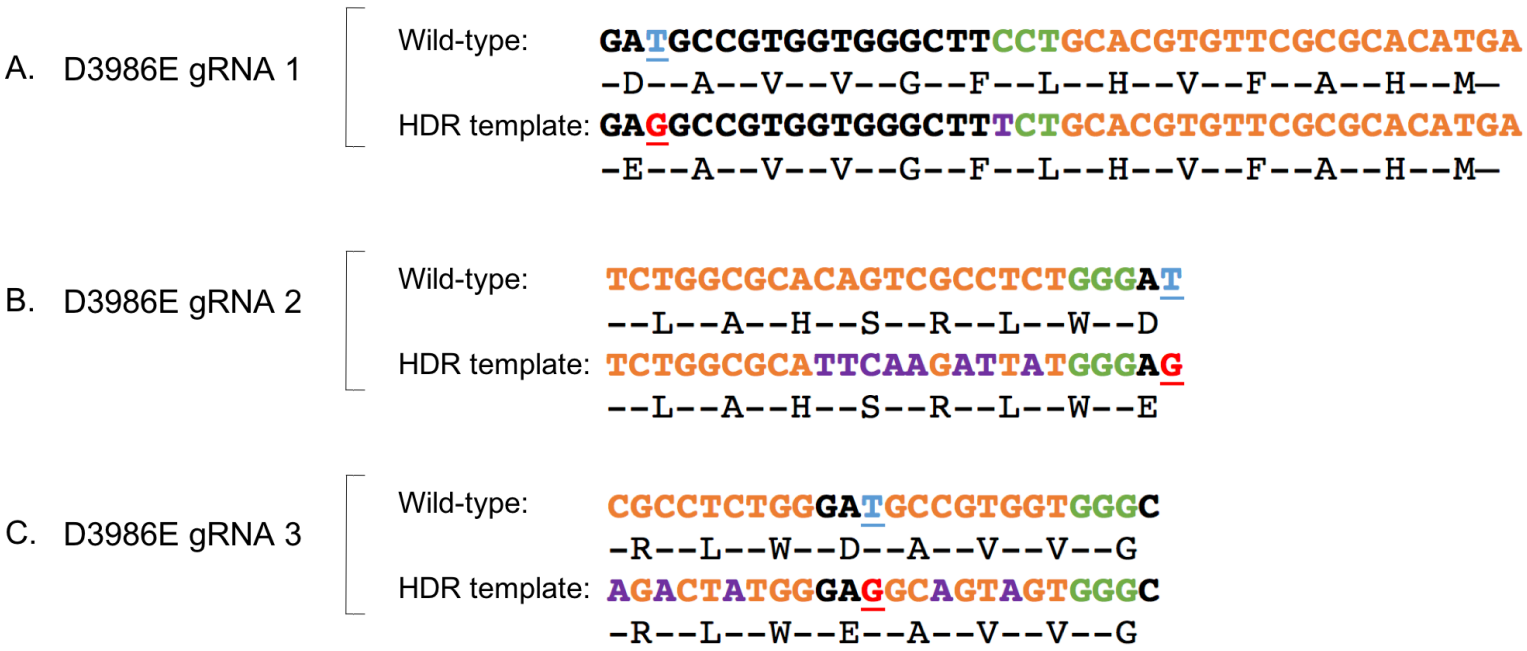

Figure 4.7 – Mouse *Ryr1* p.D3986E-targeting repair templates

HDR arms were designed to include 80 bp of homology upstream and downstream of the Cas9 cut site. HDR templates were modified from the original target sequence to prevent re-cleavage by Cas9 following insertion into the genome, by introducing silent mutations into either the PAM sequence (panel A) or the seed region (panels B and C). The gRNA sequences are shown in orange text, PAMs in green text, the base to be edited in blue text, the edited base in red and the silent mutations in purple. Beneath the DNA sequences are the amino acid single letter codes.

Figure 4.8 - Mouse *Ryr1* p.S1728F-targeting repair templates
HDR arms were designed to include 80 bp of homology upstream and downstream of the Cas9 cut site. HDR templates were modified from the original target sequence to prevent re-cleavage by Cas9 following insertion into the genome, by introducing silent mutations into either the PAM sequence. The gRNA sequences are shown in orange text, PAMs in green text, the base to be edited in blue text, the edited base in red and the silent mutations in purple. Beneath the DNA sequences are the amino acid single letter codes

4.2.6 Cloning into pSpCas9(BB)-2A-GFP

Forward and reverse gRNA sequences with 5'-CACC and 5'-AAAC overhangs, respectively, were annealed incubated in a ligation reaction with pSpCas9(BB)-2A-GFP that had be linearised with *Bbs*I. Following incubation, ligation reactions were transformed into OneShot™ chemically competent Stbl3™ cells (Invitrogen™) and colonies allowed to grow on LB agar plates containing ampicillin. Four single colonies were picked per gRNA and used to inoculate 5 ml LB broth. Cultures were used for plasmid DNA extraction by miniprep and also as starter cultures for maxipreps, to isolate transfection-grade plasmid DNA. Isolated plasmid DNA was prepared for Sanger sequencing to confirm that the gRNAs had been inserted successfully. All colonies picked contained the gRNA insert and were confirmed by Sanger sequencing (Figure 4.9).

Figure 4.9 – Sanger sequencing traces of mouse *Ryr1* p.D3986E and p.S1728F-targeting gRNAs in pSpCas9(BB)-2A-GFP

Sanger sequencing was used to confirm the insertion of gRNAs in pSpCas9(BB)-2A-GFP. At the top of the figure is the pSpCas9(BB)-2A-GFP cloning schematic. Sanger sequencing traces show the presence of Mm_D3986E_gRNA1 (panel A), 2 (panel B) and 3 (panel C) and Mm_S1728F_gRNA1 (panel D), 2 (panel E) and 3 (panel F) in pSpCas9(BB)-2A-GFP. On each trace, the vector sequence is underlined in black, the *Bbs*I-induced overhangs are underlined in green and the gRNA sequence is underlined in blue.

4.2.7 Viability of C2C12 myoblasts following Lipofectamine™ 3000 treatment

To investigate whether Lipofectamine™ 3000 had an adverse effect on C2C12 cell viability, C2C12 cells were plated in 6-well plates and incubated with Lipofectamine™ 3000 for 24 hours. Viability was estimated by trypan blue staining and cell counting using a haematocytometer. The average viabilities across 4 wells of non-treated C2C12 and 4 wells of Lipofectamine™ 3000 treated cells were 89.0% and 90.4%, respectively. No obvious cell death was observed in treated C2C12 cells compared to non-treated control C2C12 cells (Figure 4.10). Thus, Lipofectamine™ 3000 was deemed not to have a detrimental effect on C2C12 cell viability.

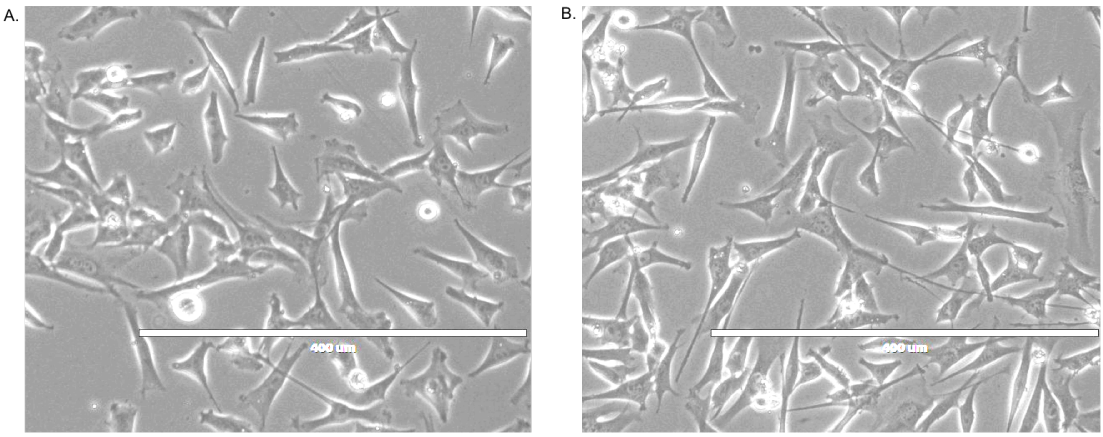

Figure 4.10 – Non-transfected C2C12 cells and Lipofectamine™ 3000 treated C2C12 cells.

C2C12 cells were maintained in growth media (panel A) and another well was treated with 125 µl Opti-MEM medium containing 7.5 µl Lipofectamine™ 3000 and 5 µl p3000 reagent (panel B). The cells were incubated for 24 hours (37°C, 5% CO2) prior to analysis. Images were captured using the EVOS™ FL microscope using the x40 objective. The scale bar indicates 400 µM.

4.2.8 Viability of C2C12 myoblasts following transfection with pSpCas9(BB)-2A-GFP

To investigate parameters for C2C12 myoblast transfection, a range of volumes and ratios of Lipofectamine™ 3000:plasmid DNA were used for an initial transfection in triplicate. Cell viabilities and transfection efficiencies were

estimated as described previously. Transfection was well tolerated in C2C12 myoblasts, with cell viabilities for cells transfected with 0.5 µg plasmid DNA and 0.75 µl Lipofectamine™ 3000, 0.5 µg plasmid DNA and 1.5 µl Lipofectamine™ 3000, 1 µg plasmid DNA and 0.75 µl Lipofectamine™ 3000 and 1 µg plasmid DNA and 1.5 µl Lipofectamine™ 3000 of 94.0%, 93.6%, 91.8% and 91.3%, respectively. Non-transfected C2C12 myoblasts had a cell viability of 93.5%. Estimates of transfection efficiencies for 0.5 µg plasmid DNA and 0.75 µl Lipofectamine™ 3000 (Figure 4.11; panel A), 0.5 µg plasmid DNA and 1.5 µl Lipofectamine™ 3000 (Figure 4.11; panel B), 1 µg plasmid DNA and 0.75 µl Lipofectamine™ 3000 (Figure 4.11; panel C) and 1 µg plasmid DNA and 1.5 µl Lipofectamine™ 3000 (Figure 4.11; panel D) were 8.8%, 9.5%, 12.0% and 17.0%, respectively. Since conditions using 1 µg plasmid DNA and 1.5 µl Lipofectamine™ 3000 produced the highest transfection efficiency in this initial experiment, these volumes and reagent:DNA ratio were used for subsequent transfections.

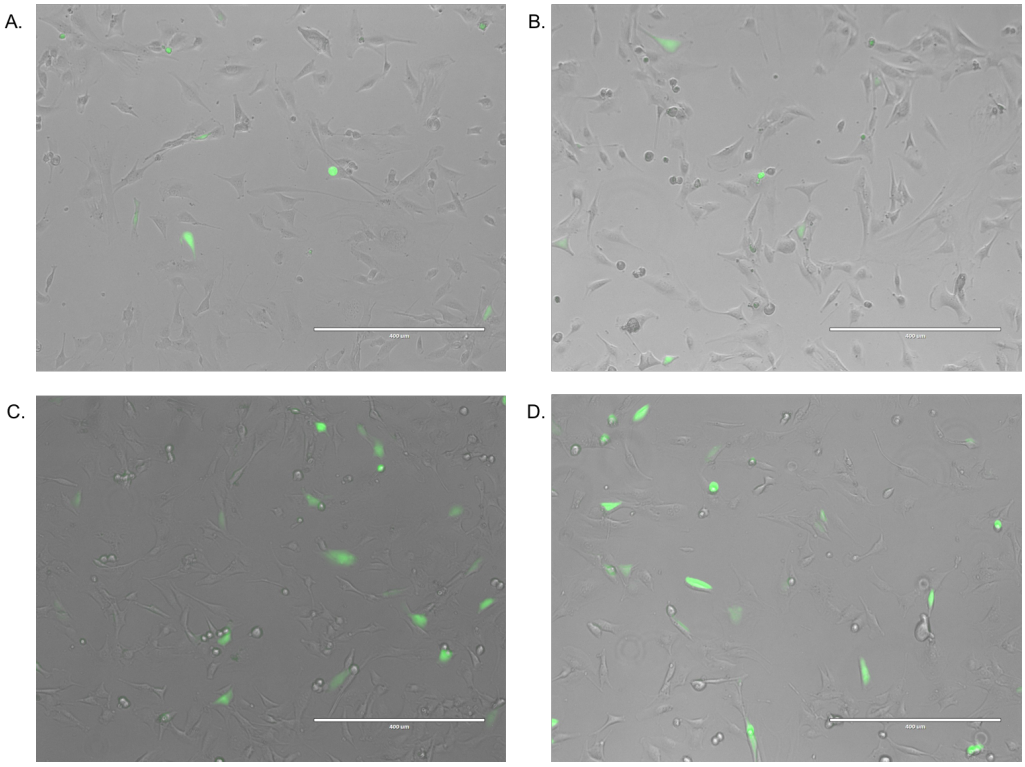

Figure 4.11 - C2C12 cells transfected with pSpCas9(BB)-2A-GFP plasmid.

C2C12 cells in 24-well plates were treated with varying volumes of Lipofectamine™ 3000 and ratios of Lipofectamine™ 3000 to plasmid DNA in triplicate – 0.5 µg plasmid DNA and 0.75 µl Lipofectamine™ 3000 (panel A), 0.5 µg plasmid DNA and 1.5 µl Lipofectamine™ 3000 (panel B), 1 µg plasmid DNA and 0.75 µl Lipofectamine™ 3000 (panel C) and 1 µg plasmid DNA and 1.5 µl Lipofectamine™ 3000 (panel D). 2 µl p3000 reagent was added per 1 µg plasmid DNA. Cells were incubated for 24 hours (37°C, 5% CO_2) prior to analysis. Images were captured using the EVOS™ FL microscope (ThermoFisher). The scale bar indicates 400 µM.

4.2.9 Determining gene-editing capacity of gRNAs

T7 endonuclease assays were performed to determine whether the gRNAs induced double stranded breaks at the desired location within the genome. The gene-editing efficiencies of each gRNA for p.D3986E and p.S1728F were estimated to inform what gRNA would be used for editing, in conjunction with positional information regarding the distance of the Cas9 cut site from the base to be edited. C2C12 cells were plated at 2.5 x 10^5/well of a 6-well plate immediately prior to transfection of all pSpCas9(BB)-2A-GFP vectors containing Mm_D3986E_gRNA1, 2 and 3 and Mm_S1728F_gRNA1, 2 and 3. For the purpose of illustration, representative traces of cells transfected with

pSpCas9(BB)-2A-GFP containing Mm_D3986E_gRNA1 and Mm_S1728F_gRNA1 are shown (Figure 4.12). As described previously, gates were drawn to exclude non-viable cells from the sort based on their SSC and FSC measurements. Non-transfected cells were used as a control to determine where to place GFP positive gates. An example FACS trace has been shown for refeence (Figure 4.12). In this instance, the proportion of intact cellular bodies, a measure of cell viability, of non-transfected C2C12 cells was 98.07%. The cell viabilities of C2C12 cells transfected with Mm_D3986E_gRNA1 and Mm_S1728F_gRNA1 were 96.90% and 94.89%, respectively. The proportions of GFP-expressing cells collected for Mm_D3986E_gRNA1 and Mm_S1728F_gRNA1 were 24.11% and 33.35%, respectively. In total, two FACS experiments per vector were performed to obtain cells for DNA extraction and T7 assay optimisation. Across experiments, the mean cell viability for non-transfected cells was 97.38%. The mean cell viabilities for C2C12 cells transfected with the pSpCas9(BB)-2A-GFP vectors containing p.D3986E and p.S1728F gRNAs were 96.10% and 95.44%, respectively. The proportion of GFP positive cells collected varied across experiments with a mean of 25.02% (range 6.37%-52.74%) for p.D3986E vectors and 25.25% (range 5.57%-53.48%) for p.S1728F vectors.

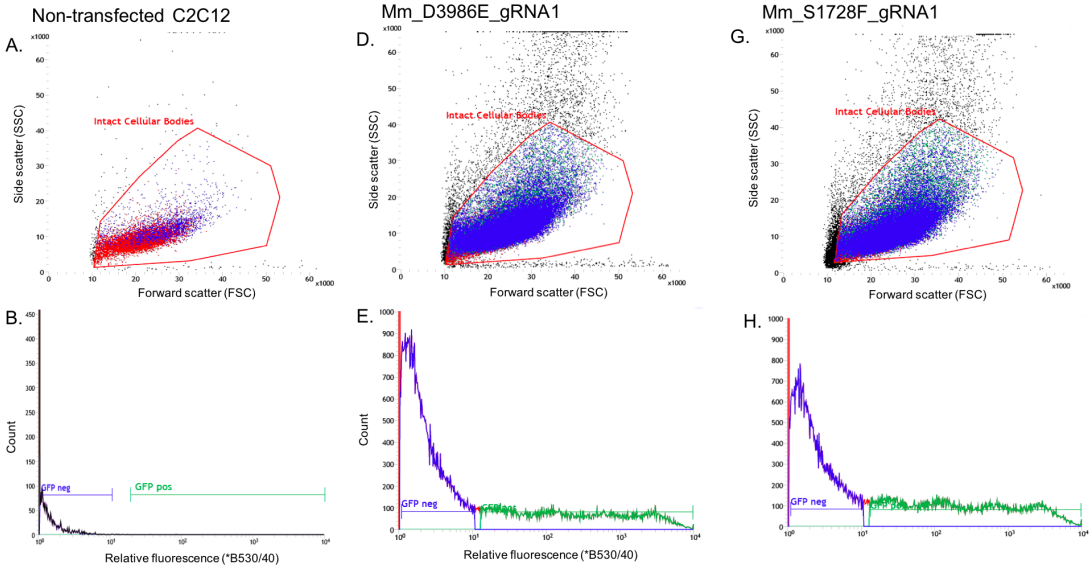

C.

Populations	Events	% Total
All events	10,000	100.00
Intact cellular bodies	9,807	98.07
GFP positive	1	0.01
GFP negative	1,809	18.09

F.

Populations	Events	% Total
All events	100,000	100.00
Intact cellular bodies	96,895	96.90
GFP positive	24,108	24.11
GFP negative	51,235	51.24

I.

Populations	Events	% Total
All events	100,000	100.00
Intact cellular bodies	94,893	94.89
GFP positive	33,349	33.35
GFP negative	45,259	45.26

Figure 4.12 – FACS traces of C2C12 myoblasts transfected with pSpCas9(BB)-2A-GFP

Transfected.C2C12 cells were incubated at 37ºC, 5% CO2 for 24 hours prior to FACS. Panels A, D and G show the side scatter (Y axis) and forward scatter (X axis) profiles of non-transfected cells, Mm_D3986E_gRNA1 transfected cells and Mm_S1728F_gRNA1 transfected cells, respectively. Panels B, E and H show the cell count (Y axis) and relative fluorescence intensity in arbitrary units (X axis) of non-transfected cells, Mm_D3986E_gRNA1 transfected cells and Mm_S1728F_gRNA1 transfected cells, respectively. Panels C, F and I show the proportion of intact cellular bodies (red), GFP positive cells (green) and GFP negative cells (blue) of non-transfected cells, Mm_D3986E_gRNA1 transfected cells and Mm_S1728F_gRNA1 transfected cells, respectively. The number of events (black) corresponds to the number of cells detected by the laser and is usually measured between 10,000-200,000 cells dependent on the sample size, to give a snapshot of the profile of the cells.

Following FACS enrichment, DNA was extracted from each pool GFP-expressing cells. A region around the Cas9 cut site was amplified by PCR and purified using AMPure XP magnetic beads (Beckman Coulter). For the p.D3986E gRNAs, the amplified region was 449 bp. For Mm_D3986E_gRNA1, the expected products following Cas9 cleavage were 268 bp and 181 bp. For Mm_D3986E_gRNA2, the expected products were 241 bp and 208 bp. Finally, for Mm_D3986E_gRNA3, the expected products were 255 bp and 194 bp. Indeed, separation of each T7 reaction on an agarose gel yielded distinct bands corresponding to the expected cleavage products for each gRNA (Figure 4.13). The cleavage products for Mm_D3986E_gRNA2 were observed as a single band, due to resolution limitations of agarose gel electrophoresis. No cleavage products were observed in the non-transfected cell sample. The proportion of cleaved products was quantified by 2D densitometry. The proportion cleaved for Mm_D3986E_gRNA1, 2 and 3 was 41.13%, 29.06% and 36.81%, respectively. Gene editing efficiencies were estimated using Equation 1 (detailed in 3.2.8; Guschin et al., 2010); Mm_D3986E_gRNA1, 2 and 3 had estimated gene-editing efficiencies of 23.27%, 15.75% and 20.50%, respectively.

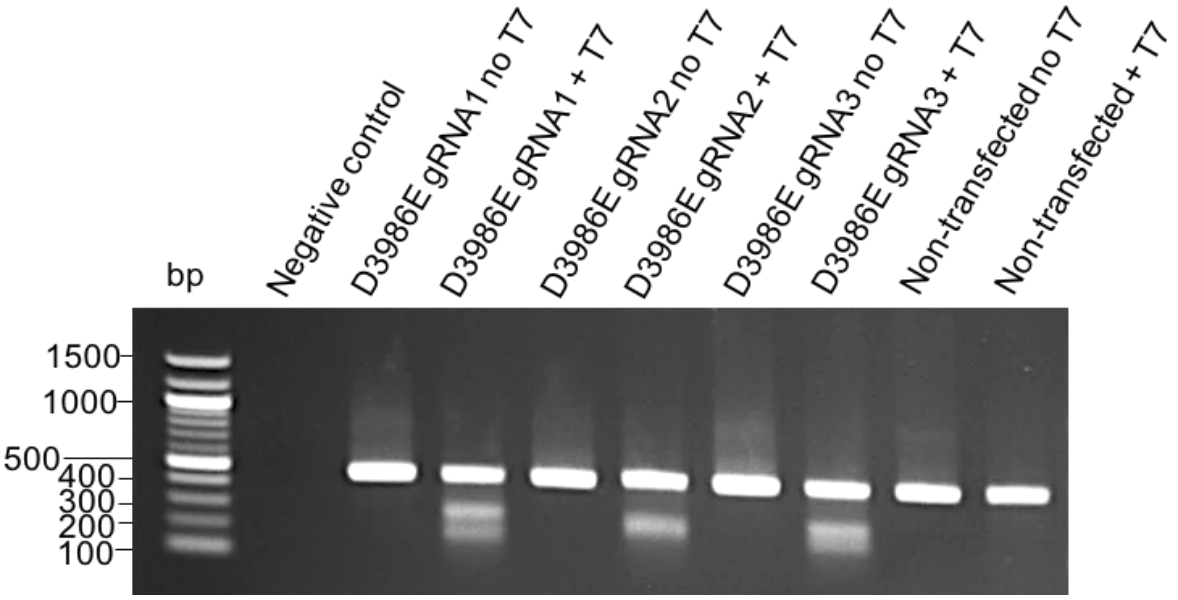

Figure 4.13 – T7 assay to determine the gene-editing efficiency of Mm_D3986E_gRNA, 2 and 3.

The T7 assay was loaded onto 1% TAE-agarose gel and products separated by gel electrophoresis. Lane 1 shows the 100 bp DNA ladder (NEB) and lane 2 shows all components of the T7 reaction minus DNA. Lanes 3 and 4 show the T7 assay from C2C12 cells transfected with Mm_D3986E_gRNA1 without and with the T7 enzyme. Lanes 5-10 show the same for Mm_D3986E_gRNA2, _D3986E_gRNA3 and non-transfected cells.

For the p.S1728F gRNAs, the amplified region for the T7 assay was 475 bp. The expected Cas9 cleavage products for Mm_S1728F_gRNA1 were 188 bp and 287 bp. For Mm_D3986E_gRNA2, the expected cleavage products were 199 bp and 275 bp. For Mm_D3986E_gRNA3, the expected cleavage products were 203 bp and 272 bp. Whilst the T7 assay for p.S1728F gRNAs did not produce bands as distinct as those for the p.D3986E gRNAs, cleavage products were separated from the main amplicon following agarose gel electrophoresis that corresponded to the expected sizes (Figure 4.14). No cleavage products were observed in the non-transfected cell sample. The fractions cleaved for Mm_S1728F_gRNA1, 2 and 3 were 5.89%, 13.78% and 8.33%, respectively. The estimated gene-editing efficiencies were 2.98%, 7.15% and 4.26%, respectively.

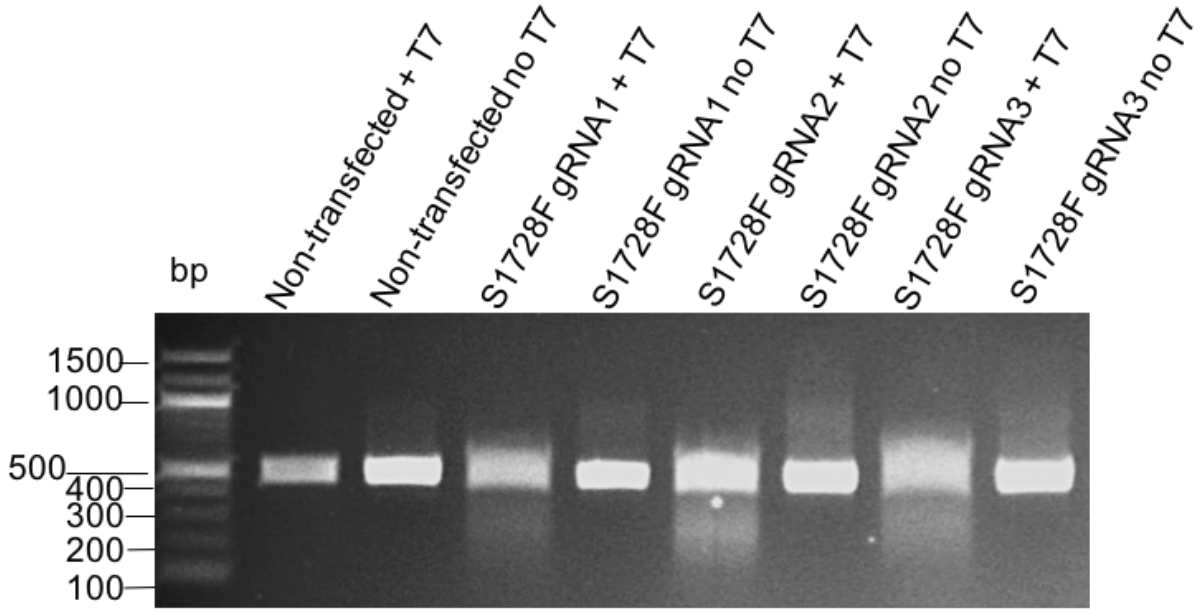

Figure 4.14 – T7 assay to determine the gene-editing efficiency of Mm_S1728F_gRNA1, 2 and 3.

The T7 assay was loaded onto a 1% TAE-agarose gel and products separated by gel electrophoresis. Lane 1 shows the 100 bp DNA ladder (NEB), lane 2 shows all components of the T7 reaction minus DNA, lanes 3 and 4 show the T7 assay from C2C12 cells transfected with Mm_S1728F_gRNA1 without and with the T7 enzyme. Lanes 5-10 show the same for Mm_S1728F_gRNA2 and gRNA3.

Following confirmation that all gRNAs for p.D3986E and p.S1728F were functional in C2C12 myoblasts, gRNAs to be used for subsequent variant introduction were selected. The gRNAs were selected based a combination of data on gene-editing efficiency, off-target ranking by CCTOP and the Cas9 cut site distance from the base to be edited. For the p.D3986E gRNAs, Mm_D3986E_gRNA1 was not used due to the 23 bp distance between the base to be edited and the Cas9 cut site. The base to be edited was <10 bp away from the Cas9 cut site for both Mm_D3986E_gRNA2 and Mm_D3986E_gRNA3. While Mm_D3986E_gRNA3 demonstrated slightly higher gene-editing efficiencies, Mm_D3986E_gRNA2 was selected for use due to its higher CCTOP ranking. For p.S1728F, Mm_S1728F_gRNA1 was excluded based on the 24 bp distance of the base to be edited from the Cas9 cut site. Whilst Mm_S1728F_gRNA3 Cas9 cut site was 9 bp from the base to be edited, in contrast to 13 bp for Mm_S1728F_gRNA2, Mm_S1728F_gRNA3

had wide-spread predicted off-targets. Consequently, Mm_D3986E_gRNA2 and Mm_S1728F_gRNA2 were used for HDR.

4.2.10 Single cell isolation and propagation

FACS was used to isolate single cells from C2C12 cells transfected with the Mm_D3986E_gRNA2 and Mm_S1728F_gRNA2 vectors that showed GFP expression. The passage number of C2C12s used for this transfection was 10 (C2C12 cells resuscitated from liquid nitrogen at the outset of this project were labelled as passage 1; however, no information was available regarding the history of these cells prior to the start of this project). A single FACS sort was performed for each vector for the collection of single cells. For p.D3986E, 10 96-well plates of single cells were collected and for p.S1728F, 8 plates were collected. Cells were collected in a 1:1 ratio of fresh:filtered, conditioned growth media and were incubated for one week at 37^{o}C with 5% CO_2. After one week, all 960 wells for p.D3986E and 768 wells for p.S1728F were manually inspected using a light microscope for signs of cell growth. Cells that had grown were transferred to a 6-well plate for cell line propagation (at this stage, 2 96-well plates worth of p.D93986E cells were each given to laboratory technicians Catherine Daly and Xiaochen Liu for their assistance in culturing the cell lines, the remainder were cultured by me). Cells were cultured until two T-75 flasks were ~60% confluent. One flask was processed for liquid nitrogen storage and the other used for DNA extraction. Throughout the propagation process, some cell lines were discarded due to contamination or lack of cell growth. In total, 160 cell lines were obtained for p.D3986E and 74 for p.S1728F.

4.2.11 Validation of edited p.D3986E and p.S1728F cell lines

4.2.11.1 TaqMan™ SNP genotyping to detect the presence of variants

DNA extracted from the single-cell derived lines was genotyped using a custom TaqMan™ SNP genotyping assay to detect the presence of the p.D3986E and p.S1728F variants. Custom probes were designed to detect only the single nucleotide variants, and not the silent mutations inserted in the PAM/seed

region. Genotyping data were analysed using the Genotyping Module on the Thermo Fisher Cloud (Applied Biosystems). For p.D3986E, an initial screening experiment was performed whereby single replicates of each sample were genotyped. Out of the 160 p.D3986E lines screened, 6 were identified by the genotyping assay to contain the variant of interest (3.75%) – cell lines 8G6, 2G7, 9H12, 1E6, 1C5 and 10G5. Variants were confirmed by repeating the genotyping assay and the 6 samples were tested in triplicate alongside a wild-type C2C12 control. The allelic discrimination plot produced three distinct genotype clusters of allele 2/allele 2, allele 1/allele 2 and allele 1/allele 1 (Figure 4.15).

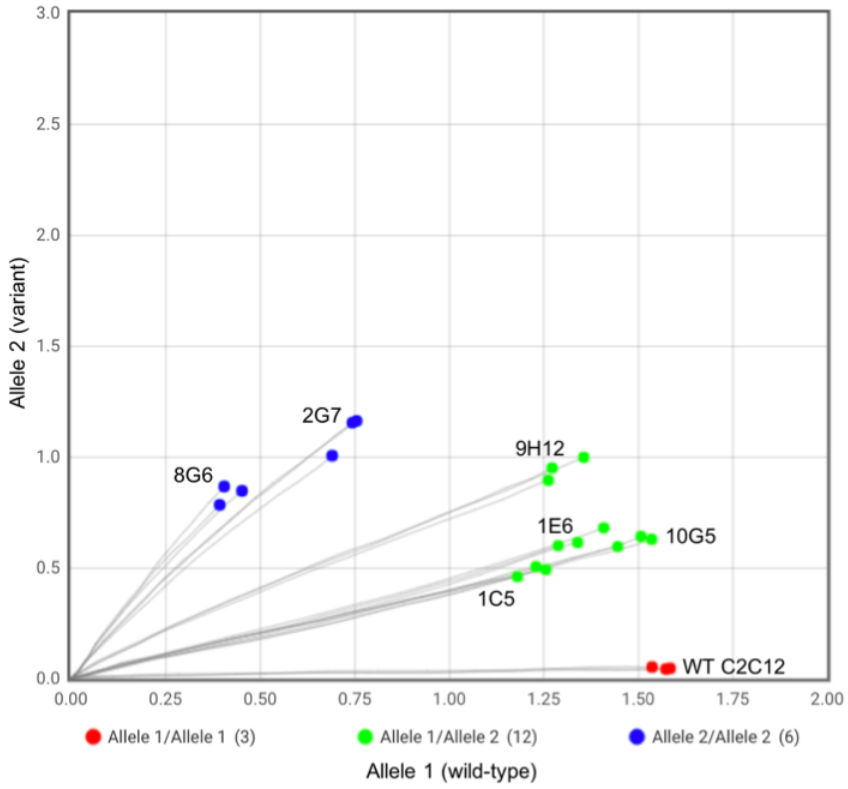

Figure 4.15 – TaqMan™ SNP genotyping of p.D3986E cell lines

Allelic discrimination plot generated by the Genotyping Module on the Thermo Fisher Cloud (Applied Biosystems) showing the genotypes of p.D3986E cell lines 8G6, 2G7, 9H12, 1E6, 1C5 and 10G5. The X axis shows deltaRn (dRn) values for allele 1 (wild-type) and the Y axis shows the dRn values for allele 2 (p.D3986E variant). The dRn values refer to the change in fluorescence from baseline, normalised to the passive reference dye, ROX. DNA was extracted from each cell line, quantified using the NanoDrop™ 1000 spectrophotometer (ThermoFisher) and diluted to 20 ng/ul, with 20 ng added to each reaction. Cell lines were genotyped in triplicate and genotypes were automatically called as either Allele1/ Allele 1 (red dots), Allele1/ Allele 2 (green dots) or Allele 2/ Allele 2 (blue dots). For autocalling, use of the Hardy-Weinberg equilibrium equation was removed from the analysis.

Cell lines 8G6 and 2G7 were called as allele 2/allele 2, while 9H12, 1E6, 1C5 and 10G5 were called as allele 1/allele 2. Within these clusters, there were so-called vector clusters, whereby the 8G6 and 2G7 clusters were diverged within the allele2/allele2 cluster and the 9H12 diverged from 1C5, 1E6 and 10G5 in the allele1/allele2 cluster. Since autocalling analyses the ratios of dRn values to determine genotype, dRn ratios were manually compared between cell lines within each cluster to infer the copy number of wild-type and variant alleles in the triploid *Ryr1* genes of each cell line (Table 4.8). Cell line 8G6 appears to have 2 copies of the p.D3986E variant and 1 wild-type sequence, with the dRn value for allele 2 roughly double those for allele 1 (1:1.99). The dRn ratios of cell line 2G7 were less clear. Whilst the 2G7 cell line was called as allele 2/allele 2, the ratio of allele 2 to allele 1 was 1.5:1. Cell line 9H12 was called as allele 1/allele 2; however, it formed a distinct group from cell lines 1E6, 1C5 and 10G5. The dRn ratios of 2G7 and 9H12 may be indicative of equal copies of allele 1 and allele 2, with dRn values at an almost 1:1 ratio (1:1.5 and 1:1.3, respectively). The dRn values for 1E6, 1C5, 10G5 indicate that each cell line has 1 copy of the p.D3986E variant and 2 copies of the wild-type sequence, with a roughly 2:1 ratio of allele 1 to allele 2 (1E6 = 2.13:1; 1C5 = 2.51:1; 10G5 = 2.40:1). No amplification of the p.D3986E allele 2 was observed in wild-type C2C12 cells. For use as a control in downstream caffeine sensitivity experiments, an un-edited cell line that had been subjected to transfection, FACS and propagation from a single cell was selected (cell line 3E1). Cell line 3E1 had average dRn values comparable to wild-type (allele 1 = 1.997, allele 2 = 0.085) and Sanger sequencing of the p.D3986E region showed a wild-type sequence (Figure 4.16).

Table 4.8 – TaqMan™ SNP genotyping dRn values for p.D3986E cell lines

Each cell line was genotyped in triplicate and dRn values for allele 1 and allele 2 averaged. For reference, dRn values from the initial screening genotyping run are shown in brackets – these values were obtained from a single replicate.

Cell line	dRn wild-type allele 1	dRn p.D3986E allele 2
8G6	0.418 (0.495)	0.833 (1.077)
2G7	0.730 (0.893)	1.107 (1.332)
9H12	1.297 (1.597)	0.948 (1.142)
1E6	1.346 (1.383)	0.632 (0.640)
1C5	1.222 (1.282)	0.486 (0.587)
10G5	1.496 (1.416)	0.622 (0.595)
WT C2C12	1.565	0.048

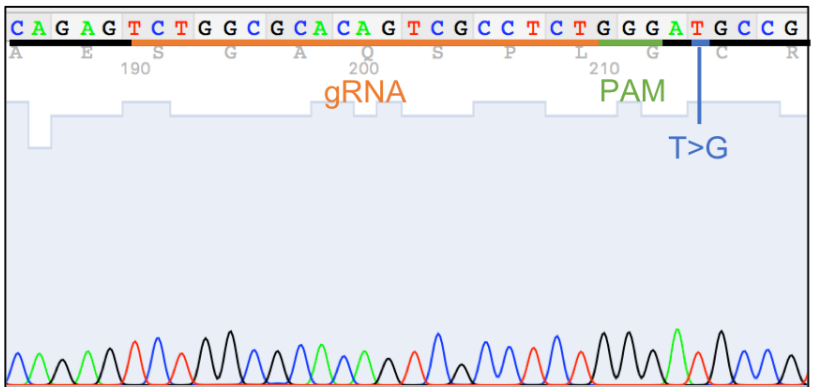

Figure 4.16 – Mm_D3986E_gRNA2 region in cell line 3E1

Sanger sequencing was performed on DNA extracted from cell line 3E1. The gRNA sequence is underlined in orange and the PAM in green. The T>G base to be edited is shown in blue. Chromatograms were viewed in 4Peaks (Nucleobytes).

For p.S1728F, 74 cell lines were screened. The initial genotyping screening assay identified 1 cell line, 6B4, as having the p.S1728F variant. Two additional cell lines, 6F12 and 6H6 were autocalled as 'undetermined' with low confidence flags. For this genotyping assay, all dRn values were low (>0.7 for allele 1 and >0.4 for allele 2; Table 4.9). While 6H6 was autocalled as 'undetermined', the amplification plot for allele 2 closely resembled that of background amplification (Figure 4.17). Indeed, following repetition of the genotyping of 6B4, 6E6 and 6F12 alongside wild-type C2C12s, it was

confirmed that only cell lines 6B4 and 6F12 contained the p.S1728F variant (2.7% of the 74 cell lines screened; Figure 4.18).

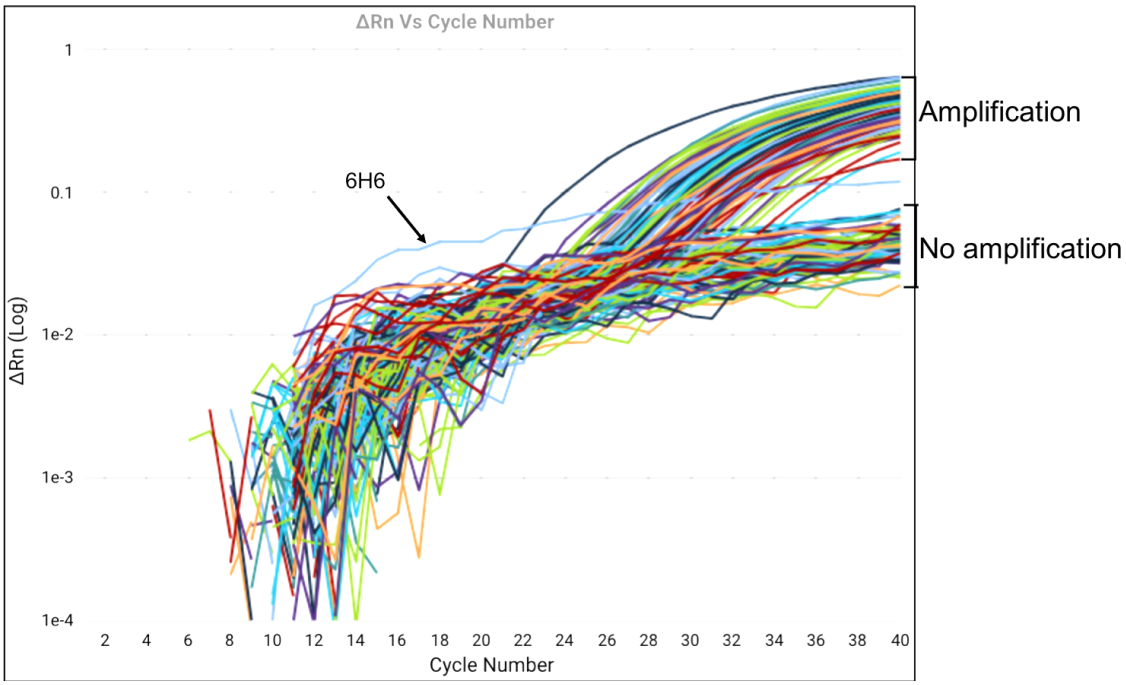

Figure 4.17 – p.S1728F TaqMan™ SNP genotype screening assay amplification plot

DNA extracted from GFP-expressing cells transfected with the pSpCas9(BB)-2A-GFP p.S1728F gRNA vector was used in a TaqMan™ genotyping assay to detect the presence of the variant. Amplification plots for each cell line were generated showing the change in fluorescence (dRn; Y axis) over cycle iterations (X axis). The amplification plot for the 6H6 cell line is indicated by an arrow.

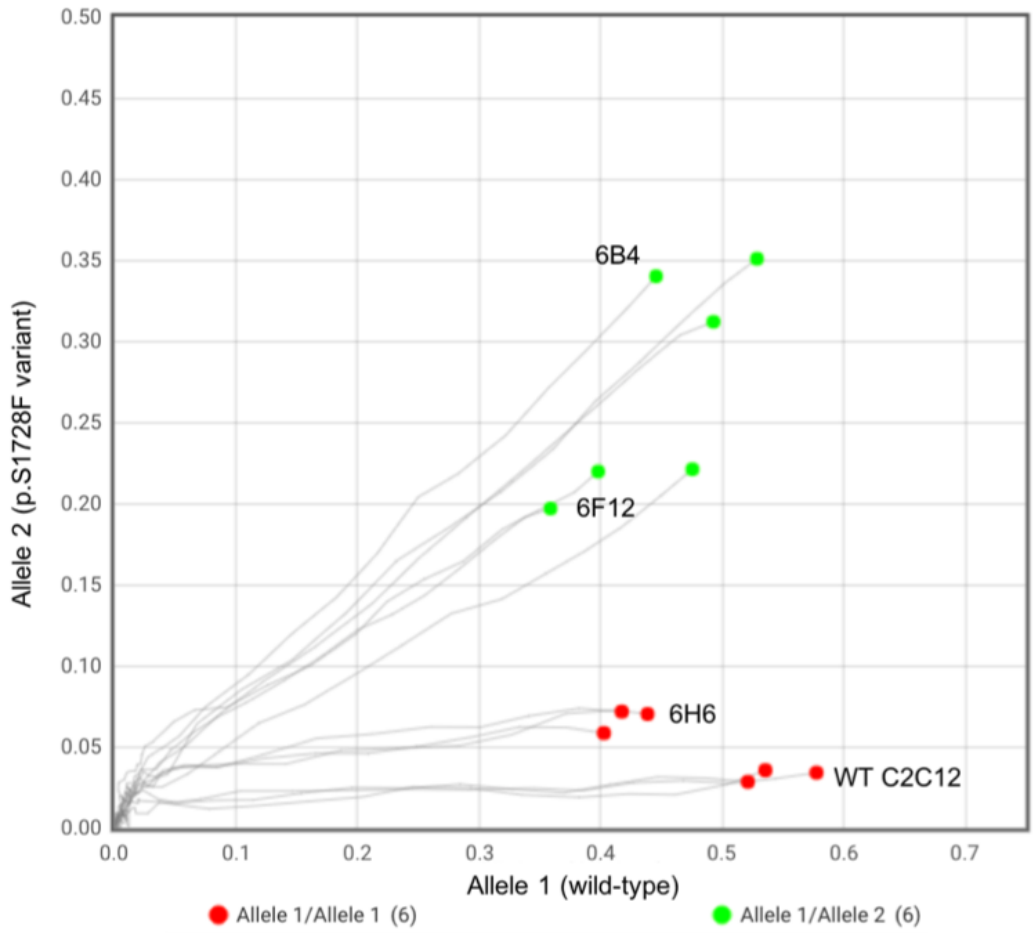

Figure 4.18 – TaqMan™ SNP genotyping of p.S1728F lines

Allelic discrimination plot generated by the Genotyping Module on the Thermo Fisher Cloud (Applied Biosystems) for p.S1728F cell line genotyping. The X axis shows dRn values for allele 1 (wild-type) and the Y axis shows the dRn values for allele 2 (p.S1728F variant). The dRn values refer to the change in fluorescence from baseline, normalised to the passive reference dye, ROX. DNA was extracted from each cell line, quantified using the NanoDrop™ 1000 spectrophotometer (ThermoFisher) and diluted to 20 ng/ul, with 20 ng added to each reaction. Each cell line was genotyped in triplicate and genotypes were automatically called as either Allele1/ Allele 1 (red dots) or Allele1/ Allele 2 (green dots). For autocalling, use of the Hardy-Weinberg equilibrium equation was removed from the analysis.

Genotypes of the p.S1728F lines were estimated as described for p.D3986E cell lines, by comparing the ratios between dRn values for allele 1 (wild-type) and allele 2 (variant) (Table 4.9). Cell line 6F12 had a 2:1 ratio of allele 1 to allele 2, suggesting 2 copies of allele 1 and a single copy of allele 2. Cell line 6B4 had a 1.5:1 ratio of allele 1 to allele 2.

Table 4.9 – TaqMan™ SNP genotyping dRn values for p.S1728F cell lines

Each cell line was genotyped in triplicate and dRn values for allele 1 and allele 2 averaged. For reference, dRn values from the initial screening genotyping run are shown in brackets – these values were obtained from a single replicate.

Cell line	dRn allele 1 wild-type	dRn allele 2 p.S1728F
6B4	0.489 (0.318)	0.334 (0.243)
6F12	0.411 (0.295)	0.212 (0.170)
6H6	0.419 (0.290)	0.067 (0.119)
WT C2C12	0.544	0.033

Since C2C12 cells have 3 copies of chromosome 7, the power of Sanger sequencing to confirm variant insertions was limited. To overcome this, a region encompassing the gRNA site was amplified by PCR and amplicons were ligated into the commercially available pGEM®-T vector (Promega) by TA cloning. Ligation reactions were transformed into TOP10 chemically competent cells (Invitrogen™) and plated on LB agar plates containing ampicillin at 100 µg/ml, 40 µl 100mM IPTG and 120 µl 20 mg/ml X-gal spread onto the surface of the plate. In theory, picking sufficient numbers of colonies would enable the detection of variants or indels within the 3 *Ryr1* genes for each cell line. The total numbers of colonies processed for Sanger sequencing for cell lines 8G6, 2G7, 9H12, 1E6, 1C5 and 10G5 were 28, 17, 18, 27, 27 and 27, respectively. A proportion of the *Ryr1* TA clones picked for Sanger sequencing either did not contain the insert (8%), produced Sanger sequencing reads too short in length to detect the region of interest (17%), produced poor sequencing chromatograms from which the sequence could not be derived (34%) or the same editing events were detected multiple times (Table 4.10). As such, not all modifications on each of the 3 *Ryr1* genes across all cell lines were detected. The modifications that were detected revealed successful incorporation of the variant alleles, in addition to a range of mutational events that occurred due to gene-editing (Table 4.10). In cell line 2G7, a 7 bp 'CAGTCGC' deletion was detected that occurred 1 bp upstream of the Cas9 cut site and a near wild-type sequence was detected that contained a 1 bp C residue deletion at the Cas9 cut site (Figure 4.19; panel A and panel B). In cell line 9H12, another 7 bp

‘AGTCGCC’ deletion was detected that occurred directly at the Cas9 cut site (Figure 4.19; panel C). In addition, the same deletion was detected with an undesired G>A substitution 9 bp downstream of the Cas9 cut site (Figure 4.19; panel C). Complex editing events were detected in the 10G5 cell line, whereby 2 bp upstream and 5 bp downstream of the Cas9 cut site had been deleted. A partial p.D3986E HDR template had been inserted downstream of these deletions and upstream of the endogenous wild-type base to be edited (Figure 4.21). Consequently, this allele contained both the wild-type and edited base. A 37 bp deletion was also detected in cell line 10G5 that occurred directly at the Cas9 cut site (Figure 4.19; panel E). Finally, a 5 bp ‘GCCTC’ deletion was detected at the Cas9 cut site (Figure 4.19; panel G). The same 1 bp C residue deletion that was detected in cell line 2G7 was also detected in cell line 1E6 (Figure 4.19; panel B). In addition, cell line 1E6 contained a successfully incorporated p.D3986E HDR template and a wild-type unedited *Ryr1* (Figure 4.19; panel D and panel H). Cell line 1C5 contained the 1 bp C residue deletion, a successfully incorporated p.D3986E HDR template and a successfully incorporated wild-type HDR template (Figure 4.19; panel B, D and F). The same 37 bp deletion detected in 10G5 was detected in cell line 8G6 (Figure 4.19; panel E). In addition, a complex editing event was detected in 8G6 whereby a partial HDR fragment was present downstream of the Cas9 cut site and downstream of a 5 bp insertion (Figure 4.20).

Eight colonies were processed for Sanger sequencing for each of the p.S1728F cell lines. Cell line 6B4 had a successfully incorporated p.S1728F variant HDR template (Figure 4.22; panel A) and a 2 bp ‘AC’ insertion that occurred directly at the Cas9 cut site (Figure 4.22; panel B).

Table 4.10 – Summary of editing events detected in p.D3986E and p.S1728F cell lines

The number of times the editing event was detected in that cell line is shown in brackets.

Cell line	Allele 1	Allele 2	Allele 3
8G6	p.D3986E HDR fragment insertion* and T>C substitution (4)	37 bp deletion (5)	Not detected
2G7	7 bp deletion (1)	1 bp deletion (1)	Not detected
9H12	7 bp deletion and G>A substitution (1)	7 bp deletion (7)	Not detected
1E6	1 bp deletion (3)	p.D3986E variant** (7)	Wild-type unedited (4)
1C5	p.D3986E variant** (3)	1 bp deletion (6)	Wild-type HDR template *** (3)
10G5	5 bp deletion (1)	37 bp deletion (5)	p.D3986E HDR fragment insertion upstream of wild-type* (3)
6B4	p.S1728F variant* (1)	2 bp insertion (2)	Not detected
6F12	Not detected	Not detected	Not detected

* HDR template inserted erroneously.

** successful recombination and incorporation of the variant HDR template.

*** successful recombination and incorporation of the wild-type HDR template.

Figure 4.19 – Graphical representation of editing events detected in p.D3986E cell lines

The nature of the editing event and the cell lines in which it has been detected is shown above the diagrams. Wild-type sequences are shown in black, gRNA sequences are shown in orange, PAM sites are shown in green, silent mutations within the p.D3986E HDR template are shown in purple, the desired base change for introduction of the p.D3986E variant is shown in red and undesired substitutions are shown in pink. The Cas9 cut site is indicated by /. The 7 bp deletion in 9H12 (panel C) was also detected without the G>A substitution.

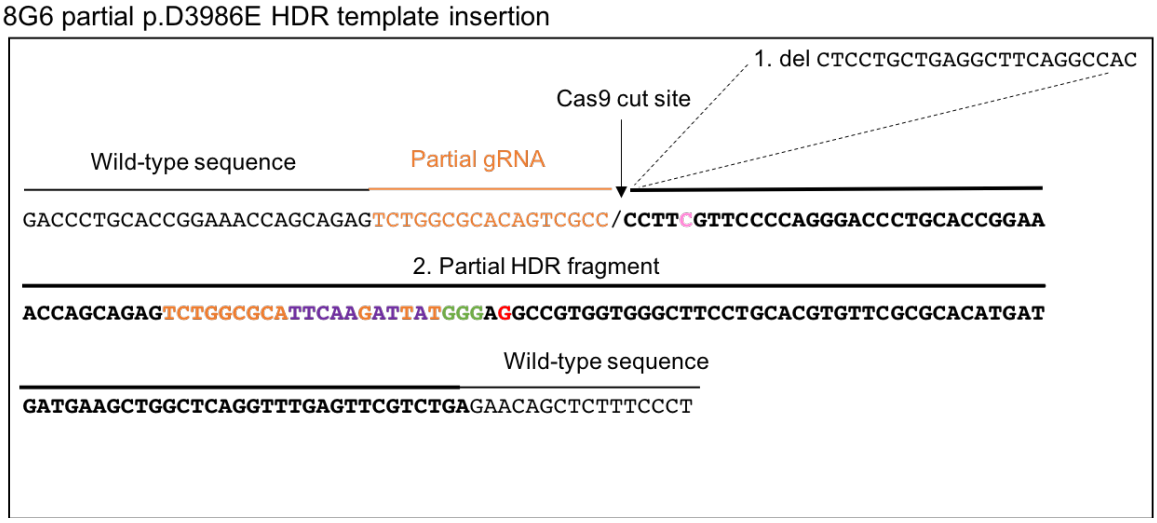

Figure 4.20 – Graphical representation of the HDR template insertion detected in p.D3986E cell line 8G6

Sanger sequencing of an 8G6 cell line TA clone revealed a partial insertion of the p.D3986E HDR template (shown in black, bold text), with a T>C substitution (pink) near the Cas9 cut site. Wild-type sequences are shown in black (not bold), gRNA sequences are shown in orange, silent mutations within the HDR template are shown in purple, the PAM site is shown in green and the desired base change is shown in red.

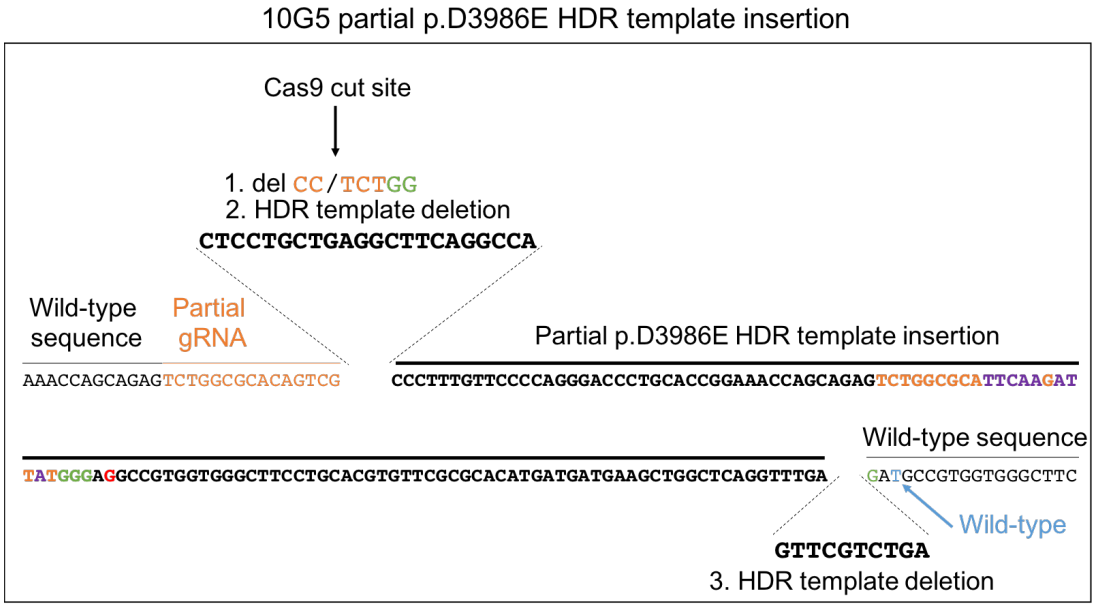

Figure 4.21 – Graphic representation of the partial HDR template insertion detected in the p.D3986E 10G5 cell line

Sanger sequencing of a 10G5 cell line TA clone revealed an insertion of a partial p.D3986E HDR template. Endogenous wild-type sequences are shown in black text (not bold). The gRNA sequences are shown in orange, the silent mutations within the p.D3986E HDR template are shown in purple, PAM sequences are shown in black. The partial HDR template insertion is shown in bold black text. The endogenous wild-type base to be edited is shown in blue and the edited variant base is shown in red. 1. Two bases upstream of the Cas9 cut site (indicated by an arrow and /) had been deleted in addition to 5 bp downstream of the Cas9 cut site. 2. A 22 bp deletion at the start of the p.D3986E HDR template was detected. 3. The final 10 bp of the HDR template were also deleted. The remaining fragment of the p.D3986E HDR template was inserted upstream of the endogenous C2C12 wild-type sequence (wild-type base is shown in blue).

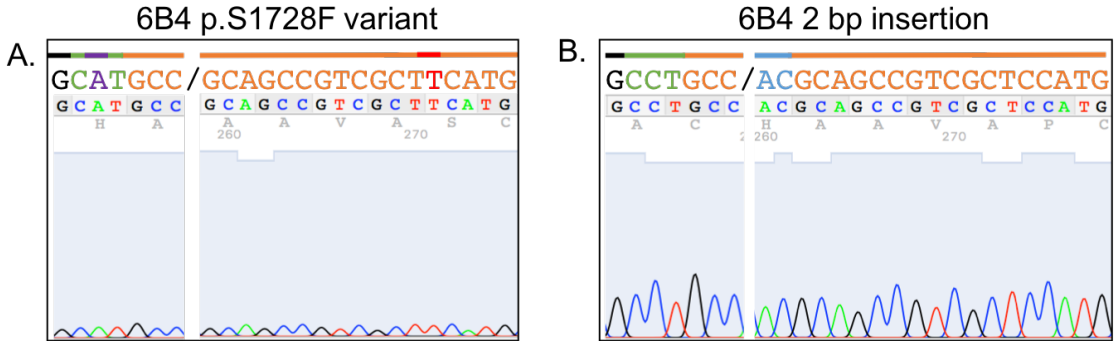

Figure 4.22 – Editing events detected in the p.S1728F 6B4 cell line

The nature of the editing event is shown above the diagrams. Wild-type sequences are shown in black, gRNA sequences are shown in orange, PAM sites are shown in green, silent mutations within the p.S1728F HDR template are shown in purple, the desired base change for introduction of the p.S1728F variant is shown in red and insertions are shown in blue. The Cas9 cut site is indicated by /.

4.2.11.2 Sanger sequencing of *in-silico* predicted off-target sites for p.D3986E and p.S1728F cell lines

The top 10 off-target sites predicted by CCTOP and CRISPOR were selected for PCR amplification and Sanger sequencing to detect off-target activities within the resultant cell lines. All p.D3986E cell lines with the exception of 9H12 (which did not survive liquid nitrogen resuscitation) were sequenced at selected off-target sites. For Mm_D3986E_gRNA2, CCTOP and CRISPOR shared 2 (Smtnl-Ggt6 and Nkx6-2) off-target sites within the top 10 predicted off-targets. Of the 18 off-target sites to be sequenced, PCR primers were unable to be designed for 3 (Hspg2; GC content of the surrounding region was 75%), Gm5385; surrounding region was repetitive and Pfdn1-Hbergf; surrounding region was repetitive), 1 (Smtnl-Ggt6; surrounding region was repetitive) failed to produce amplicons despite repeated attempts and the use of alternative primers and 2 (RP23-267G12.1 and Gm3898; both within highly repetitive regions) did not produce clear Sanger sequencing traces despite repeated attempts. All of the remaining 12 off-target sites that were sequenced across the 1C5, 1E6, 2G7, 8G6 and 10G5 cell lines showed wild-type sequences (all p.D3986E off-target Sanger sequencing traces can be found in Appendix A), with the exception of the Optn and 6030407O03Rik sites for which the 2G7 sequencing reactions failed. For the Med23 off-target site, dye blobs at ~70 bp were present within the off-target sequences; however, the

wild-type sequences were still distinguishable beneath the dye blob (Figure 4.23).

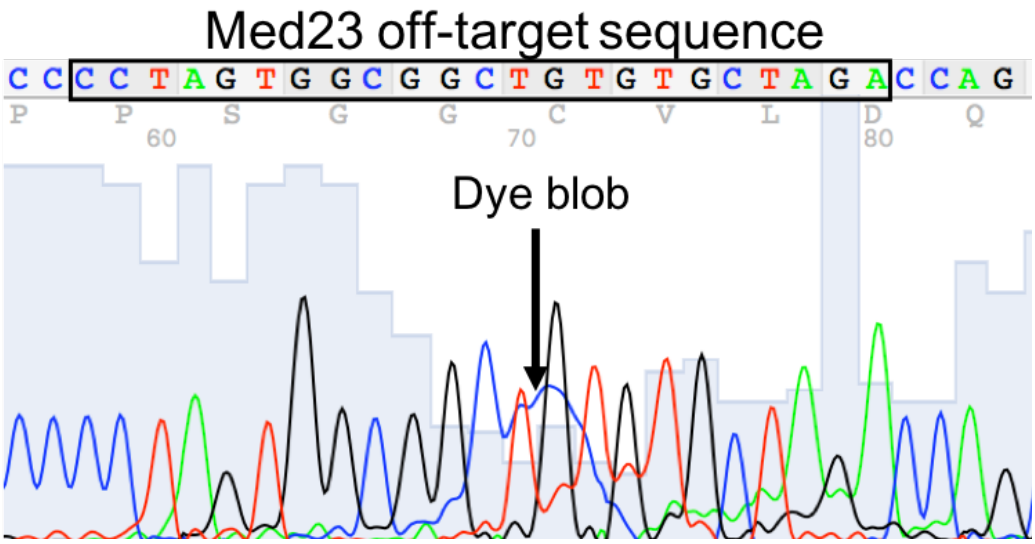

Figure 4.23 – Example of dye blob present within the Med23 off-target sequence

DNA was extracted from each of the p.D3986E cell lines. A region around the *in-silico* predicted Med23 off-target site was amplified by PCR and the amplicon processed for Sanger sequencing. The sequencing chromatogram was analysed in 4Peaks (Nucleobytes, Amsterdam, Netherlands). The off-target sequence is shown within a black box and the presence of a dye blob at ~70 bp indicated by an arrow.

As described for Mm_D3986E_gRNA2 off-targets, the top 10 off-target sites for Mm_S1728F_gRNA2 from CCTOP and CRISPOR were selected for sequencing. The two programs shared 4 off-target sites within their respective top 10 predicted sites (Zhx2, Rpgrip1l, 2310022B05Rik and Dusp26). Primers were unable to be designed for CCTOP-predicted sites Grm4 (GC content 77%) and Asmt (GC content 78% and the sequence downstream of the target site was incomplete in the GRCm38/mm10 genome). Since there was considerable overlap within the top 10 sequences, an additional 2 off-target sequences were selected from the 11th and 12th predicted sites by CRISPOR (Hmcn2 and Scara5). All off-target sites that were sequenced for cell lines 6B4 and 6F12 were wild-type, with the exception of Ptprs for both cell lines which failed to produce clear Sanger sequencing traces (GC content 77%). Sequencing traces for the Aqp9-Aldh1a2 site in cell line 6B4 had a dye blob between 130 and 140 bp; however, the wild-type sequence was still

distinguishable (all p.S1728F off-target Sanger sequencing traces can be found in Appendix B).

4.2.11.3 Differentiation of single cells into myotubes

Cells were plated at ~2 x 10^4 cells per well of a 96-well plate coated with Extracellular Matrix (ECM) Gel from Engelbreth-Holm-Swarm murine sarcoma (Sigma Aldrich). The following day, media was changed to differentiation media and replaced every other day for 5-6 days. Of the 6 p.D3986E single-cell derived lines obtained, only 10G5 and 8G6 formed myotubes following 5 days of differentiation (Figure 4.24). Myotube diameter and length was generally comparable between all cell lines; however, there appeared to be a greater proportion of smaller myotubes in cell lines 3E1 and 8G6.

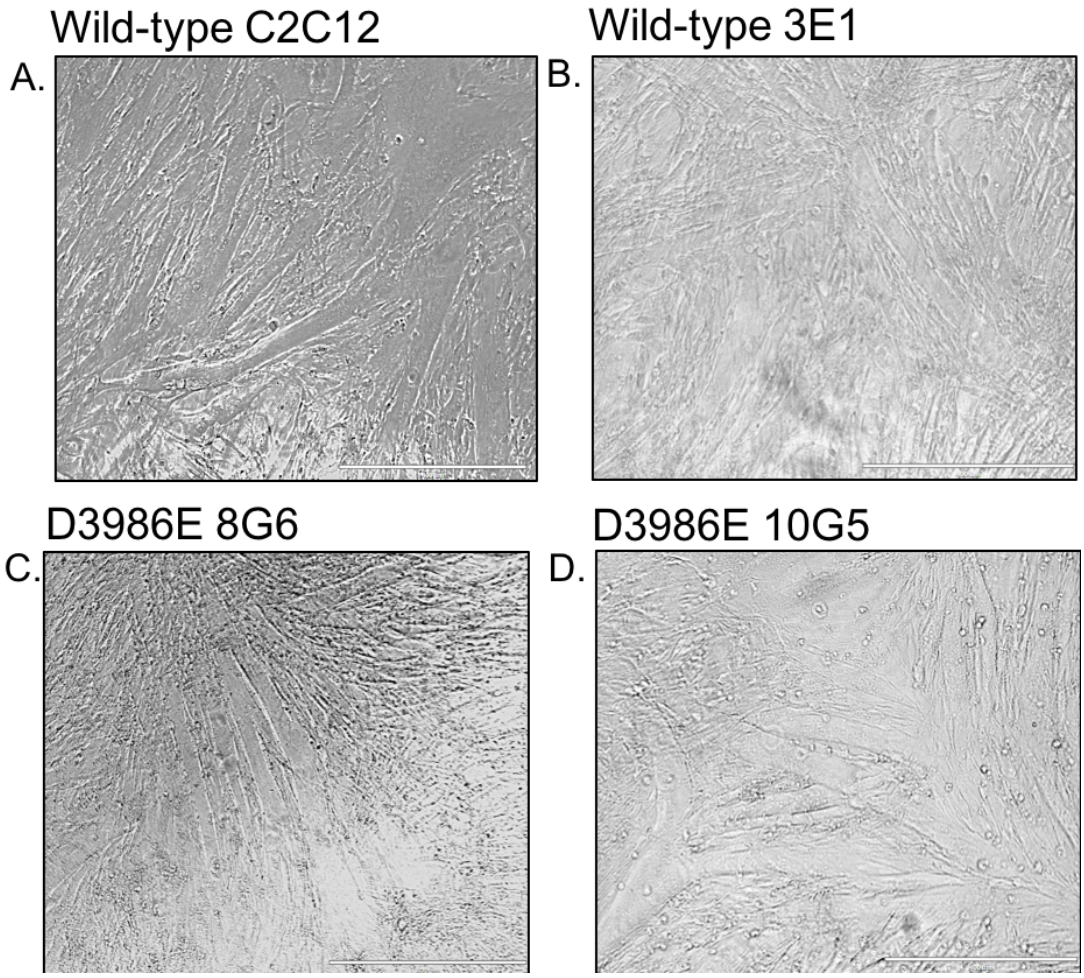

Figure 4.24 – C2C12 and p.D3986E derivative cell lines following 5 days of differentiation

Polyclonal wild-type C2C12 cells (panel A), monoclonal wild-type C2C12 3E1 cells (panel B) and the p.D3986E derivatives (panels C and D) were plated on ECM Gel (Sigma Aldrich) coated plates and differentiated for 5-6 days with media replaced every other day. Images were captured using the EVOS^{TM} FL imaging system (ThermoFisher) with a 10x objective. The scale bar (bottom right) indicates 400 uM.

Neither of the p.S1728F cell lines differentiated in a manner comparable to wild-type C2C12 cells. At 5 days post differentiation, following plating at 2 x 10^4 cells per well of a 96-well plate, both 6B4 and 6F12 became confluent and it was difficult to distinguish between individual cells. No elongated structures were observed for the 6B4 cell line. For 6F12, elongated cells were observed (Figure 4.25; panel A and C); however, these did not appear to be multinucleated and were considerably smaller than myotubes observed for other cells (Figure 4.24). Since plating at 2 x 10^4 resulted in overly confluent cells, plating at 5 x 10^3 prior to differentiation was attempted. Again, cell line

6B4 showed no evidence of myotube formation and the elongated cells observed in the 6F12 cell line were smaller than those observed for other cell lines in both length and diameter (Figure 4.25; panel B and D).

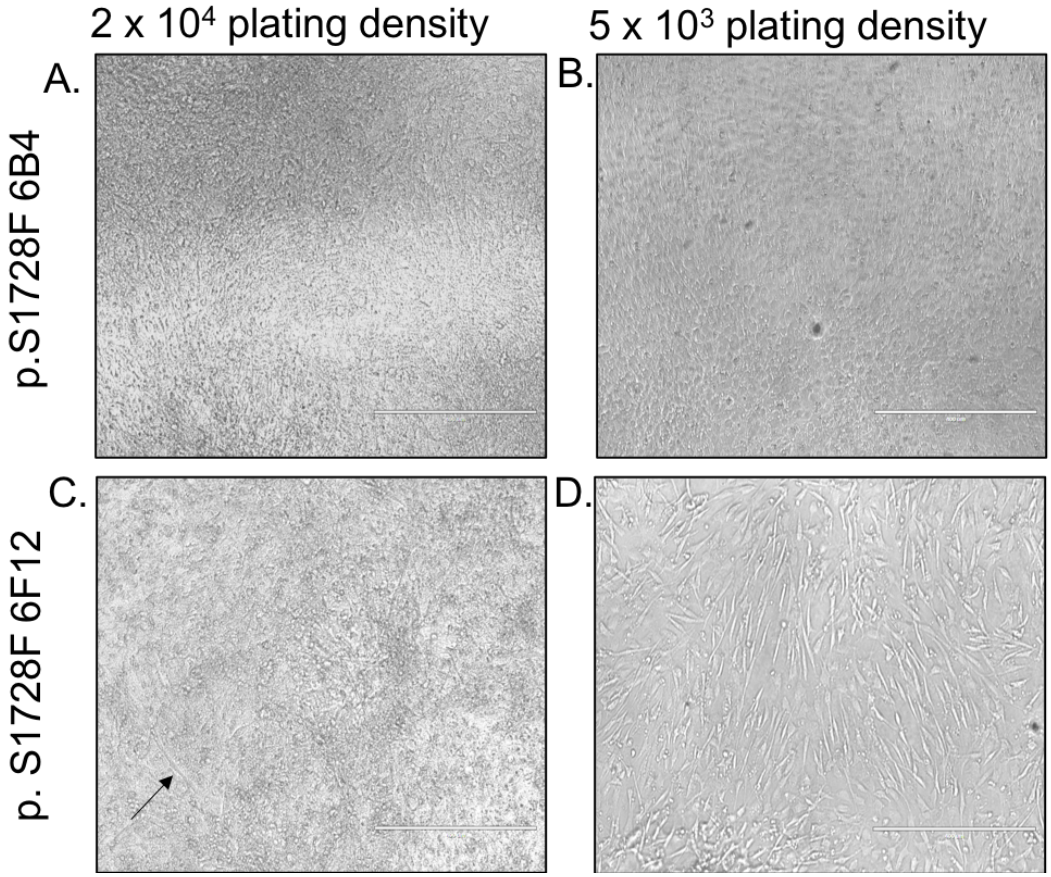

Figure 4.25 – p.S1728F cell lines following 5 days of differentiation

The p.S1728F cell lines 6B4 and 6F12 were plated at 2 x 10^4 cells (panels A and C) and 5 x 10^3 (panels B and D) per well of a ECM Gel (Sigma Aldrich) coated 96-well plate. Cells were incubated for 24 hours (37°C, 5% CO_2) prior to the replacement of growth media with differentiation media. Differentiation media was changed every other day for up to 5 days. An arrow indicates where an elongated structure was observed for 6F12 cells plated at a density of 2 x 10^4 (panel C). Images were captured using the EVOS™ FL imaging system (ThermoFisher) with a 10x objective. The scale bar (bottom right) indicates 400 uM.

4.2.12 Determination of caffeine sensitivity of edited cell lines

4.2.12.1 p.D3986E cell lines caffeine EC_{50} analysis

Wild-type C2C12 myoblasts and the 3E1, 8G6 and 10G5 cell lines were plated at 2 x 10^4 cells per well of ECM Gel from Engelbreth-Holm-Swarm murine sarcoma-coated black, clear bottom 96-well plates. The following day, with myoblasts at ~90% confluency, growth factors were depleted by replacing growth media with differentiation media to encourage the formation of myotubes (Clegg et al., 1987). On days 5 or 6, myotubes were loaded with Fluo-8 AM (Abcam) to a final concentration of 10 µM with 0.04% Pluronic® F-127 acid. Following loading, cells were equilibrate at room temperature in imaging buffer for 20 min prior to experiments. The washes and equilibration step at room temperature allow for the removal of extracellular dye and redistribution of compartmentalised dye within the cell (Paredes et al., 2008). Prior to Ca^{2+} imaging, a caffeine series was prepared in imaging buffer to final concentrations of 0.1 mM, 1 mM, 3 mM, 5 mM, 10 mM and 20 mM and warmed, along with calcium imaging buffer, to 37^{o}C. Caffeine-induced Ca^{2+} release was observed as transient increases in fluorescence following perfusion, detected using the Nikon TE2000 inverted microscope attached an intensified CCD camera (Figure 4.26). Cells were allowed to rest for 1 min between caffeine doses.

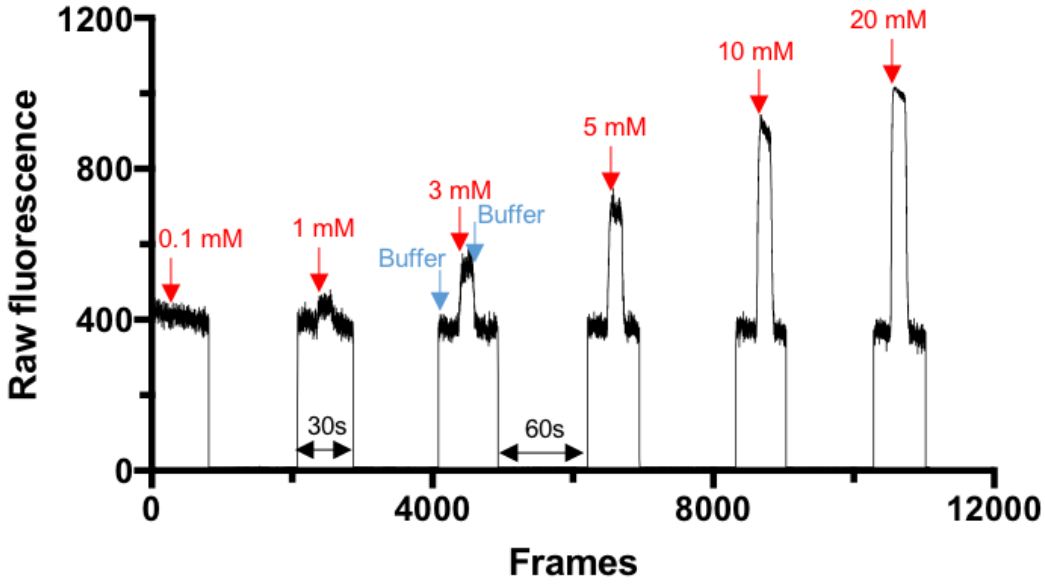

Figure 4.26 – Example of a caffeine-evoked Ca^{2+} transient trace

Cells loaded with Fluo-8 AM (Abcam) were perfused for 10 seconds with imaging buffer, 10 seconds with caffeine at the desired concentration and 10 seconds with imaging buffer (total of 30 seconds perfusion). Increases in Ca^{2+} are observed as increases in raw fluorescence values measured in arbitrary fluorescence units (Y axis). Recordings were made at a rate of 20 frames per second (the number of frames is shown on the X-axis). Cells were allowed to equilibrate in imaging buffer for approximately 60 seconds following caffeine exposure. The fluorescence light source was turned off after fluorescence had reached baseline again following caffeine exposure to avoid photobleaching, hence fluorescence values decreased to 0 between application of each caffeine concentration. Recordings were made using Piper Control™ Acquisition Software (Stanford Photonics, Inc).

The sensitivity of each cell line to caffeine was determined by the half maximal effective concentration (EC_{50}). EC_{50} values were generated by performing two separate analyses. Baseline measurements of fluorescence prior to each application of caffeine in the dose response experiment were taken by averaging fluorescence values for 20 frames (1 second) prior to caffeine application. The first analysis measured the increase in fluorescence from baseline, determined by the maximum peak height for each caffeine-induced peak. The second analyses utilised area under the curve (AUC) measurements for each caffeine-induced peak.

To account for variability in the magnitude of fluorescence response between individual myotubes, peak height and AUC measurements for each caffeine-

induced peak were normalised to the maximal response at 20 mM caffeine of that myotube. For both analyses, cells that did not show a dose-dependent increase in fluorescence and/or did not respond to concentrations ≥3 mM were excluded from the analysis. Furthermore, cells showed a minor, yet significant, negative correlation of baseline fluorescence values and EC_{50} values (correlation coefficient (r) -0.2125; 95% CI -0.2889 to -0.1334; p<0.0001), whereby cells with lower and higher baseline fluorescence values were correlated with higher and lower EC_{50} values, respectively (Figure 4.27). The negative correlation was more pronounced at fluorescence values <50 and >600, with cells between these values showing less variation in EC_{50} values. A small number of cells (7) with fluorescence values between 50 and 100 clustered at higher EC50s (9-12 mM) alongside cells with fluorescence values <50; however, these cells accounted for a small proportion of the total cells in the correlation analysis (588). Thus, cells with initial baseline fluorescence values <50 and >600 were also excluded from the analysis. Determination of statistical significance was performed using one-way analysis of variance (ANOVA) and Tukey's test for multiple comparisons (Tukey, 1949).

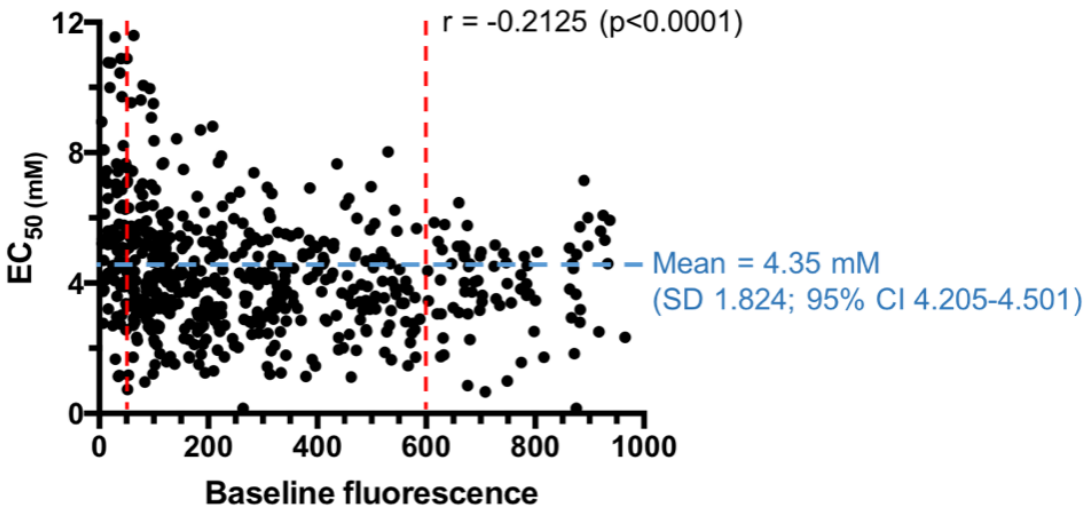

Figure 4.27 – Correlation of baseline fluorescence values and EC_{50} values

A Pearson correlation test was performed using EC_{50} (Y axis) and average baseline fluorescence values (X axis) for 588 myotubes that showed dose dependent increases in fluorescence. The correlation co-efficient (r) was significant (p<0.0001). Cells outside of the dashed red lines were excluded from the analysis and the dashed blue line shows the mean EC_{50} value (SD; 95% CI).

Analysis of peak height data showed that polyclonal wild-type C2C12 cells had a mean EC_{50} of 5.388 mM (SD 2.328; 95% confidence interval (CI) 5.094 to 5.697) (Figure 4.28; panels A and B). The monoclonal wild-type 3E1 cell line was similar to wild-type C2C12 cells, with an EC_{50} of 5.009 mM (SD 1.627; 95% CI 4.744 to 5.288). There was no significant difference between the polyclonal wild-type C2C12s and the monoclonal wild-type 3E1 line (p=0.6185). The p.D3986E 8G6 cell line had an EC_{50} of 3.776 (SD 0.8779; 95% CI 3.599 to 3.96) and the p.D3986E 10G5 cell line had an EC_{50} of 3.311 (SD 1.943; 95% CI 3.085 to 3.543). The EC_{50} values for 8G6 and 10G5 were both significantly reduced compared to polyclonal wild-type C2C12 cells ($p<0.0001$) and the monoclonal wild-type 3E1 cell line (8G6 p=0.0043; 10G5 p=0.001). While the EC_{50} of 8G6 was greater than that of 10G5, this was not statistically significant (p=0.9721).

The EC_{50} values generated from AUC analysis followed a similar pattern to those generated in the peak height analysis (Figure 4.28; panels C and D). Wild-type C2C12 cells had an EC_{50} of 6.232 mM (SD 2.386 ; 95% CI 5.9 to 6.582) and the 3E1 cell line had an EC_{50} of 6.283 mM (SD 1.538; 95% CI 6.01 to 6.568) with no statistically significant difference between the EC_{50} values for the two cell lines (p=0.9732). The p.D3986E cell line 8G6 had an EC_{50} of 5.092 mM (SD 1.04; 95% CI 4.857 to 5.337) and the 10G5 cell line had an EC_{50} of 4.04 mM (SD 1.839; 95% CI 3.813 to 4.276). The mean EC_{50} values for both 8G6 and 10G5 were significantly statistically different to wild-type (8G6 p=0.0011; 10G5 $p<0.0001$) and 3E1 (8G6 p=0.0127; 10G5 $p<0.0001$) but there was no statistically significant difference in EC_{50} values between 8G6 and 10G5 (p=1.839).

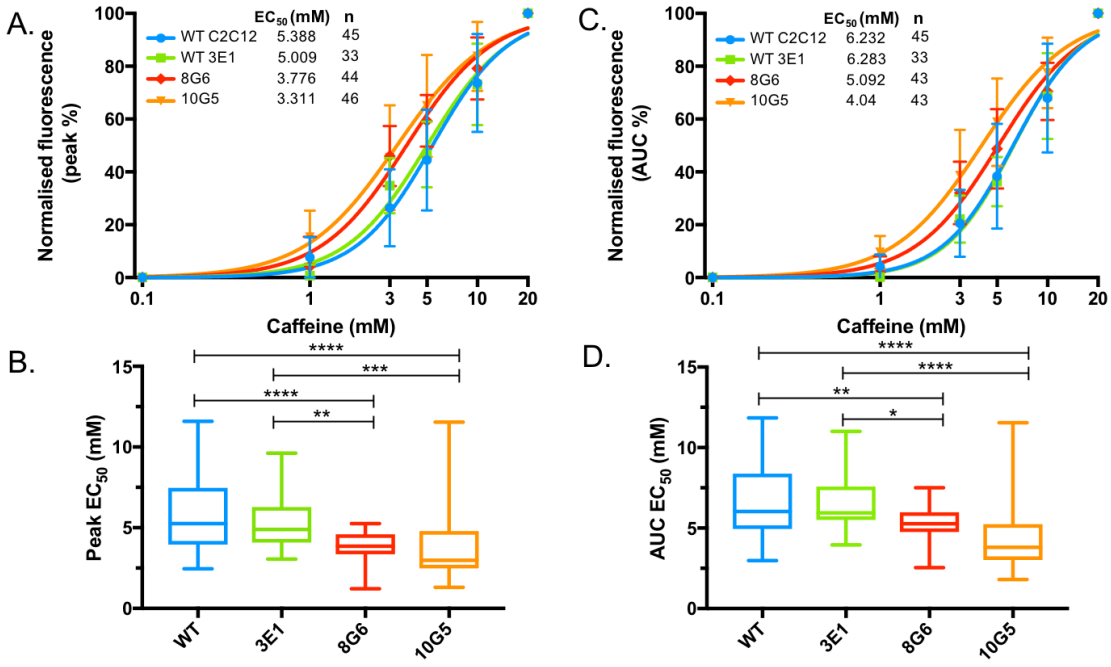

Figure 4.28 – Caffeine dose-response analysis of Ca^{2+} imaging of wild-type C2C12 cells and p.D3986E derivatives

Panels A and C show the peak and AUC sigmoidal dose-response analysis, respectively, of wild-type C2C12s (blue circles), wild-type 3E1 cells (green squares), 8G6 (red diamonds) and 10G5 (orange triangles). Normalised fluorescence (a percentage of the maximal response at 20 mM caffeine) is shown on the Y axis and the caffeine concentration (mM) is on the X axis. Peak height data points are means of 33-46 myotubes and AUC data points are means of 33-45 myotubes (plated and imaged on at least 3 different days, with the exception of 3E1 from which data was collected on 2 different days) and error bars show the SD. Panels B and D show box plots of the peak and AUC EC_{50} values, respectively. Box plots show the median data point, upper and lower quartiles and the minimum and maximum data points. Curves were fitted and graphs plotted using Prism 7 (GraphPad). One-way ANOVA and Tukey's test for multiple comparisons were used to determine significance. *p<0.05, **p<0.01, ***p<0.001, ****p<0.0001.

Values of the mean peak percentage maximal response (%MR) at each caffeine concentration are shown in Figure 4.29; Panel A. Wild-type C2C12 cells and cell line 3E1 responded to caffeine similarly at all concentrations, as did cell lines 8G6 and 10G5 with the exception of at 1 mM caffeine. The %MR of wild-type polyclonal C2C12 cells was 7.698% at 1 mM caffeine. In contrast, the %MR of cell line 3E1 was 0.7449 and was significantly different to wild-type C2C12 (p= 0.0046). Cell line 8G6 had a %MR of 4.225, which was not significantly different to wild-type C2C12 (p=0.2654) or 3E1 (p=0.3347). Cell

line 10G5 had %MR of 14.92%, which was significantly different to wild-type C2C12 ($p=0.0006$), 3E1 ($p<0.0001$) and 8G6 ($p<0.0001$).

At 3 mM caffeine, %MR was 26.39 for wild-type C2C12 cells, 34.76 for 3E1, 46.01 for 8G6 and 46.08 for 10G5. There was a significant difference between the %MR for wild-type C2C12 cells and cell lines 8G6 ($p <0.0001$) and 10G5 ($p <0.0001$). Furthermore, there was a significant difference between 3E1 and cell lines 8G6 ($p=0.0090$) and 10G5 ($p=0.0058$). There was no significant difference between wild-type C2C12 and 3E1 at 3 mM caffeine ($p=0.0808$), nor was there a significant difference between 8G6 and 10G5 at 3 mM caffeine ($p>0.9999$).

At 5 mM caffeine, the %MR of wild-type C2C12 cells was 44.49 and the %MR of 3E1 cells was 46.58, with no significant difference between the two ($p= 0.9430$). The %MR of 8G6 and 10G5 at 5 mM caffeine was 59.33 and 64.53, respectively. Like 3 mM caffeine, there was no significant difference in %MR between 8G6 and 10G5 ($p= 0.4134$). The %MR for cell line 8G6 was significantly different to both wild-type C2C12 ($p= 0.0002$) and cell line 3E1 ($p=0.0048$). Similarly, the %MR for cell line 10G5 was significantly different to both wild-type C2C12 ($p <0.0001$) and cell line 3E1 ($p<0.0001$).

At 10 mM caffeine, the %MR of wild-type C2C12 cells was 73.64 and 3E1 was 73.13, with no significant difference between the two cell lines ($p=0.9987$). The %MR of 8G6 was 79.13, which was not significantly different to wild-type C2C12 cells ($p=0.3031$), 3E1 ($p=0.2965$) or 10G5 ($p=0.3206$). The percentage release of 10G5 cells was 84.35 and this was significantly different to wild-type C2C12 cells ($p=0.0028$) and 3E1 cells ($p=0.0045$).

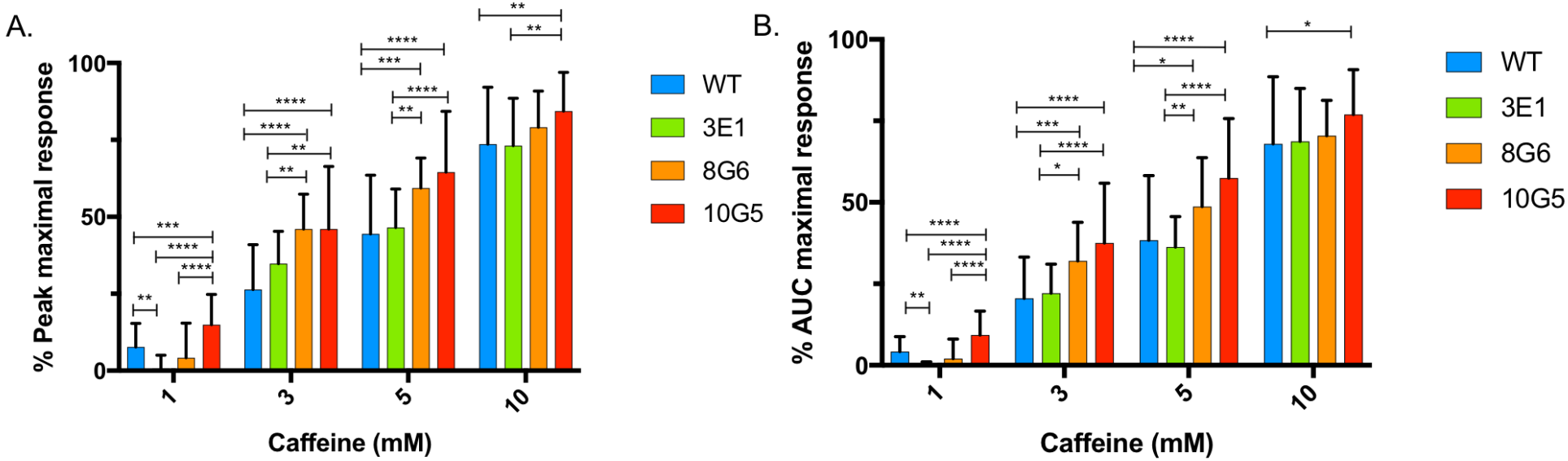

Figure 4.29 – Peak and AUC percentage maximal response of p.D3986E and wild-type C2C12 at 1, 3, 5 and 10 mM caffeine

The peak (panel A) and AUC (B) percentage maximal response of each cell line at 1 mM, 3 mM, 5 mM and 10 mM caffeine. Baseline fluorescence values were calculated from an average of 20 frames prior to caffeine perfusion at each dose. Baseline was used to define peaks for the AUC analysis and was subtracted from the peak height increase in fluorescence for the peak height analysis. The resultant values for each caffeine concentration were calculated as a percentage of the maximal response at 20 mM caffeine. Data are shown as the mean (33-46 cells in the peak analysis; 33-45 cells in the AUC analysis) and error bars are the SD. One-way ANOVA and Tukey's test for multiple comparisons were used to determine significance. *p<0.05, **p<0.01, ***p<0.001, ****p<0.0001.

The %MR at each caffeine concentration from AUC analysis followed a similar pattern the data gleaned from peak height analysis (Figure 4.29; Panel B). Again, wild-type C2C12 cells and cell line 3E1 responded in a similar manner throughout the dose response experiment, as did cell lines 8G6 and 10G5, with the exception of at 1 mM caffeine. At 1 mM caffeine, polyclonal wild-type C2C12 cells had a %MR of 4.233. Cell line 3E1 had a %MR of 0.1552, which was significantly different to wild-type C2C12 ($p=0.0090$). Cell line 8G6 had a %MR of 2.001, which was not significantly different to wild-type C2C12 or 3E1 cells ($p=0.2410$). Cell line 10G5 had a %MR of 9.296 which was significantly different to wild-type C2C12 ($p<0.0001$), 3E1 ($p<0.0001$) and 8G6 ($p<0.0001$).

At 3 mM caffeine, wild-type C2C12 cells and cell line 3E1 had %MRs of 20.55 and 22.13, which were not significantly different to each other ($p=0.9602$). In contrast, cell line 8G6 had a %MR of 32.06, which was significantly different to 3E1 ($p=0.0130$) and wild-type ($p=0.0009$). Cell line 10G5 had a %MR of 37.54 which was not significantly different to 8G6 ($p=0.2224$) but was significantly different to wild-type C2C12 ($p<0.0001$) and 3E1 (<0.0001).

At 5 mM caffeine, wild-type C2C12 cells and 3E1 had %MRs of 38.41 and 36.33. As found at previous caffeine concentrations, these values were not significantly different ($p=0.9477$). Cell line 8G6 and 10G5, with %MRs of 48.74 and 57.45 were significantly different to both wild-type C2C12 (8G6 p.= 0.0207; 10G5 $p<0.0001$) and 3E1 (8G6 $p=0.0080$; 10G5 $p<0.0001$), but not to each other ($p=0.0541$).

At 10 mM caffeine, wild-type C2C12, 3E1, 8G6 and 10G5 had %MRs of 67.94, 68.7, 70.44 and 76.98, respectively. The %MR of wild-type C2C12 cells was not significantly different to 3E1 ($p=0.9967$) or 8G6 ($p=0.8772$) but was significantly different to 10G5 ($p=0.0244$). Cell line 3E1 was not significantly different to 8G6 ($p=0.9633$) or 10G5 ($p=0.0821$). Finally, the %MR of cell line 8G6 was not significantly different to that of cell line 10G5 ($p=0.1762$).

4.2.12.2 p.D3986E cell lines raw fluorescence increase from baseline observations

Between myotubes, the magnitude of raw fluorescence increases from baseline in response to caffeine perfusion was variable. On average, wild-type

C2C12 and cell line 10G5 consistently produced greater increases in raw FUs following caffeine perfusion than 3E1 and 8G6 (Figure 4.30). This was observed at all caffeine doses. For example, where 20 mM caffeine was perfused, the mean increase in raw FUs from baseline following perfusion for wild-type C2C12s was 648.3 (SD 252.2; 95% CI 575.1-721.5). This was significantly different to cell line 8G6, which had a mean increase of 168.5 FUs (SD 71.27; 95% CI 144-193; $p<0.0001$) and cell line 3E1, which had a mean increase of 194.2 FUs (SD 95.96; 95% CI 161.3- 227.2; $p<0.0001$). There was no significant difference between wild-type C2C12 and 10G5 which had a mean increase in raw FUs of 672.9 (SD 224.3; 95% CI 613.4- 732.4; $p= 0.9136$). The response of cell line 3E1 was not significantly different to 8G6 ($p= 0.9434$) but was significantly different to 10G5 ($p<0.0001$). Finally, the magnitude of the responses of cell lines 8G6 and 10G5 was also significantly different ($p<0.0001$). It should be noted that the reduced response at 1 mM caffeine in cell lines 3E1 and 8G6 is likely a result of the low magnitude responses not producing peaks 10% greater than baseline; as such, these peaks would not have been detected during data analysis (Figure 4.29).

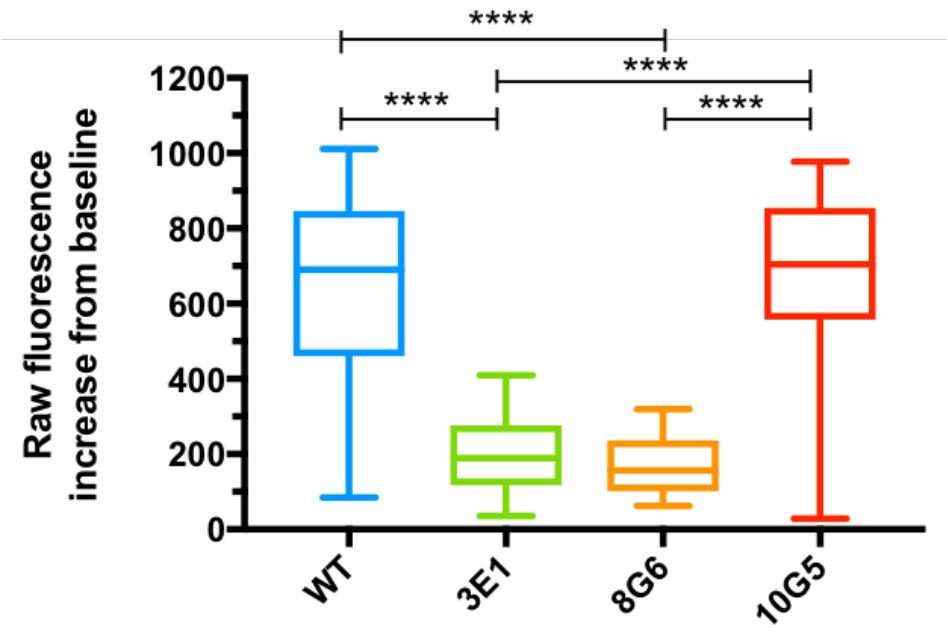

Figure 4.30 – Mean raw fluorescence increases in response to 20 mM caffeine for p.D3986E lines and wild-type C2C12 cells

Baselines were calculated for each myotube by averaging fluorescence values for 20 frames (1 second) prior to perfusion with 20 mM caffeine. Baseline measurements were subtracted from the peak height measurement for each myotube, to generate the raw fluorescence increase. Raw fluorescence increases were averaged across 33-46 genotypes per cell line, generating the mean raw fluorescence increase in response to 20 mM caffeine. The 20 mM caffeine dose has been used for reference; however, the pattern was the same across all caffeine doses. Box plots show the median data point, upper and lower quartiles and the minimum and maximum data points. One-way ANOVA and Tukey's test for multiple comparisons were used to determine significance. ****$p<0.0001$.

The differences in the magnitude of response from baseline between genotypes could reflect reductions in the number of SR in cell lines 3E1 and 8G6. In agreement with that, it was observed that cell lines 3E1 and 8G6 produced a greater proportion of smaller myotubes than 10G5 and wild-type C2C12 cells; however, these were still elongated and multinucleated (Figure 4.24). Furthermore, differences in magnitude of the response were not associated with different mean EC_{50} values within genotypes. Analysis of the EC_{50} values generated when myotubes had raw baseline increase fluorescence values that were low (defined as <200 FU) and high (defined as >=200 FU) showed no significant difference in EC_{50} values between the low and high groups, in any of the genotypes (WT $p>0.999$ low n=5 and high n=40;

3E1 p=0.0884 low n=16 and high n=17; 8G6 p=0.9505 low n=24 and high n=20; cell line 10G5 was not included in this analysis since the low group had n=1). Indeed, all responses were normalised to the maximum of that myotube for the EC_{50} analysis.

4.3 Discussion

The primary aim of this chapter was to introduce the p.D3986E and p.S1728F variants into C2C12 myoblasts with the view to determine the sensitivity of the resultant cell lines to caffeine by Ca^{2+} imaging. Whilst a number of cell lines were generated that contained the variants of interest, the work presented in this chapter has been unable to conclusively determine the functional significance of the RYR1 p.D3986E and p.S1728F variants due to complex mutational patterns induced by the NHEJ and HDR DNA repair mechanisms. Nonetheless, this work provides a substantial foundation for the introduction of MH-associated VUS into C2C12 myoblasts using CRISPR-Cas9 gene-editing, in the first study of its kind within the MH field. Importantly, this work has highlighted the complexity of the gene-editing events that can occur as a result of CRISPR-Cas9 gene-editing and the limitations associated with the use of myoblasts that must be considered for future work in developing a CRISPR-Cas9 pipeline for the functional characterisation of MH-associated VUS.

4.3.1 Evaluation of the CRISPR-Cas9 genome editing strategy

In theory, the apparent polyploidy of C2C12 cells does not pose a major issue with regard to functional characterisation. Successful incorporation of the variants of interest by HDR in varying copy numbers of 1 to 3 would provide insight into the gene dosage effect of the variant of interest following Ca^{2+} imaging. Practically, the main complication of using polyploid C2C12 cells was the determination of editing events on each copy of the mouse *Ryr1* gene. Whilst the TaqMan™ genotyping assays utilised in this chapter provided an effective screening tool for the detection of cell lines containing the variant of interest, the utility of the assays in determining the composition of each allele was limited. Unlike TaqMan™ gene expression assays, the genotyping assays are designed to optimise single nucleotide specificity over reaction efficiency

(Hui et al., 2008). As a result, cycle threshold (Ct) values cannot be used to determine copy number and the Genotyping Module assigns genotype calls based on cluster orientation and the end-point ratios of the VIC™ (allele 1; wild-type) and FAM™ (allele 2; variant) reporter dyes, measured by dRn values. Given this, dRn ratios were compared to infer the genotype of vector clusters that appeared following genotyping. The extrapolations from the genotyping assay were supported by TA cloning and subsequent Sanger sequencing data.

In cell line 8G6, editing events detected by Sanger sequencing account for one of the variant alleles detected by the genotyping assay. The 37 bp deletion in 8G6 would have removed the TaqMan™ probe site; as such, this allele would not have been detected by the genotyping assay. Further sequencing analysis is required to determine the composition of the third allele; however, it is plausible that this allele has undergone a complex editing event whereby the p.D3986E variant has been incorporated whilst maintaining the wild-type sequence, accounting for the dRn ratios observed in the genotyping assay. Accordingly, an editing event that resulted in the wild-type and variant p.D3986E sequences on a single chromosome was detected in cell line 10G5. Similarly to cell line 8G6, the 37 bp deletion in cell line 10G5 would have removed the TaqMan™ probe site. Identification of a small 5 bp deletion on the third *Ryr1* allele in cell line 10G5 accounts for the second wild-type allele identified by the genotyping assay.

Combining genotyping and Sanger sequencing for cell line 2G7 suggests that it has two copies of both the wild-type and variant alleles, since dRn ratios were 1:1.5 wild-type allele to variant allele and two editing events that would have been identified as wild-type by the genotyping assay were detected. The composition of the third allele was not been detected; however, it may have undergone a complex editing event that resulted in two copies of the p.D3986E variant allele.

The dRn values for cell line 9H12 could be indicative of a single copy of each allele, with the remaining allele unable to be amplified due to the presence of

an additional mutation or deletion within the TaqMan™ probe sequence. TA cloning revealed a 7 bp deletion in cell line 9H12 that would have been identified as wild-type by the genotyping assay. In one case, this deletion was followed by a G>A substitution within the TaqMan™ probe sequence. Since TaqMan™ genotyping assays are designed to discriminate between a single base, this substitution would prevent hybridisation of the wild-type probe. Whilst this would account for the detection of just two alleles by the genotyping assay, it is important to consider that this could be an error introduced by PCR of the region of interest. Further sequencing to detect the composition of the remaining allele(s) would determine whether this is a genuine mutation or an error. If the G>A substitution was found to be a technical error, a large deletion that removed the TaqMan™ probe sequence would account for a single copy of variant and wild-type alleles. Alternatively, 9H12 could contain two copies of each allele that could have been introduced by complex editing events such as those observed in 8G6 and 10G5. All three alleles identified by the genotyping assay have been accounted for by Sanger sequencing data for cell lines 1E6 and 1C5.

For the p.S1728F genotyping assay, dRn values were considerably lower than that of the p.D3986E assay, with allele 1 dRn values for wild-type C2C12s of 1.565 in the p.D3986E assay and 0.544 in the p.S1728F assay. This likely reflects an inherent property of the TaqMan™ probe sequences in the p.S1728F assay, since the same wild-type DNA was used in both the p.S1728F and p.D3986E assays. Since both assays were custom designed and non-human, they were not functionally validated by the supplier prior to this experiment. Nonetheless, the p.S1728F assay detected two cell lines that contained the variant. The comparison of dRn ratios and cluster orientations suggested that both cell lines have a single copy of the p.S1728F variant. The 6F12 cell line had a 2:1 ratio of allele 1 (wild-type) to allele 2 (variant); whereas the 6B4 cell line had a 1.5:1 ratio of allele 1 to allele 2. Two editing events, a successful incorporation of the p.S1728F HDR template and a 2 bp insertion at the Cas9 cut site, were detected in cell line 6B4. These editing events account for the variant and wild-type allele detected by the genotyping assay; however, there was insufficient data to conclude whether cell line 6B4 has another wild-

type allele or whether a deletion of the TaqMan™ probe sequence resulted in the detection of only 2 alleles by the genotyping assay. No further information was obtained from Sanger sequencing of the TA clones picked from 6F12 vectors, either due to poor sequencing quality or the clones not containing the insert.

In conclusion, the TaqMan™ genotyping assays served their function as low-cost, moderate-throughput screening tools to robustly detect cell lines containing the variant of interest. The comparisons of dRn ratios between alleles was largely supported by Sanger sequencing data; however, when dRn ratios are roughly equal, it is not possible to determine allele 1/allele 2 copy number without sequencing confirmation. In addition, any gene-editing events outside of the TaqMan™ probe sequences could not be detected. Consequently, wild-type alleles detected by the genotyping assay were later confirmed to have subtle modifications. This highlights the importance of confirming the composition of *Ryr1* loci by sequencing. Whilst considerable progress was made using TA cloning and subsequent Sanger sequencing to confirm editing events on each allele, alternative sequencing technologies would provide increased throughput and greater sensitivity for the detection of gene-editing events that occurred. Multiple reports in the literature describe the use of deep sequencing to detect CRISPR-induced editing events in myoblasts and other cell types (Dastidar et al., 2018; Min et al., 2019; Wojtal et al., 2016). Since Sanger sequencing can only confirm the presence of a specific editing event and not the copy number, deep sequencing would provide a more comprehensive analysis of editing events on each allele and is rapidly becoming the gold standard for the analysis of indel generation at the target site. This technique would overcome the limitations associated with the polyploidy of C2C12 cells, providing a promising outlook for their utilisation in a CRISPR-Cas9 pipeline for the characterisation of MH-associated VUS.

4.3.1.1 Mechanims of DSB repair

The HDR efficiencies demonstrated in this study were low, with 3.75% of single cell colonies containing the variant of interest for p.D3986E and 2.70% for

p.S1728F, although the low efficiency of HDR is well documented and these values are similar those reported in the literature (Liu et al., 2019; Boel et al., 2018). HDR was used to correct a premature stop codon in exon 23 of the *DMD* gene that interferes with dystrophin expression in Duchenne Muscular Dystrophy (DMD), achieving HDR efficiencies of up to 9% following injection into DMD mouse model, *mdx,* zygotes (Long et al., 2014).

Strikingly, a range of mutational events introduced by CRISPR-Cas9 gene-editing were observed in this study. The presence of small insertions and deletions can be explained by NHEJ – the primary mechanism by which DSBs are repaired in mammalian cells (Davis and Chen, 2013) . The most common form, canonical NHEJ (c-NHEJ) involves the recognition of DSBs by the dimeric Ku70/Ku80 protein complex. The Ku complex recruits a number of proteins that allow for processing of the DNA ends to render them ligatable. Processing of the DNA ends can result in minor resection or the introduction of random sequences, usually up to 10 bp (Ata et al., 2018). Following processing, ligase IV acts to ligate the DSB. Interestingly, some of the indels detected in this study were detected multiple times in different cell lines. This suggests that, at least in some cases, preferential editing events may occur and this could be sequence context dependent. Indeed, non canonical NHEJ, also known as microhomology mediated end joining (MMEJ) is another pathway implicated in the repair of DSBs (Bae et al., 2014). MMEJ uses short regions of homology for the repair of double-stranded breaks, resulting in more homogenous editing events than canonical NHEJ (Ata et al., 2018).

Resection of the 5’ ends of the DSB allows for the commitment of the cell to an HDR pathway. Whilst the mechanism of single strand oligonucleotide integration has not been fully elucidated, it is believed to occur by a HDR mechanism called synthesis dependent strand annealing (SDSA; Paix et al., 2017; Boel et al., 2018). In SDSA, the 5’ ends of the DSB are resected to produce large 3’ overhangs. The single stranded oligonucleotide template then binds to the complementary 3’ overhang and acts as a template for DNA

polymerase to extend, filling in the 5' resection. Finally, DNA ligase acts to ligate nicks in the DNA.

The observation that some HDR templates were scarlessly recombined into the C2C12 genome was highly encouraging, ultimately providing proof of principle for the introduction of MH-associated VUS into a myoblast cell line for downstream functional characterisation. In some instances, HDR templates were found to have been integrated erroneously. Aberrant DNA synthesis during SDSA can occur by a mechanism referred to as template switching whereby the newly synthesised DNA strand binds to regions of microhomology elsewhere on the repair template or in the endogenous DNA. This results in erroneous DNA synthesis and the incorporation of inverted, duplicated or fragmented repair templates (Boel et al., 2018). As such, this work provides support for the role of SDSA in the integration of single stranded oligonucleotide HDR templates through the observation of such erroneous HDR template integrations.

4.3.1.2 Optimisation of HDR efficiency

In this study, attempts to improve HDR efficiency were primarily focused on the optimisation of the distance between the cut site and base to be edited (cut to base distance). Whilst HDR efficiency is locus and cell type dependent, in general, reductions in HDR efficiency of ~50% are observed when the cut to base distance is 10 bp. When this increased to 20 bp, a reduction of ~70% is observed. HDR efficiencies of near 0% are observed with a cut to base distance of 35 bp (Paquet et al., 2016). As such, the major criterion in gRNA design was the cut to base distance. Furthermore, single stranded oligonucleotide HDR templates were used in this study due to reports of increased HDR efficiencies compared to vector-encoded double stranded HDR templates and reduced illegitimate recombination events (Ran et al., 2013a; Würtele et al., 2003). HDR templates with 80 bp homology flanking the cut site (total length of 161 bp) were selected since each arm of homology should be 50-100% the size of the insertion, typically 50-80 bp for small changes (Ran et al. 2013a; Li et al., 2014). Recently, a growing body of literature has emerged

concerning the improvement of HDR efficiencies by optimisation of several parameters. Firstly, since undesired editing events introduced by NHEJ are widespread, efforts to inhibit the mechanism using chemical inhibitors have been explored elsewhere. Success has been limited in using Ligase IV inhibitor, SCR7 (Maruyama et al., 2015). While Maruyama and colleagues found improvements in HDR efficiency by up to 19-fold in human epithelial and melanoma cells, others have found no improvement to HDR efficiencies using SCR7 in zebrafish (Boel et al., 2018). Two proteins from the adenovirus 4 genome, E1B55K and E4orf6, have also been used to suppress NHEJ by facilitating the degradation of Ligase IV (Chu et al., 2015). Furthermore, modified Cas9 proteins with one inactive catalytic site, resulting in the introduction of single-stranded breaks, can undergo HDR with reduced NHEJ events (Ran et al., 2013a). Interestingly, Guo et al., (2018a) reported increased 'perfect' HDR (that is, scarless recombination) using a cold-shock protocol whereby iPSCs exposed to 32^{o}C for 24 hours following transfection had increased perfect HDR rates by two-fold, potentially due to temperature stabilisation of recombination intermediates (Guo et al., 2018a).

In conclusion, despite the considered design of HDR templates, mainly concerning the cut to base distances, HDR efficiencies in this study were low and undesired NHEJ events were widespread. Nonetheless, the nature of CRISPR-Cas9 as a rapidly developing technology means that there are a number of areas that could be explored for the improvement of HDR efficiencies and scarless integration. This work highlights areas for future development of the CRISPR-Cas9 pipeline within the MH field for the characterisation of MH-associated VUS.

4.3.1.3 Analysis of *in-silico* predicted off-target sites

A key consideration in any gene-editing experiment is the potential for introduction of editing events at sites other than the target. The CRISPOR off-target prediction tool consistently predicted more off-target sites than CCTOP. Where off-target sites were predicted by both programs, they were often ranked at different likelihoods of binding. These differences reflect variations in

the algorithms used by each programme to detect off-target sites. To account for this, a selection of the top off-target sites predicted by both programs were sequenced. Encouragingly, all off-target sites within the p.D3986E and p.S1728F cell lines for which sequences were successfully generated were wild-type. These sequences were generated by direct Sanger sequencing of the sites within the C2C12 genome (as opposed to TA cloning and subsequent Sanger sequencing). Detection of multiple sequences as a consequence of editing events would result in overlapping traces within a sequencing chromatogram that start near the Cas9 cut site. Such overlapping traces were not observed for any of the off-target sites sequenced. Thus, it appears that the Mm_D3986E_gRNA2 and Mm_S1728F_gRNA2 guides did not induce undesired editing events, at least at the predicted off-target sites for which sequences were generated. The location of off-target sites within GC-rich and repetitive regions was problematic. Primer design tool, PrimerBLAST (Ye et al., 2012), was unable to generate PCR primers for the sequencing of the top 2 off-target sites predicted by CCTOP and the second off-target site predicted by CRISPOR for Mm_D3986E_gRNA2. The top off-target site predicted by CRISPOR failed to produce PCR amplicons despite primer re-design and PCR optimisation with the addition of DMSO which enhances primer binding to the template (Mammedov et al., 2008). Further primer re-design and optimisation of the PCR reaction using non-traditional parameters such as the addition of ethylene glycol and 1,2-propanediol could prove successful for the generation of amplicons from these difficult regions (Zhang et al., 2009).

For the p.S1728F cell lines, primers were unable to be designed for the 5th and 8th off-target site predicted by CCTOP. Since off-target sites are ranked based on the likelihood of binding and only wild-type sequences were detected at higher ranked off-target sites, it is unlikely that gene editing occurred at the 5th and 8th off-target sites for which no sequences could be generated. Whilst *in-silico* tools are widely used to predict potential off-target sites, reports in the literature have detailed the detection of off-target editing events at sites not predicted by conventional *in-silico* tools (Zhang et al., 2015). Consequently, whole-genome sequencing remains the only method by which all off-target activities can be ruled out; however, the feasibility of performing whole-genome sequencing for each cell line created is limited by the high cost and extensive

data analysis required to interpret genomic data. For the use of CRISPR-Cas9 gene-editing for the introduction of MH-associated VUS, it is more feasible to optimise HDR efficiency and inhibit NHEJ to increase success in generating cell lines that contain only the variant of interest. Functional analysis of multiple lines containing different copy numbers would allow for the analysis of gene dosage effects, providing conclusive evidence that any effect observed is due to the variant in question, rather than activity at off-target sites.

4.3.1.4 Gene-editing efficiencies

The gene-editing efficiencies of the gRNAs utilised in this study, as determined by T7 assay, and theCRISPRater efficacy predictions did not follow a similar trend. For the p.D3986E gRNAs, CRISPRater ranked them (in order of highest efficacy) Mm_D3986E_gRNA2, Mm_D3986E_gRNA3 and Mm_D3986E_gRNA1. In contrast, the T7 assay showed the highest gene-editing efficiencies in Mm_D3986E_gRNA1, followed by Mm_D3986E_gRNA3 and then Mm_D3986E_gRNA2. As such, *in-silico* efficacy predictions should not be solely relied upon for gRNA selection.

4.3.2 Utilisation of C2C12 myoblasts

The C2C12 cells used in this project tolerated transfection well, with only a minor reduction in cell viability following transfection and the proportion of GFP-expressing cells following transfection reaching up to 50%, with an average of 25%, similar to values reported in the literature (Dodds et al., 1998). C2C12 cells consistently survived FACS for both bulk GFP-enrichment sorts and single cell sorts into 96-well plates. In total, out of the 1728 single cells collected for the p.D3986E and p.S1728F experiments, 234 formed cell lines that grew well (13.54%). Thus, C2C12 cells provide a robust cell type in which characterisation of MH-associated VUS can be performed following improvements to HDR efficiency and NHEJ suppression. In addition to wild-type C2C12 cells and the 3E1 wild-type monoclonal line, only two of the edited cell lines formed multinucleated myotubes. The reason for impaired myotube formation in some cell lines is unclear. It has been observed here and elsewhere that not all myoblasts form myotubes following culture in conditions

that induce differentiation; however, Yoshida et al., (1998) showed that subcloning of these undifferentiated cells resulted in the formation of roughly equal ratios of differentiated and undifferentiated cells, subsequently terming these undifferentiated cells 'reserve cells'. One explanation for the impaired myotube formation in some cell lines within this project is that the multiple doublings required for the propagation of a single cell affected the ability of cells to differentiate. Impaired differentiation capacity has been observed in C2C12 cells that have undergone repeated passage and this is associated with reductions in key myogenic regulatory factors (MRFs) Myf5, MyoD, MRF4 and myogenin (Sharples et al., 2011; Shahini et al., 2018). As described in 4.2.3, the C2C12 cells utilised in this project were labelled as passage 0 following retrieval from cryostorage and cells were transfected with the pSpCas9(BB)-2A-GFP vector at passage 10; however, no information was known about passage number prior to freezing. As such, it may be advisable for future work to obtain C2C12 myoblasts of known low passage number to improve the yield of differentiation competent cell lines.

4.3.3 The scope for use of cytidine deaminase vectors

Since the introduction of specific variants by HDR is largely inefficient and can result in undesired NHEJ events, the use of a Cas9 nickase (D10A) fused to a cytidine deaminase base editor and uracil glycosylase inhibitor (BE3) was explored as a means for the characterisation of MH-associated VUS that result from C>T or G>A substitutions. Since these base editors act to modify C/G residues within 8 bp of the PAM-distal end of the gRNA, albeit with variable efficiency, base editing is not targeted to a single nucleotide; as such, if there are other C or G bases near the desired base to be edited, these will likely undergo deamination as well (Komor et al., 2016). Given this, the Cas9 D10A-BE3 base editor was deemed not to act with sufficient specificity to confer successful gene-editing for the majority of MH-associated VUS investigated. The only exception was the p.R3366H variant (MAF 0.0008; gnomAD). As such, the Cas9 D10A-BE3 system does not provide a robust platform for the introduction and downstream functional characterisation of MH-associated VUS but it could be used to investigate the effect of the p.R3366H variant. The p.R3366H variant was identified in 2 referrals to the Leeds MH Unit. The first

patient, determined as MHSh by IVCT, was a central core disease (CCD) patient. CCD is characterised by cores lacking mitochondria and oxidative enzymes in type 1 muscle fibres and the main symptom is muscle weakness. CCD is associated with MH susceptibility (McCarthy et al., 2000; Robinson et al., 2006). Interestingly, this patient inherited the p.R3366H variant in *cis* alongside RYR1 variants p.Y3933C and p.I1571V and this haplotype has been reported previously (Garibaldi et al., 2019; Kraeva et al., 2015). The second patient was an EHI referral determined as MHShc by IVCT. In this patient, the p.R3366H, p.Y3933C, p.I1571V haplotype was identified in addition to the RYR1 p.T3711M variant and RYR1 p.G2050C variant. This illustrates the range of complex phenotypes associated with variants in the *RYR1* gene and the determination of the effect of the p.R3366H variant would provide insight into the roles of each variant present within these individuals.

4.3.4 Sensitivity of resultant cell lines to caffeine

Cell line 3E1 was selected as a control for Ca^{2+} imaging to ensure that any results observed were not due to a differential phenotype induced by processing of the cell line through the CRISPR-Cas9 pipeline and propagation from a single cell. The sensitivity of cell line 3E1 to caffeine was not significantly different to wild-type polyclonal C2C12 cells, demonstrating that its Ca^{2+} handling properties had not been altered. Plotting %MR for each cell line at each caffeine concentration revealed that wild-type C2C12 cells and cell line 10G5 had a greater %MR at 1 mM caffeine than cell line 3E1 and cell line 8G6, despite wild-type cells having a higher EC_{50} than 8G6. This result is explained by the observation that wild-type C2C12 cells and cell line 10G5 both consistently produced greater increases in raw fluorescence following caffeine perfusion. As such, at 1 mM caffeine, some responses of cell lines 3E1 and 8G6 would not have been recognised by the analysis if the increase in fluorescence was not >10% greater than baseline. This criterion was included to ensure that any peaks identified were bona fide responses to caffeine rather than experimental noise. Nonetheless, despite the reduction in magnitude of response in cell lines 3E1 and 8G6 (presumably due to the greater proportion of smaller myotubes observed in these cell lines), stratification of individual cells within cell lines into ‘low’ and ‘high’ responder groups did not reveal any

significant differences in the EC_{50} values generated between each group, giving confidence that the results observed are a consequence of the genotype of the cell line. The reduced EC_{50} values for cell lines 8G6 and 10G5 compared to wild-type polyclonal C2C12 cells and cell line 3E1 cannot be conclusively determined to result from the p.D3986E variant since both cell lines contained erroneous HDR integration events and NHEJ events on other *Ryr1* alleles. Indels that arise from NHEJ tend to introduce out-of-frame premature stop codons (Ran et al., 2013a). Premature stop codon sequences in the mRNA are recognised by components that initiate nonsense mediated decay, resulting in transcript degradation (Popp and Maquat, 2016). Given this, it is likely that *Ryr1* expression was reduced through loss of two *Ryr1* alleles in the 10G5 cell line and at least one in the 8G6 cell line. In both cases, the HDR integration events were in-frame and thus likely resulted in an Ryr1 protein with altered function.

Since p.S1728F cell lines did not form multinucleated myotubes, EC_{50} values were not calculated. Although the p.S1728F cells did show a response to caffeine, albeit small, the drastic difference in morphology compared to polyclonal C2C12 cells and cell line 3E1 meant that any results observed were not comparable. As such, the pathogenicity of p.S1728F remains unclear. The p.S1728F variant is conserved across mammals but not all species included in the multiple sequence alignment. *In-silico* pathogenicity prediction tools gave conflicting results due to the different annotations used by each program. For example, SIFT, which predicts pathogenicity based on conservation, scored the p.S1728F variant as tolerated. In contrast, CADD, which provides the most comprehensive and robust pathogenicity prediction due to its combination of 63 annotations, assigned a C-score of 24 indicating that p.S1728F is likely a deleterious variant. Whilst *in-silico* tools can provide a means to filter variants of interest in large data sets, they cannot be relied upon to confirm pathogenicity. The *in-silico* pathogenicity prediction results could reflect the mild putative effect on RYR1 channel function, with patients harbouring the p.S1728F variant produce relatively weak contracture strength during IVCT (Carpenter et al., 2009). Another *in-silico* pathogenicity tool that has been developed in recent years for variant prioritisation is The Rare Exome Variant Ensemble Learner (REVEL) that, like CADD, integrates scores from multiple

programs (Ioannidis et al., 2016). Whilst REVEL was not utilised within this project, it is now being used in conjunction with CADD in the Leeds MH Unit.

4.3.5 Future directions - can CRISPR-Cas9 genome editing be used to replace current characterisation methods?

The work presented here provides the first report of the introduction of MH associated VUS into a myoblast cell line by CRISPR-Cas9 genome editing and provides a substantial foundation for future development of the technique. Key areas for future optimisation have been highlighted and include the suppression of NHEJ, potentially using small molecules that inhibit Ligase IV or by using a Cas9 nickase nuclease that has shown reduced rates of NHEJ activity. Secondly, for genome editing in C2C12 cells, deep sequencing should be considered for the determination of editing events on each Ryr1 allele to overcome the limitations associated with TA cloning. Another consideration for the utilisation of CRISPR for the characterisation of MH-associated VUS is the ability to generate gRNAs that contain appropriate cut to base distances for all of the MH-associated VUS. The introduction of the p.D3986E and p.S1728F variants was not hindered by design of gRNAs, with three medium to high quality gRNAs were designed per variant, of which 2 for each variant had cut to base distances of ≤13 bp; however, it is important to consider that this may be a limiting factor for some MH-associated VUS. Ultimately, the development of a CRISPR-Cas9 genome editing pipeline for the characterisation of MH-associated VUS overcomes existing limitations of variant characterisation and provides the potential to accelerate a DNA-level diagnostic approach to MH. As such, with further optimisation of the aforementioned parameters, it is likely that CRISPR-Cas9 genome editing will be adopted as a method of variant characterisation. Indeed, recently, a similar strategy was used in human colonic Caco-2 cells cells for the functional characterisation of a variant associated with congenital chloride diarrhea. The variant, in the *SLC26A3* gene which encodes the chloride anion exchanger, was found to affect the function of the epithelial barrier, providing insight into the mechanisms of the disease (Zhang et al., 2019).

Chapter 5 - Developing cellular and *in-vitro* systems to investigate the role of Calsequestrin-1 in MH and associated conditions

5.1 Introduction

5.1.1 A role for CASQ1 in MH

The realisation of CASQ1 as a regulator of RYR1 activity and the subsequent generation of Casq1-null mice has led to the proposal that variants in the *CASQ1* gene could act to influence MH susceptibility. Indeed, Casq1-null mice exhibit halothane-induded MH-like responses and heat-induced EHI-like responses (Dainese et al., 2009; detailed in 1.4.1.2). To date, no CASQ1 variants have been conclusively linked to MH. Efforts to identify CASQ1 variants in MH susceptible individuals in the North American population revealed the relatively common p.M87T variant (resulting from a T to C substitution at cDNA position 206), which is annotated with a MAF of 0.02 (2%) in the gnomAD browser (Kraeva et al., 2013). The allele frequency of p.M87T in MH susceptible individuals was not significantly different to the allele frequency of the variant in MH negative individuals nor control groups, suggesting that it is unlikely to represent the underlying genetic cause of MH. Interestingly though, out of the 15 MH susceptible individuals with the CASQ1 p.M87T variant, 4 of them also harboured a diagnostic variant in the *RYR1* gene. *In-vitro* investigations into the effect of the p.M87T on CASQ1 Ca^{2+} binding and polymerisation revealed that the variant has a reduced Ca^{2+} binding capacity, likely as a result of a diminished ability to polymerise. Indeed, X-ray crystallography revealed that the p.M87T variant alters the front-to-front dimer interface that inhibits the linear formation of back-to-back tetramers (Lewis et al., 2015). These data suggest that whilst the presence of the CASQ1 p.M87T may not be sufficient to induce an MH phenotype, it could act to modify the phenotype in the presence of an additional variant in the *RYR1* gene.

5.1.2 CASQ in disease

The heterozygous p.D244G variants in the *CASQ1* gene has been linked to vacuolar aggregate myopathy (VAM), which is characterised by muscular

weakness, episodes of muscle cramps, increased CK levels, fatigue and the presence of cellular inclusions of aggregated CASQ1 (D'Adamo et al., 2016; Rossi et al., 2014). The expression of GFP-tagged recombinant p.D244G *CASQ1* cDNAs in rat myotubes has shown co-localisation of D244G CASQ1 with the RYR1 and the formation of large aggregates (Rossi et al., 2014). *In-vitro* studies of the purified D244G CASQ1 protein have shown reduced Ca^{2+} binding capacity compared to wild-type (Lewis et al., 2015). Furthermore, primary muscle fibres from VAM patients showed a decreased sensitivity to caffeine compared to unaffected control fibres (Rossi et al., 2014).

Tubular aggregate myopathy (TAM) is characterised by the presence of aggregates in muscle fibres that are comprised of a number of proteins including SERCA, triadin and CASQ1 (Barone et al., 2017). Symptoms include muscle weakness and cramps, in addition to myalgia. Recently, 3 novel CASQ1 variants in patients with TAM have been characterised. The p.D44N, p.G103D and p.I385T variants all showed reduced Ca^{2+} binding capacity *in-vitro* and the p.I385T and p.D44N variants showed a reduction in CASQ1-mediated inhibition of SOCE (Barone et al., 2017). Interestingly, TAM is also associated with variants in the *STIM1* and *ORAI* genes, which produce a more severe phenotype than that associated with CASQ1 variants. VAM and TAM present clinical examples of how alterations in the Ca^{2+} binding and polymerisation capacity of CASQ1 can perturb normal Ca^{2+} handling mechanisms.

Catecholaminergic polymorphic ventricular tachycardia (CPVT) is a cardiac condition characterised by episodes of ventricular tachycardia, causing syncope during strenuous exercise or periods of intense emotion. In some cases, tachycardia develops into ventricular fibrillation causing sudden death (Behere and Weindling, 2016). Interestingly, CPVT can be inherited in an autosomal dominant manner, caused by heterozygous variants in the ryanodine receptor 2 gene (*RYR2*; the RYR isoform expressed in cardiac cells) or the calmodulin 1 gene (*CALM1;* Nyegaard et al., 2012). Alternatively, CPVT can be inherited as an autosomal recessive disorder, caused by homozygous variants in the *CASQ2* gene or the triadin gene (*TRDN*; Faggioni et al., 2012; Laitinen et al., 2003). Since CPVT results from Ca^{2+} dysregulation via premature activation of the RYR2, a mechanism analogous to MH in skeletal

muscle, a role for CASQ1 in MH was proposed as a corollary of this (MacLennan and Chen, 2009).

5.1.3 CASQ1 variants identified by the Leeds MH Unit

In an effort to identify variants in genes other than the *RYR1* and *CACNA1S* that could contribute to the MH phenotype, the Leeds MH Unit uses a targeted gene approach to sequence the coding regions of 50 genes associated with Ca^{2+} handling by NGS. The CASQ1 p.F186Y variant, a phenylalanine to tyrosine substitution as a result of a T>A transition at cDNA position 557, was identified in an EHI individual (IVCT result MHN). As mentioned previously, EHI has significant clinical overlap with MH and whilst the pathophysiology underlying EHI is not fully understood, Ca^{2+} dysregulation has been shown to underly heat-induced EHI like responses in mice (Dainese et al., 2009; Lopez et al., 2018; Yang et al., 2006). The CASQ1 p.F186Y variant has a MAF of 0.000008 (gnomAD). Out of the 50 genes sequenced, CASQ1 p.F186Y was identified alongside one VUS, the p.P371L c.1112C>T variant in the *CHERP* gene which encodes the calcium homeostasis endoplasmic reticulum protein. This variant was previously unreported and no information was available regarding its frequency. Variants in the *CHERP* gene have not previously been associated with EHI or MH; as such, the relevance of this variant is not clear.

The CASQ1 p.I138T variant, an isoleucine to threonine substitution as a result of a T>C transition at cDNA position 413, was identified in an MHSh proband. The variant has a MAF of 0.0002 (gnomAD). One rare variant (MAF 0.001; gnomAD), the p.H80Y c.238C>T variant in the *DNM2* gene, which encodes dynamin 2, was identified in the same individual as CASQ1 p.I138T. Variants in the *DNM2* gene are known to cause autosomal dominant centronuclear myopathy (CNM), which is characterised by muscle weakness and atrophy (Catteruccia et al., 2013); however, the relevance of the DNM2 p.H80Y variant is unknown. Whether family members of the individual the CASQ1 p.I138T variant was identified in also harbor the variant remains to be determined by DNA sequencing. Colleagues also identified the CASQ1 p.E364K variant in the Australian population, which is a glutamate to lysine substitution resulting

from a G>A substitution at cDNA position 1090 (Bjorksten et al., 2016). The variant has a MAF of 0.00002 (gnomAD) and was identified in an MHShc proband.

5.1.4 Chapter aims and strategy

The primary aim of this chapter is to develop a *Casq1* knockout C2C12 cell line that can be used for the re-introduction of *CASQ1* variant cDNAs using lentiviral vectors for functional characterisation. In contrast to the *RYR1*, the *CASQ1* coding sequence is approximately 1 kb in length and encodes a ~44 kDa protein. As such, it is more amenable to site directed mutagenesis and cloning required for heterologous expression than the *RYR1*. Since the HEK293 system lacks the expression of calcium handling apparatus that is characteristic of muscle cells, the development of a *Casq1* knockout C2C12 line affords the opportunity to functionally characterise *CASQ1* variants identified in MH patients in a muscle specific context. Whilst *Casq1*-null mice have been generated previously (Dainese et al., 2009), at the outset of this project there were no immortalised *Casq1*-null cells available for use. C2C12 cells, however, are inherently immortalised, overcoming the limitations associated with limited replicative potential in primary mouse cells (Shay and Wright, 2000). The effect of *Casq1* ablation in mice has been characterised previously (Dainese et al., 2009), as such, the effect of *Casq1*-knockout in the resultant C2C12 lines affords the opportunity to determine the consistency in the response of *Casq1*-null cells. The effect of the *Casq1*-knockout on caffeine sensitivity in C2C12 cells will be determined by fluorescence Ca^{2+} imaging, as performed in 4.2.12.

The secondary aim of this chapter is to perform preliminary *in-vitro* investigations into the effects of three *CASQ1* variants on the Ca^{2+} binding and polymerisation properties of the CASQ1 protein, an area previously unexplored within the Leeds MH unit. CASQ1 WT, CASQ1 p.I138T, p.F186Y and p.E364K variants will be cloned into an expression vector for heterologous expression and purification. A range of *in-vitro* methods will be explored to aid gathering of this preliminary data including microscale thermophoresis (MST), mass

spectrometry (MS) and dynamic light scattering (DLS). Since cell-based systems of functional characterisation are generally time-consuming and encounter limitations such as myoblast differentiation potential, the development of an *in-vitro* system could serve as a method to stratify variants of interest in genes other than the *RYR1* for further cell-based characterisation. A range of *in-silico* tools will also be utilised to investigate the predicted pathogenicity of the three *CASQ1* variants selected for use in this project.

5.2 Results

5.2.1 *In-silico* pathogenicity predictions, conservation analysis and mutagenesis

As performed for the other variants explored within this project, a range of *in-silico* means were employed to predict pathogenicity of the *CASQ1* variants selected for use in this project. The CADD tool (version 1.4) predicted C-scores for p.I138T, p.F186Y and p.E364K of 24.9, 26.9 and 21.8, respectively, placing them all within the top 0.1% of potentially deleterious variants. SIFT (version 6.2.1) categorised p.I138T as deleterious with a score of 0, p.F186Y as deleterious with a score of 0.01 and p.E364K as tolerated with a score of 0.16. Finally, Poly-Phen2 (version 2) categorised p.I138T as possibly damaging with a score of 0.935, p.F186Y as probably damaging with a score of 0.997 and p.E364K as possibly damaging with a score of 0.672. The ConSurf server (Ashkenazy et al., 2016; Celniker et al., 2013; Asheknazy et al., 2010; Berezin et al., 2004) was used to determine the conservation of the ancestral residue of each *CASQ1* variant. ConSurf was programmed to search for 100 CASQ1 homologues with at least 50% homology to the human sequence. The I residue at position 183 in the CASQ1 protein sequence was scored a conservation score of 9 – the highest conservation score possible as determined by ConSurf (Figure 5.1). It was conserved across all 99 of the 100 homologues identified, with *Poecilia formosa* (Amazon molly freshwater fish) containing a valine residue at the same position. The p.I183 residue was embedded in a cluster of highly conserved residues and was predicted to be buried within the protein structure with a structural role (Figure 5.1; panel B).

The F residue at position 186 in the CASQ1 protein sequence was also scored the highest possible conservation score by ConSurf and was conserved within all 100 homologues identified. The p.F186 residue was predicted to be buried within the protein structure and to have a structural role. Lastly, the E residue at position 364 in the CASQ1 protein sequence was deemed to be variable, with just 40% of the homologues identified having the E residue conserved at this position. Aspartic acid (an amino acid with acidic properties like glutamate) accounted for the amino acid at position 364 in 41% of the homologues. The p.E364 residue was predicted to be exposed but no prediction was made regarding a structural or functional role due to low conservation.

The PyMOL (Schrödinger, LLC) mutagenesis wizard was used to explore the consequence of each CASQ1 variant on local hydrogen bonding and VdW interactions (Figure 5.2). Substitution of the I residue with a T residue at position 138 in the human CASQ1 protein sequence did not affect hydrogen bonding nor did it produce any VdW clashes when shown in its most likely rotamer conformation (94.4% probability). Two other rotamer conformations were suggested that both produced minor and severe VdW clashes. Substitution of the F residue with a Y residue at position 186 in the human CASQ1 protein sequence did not affect hydrogen bonding but did produce severe VdW clashes in its most likely rotamer conformation (53.8% probability) and in the 3 alternative potential rotamer conformations. Substitution of the E residue to K at position 364 in the human CASQ1 protein sequence produced minor VdW clashes in its most likely rotamer conformation (15.9% probability), out of the remaining 14 alternative rotamer conformations, one of them (5.1% probability) did not produce any VdW clashes.

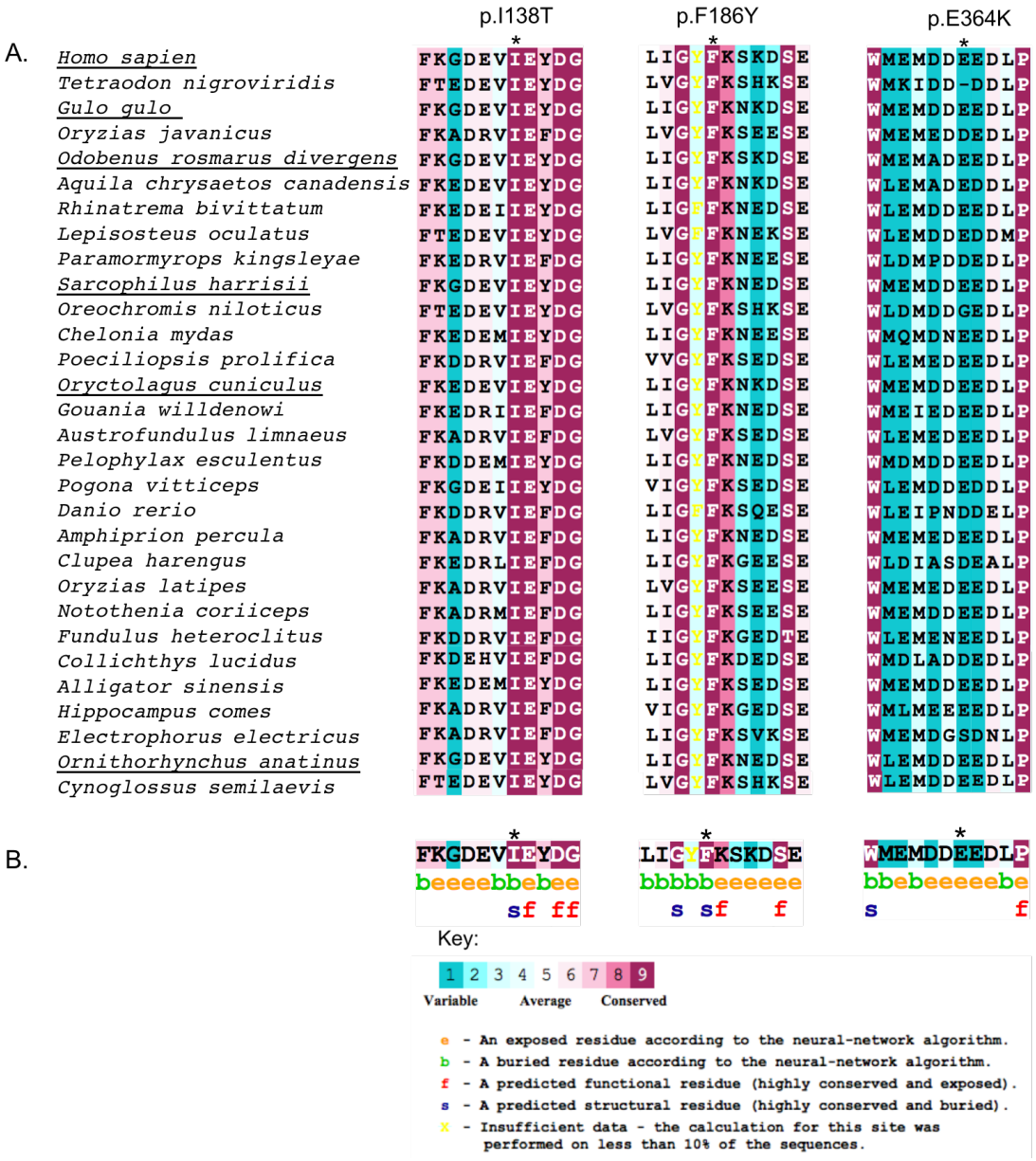

Figure 5.1 – Multiple sequence alignment of CASQ1 homologues

CSI-BLAST was used to search for 100 CASQ1 homologues with at least 50% homology to the human CASQ1 protein and MAFTT was used to create a multiple sequence alignment. The first 30 homologues identified (in a random order) are shown here for reference. ConSurf was used to determine and colour code the conservation of residues across homologues. Regions around each residue of interest are shown in panel A. Predictions of the exposure and role of the residue are shown in panel B along with a key. Mammalian species are indicated by underlining and an asterisk highlights the residue of interest.

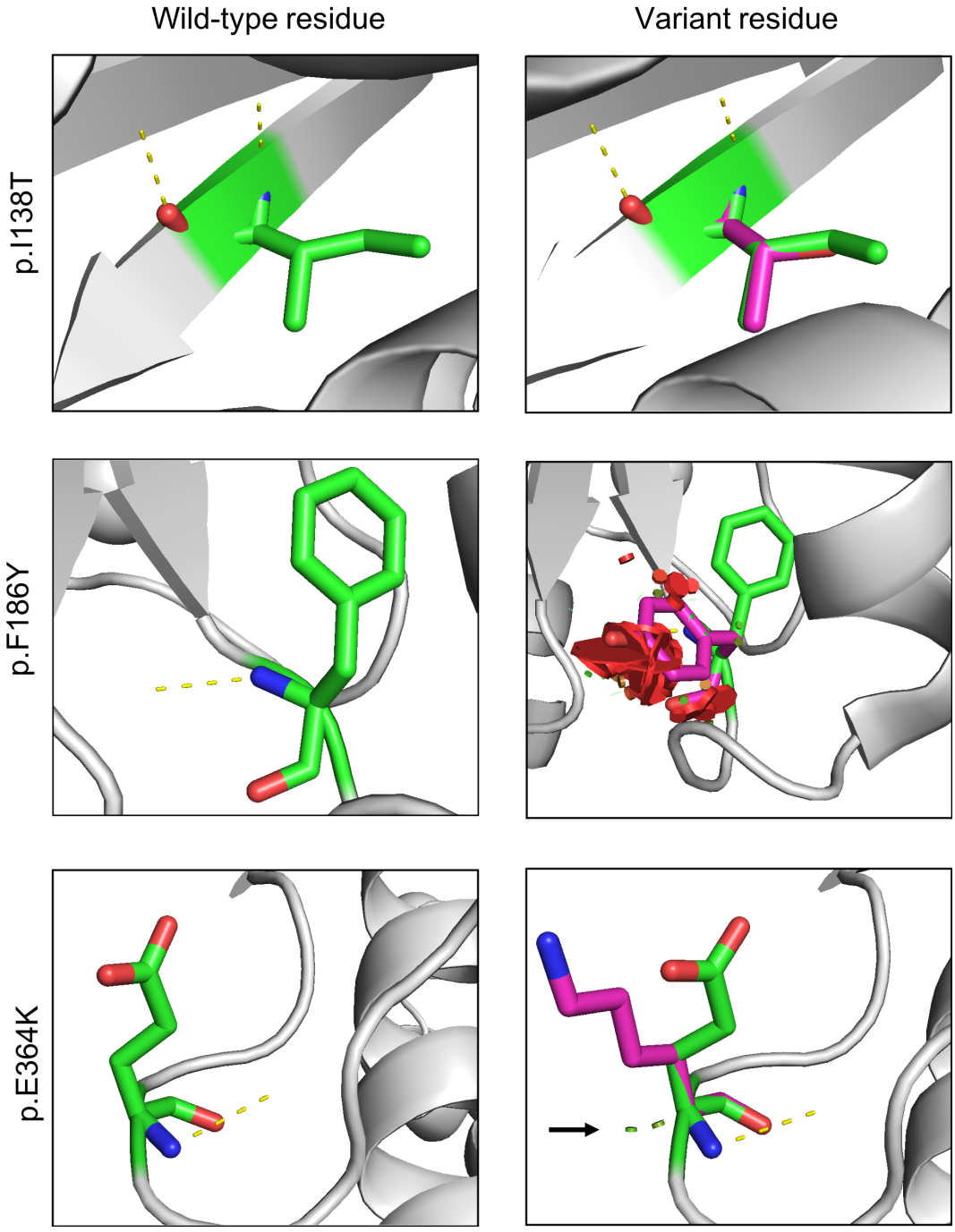

Figure 5.2 – PyMOL mutagenesis of CASQ1 variants

The PyMOL mutagenesis wizard was used to model the CASQ1 p.I138T, p.F186Y and p.E364K substitutions using the human CASQ1 protein structure (PBD ID: 5CRD). The wild-type residue is shown in green and the variant residue is in pink. Hydrogen bonds are shown by yellow dashes and VdW clashes are shown by green (less severe) and red (more severe) disks. Black arrows are used to highlight VdW clashes that are difficult to see. The most likely rotamer conformations for each variant are shown.

5.2.2 gRNA design

The gRNAs designed for the knockout of the *Casq1* gene in C2C12 myoblasts were designed using CCTOP (Stemmer et al., 2015), searching the GRCm38/mm10 genome for unique sequences 20 nt in length and immediately upstream of an NGG PAM recognition sequence, as described in 4.2.4. To search for the gRNAs, a 450 bp sequence starting at base position 1 of exon 1 in the *Casq1* gene was entered into CCTOP. The search returned 88 results and two of the top-ranked gRNAs were selected for testing in C2C12 myoblasts. The first gRNA, hereafter referred to as Mm_Casq1_gRNA1 was 301 bp downstream of the first base of exon 1. Mm_Casq1_gRNA1 targeted the reverse DNA strand and the PAM was AGG (CCT on the reverse strand), it had an efficacy prediction by CRISPRater of 0.65 (medium efficacy) and 4 predicted off-target sites, all of which were intronic (Labhun et al., 2017). The CRISPOR tool predicted a further 2 off-target sites (Haeussler et al., 2016). The second gRNA, hereafter referred to as Mm_Casq1_gRNA2, was 402 bp downstream of the first base of exon 1. Mm_Casq1_gRNA2 also targeted the reverse strand anf the PAM was GGG (CCC on the reverse strand), it had an efficacy prediction of 0.71 (medium efficacy) and 8 predicted off-target sites, of which 3 were in exons, 4 were in introns and 1 was intergenic. The CRISPOR tool predicted 19 off-targets, including the 8 identified by CCTOP. The gRNA sequences were commercially synthesised by IDT containing overhangs to facilitate cloning into pSpCas9(BB)-2A-GFP (Table 5.1).

Table 5.1 – Mm_Casq1 gRNA sequences with pSpCas9(BB)-2A-GFP overhangs

Overhangs to facilitate cloning into pSpCas9(BB)-2A-GFP are shown in green. The additional ‘G’ nucleotide to enhance transcription from the hU6 promoter in the vector is shown in blue. Both gRNA sequences target the reverse DNA strand.

gRNA	Forward sequence 5’-3’	Reverse sequence 5’-3’
Mm_Casq1_gRNA1	CACCgCGGTCCACACCGTCGTACTC	AAACGAGTACGACGGTGTGGACCGc
Mm_Casq1_gRNA2	CACCGCGAGGCCTTGTCGTCCTCG	AAACCGAGGACGACAAGGCCTCGC

5.2.2.1 Cloning into pSp(BB)-2A-GFP

The gRNAs were cloned into the pSpCas9(BB)-2A-GFP as described in 4.2.6. Following transformation into Stbl3™ cells (Invitrogen™), four single colonies were used to inoculate 5 ml of LB media containing 100 µg/ml ampicillin. Plasmid DNA was isolated by miniprep and the plasmids were digested with *Bbs*I and *Age*I to confirm the presence of the insertion. As mentioned previously, gRNA insertion results in the excision of the *Age*I cut site; as such, only the *Bbs*I site is available for digest and the plasmid is linearised (Ran et al., 2013a). All of the clones screened appeared to contain the insert (Figure 5.3). The isolated plasmid DNA was prepared for Sanger sequencing to confirm the insertions. Indeed, both gRNA sequences were successfully ligated into pSpCas9(BB)-2A-GFP (Figure 5.4).

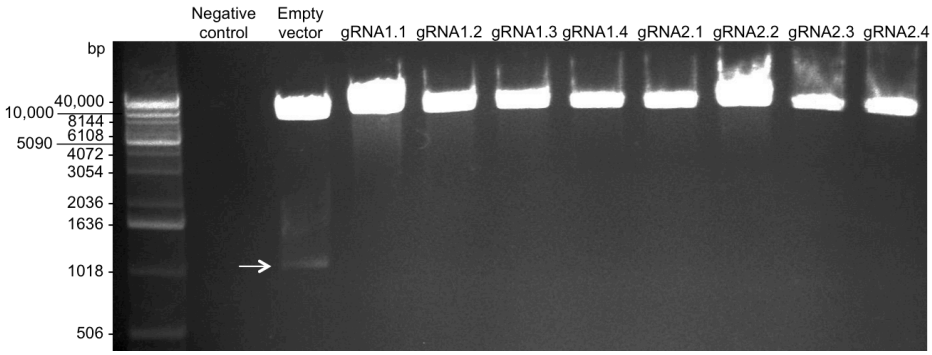

Figure 5.3 – Restriction digest screen of pSpCas9(BB)-2A-GFP

Plasmid DNA isolated from clones transformed with pSpCas9(BB)-2A-GFP and Mm_Casq1_gRNA ligation products was digested with *Bbs*I and *Age*I. The reaction was loaded onto a 1% TAE-agarose gel and the products separated by gel electrophoresis. Lane 1 shows the 1 kb extension ladder (Invitrogen™) and lane 2 is a negative control comprising the reaction contents without DNA. Lane 3 shows the digestion products of pSpCas9(BB)-2A-GFP containing no insert. Lanes 4-7 show the digestion product of Mm_Casq1_gRNA1-containing pSpCas9(BB)-2A-GFP vectors and lanes 8-11 show the digestion product of Mm_Casq1_gRNA2-containing pSpCas9(BB)-2A-GFP vectors.

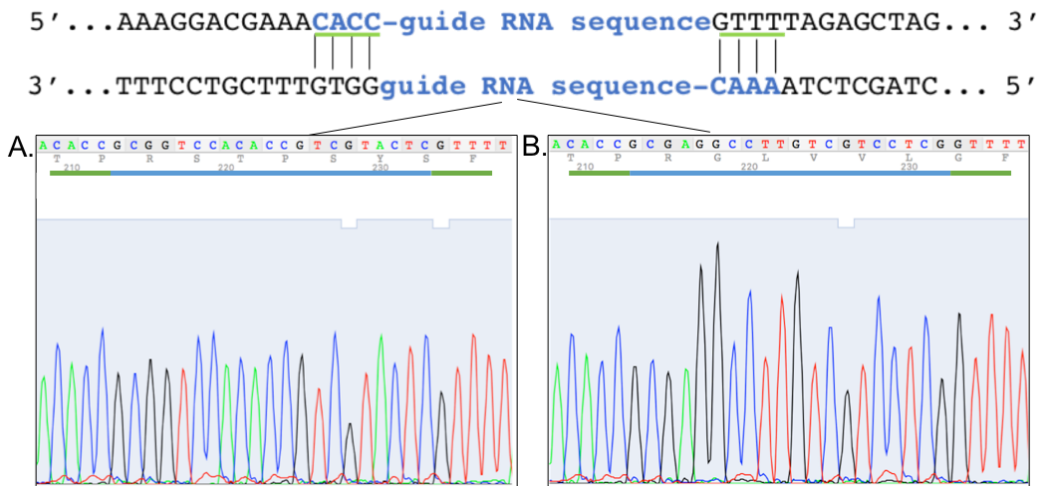

Figure 5.4 – Sanger sequencing traces showing the insertion of Mm_Casq1_gRNA1 and Mm_Casq1_gRNA2 in pSpCas9(BB)-2A-GFP

Panels A and B show the insertion of Mm_Casq1_gRNA1 and Mm_Casq1_gRNA2 in the pSpCas9(BB)-2A-GFP vector, respectively. The gRNA sequences are underlined in blue and the 5' CACC and 3' GTTT (AAAC reverse complement) are underlined in green.

5.2.3 Estimation of gene-editing efficiency

C2C12 cells were transfected using Lipofectamine™ 3000 with pSpCas9(BB)-2A-GFP containing Mm_Casq1_gRNA1 and Mm_Casq1_gRNA2 and the GFP-expressing cells were enriched by FACS as described in 4.2.9. The proportion of GFP positive cells collected for the Mm_Casq1_gRNA1 transfection after gating was 10.0% and 91.32% of the cell population was viable based on SSC and FSC measurements. For cells transfected with Mm_Casq1_gRNA2, the proportion of GFP-expressing cells after gating was 9.55% and the proportion of viable cells was 87.41%. A single cell sort was sufficient to obtain cells for the T7 assay. Prior to performing the T7 assay, it was uncovered that there was a C>T (G>A reverse strand) SNP within the gRNA site for Mm_Casq1_gRNA2 in the C2C12 genome (Figure 5.5; panel B), the gRNA site for Mm_Casq1_gRNA1 was wild-type (Figure 5.6; panel A). Since reports in the literature show that at least 2 mismatches in the gRNA seed region are required to abolish Cas9 cleavage, the T7 assay was still performed for Mm_Casq1_gRNA2. A 1005 bp region was amplified around the gRNA sites and a T7 assay performed for each gRNA. The expected cleavage product sizes for Mm_Casq1_gRNA1 were 768 bp and 237 bp. Mm_Casq1_gRNA1 produced cleavage products corresponding to the expected band sizes (Figure

5.6). The estimated gene-editing efficiency of Mm_Casq1_gRNA1 was 12.2%. As expected, Mm_Casq1_gRNA2 produced a cleavage product corresponding to 869 bp; however, the remaining expected 136 bp cleavage product was not detected. This was presumably due to the quantity of DNA in the cleavage product being lower than the limit of detection of ethidium bromide. The calculation of gene-editing efficiency requires the relative intensity of both cleavage products. Equation 2 was used to determine the small fragment intensity.

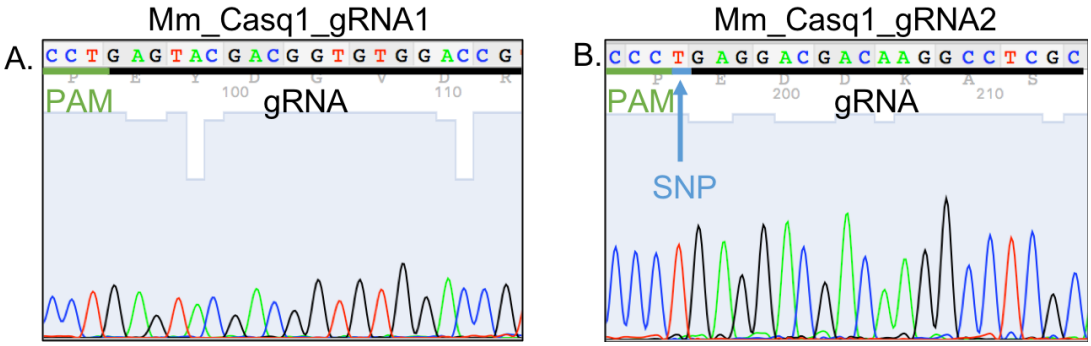

Figure 5.5 – Mm_Casq1_gRNA1 and Mm_Casq1_gRNA2 target sequences in the C2C12 genome

DNA was extracted from C2C12 cells and a region surrounding gRNA sequences was amplified. The resultant amplicon was processed for Sanger sequencing. The gRNA sequences are underlined in black and the PAM sequences are in green. The C>T (G>A on reverse strand) SNP present in the Mm_Casq1_gRNA2 sequence in shown underlined in blue. The forward DNA strand is shown hence the gRNAs are shown in their reverse complement form.

The estimated gene-editing efficiency of Mm_Casq1_gRNA2 was 7.5%. The impact of the SNP on the gene editing efficiency of Mm_Casq1_gRNA3 is not known.

Equation 2.

$$\textit{small fragment intensity} = \frac{\textit{large fragment intensity} \times \textit{small fragment size (bp)}}{\textit{large fragment size (bp)}}$$

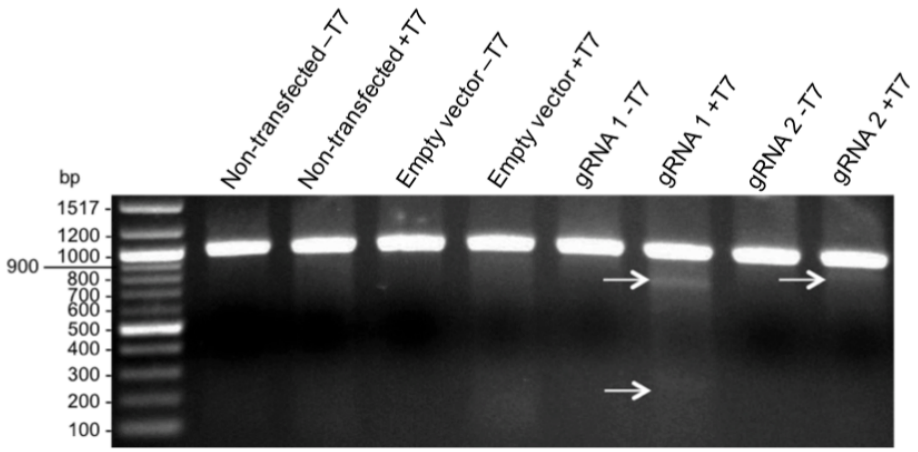

Figure 5.6 – T7 assay of Mm_Casq1_gRNA1 and Mm_Casq1_gRNA2

The T7 assay was loaded onto 1% TAE-agarose gel and products were separated by gel electrophoresis. Lane 1 shows the 100 bp DNA ladder (NEB). Lanes 2 and 3 show the T7 assay from non-transfected cells, without and with the T7 enzyme, respectively. Lanes 4-9 show the same for cells transfected with the empty pSpCas9(BB)-2A-GFP vector, Mm_Casq1_gRNA1 and Mm_Casq1_gRNA2. Arrows show the presence of the cleavage products.

Since Mm_Casq1_gRNA1 produced greater estimated gene-editing efficiencies than Mm_Casq1_gRNA2 and had only 6 predicted off-target sites, this gRNA was selected for use in generating the Casq1 knockout cells. Following transfection with pSpCas9(BB)-2A-GFP containing Mm_Casq1_gRNA1, cells were sorted into single cells in 10 96-well plates containing a 1:1 ratio of filtered conditioned growth media to fresh growth media. Proportions of GFP-expressing cells collected range from 16.4%-19.6% across plates, with a mean of 17.2%. The mean proportion of viable cells based on FSC and SSC measurements was 99.77%. In total, 84 cell lines showed growth and were propagated to T-75 flasks at ~60% confluency. This was 8.75% of the total single cells collected across 10 96-well plates.

5.2.4 Identification and validation of edited lines

To identify the single cell-derived lines that had been edited by CRISPR-Cas9, a direct PCR reaction was performed from aliquots of single-cell derived lines taken following trypsinisation during cell splitting. The cells were lysed and treated with proteinase K before the crude lysate was added to a PCR. The resultant PCR products were processed for Sanger sequencing. Since there

are 4 copies of chromosome 1 on which the *Casq1* gene lays, and random indels were expected at each Cas9 cut site, it was expected that a wild-type sequence would be observed until the vicinity of the Cas9 cut site, followed by overlapping traces there onwards reflecting different indels on each *Casq1* gene. In the first instance, 32 single-cell derived C2C12 lines were sequenced. This identified 8 cell lines that had some form of editing event near the Cas9 cut site (25%). Out of the 8 edited cell lines detected, 3 of them consistently formed myotubes (cell lines 3B9, 8E10 and 7E5) and were therefore selected for further analysis in this project (Figure 5.7).

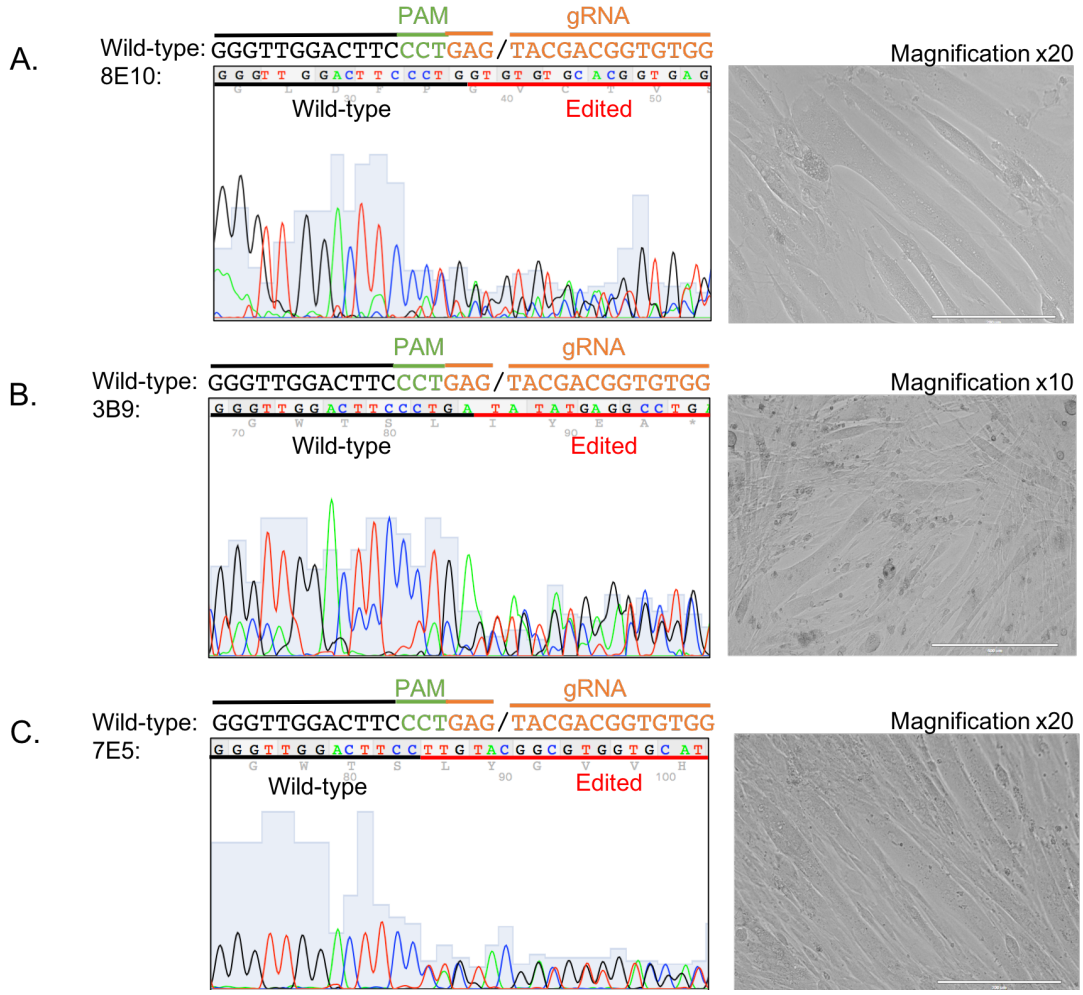

Figure 5.7 – Sanger sequencing chromatograms and differentiation images for cell lines 8E10, 3B9 and 7E5

Direct PCR reactions were performed on crude lysates obtained from single cell-derived lines. Amplicons were processed for Sanger sequencing to detect editing events in each cell line. Editing events were evident by the presence of overlapping sequencing traces downstream of the gRNA sequence, reflecting different indels on each *Casq1* allele. Three edited cell lines that formed myotubes, 8E10 (panel A), 3B9 (panel B) and 7E5 (panel C) were selected for use and their respective Sanger sequencing chromatograms shown here. Above each sequencing chromatogram is the wild-type *Casq1* sequence for comparison. Wild-type, single peak sequences are shown in black and the edited, overlapping sequences are shown underlined in red. The gRNA sequences are shown in orange and the PAM is in green. The gRNAs target the reverse strand and the forward strand sequence is shown here, hence the gRNAs are shown as their reverse complement. Images of myotubes (right) were taken following 6 days of differentiation on ECM from Engelbreth-Holm-Swarm sarcoma-coated plates. Images were captured using the EVOS™ FL imaging system with x20 magnification for cell lines 8E10 (panel A) and 7E5 (panel C) and x10 magnification for cell line 3B9 (panel B).

As expected, the presence of overlapping sequences that occurred near the predicted Cas9 cut site meant it was not possible to ascertain with confidence the editing events on each *Casq1* allele for cell lines 8E10 and 3B9. For these cell lines, at least three overlapping sequences could be clearly observed (Figure 5.7; panels A and B). Despite base-calling of the wild-type sequence until the vicinity of the Cas9 cut site, the presence of additional peaks beneath the wild-type sequence suggested that a larger indel had occurred on at least one of the *Casq1* alleles in each cell line that affected the region downstream of the Cas9 cut site (Figure 5.7; panels A and B). For cell line 7E5, only two overlapping sequences could be observed in the Sanger sequencing chromatogram. Given this, it was possible to manually deconvolute the overlapping traces and a 5 bp CTGAG deletion and 2 bp AG deletion could be discerned on each trace (Figure 5.7; panel C).

To elucidate the composition of each *Casq1* allele within the 8E10 and 3B9 cell lines and to confirm the editing events observed in cell line 7E5, TA cloning and subsequent Sanger sequencing was performed. DNA was extracted from each cell line using a salting-out method and a PCR was performed to amplify a 330 bp region surrounding the Mm_Casq1_gRNA1 sequence. Amplicons were purified using AMPure XP beads (Beckman Coulter) and phosphorylated with T4 PNK. Purified, phosphorylated amplicons were incubated in a ligation reaction with the dephosphorylated, linearised pGEM®-T vector prior to transformation into OneShot® TOP10 *E. coli* cells. Transformation reactions were plated on LB agar plates containing ampicillin at 100 µg/ml and 40 µl 100mM IPTG and 120 µl 20 mg/ml X-gal spread onto the surface of the plate. White colonies were picked and used to inoculate 5 ml LB media cultures for plasmid isolation by miniprep. The number of colonies processed for Sanger sequencing for cell lines 8E10, 3B9 and 7E5 was 18, 20 and 19, respectively. Three editing events were detected in cell lines 8E10 and 3B9, and the two editing events inferred from the sequencing chromatograms in cell line 7E5 were confirmed (Table 5.2). Cell line 8E10 contained a 5 bp ‘CTGAG’ deletion which was also detected in cell line 7E5 (Figure 5.8; panel A and panel G). A single ‘T’ residue insertion was also identified in cell line 8E10 at the Cas9 cut site (Figure 5.8; panel C) and a large 98 bp deletion was identified (Figure 5.8;

panel B). In cell line 3B9, an out of frame 9 bp 'TCCCTGAGT' deletion was detected (Figure 5.8; panel D) in addition to a 7 bp 'AGTACGA' deletion (Figure 5.8; panel E) and a 19 bp 'TACGACGGTGTGGACCGTG' deletion at the Cas9 cut site (Figure 5.8; panel F). In addition to the 'CTGAG' deletion also detected in cell line 8E10, the 'AG' deletion in cell line 7E5 was also confirmed (Figure 5.8; panel H). No wild-type alleles were detected in any of the cell lines. As discussed in Chapter 4, TA cloning generated some clones without inserts, unclear Sanger sequencing chromatograms and the same editing events were detected multiple times. As such, the composition of the fourth *Casq1* allele in cell lines 8E10 and 3B9 remains to be determined. Only two editing events were detected in cell line 7E5 and only two overlapping traces were identified in the initial screening of single-cell derived lines (Figure 5.7). Since the same editing events have been detected in multiple cell lines here and in Chapter 4, it is a possibility that cell line 7E5 contains two alleles with the 'AG' deletion and two alleles with the 'CTGAG' deletion. An alternative explanation for the seemingly diploid Sanger sequencing chromatogram would be that the single cell from which cell line 7E5 was derived represented a rare subpopulation of cells within the C2C12 population that had only two copies of chromosome 1 and its rarity within the population prevented its detection by karyotyping. Alternatively, it is possible that the PCR consistently preferentially amplified the alleles containing the AG and CTGAG deletion, meaning other alleles were not detected by Sanger sequencing. All in-silico predicted off-target sites were sequenced in each putative Casq1 knockout cell line. All off-target sequences appeared wild-type (Appendix C).

Table 5.2 – Summary of editing events detected in edited *Casq1* cell lines

Values in brackets indicate whether the same editing event was detected in another cell line and the number of times the editing event was detected.

Cell line	Editing event 1	Editing event 2	Editing event 3
8E10	5 bp del (7E5; 4)	98 bp del (1)	1 bp ins (2)
3B9	9 bp del (3)	7 bp del (3)	19 bp del (3)
7E5	5 bp del (8E10;4)	2 bp del (6)	Not detected

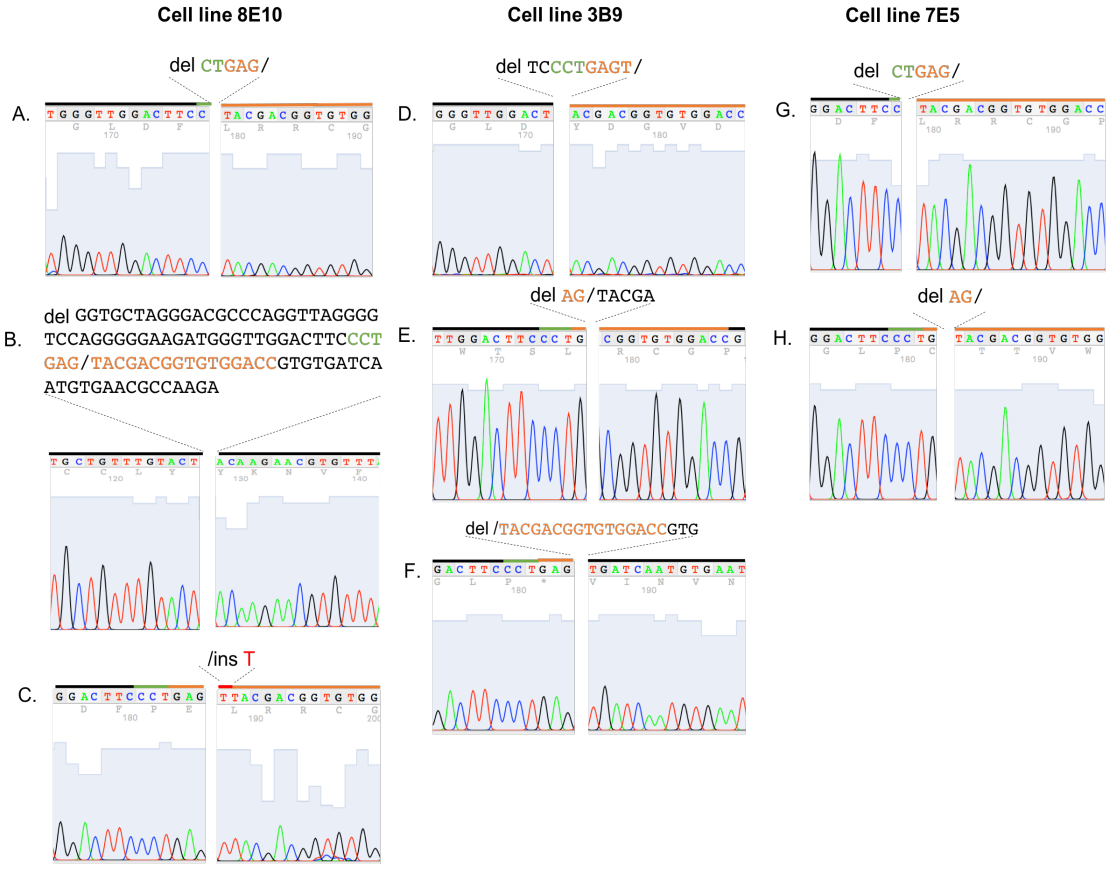

Figure 5.8 – Graphical representation of editing events detected in edited *Casq1* cell lines

Panels A-C, D-F and G-H show editing events in cell lines 8E10, 3B9 and 7E5, respectively. Wild-type sequences are shown in black, PAM sites are in green, gRNA sequences are in orange and insertions are shown in red. The Cas9 cut site is indicated by /. The forward DNA strand is shown hence gRNAs are shown in their reverse complement. Sanger sequencing chromatograms were viewed using 4Peaks software (Nucleobytes).

A western blot was performed to confirm knockout of the Casq1 protein (Figure 5.9). Since Casq1 is expressed following the differentiation of myoblasts into myotubes, wild-type C2C12 cells and the edited cell lines 8E10, 3B9 and 7E5 were plated on ECL-coated T-75 tissue culture flasks and allow to reach ~90% confluency (Ehrlich et al., 2016). At this point, growth media was replaced with differentiation media and changed every other day for 6 days. Total protein was extracted from the cells using RIPA buffer with Halt™ protease inhibitor cocktail (ThermoFisher) to prevent protein degradation. The concentration of total protein was quantified using the Pierce™ BCA assay (ThermoFisher) and 50 µg total protein loaded onto an 8-16% gradient SDS-PAGE gel (BioRad). The myotubes produced by each cell line were comparable in diameter and

length to each other and wild-type C2C12 cells; however, since a lack of Casq1 protein could, in theory, be due to a lesser degree of differentiation in the edited cell lines, the myosin heavy chain (MHC) was probed for in the western blot. MHC is a well-established marker of differentiation and the antibody used, MF-20 (DSHB, deposited by D.A. Fischman), recognises all MHC isoforms (Brown et al., 2012; Mizunoya et al., 2008). The expected band sizes of Casq1 and MHC were 50 kDa and ~223 kDa, respectively. GAPDH was used as a loading control and had an expected band size of 30 kDa. In the C2C12 wild-type sample, distinct bands were observed at ~200 kDa, ~ 50 kDa and ~32 kDa. In the edited cell line samples, no band was observed at ~50 kDa, indicating the Casq1 protein was not present in these samples and successful knockouts had been generated. In all samples, two bands were present at approximately 200 kDa, potentially reflecting the separation of different MHC isoforms. Interestingly, cell line 7E5 appeared to have an additional high Mw band with increased migration compared to the MHC bands in the other samples. The identity of this band was not determined but it could represent an additional MHC isoform or a degradation product. Despite lysate clarification by centrifugation and quantification of the cell lysates, it appeared that proteins within the samples were not homogenously resuspended resulting in uneven cell loading, particularly for the 7E5 cell line sample. Nonetheless, clear bands were observed at Mws corresponding to MHC and GAPDH, but not for Casq1.

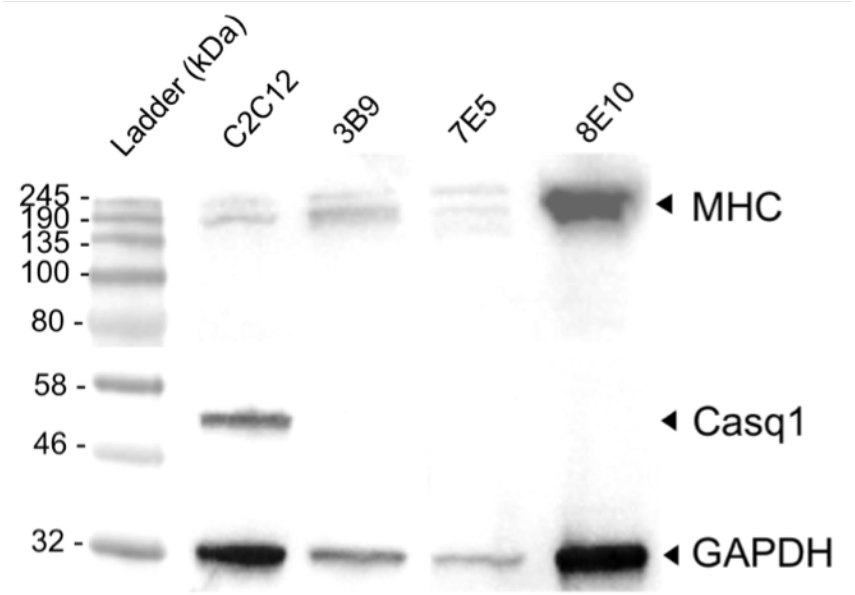

Figure 5.9 – Confirmation of Casq1 knockout by western blot

Wild-type C2C12 cells and the edited Casq1 derivative lines were differentiated into myotubes in ECL-coated flasks for 6 days. Fifty µg total protein was loaded onto a 8-16% acrylamide gradient gel (BioRad). Proteins were transferred to PVDF membrane using a Trans-Blot® transfer cell (BioRad). Blots were visualised by incubation with a HRP-conjugated secondary antibodies prior to development with the SuperSignal West Femto Maximum Sensitivity Substrate (ThermoFisher). Blots were visualised and images captured using the BioRad XR+ Gel Doc™. The first lane shows the broad range protein standard (NEB) and subsequent lanes show wild-type C2C12, 3B9, 7E5 and 8E10 samples, respectively.

5.2.5 Ca^{2+} imaging of Casq1 knockout lines

Skeletal muscle fibres from Casq1-null mice have been reported to have increased sensitivity to caffeine and reductions in the amount of releasable Ca^{2+} (Dainese et al., 2009). To determine whether this was observed in the C2C12 Casq1 knockout (KO) cell lines generated here, the response of cells to caffeine was determined by fluorescent Ca^{2+} imaging as described in Chapter 4. Briefly, cells were allowed to reach ~90% confluency on ECM-coated 96-well plates and differentiated into myotubes for 5-6 days. Cells were loaded with 10 µM Fluo-8AM at 37°C for 30 min prior to equilibration at room temperature for 20 min in imaging buffer. Cells were sequentially perfused with caffeine solutions at 0.1 mM, 1 mM, 3 mM, 5 mM, 10 mM and 20 mM with 1 min rest in between caffeine doses. Transient increases in fluorescence, indicative of Ca^{2+} release, were detected and recorded using the Nikon TE2000

inverted microscope attached to an intensified CCD camera. To determine caffeine sensitivity, EC_{50} values were generated for each cell line from peak height measurements and AUC measurements and compared to the same measurements from wild-type C2C12 cells and a wild-type monoclonal C2C12 cell line, 3E1. Cells were excluded from the analysis based on criteria detailed in 4.2.12.

The peak height analysis showed that cell line 8E10 had an EC_{50} of 3.435 mM (SD 1.769; 95% CI 3.245 to 3.629; Figure 5.10; panel A). This was significantly different to both wild-type C2C12 cells ($p<0.0001$) and cell line 3E1 ($p=0.0023$) but not cell line 3B9 ($p=0.9942$) or 7E5 ($p=0.1894$) (Figure 5.11). Cell line 3B9 had an EC_{50} of 3.726 (SD 1.559; 95% CI 3.505 to 3.955; Figure 5.10; panel B) which again was significantly different to wild-type C2C12 cells ($p<0.0001$) and cell line 3E1 ($p=0.0107$), but not cell lines 8E10 or 7E5 ($p=0.4235$) (Figure 5.11). The dose response curve for cell line 7E5 indicated that it responded similarly to wild-type C2C12 cells and cell line 3E1 until 10 mM caffeine at which the cell line responded maximally. The normalised fluorescence value at 10 mM was greater than that for 20 mM (i.e. greater than 100%), hence the data point is not shown in the dose response curve. The EC_{50} for cell line 7E5 was 4.415 (SD 1.401; 95% CI 4.205 to 4.63; Figure 5.10; panel C). This was significantly different to wild-type C2C12 cells ($p=0.0108$) but not 3E1 ($p=0.4103$), 8E10 or 3B9 (Figure 5.11).

Values obtained from the AUC analysis followed a similar pattern to the peak height analysis. Cell line 8E10 had an EC_{50} of 4.464 (SD 2.049; 95% CI 4.248 to 4.687; Figure 5.10; panel D) which was significantly different to wild-type C2C12 cells ($p<0.0001$) and cell line 3E1 ($p=0.0017$) but not cell lines 3B9 ($p=0.9996$) or 7E5 ($p=0.7912$) (Figure 5.11). Cell line 3B9 had an EC_{50} of 4.905 (SD 1.756; 95% CI 4.683 to 5.137; Figure 5.10; panel E) which was significantly different to wild-type C2C12 cells ($p=0.0002$) and cell line 3E1 ($p=0.0047$) but not 8E10 or 7E5 ($p=0.9011$) (Figure 5.11). Finally, cell line 7E5 had an EC_{50} of 5.255 (SD 1.245; 95% CI 5.058 to 5.459; Figure 5.10; panel F) which was significantly different to wild-type C2C12 cells ($p=0.0060$) but not cell line 3E1 ($p=0.0525$), 8E10 or 3B9 (Figure 5.11).

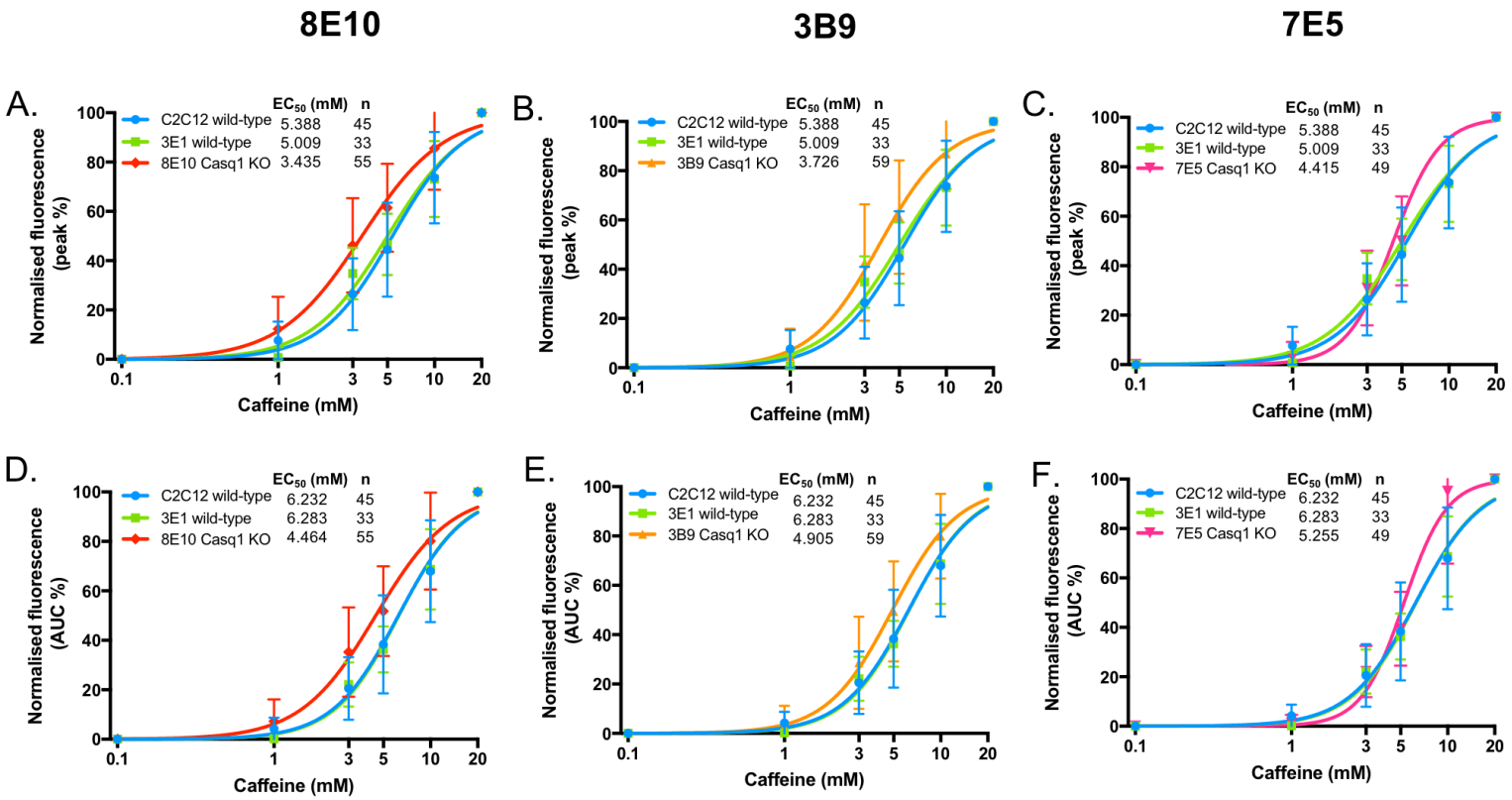

Figure 5.10 – Caffeine dose-response analysis of Ca^{2+} imaging of wild-type C2C12 cells and Casq1 KO cells

Panels A, B and C show the peak sigmoidal dose response analysis for cell lines 8E10 (red diamonds), 3B9 (orange upward triangles) and 7E5 (pink downward triangles) compared to wild-type C2C12 cells (blue circles) and cell line 3E1 (green squares). Panels D, E and F show the AUC analysis. Normalised fluorescence (a percentage of the maximal response at 20 mM caffeine) is shown on the Y axis and the caffeine concentration (mM) is on the X axis. Data points are means of 33-59 myotubes (plated and imaged on at least 3 different days, with the exception of 3E1 from which data was collected on 2 different days) and error bars show the SD. Curves were fitted and graphs plotted using Prism 7 (GraphPad).

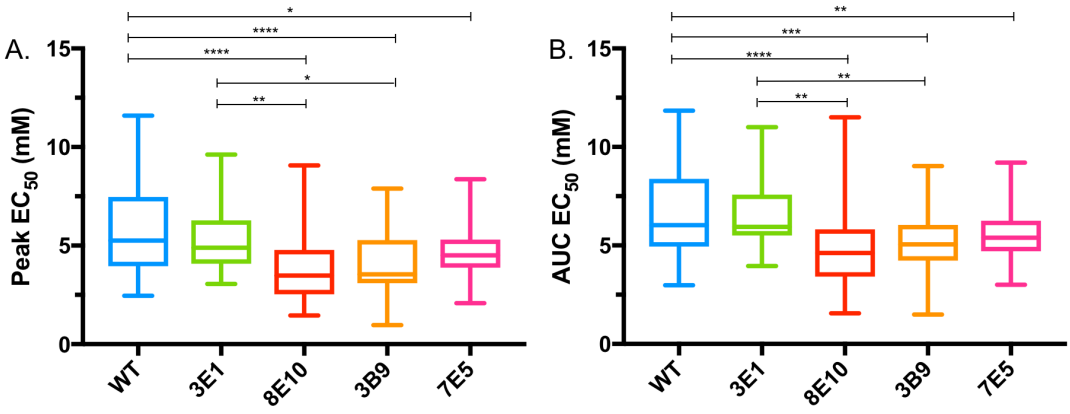

Figure 5.11 – Comparison of EC_{50} values for wild-type C2C12 cells and Casq1 KO cell lines

Panels A and B show box plots of the EC_{50} values from the peak height analysis and AUC analysis, respectively. Box plots show the median data point, upper and lower quartiles and the minimum and maximum data points. Graphs plotted using Prism 7 (GraphPad). One-way ANOVA and Tukey's test for multiple comparisons were used to determine significance. *p<0.05, **p<0.01, ***p<0.001, ****p<0.0001.

The %MR at each caffeine concentration is shown for the peak height analysis (Figure 5.12; panel A) and AUC analysis (Figure 5.12; panel B). In the peak height analysis at 1 mM caffeine, the %MR for cell line 8E10 was 13.51 (SD 13.41; 95% CI 9.814-17.21). This was significantly different to cell line 3E1 which had a %MR of 0.7449 (SD 4.279; 95% CI -0.7724-2.262; p <0.0001), cell line 3B9 (%MR 7.194; SD 16.83; 95% CI 2.412-11.98; p=0.0389) and cell line 7E5 (%MR 3.393; SD 6.747; 95% CI 1.456-5.331 p <0.0001) but not wild-type C2C12 cells (%MR 7.698; SD 7.693; 95% CI 5.386-10.01 p=0.0848). The %MR of cell line 3B9 was not significantly different to wild-type C2C12 cells (p=0.9995), cell line 3E1 (p=0.0834) or cell line 7E5 (p= 0.4504). Cell line 7E5 was also not significantly different to wild-type C2C12 cells (p=0.3483) or cell line 3E1 (p=0.8350).

At 3 mM caffeine, wild-type C2C12 cells (%MR 26.39; SD 14.57; 95% CI 22.01-30.77) responded in a similar manner with no significant differences in %MR to cell line 3E1 (%MR 34.76; SD 10.49; 95% CI 31.04-38.48; p=0.2646) and 7E5 (%MR 33.02; SD 16.28; 95% CI 28.35-37.7; p=0.3951). There was also no significant difference between cell line 3E1 and 7E5 (p=0.9932). In contrast, cell lines 8E10 (%MR 46.63; SD 18.64; 95% CI 41.49-51.7) and 3B9 (%MR 43.7; SD 25; 95% CI 36.6-50.81) responded similarly to each other, with

no significant difference in the %MRs between the two cell lines (p=0.9252). The %MR of cell line 8E10 was significantly different to wild-type C2C12 cells (p <0.0001), cell line 3E1 (p= 0.0290), and cell line 7E5 (p=0.0019). The %MR of cell line 3B9 was significantly different to wild-type C2C12 cells (p <0.0001) and cell line 7E5 (p=0.0309). Whilst 3B9 did have an increased %MR than cell line 3E1, this was not statistically significant (p= 0.1856).

At 5 mM caffeine, wild-type C2C12 cells (%MR 44.49; SD 19.09; 95% CI 38.75-50.22), cell line 3E1 (%MR 46.58; SD 12.43; 95% CI 42.17-50.99) and cell line 7E5 (%MR 48.33; SD 19.38; 95% CI 42.77-53.9) continued to respond in a similar manner. There was no significant difference in the %MR between wild-type C2C12 cells and 3E1 (p=0.9899) or 7E5 (p), nor was there a significant difference between cell lines 3E1 and 7E5 (p=0.8733). Cell lines 8E10 (%MR 60.9; SD 18.05; 95% CI 55.93-65.87) and 3B9 (%MR 62.51; SD 24.37; 95% CI 55.58-69.43) continued to respond in a similar manner at 5 mM caffeine, with no significant difference in %MR between the two cell lines (p=0.9935). The %MR of both 8E10 and 3B9 were significantly different to wild-type C2C12 cells (p=0.0004; p=0.0001, respectively), 3E1 (p=0.0092; p=0.0030, respectively) and 7E5 (p=0.0111; p=0.0032, respectively).

At 10 mM caffeine, wild-type C2C12s (%MR 73.64;SD 18.52; 95% CI 68.07-79.2) responded similarly to cell line 3E1 (%MR 73.13; SD 15.42; 95% CI 67.66-78.59; p>0.9999) and cell lines 8E10 (%MR 83.31;SD 17.71; 95% CI 78.43-88.19) and 3B9 (%MR 86.21; SD 14.65; 95% CI 82.05-90.37) continued to respond similarly to each other (p=0.2387). There was no significant difference in %MR between wild-type C2C12 cells and 8E10 (p=0.2045); however, there was a statistically significant difference between wild-type C2C12 cells and cell line 3B9 (p=0.0498). No significant difference was observed between cell line 3E1 and 8E10 (p=0.2387) or 3B9 ($p_{=}$0.0695). Interestingly, despite responding similarly to wild-type C2C12 cells throughout the dose response experiment, at 10 mM caffeine cell line 7E5 responded maximally (%MR 111; SD 35.85; 95% CI 100.7-121.3). This was significantly different to the response at 10 mM for wild-type C2C12 cells (p<0.0001), cell line 3E1 (p<0.0001), cell line 8E10 (p<0.0001) and cell line 3B9 (p<0.0001).

Values for the %MR in the AUC analysis followed the same pattern as the peak height analysis, with wild-type C2C12 cells, cell line 3E1 and cell line 7E5 responding in a similar manner until 10 mM caffeine when 7E5 showed an increased response compared to the other cell lines (Figure 5.12; panel B). Cell lines 8E10 and 3B9 also responded similarly throughout the dose-response experiment. At 1 mM caffeine, cell line 8E10 had a %MR of 7.919 (SD 8.994; 95% CI 5.488-10.35). This was significantly different to cell line 3E1 (%MR 0.1552; SD 0.8916; 95% CI -0.1609-0.4713; $p<0.0001$), cell line 3B9 (%MR 3.799; SD 10.73; 95% CI 1.002-6.596; $p=0.0249$) and cell line 7E5 (%MR 1.566; SD 3.785; 95% CI 0.4787-2.653; $p=0.0002$). The %MR of cell line 8E10 was not significantly different to wild-type C2C12 cells (%MR 4.233; SD 4.595; 95% CI 2.852-5.613; $p=0.0939$) There was also no significant difference between wild-type and 3E1 ($p=0.1119$), 3B9 ($p=0.9983$) or 7E5 ($p=0.3987$), nor was there a significant difference between cell lines 3B9 and 7E5 ($p=0.5144$).

At 3 mM caffeine, wild-type cells had a %MR of 20.55 (SD 12.68; 95% CI 16.74-24.36) and responded in a similar manner to both cell line 3E1 (%MR 22.13; SD 8.92; 95% CI 18.96-25.29; p) and 7E5 (%MR 23.73; SD 10.58; 95% CI 20.69-26.77; p). Cell lines 8E10 (%MR 35.63; SD 17.3; 95% CI 30.96-40.31) and 3B9 (%MR 30.48; SD 19.82; 95% CI 25.32-35.65) responded similarly with no significant difference in %MR between the two cell lines ($p=0.3665$). Cell line 8E10 was significantly different to wild-type C2C12 cells ($p<0.0001$), cell line 3E1 ($p=0.0006$) and 7E5 ($p=0.0008$). Cell line 3B9 was significantly different to wild-type C2C12 cells ($p=0.0091$) but not 3E1 ($p=0.0848$) or 7E5 ($p=0.1449$).

At 5 mM caffeine, wild-type cells (38.41; SD 19.82; 95% CI 32.45-44.36), cell line 3E1 (%MR 36.33; SD 9.33; 95% CI 33.02-39.64) and 7E5 (%MR 39; SD 16.38; 95) continued to respond in a similar manner. There were no significant differences between in the %MR wild-type C2C12 cells and 3E1 ($p=0.9874$) or 7E5 ($p=0.9999$), nor was there significant difference between 7E5 and 3E1 ($p=0.9659$). Cell line 8E10 had a %MR of 51.46 (SD 18.64; 95% CI 46.42-56.5) and responded similarly to cell line 3B9 (%MR 50.57; SD 21.15; 95% CI 45.06-56.08) , with no significant difference between the two cell lines ($p=0.9990$). The %MR for cell line 8E10 was significantly different to wild-type

C2C12 (p=0.0038), cell line 3E1 (p=0.0018) and cell line 7E5 (p=0.0051). Likewise, the %MR for cell line 3B9 was significantly different to wild-type C2C12 cells (p=0.0038), cell line 3E1 (p=0.0034) and cell line 7E5 (p=0.0097).

Finally, at 10 mM caffeine, there were no significant differences in the %MR between wild-type C2C12 cells (% MR 67.94; SD 20.57; 95% CI 61.76-74.12) and cell lines 3E1 (%MR 68.7; SD 16.27; 95% CI 62.93-74.47; p=0.9999) or 8E10 (%MR 77.17; SD 20.09; 95% CI 71.73-82.6; p=0.2284); however, cell line 3B9 (%MR 81.76; SD 16.87; 95% CI 77.36-86.15) did have a significantly increased %MR compared to wild-type cells (p=0.0144) As observed in the peak height analysis, cell line 7E5 responded maximally at 10 mM (%MR 101.8; SD 31.8; 95% CI 92.63-110.9) and had a significantly increased response compared to wild-type C2C12 cells (p<0.0001), 3E1 (p<0.0001), 8E10 (p<0.0001) and 3B9 (p<0.0001).

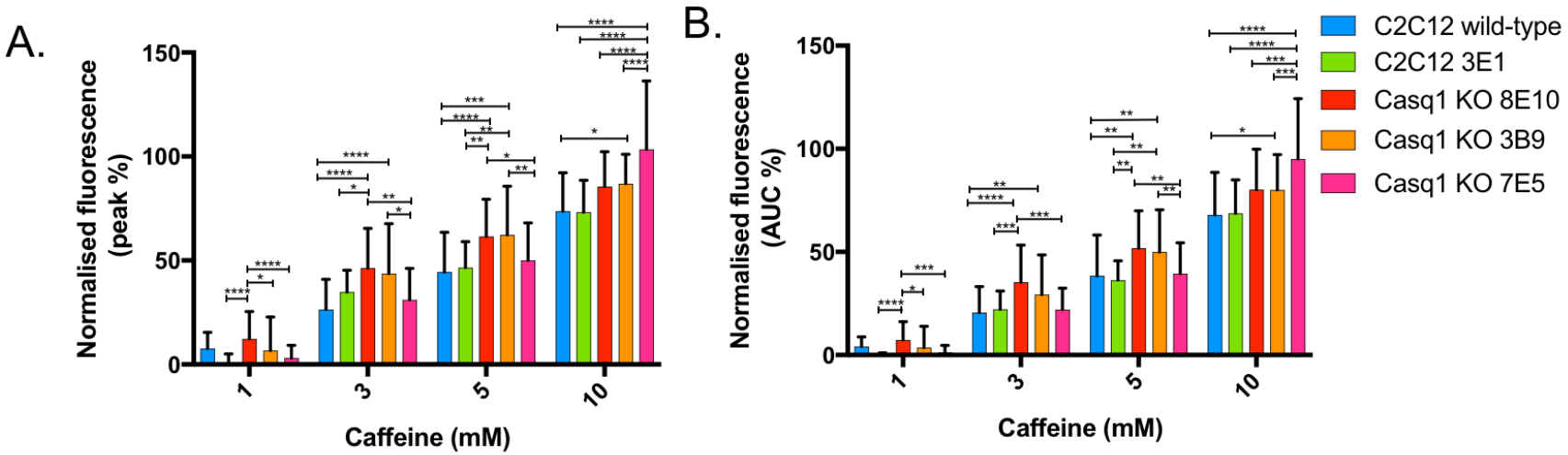

Figure 5.12 – Peak and AUC percentage maximal response of wild-type C2C12 cells and Casq1 KO cell lines at 1, 3, 5 and 10 mM caffeine

The peak (panel A) and AUC (B) percentage maximal response of each cell line at 1 mM, 3 mM, 5 mM and 10 mM caffeine. Baseline fluorescence values were calculated from an average of 20 frames prior to caffeine perfusion at each dose. Baseline was used to define peaks for the AUC analysis and was subtracted from the peak height increase in fluorescence for the peak height analysis. The resultant values for each caffeine concentration were calculated as a percentage of the maximal response at 20 mM caffeine. Data are shown as the mean (from 33-59 myotubes) and error bars are the SD. One-way ANOVA and Tukey's test for multiple comparisons were used to determine significance. *p<0.05, **p<0.01, ***p<0.001, ****p<0.0001.

The increase in fluorescence values from baseline following caffeine perfusion showed a modest, yet significant, reduction in magnitude for cell lines 8E10 and 3B9 compared to wild-type C2C12 cells which is in agreement with data obtained elsewhere (Figure 5.13; Dainese et al., 2009). Following perfusion with 20 mM caffeine, the mean increase in fluorescence from baseline was 648.3 FUs (SD 252.2; 95% CI 575.1-721.5) for wild-type C2C12 cells, 420.6 FUs (SD 251.9; 95% CI 351.9-489.4) for cell line 8E10, 437.9 FUs (SD 295.2; 95% CI 348.1-527.6) for cell line 3B9 and 508.6 FUs (SD 291.9; 95% CI 424.8-592.4) for cell line 7E5. The mean increase in fluorescence for cell lines 8E10 and 3B9 were significantly different to wild-type ($p<0.0001$; $p=0.0009$, respectively) but not to each other ($p=0.9973$) or cell line 7E5 (8E10 $p=0.4016$; 3B9 $p=0.6654$). The mean increase in fluorescence from baseline for cell line 7E5 was not significantly different to wild-type C2C12 cells ($p=0.4016$; $p=0.6654$, respectively). Cell line 3E1 also showed a significant reduction in the increase in fluorescence from baseline compared to wild-type C2C12 cells ($p<0.0001$) and all of the Casq1 KO lines (8E10 $p=0.0005$; 3B9 $p=0.0003$; 7E5 $p<0.0001$); however, this was deemed to be due to reduced SR since a greater proportion of smaller myotubes were produced in this cell type compared to others in section 4.2.12.2. In contrast, no clear difference in the proportions of the size of myotubes could be observed between wild-type C2C12 cells, 8E10, 3B9 and 7E5 (Figure 5.7). As such, the reduction in the magnitude of the response could be due to reduced SR Ca^{2+} stores in the Casq1 KO cell lines 8E10 and 3B9, which has been shown in Casq1 null myofibres previously (Dainese et al., 2009).

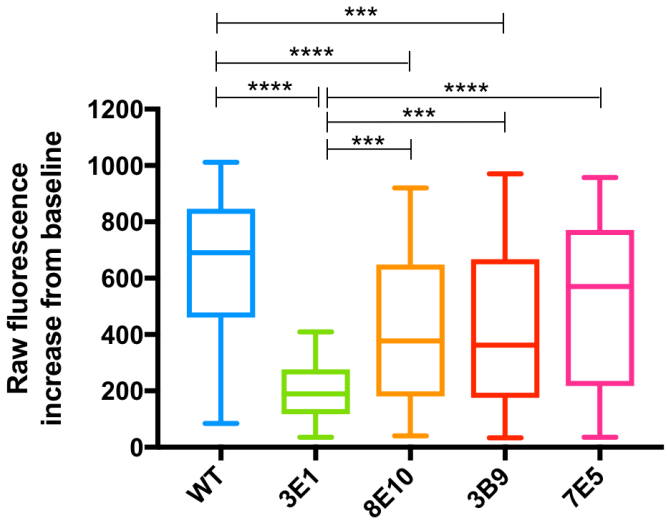

Figure 5.13 – Mean raw fluorescence increases in response to 20 mM caffeine for wild-type C2C12 cells and Casq1 KO cell lines

Baselines were calculated for each myotube by averaging fluorescence values for 20 frames (1 second) prior to perfusion with 20 mM caffeine. Baseline measurements were subtracted from the peak height measurement for each myotube, to generate the raw fluorescence increase. Raw fluorescence increases were averaged across 33-59 genotypes per cell line, generating the mean raw fluorescence increase in response to 20 mM caffeine. The 20 mM caffeine dose has been used for reference; however, the pattern was the same across all caffeine doses. Box plots show the median data point, upper and lower quartiles and the minimum and maximum data points. One-way ANOVA and Tukey's test for multiple comparisons were used to determine significance. ****p<0.0001.

5.2.6 Cloning *CASQ1* cDNAs into pOPINF

To investigate the effect of three *CASQ1* variants on the Ca^{2+} binding and polymerisation abilities of the CASQ1 protein, CASQ1 cDNAs were cloned into an expression vector for heterologous expression and purification, and subsequent downstream *in-vitro* studies. Gibson cloning was used to insert the human *CASQ1* cDNAs for *CASQ1* WT, *CASQ1* p.I138T, *CASQ1* p.F186Y and *CASQ1* p.E364K into the expression vector, pOPINF (a gift from Ray Owens, addgene plasmid 26042). The *CASQ1* cDNAs were amplified without their 102 bp (34 amino acid) N terminal signal peptides from pre-existing vectors. The forward primer used for amplification was designed to contain a 5' overhang with a region of complementarity to the pOPINF vector and a sequence for the completion of the 3C cleavage site upstream of the *CASQ1* cDNA and downstream of the N terminal 6His-tag. The reverse primer contained a 5' overhang containing a region of complementarity to the pOPINF vector and a

stop codon downstream of the *CASQ1* cDNA. Digestion of pOPINF with *Kpn*I and *Hind*III and the subsequent 5' exonuclease digestion of the PCR amplicon and linearised vector yielded large 3' overhangs that annealed via complementary base pairing in a ligation reaction (see Methods for a schematic of the cloning reaction). Ligation reactions were transformed into XL10-gold® ultracompetent *E. coli* cells (Agilent) and plated on LB agar plates containing 100 µg/ml ampicillin with 40 µl 100 mM IPTG and 120 µl 20 mg/ml X-gal spread onto the surface of the plate. Four single colonies (with the exception of *CASQ1* p.E364K transformants for which only 3 white colonies were generated) were used to inoculate 5 ml LB media and cultures were incubated overnight at 37°C with shaking at 200 rpm. Plasmid DNA was isolated by miniprep. The resultant plasmid DNA was linearised with *Eag*I and the products separated by gel electrophoresis to confirm the size of the vector. Insertion of the 1086 bp *CASQ1* cDNA increased the size of the 5.5 kb vector to approximately 6.5 kb (Figure 5.14). With the exception of CASQ1 WT colony 4, all colonies appeared to contain the *CASQ1* cDNA insert. A series of overlapping primers were designed across the entire *CASQ1* insert within pOPINF for Sanger sequencing confirmation of the insertion. All variants were confirmed and plasmids were selected for use that had no additional point mutations introduced by erroneous PCR (Figure 5.15).

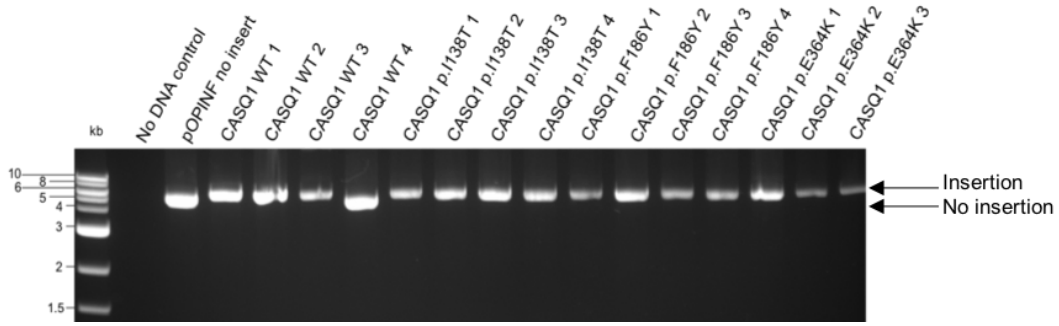

Figure 5.14 – EagI digest of pOPINF to confirm *CASQ1* cDNA insertion

Plasmid DNA from putative recombinant CASQ1 expression vectors was digested with *Eag*I and reaction products were separated by gel electrophoresis. Lane 1 shows the 1 kb ladder (NEB), lane 2 shows a DNA negative control reaction and the subsequent lanes show the linearised vectors from colonies picked for CASQ1 WT, CASQ1 p.I138T, CASQ1 p.F186Y and CASQ1 p.E364K ligation reactions.

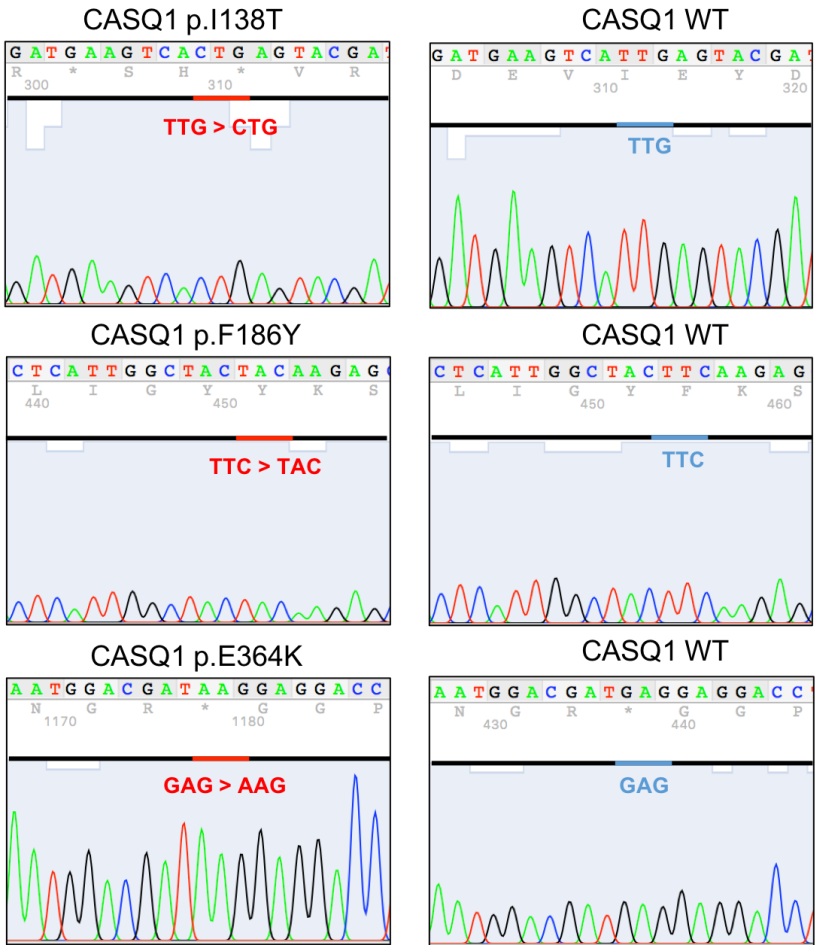

Figure 5.15 – Sanger sequencing confirmation of CASQ1 variants in pOPINF

Plasmids confirmed to contain the *CASQ1* cDNA insertion were processed for Sanger sequencing using a series of overlapping primers to enable sequencing of the entire insert. Wild-type sequences are underlined in black, the edited codon is shown in red and the wild-type codon is shown in blue.

5.2.7 Purification of CASQ1 WT and CASQ1 variant proteins

Plasmids containing *CASQ1* WT and variant cDNA sequences were transformed into BL21(DE3) Rosetta™ *E. coli* cells (Novagen) that supply transfer RNAs (tRNAs) for eukaryotic codon optimisation. DE3 denotes that the strain contains the λDE3 lysogen which encodes the T7 RNA polymerase for high level transcription of the *CASQ1* cDNA sequence following induction with IPTG. The culture was incubated overnight at 18°C with shaking prior to centrifugation, cell lysis and lysate clarification. Samples of the pellet following centrifugation to clarify lysates were retained for analysis by SDS-PAGE to ensure that CASQ1 proteins were not within the insoluble fraction. Proteins were initially purified from the clarified cell lysates by nickel affinity

chromatography using nickel-charged HisTrap™ HP 1 ml columns (GE Healthcare) on the AKTA Pure FPLC system (GE Healthcare). The elution of proteins was monitored using ultraviolet (UV) absorbance at 280 nm in UNICORN software (GE Healthcare) (Figure 5.16). The application of the sample to the column and its subsequent flow-through resulted in an increase in UV absorbance at 280 nm, as was observed for wash steps. Samples from the flow-through and wash steps were retained for analysis by SDS-PAGE along with selected fractions within the elution peak starting at 60 ml to confirm the presence of the CASQ1 proteins (Figure 5.17).

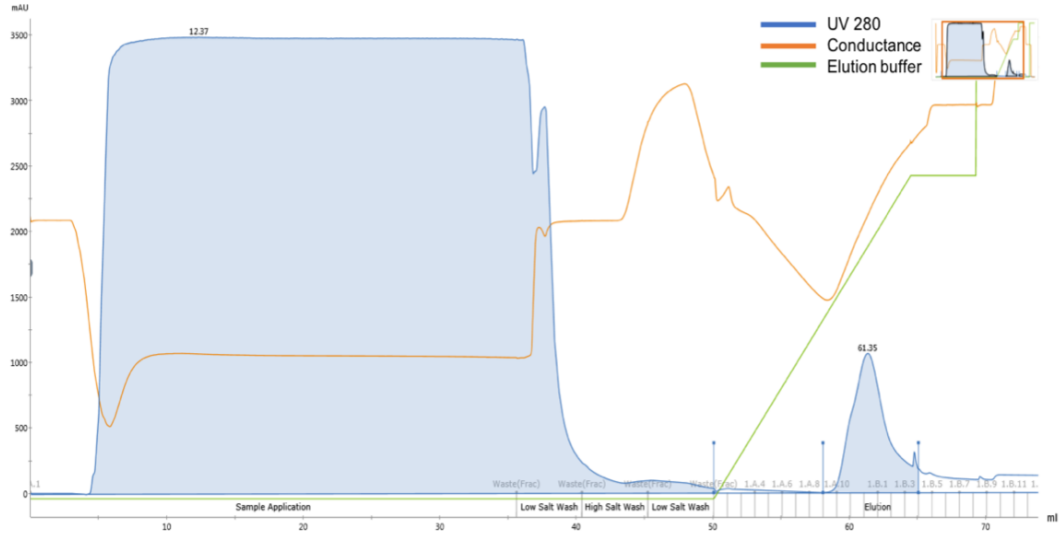

Figure 5.16 – Nickel affinity chromatogram for CASQ1 purification

Proteins eluted from the column were measured by UV absorbance at 280 nm (blue line) and this is shown as milli absorbance units (mAU). Changes in conductance throughout the run are shown by an orange line and the concentration of elution buffer is shown by a green line indicating the linear gradient to 70% and followed by a step up to 100% elution buffer. Numbers above the peaks in absorbance at 280 nm show the number of mls at which the peak is present. For reference, an example trace following nickel affinity purification of the CASQ1 WT protein is shown. In total, 2 batches of each CASQ1 protein were used for the collection of data presented in this chapter. Chromatograms were generated in UNICORN software (GE Healthcare).

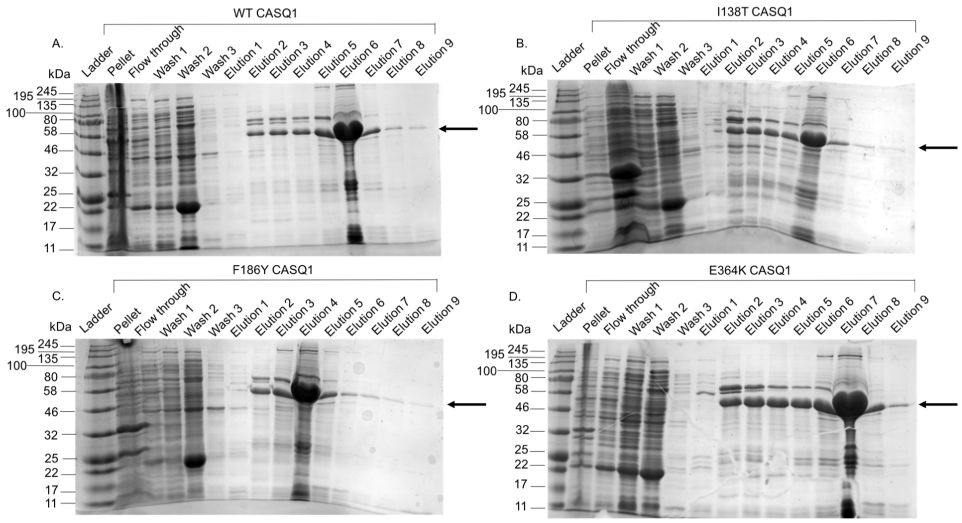

Figure 5.17 – SDS-PAGE analysis of nickel affinity purification of CASQ1 WT and variant proteins

The CASQ1 WT (panel A), CASQ1 p.I138T (panel B), CASQ1 p.F186Y (panel C) and CASQ1 p.E364K (panel D) proteins were initially purified by nickel affinity chromatography using the AKTA Pure FPLC system and the eluted proteins analysed by SDS-PAGE on 12% gels. Lane 1 shows the Broad Range Colour Prestained Protein Standard (NEB). Lane 2 shows the sample of the cell pellet following centrifugation prior to cell lysis. Lane 3 shows the flow through upon sample loading i.e sample that did not bind to the HisTrap™ 1 ml column. Lanes 4-6 show samples eluted following washing of the column and lanes 7-15 show eluted fractions that showed a peak in UV absorbance at 280 nm. An arrow indicates the band corresponding to CASQ1.

For all samples, a large band was identified in one of the eluted fractions (elution 6 for CASQ1 WT, elution 6 for p.I138T, elution 4 for p.F186Y and elution 7 for p.E364K), corresponding to a molecular weight between 46 kDa and 58 kDa. Whilst the expected molecular weight (Mw) of the CASQ1 proteins (without the N terminal signal peptide and with the 6His-tag and 3C cleavage site) is approximately 43.8 kilodaltons (kDa), reduced migration during SDS PAGE has been reported for other acidic proteins (Graceffa et al., 1992). Additional eluted fractions contained smaller, yet substantial, bands at the same molecular weight. No significant bands at the same molecular weight were identified in the pellet, flow through or wash steps in CASQ1 WT, CASQ1 p.I138T, CASQ1 p.F186Y or CASQ1 p.E364K; however, all of the fractions contained contaminant proteins. To remove contaminants, the eluted fractions containing the supposed CASQ1 protein were pooled and size exclusion chromatography (SEC) using a HiLoad Superdex 26/600 200 pg column (GE

Healthcare) was performed. Again, protein elution was monitored by UV absorbance at 280 nm (Figure 5.18). Eluted fractions that showed distinct peaks in absorbance at 280 nm were analysed by SDS PAGE. For all CASQ1 proteins, fractions eluted at approximately 200 ml contained CASQ1, as did fractions eluted at approximately 116 ml. The other peaks did not contain detectable amounts of protein by SDS-PAGE and InstantBlue™ Coomassie staining. Since larger species are eluted first, it is likely that the fractions eluted at 116 ml contained CASQ1 proteins that were not present in monomeric form; however, at the time of these experiments, the AKTA Pure FPLC system had not been calibrated with Mw standards to enable Mw determination of the peaks. Nonetheless, fractions containing CASQ1 following SEC elution were pooled and concentrated using Pierce™ spin concentrators. SDS PAGE was performed followed by 2D densitometry to determine the purity of the CASQ1 proteins produced (Figure 5.19). Across the 2 batches of protein used to generate the data presented in this chapter, CASQ1 WT had a mean percentage purity of 89.4%. The mean percentage purities of CASQ1 p.I138T, CASQ1 p.F186Y and CASQ1 p.E364K were 91.5%, 93.0% and 94.0%, respectively.

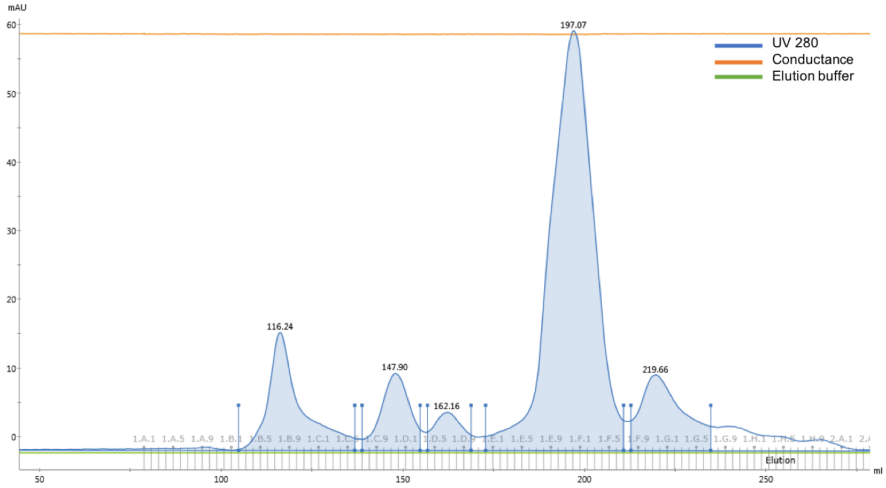

Figure 5.18 – SEC chromatogram for CASQ1 purification

Increases in UV absorbance at 280 nm (blue line) are shown as mAUs. Conductance, which remains stable since a single buffer is used for SEC, is shown by an orange line. The concentration of elution buffer, which is not required for SEC and thus remains at 0, is shown by a green line. Numbers above the peaks show the number of mls at which that peak is present. Note that the chromatogram has been cropped at the left side to enable fitting to the page. The actual total volume of solution applied to the column was 356 ml; however, no further increases in absorbance at 280 nm were observed after the return to 0 mAUs shown here at 274 ml. For reference, a representative trace is shown here from the SEC purification of CASQ1 F186Y; however, all proteins consistently showed a similar elution pattern. Chromatograms were generated in UNICORN software (GE Healthcare).

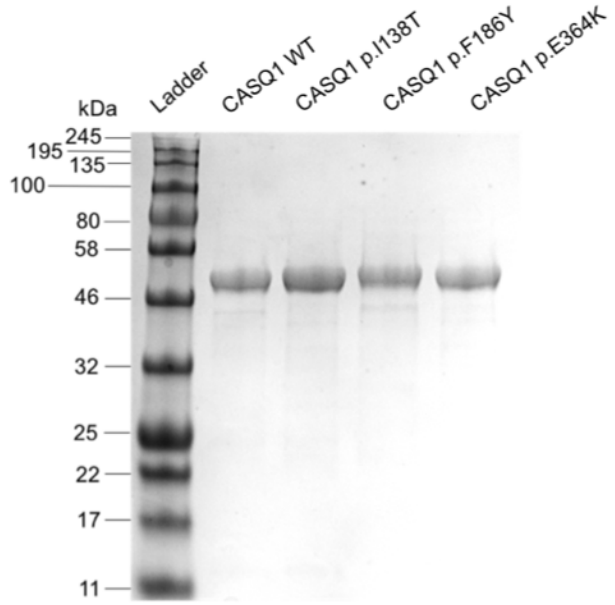

Figure 5.19 – Purified CASQ1 WT, CASQ1 p.I138T, CASQ1 p.F186Y and CASQ1 p.E364K proteins

CASQ1 proteins were purified by nickel affinity chromatography followed by SEC. To calculate percentage purity, 10 µg protein was heated at 95°C for 5 min with loading buffer and loaded onto a 12% acrylamide SDS-PAGE gel. Densitometry was performed using ImageJ.

5.2.8 Confirmation of protein identity

To confirm the identity of the proteins produced, samples of purified CASQ1 WT, CASQ1 p.I138T, CASQ1 p.F186Y and CASQ1 p.E364K proteins were submitted to the Leeds Mass Spectrometry facility for digestion and peptide mass fingerprinting by MS. The resultant peptides were searched against against a Uniprot database for CASQ1 for amino acid sequence assembly. (Figure 5.20). The presence of each variant was confirmed within the amino acid sequences, although coverage was not obtained across all of the variant residues in the CASQ1 WT sample. The identity of the CASQ1 WT protein was confirmed by determination of its Mw by denatured intact liquid chromatography MS (LC-MS) (Figure 5.21; Figure 5.22).

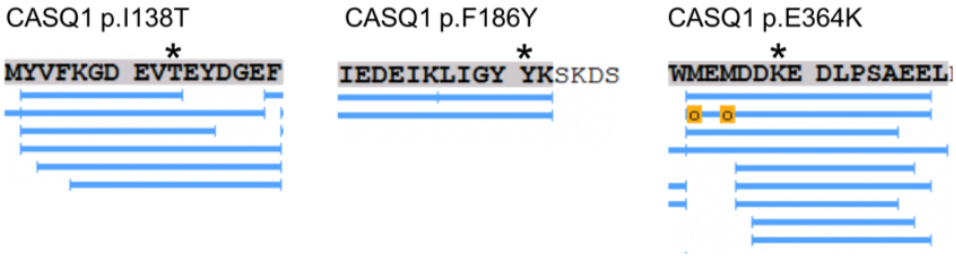

Figure 5.20 – Protein ID of variant CASQ1 proteins

Samples of purified CASQ1 variant proteins were submitted for peptide mass fingerprinting as a service at the Leeds Mass Spectrometry facility. An asterisk indicates the substituted residue. Coverage of the region is indicated by blue bars beneath the amino acid sequence and oxidation events are shown by O.

The expected molecular weights (Mw) of each CASQ1 protein (taking into account the loss of the N terminal signal peptide and introduction of an N terminal 6His-tag and 3C cleavage site) were calculated using the ExPASy pI/Mw tool (available at web.expasy.org/compute_pi/) (Table 5.3). For all CASQ1 proteins, the major species present within the MS spectrum represented the full-length protein minus the 132 Da N terminal methionine residue (Table 5.3). Cleavage of the N terminal methionine residue is a common occurrence during recombinant protein expression in *E. coli* via the activity of methionine aminopeptidase (Wingfield, 2017). In addition to N terminal methionine cleavage, the denatured intact analysis revealed a range of modifications to the CASQ1 proteins; however these were present in considerably smaller amounts than the desired protein (Figure 5.21; Figure 5.22). The putative identities of these species are provided in Appendix D.

Table 5.3 – Predicted and identified Mw by denatured intact MS

Values are shown in kDa.

Protein	Predicted Mw	Identified Mw	Predicted Mw minus N' Met
CASQ1 WT	43.829	43.697.36±0.62	43.697
CASQ1 p.I138T	43.817	43.685.21±0.68	43.685
CASQ1 p.F186Y	43.845	43.713.49±0.71	43.713
CASQ1 p.E364K	43.828	43696.57±0.69	43.696

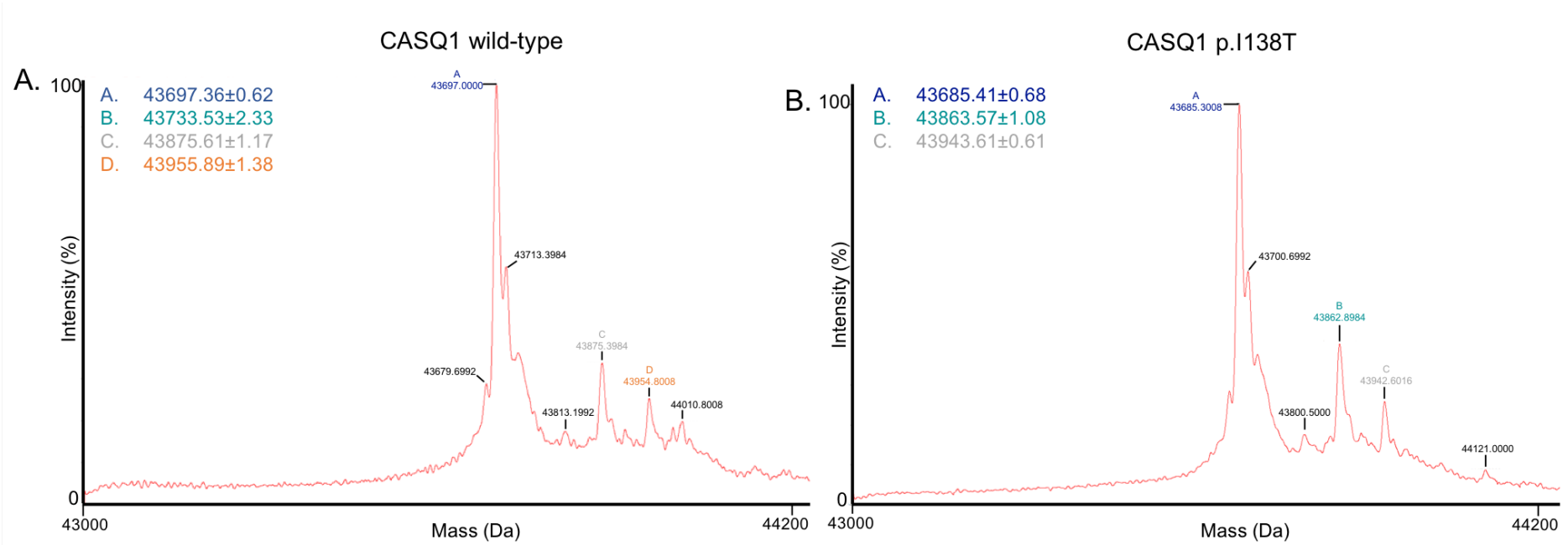

Figure 5.21 – Denatured intact LC-MS of CASQ1 WT and CASQ1 p.I138T

Denatured intact LC-MS and analysis was provided as a service by the Leeds Mass Spectrometry Facility at the Astbury Centre for Structural Molecular Biology using the Synapt G1 mass spectrometer (Waters). Spectra were analysed in MassLynx^{TM} (Waters) and the maximum peak normalised to 100% intensity (Y axis). The Mw in Da is shown on the X axis. The Mws of the most resolved peaks are shown to the left of the spectra. Note that the labelling does not correspond between CASQ1 proteins i.e. species B in the CASQ1 WT sample (panel A) does not correspond to species B in the CASQ1 p.I138T sample (panel B). Where species are labelled to the left of the spectrum, but the peak is not labelled on the trace, this is due to the trace not being sufficiently 'zoomed in' on the software to achieve resolution. In such cases, the peaks to which the label corresponds can be inferred from the Mw of adjacent peaks.

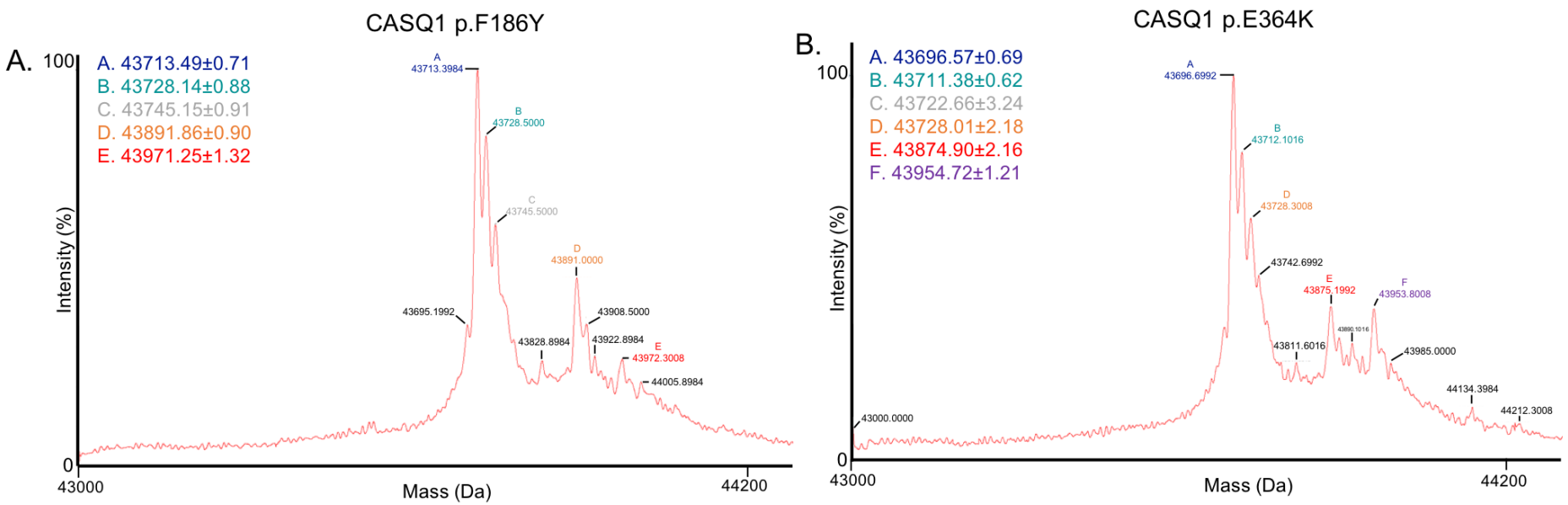

Figure 5.22 – Denatured intact LC-MS of CASQ1 p.F186Y and CASQ1 p.E364K

Denatured intact LC-MS and analysis was provided as a service by the Leeds Mass Spectrometry Facility at the Astbury Centre for Structural Molecular Biology using the Synapt G1 mass spectrometer (Waters). Spectra were analysed in MassLynx^{TM} (Waters) and the maximum peak normalised to 100% intensity (Y axis). The Mw in Da is shown on the X axis. The Mws of the most intense peaks are shown to the left of each spectrum with colour-coded labels. Note that the labelling does not correspond between CASQ1 proteins i.e. species C in the CASQ1 p.F186Y sample (panel A) does not correspond to species C in the CASQ1 p.E364K sample (panel B). Where species are labelled to the left of the spectrum, but the peak is not labelled on the trace, this is due to the trace not being sufficiently 'zoomed in' on the software to achieve resolution. In such cases, the peaks to which the label corresponds can be inferred from the Mw of adjacent peaks.

5.2.9 Investigation of Ca^{2+} binding by MST

MST was used to investigate the effect of Ca^{2+} addition on the CASQ1 WT, CASQ1 p.I138T, CASQ1 p.F186Y and CASQ1 p.E364K proteins (Figure 5.23). MST is based on the thermophoresis (movement along a temperature gradient) of fluorescently labelled protein molecules. Thermophoresis, and subsequently the fluorescent signal, is altered by changes in the size, charge, conformation and hydration shell of the protein (Jerabek-Willemsen et al., 2011). CASQ1 proteins were labelled with FITC and allowed to equilibrate with a Ca^{2+} titration from 100 mM-6 µM (including a no Ca^{2+} control), prior to loading on the Monolith NT.115 system (NanoTemper). As expected, the CASQ1 WT protein (Figure 5.23; Panel B) produced a multiphasic binding curve that appeared to contain at least two phases, in agreement with reports in the literature (Sanchez et al., 2012; Beard et al., 2004). The first binding phase was initiated at 0.1 mM Ca^{2+}, indicated by a reduction in the fluorescence signal (i.e. increased thermophoresis) between 0.1 mM Ca^{2+} to 0.4 mM Ca^{2+}. Between 0.4 mM Ca^{2+} and 1.5 mM Ca^{2+}, the fluorescence signal stabilised prior to another reduction in fluorescence between 1.5 mM Ca^{2+} and 3 mM Ca^{2+}. It is unclear whether the apparent stabilisation in fluorescence between 3 mM Ca^{2+} and 6 mM Ca^{2+} represents a plateau of the second binding phase. As such, the reduction in fluorescence observed from 6 mM Ca^{2+} may represent a third binding phase or may be a continuation of the second binding phase. Between 0 mM Ca^{2+} and 100 mM Ca^{2+}, the fluorescence values reduced by approximately 40 FUs.

The binding phases observed for the CASQ1 p.I138T and CASQ1 p.F186Y proteins were less distinct than that of CASQ1 WT (Figure 5.23; Panel C) with normalised fluorescence values not reducing by more than 20 FUs across the Ca^{2+} serial dilution. For both proteins, fluorescence measurements between 0 mM Ca^{2+} and 0.1 mM Ca^{2+} were similar to CASQ1 WT. For CASQ1 p.I138T, a minor reduction in fluorescence was observed between 0.4 mM Ca^{2+} and 3 mM Ca^{2+} and between 12 mM Ca^{2+} and 50 mM Ca^{2+} at which the signal plateaus. For CASQ1 p.F186Y, a minor reduction in fluorescence is seen between 0.1 mM Ca^{2+} and 0.4 mM Ca^{2+}. At 12 mM Ca^{2+}, another reduction in the fluorescence signal is observed. For CASQ1 p.E364K, the fluorescence values were increased compared to CASQ1 WT and the two other variant CASQ1

proteins; however, the magnitude of changes in thermophoresis, as indicated by reductions in fluorescence, were comparable to CASQ1 WT. Between 0 mM Ca^{2+} and 0.1 mM Ca^{2+}, fluorescence values were generally stable and, with the exception of values at 0.2 mM Ca^{2+} and 0.4 mM Ca^{2+}, a similar pattern in fluorescence changes were observed as in CASQ1 WT.

Since changes in thermophoresis depend on several factors including size, charge and conformation, the binding events shown in these data likely represent changes in thermophoresis as a result of CASQ1 polymerisation in addition to Ca^{2+} binding. As such, Ca^{2+} binding affinities could not be derived. Nonetheless, qualitatively, these data suggest alterations in Ca^{2+} binding and polymerisation in at least CASQ1 p.I138T and CASQ1 p.F186Y.

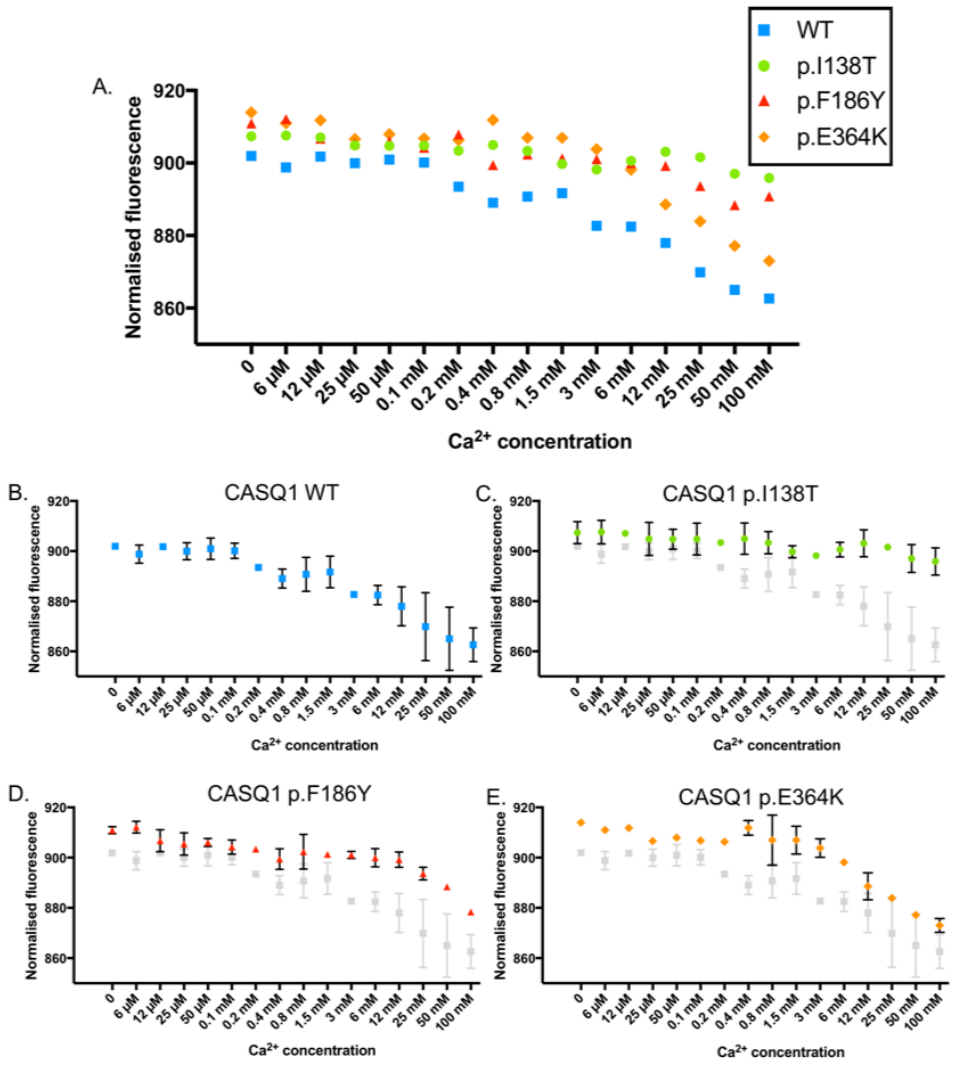

Figure 5.23 – Effect of Ca^{2+} addition on CASQ1 WT and variant proteins determined by MST

FITC-labelled proteins were incubated with a 2-fold $CaCl_2$ serial dilution to final concentrations of 6 µM to 100 mM. MST was performed using the Monolith NT.115 (NanoTemper Technologies) and values obtained using MST power 20% are shown. Fluorescence units were normalised to baseline measurements taken prior to thermophoresis and are shown on the Y axis. Ca^{2+} concentration is on the X axis. Panel A shows an overlay of the binding events for CASQ1 WT (blue squares), CASQ1 p.I138T (green circles), CASQ1 p.F186Y (red triangles) and CASQ1 p.E364K (orange diamonds) without error bars for clarity. Individual graphs for CASQ1 WT (panel B), CASQ1 p.I138T (panel C), CASQ1 p.F186Y (panel D) and CASQ1 p.E364K (panel E) are shown, with CASQ1 variant graphs showing an overlay of the CASQ1 WT trace in grey. Fluorescence values from two experiments were averaged and error bars show the SD. Where error bars are not shown, their height was shorter than the symbol indicating the fluorescence value with the exception of the 200 µM and 100 mM points for p.F186Y which are comprised of 1 n since the others showed anomalous fluctuations in fluorescence.

5.2.10 Native MS in the absence of Ca^{2+} and presence of 1 mM Ca^{2+}

Since a single quantitative effect on Ca^{2+} binding could not be distinguished by MST, a combination of native and denatured MS was performed to determine whether Ca^{2+} binding to the CASQ1 proteins could be detected. In theory, Ca^{2+} binding to CASQ1 would result in a shift of the expected mass in the native samples by a number divisible by 40 Da (the size of a Ca^{2+} ion), that would not be observed in the denatured samples due to Ca^{2+} release following unfolding. X-ray crystallography has previously shown that CASQ1 is purified bound to 3 high affinity Ca^{2+} ions that are important for protein folding (Sanchez et al., 2012). To determine whether that was the case here, the CASQ1 WT protein was initially submitted for native analysis without added Ca^{2+}. The heterogenous nature of the CASQ1 complicated the determination of the number of Ca^{2+} bound to CASQ1. Two major species were resolved that had masses of 43818.05 Da and 44037.91 Da (Figure 5.24). The major species at 43818 Da was ~120 Da larger than the predominant peak identified by the denatured analysis which was the expected mass of CASQ1 WT minus the N terminal methionine residue (43696 Da), suggesting that 3 Ca^{2+} ions were bound to CASQ1 WT following purification which is in agreement with reports in the literature (Sanchez et al., 2012). The second species at 44037 Da was ~340 kDa larger than CASQ1 WT minus the N-terminal methionine, and 324 Da larger than the second most intense peak identified in the denatured analysis (43713 Da). This mass could represent CASQ1 WT minus the N terminal methionine residue with an oxidation event (+16 Da) bound to 8 Ca^{2+} ions (+320 Da). These masses were unaltered following dialysis against 1 mM EGTA, suggesting that if Ca^{2+} was bound, it was with high affinity.

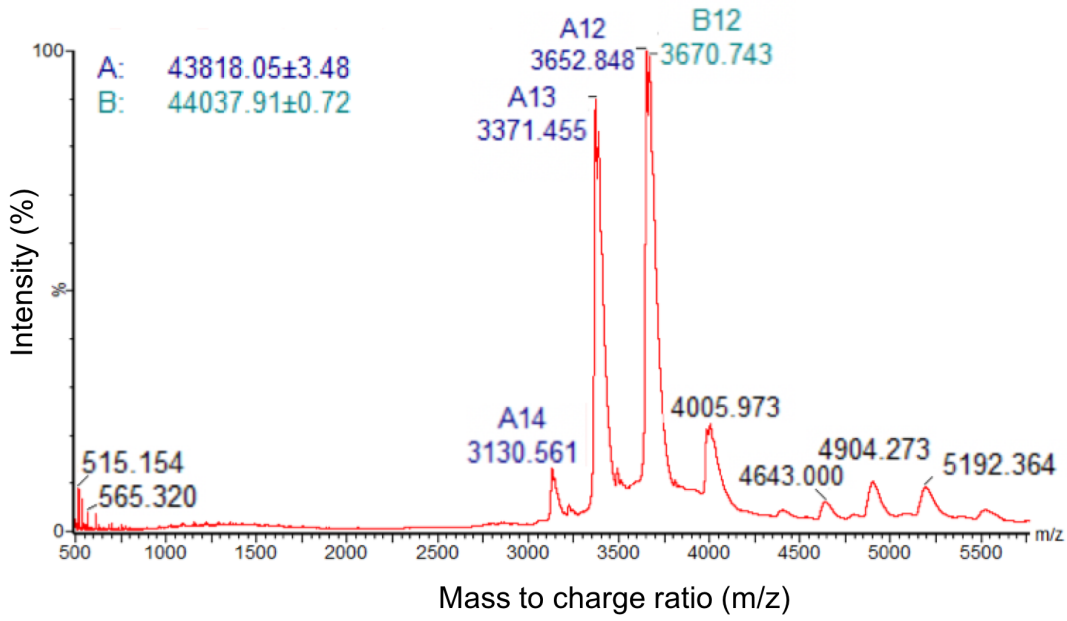

Figure 5.24 – Native MS of CASQ1 WT with no added Ca^{2+} using the Synapt G1 instrument

CASQ1 WT samples were buffer exchanged into 200 mM ammonium acetate and native mass spectrometry was performed in ESI TOF positive ion mode using the Synapt G1 high definition mass spectrometer. The Y axis shows the percentage intensity of each peak identified, where the predominant peak is normalised to 100%. The X axis shows the mass to charge ratio (m/z) and peaks are labelled with their m/z ratio and charge state. The masses of the most resolved peaks are shown to the left of the m/z spectrum.

The heterogeneity of CASQ1 WT-Ca^{2+} stoichiometries (in the absence of added Ca^{2+}) was further revealed using the Q Exactive™ Plus mass spectrometer which provided increased resolution of species in the absence of Ca^{2+}; however, the parameters of this instrument were still in the process of optimisation at the time of these experiments and masses may not be accurate to the Dalton (Dr Rachel George, pers comms.) (Figure 5.25). The predominant species (species C) had a mass of 43810 Da. This was 114 Da greater than predominant mass detected in the denatured analysis corresponding to CASQ1 WT minus the N terminal methionine residue (43696 Da; Figure 5.21) and 6 Da less than the predominant species detected in the initial native analysis (Figure 5.24). Interestingly, species A identified in this native analysis was ~39 Da larger than CASQ1 WT minus the N terminal methionine and species B was, in turn, 40 Da larger than species A. The predominant species C was 35 Da larger than species B. As such, it is possible that species C represents 3 Ca^{2+} bound to CASQ1 WT minus the N

terminal methionine, as identified in previous analyses (Figure 5.24). The pattern of the sequential addition of 35-40 Da continued until species M and could reflect different CASQ1-Ca^{2+} stoichiometries.

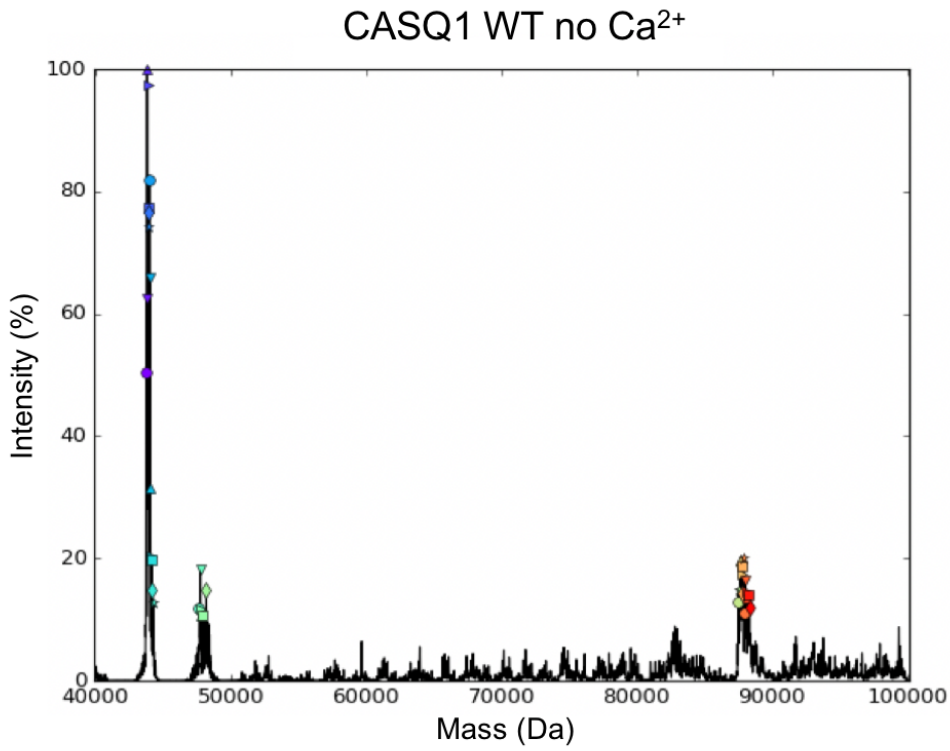

Mass (Da)	Intensity	Name
43735.0	50.27	A
43775.0	62.57	B
43810.0	100.00	C
43845.0	97.46	D
43880.0	77.37	E
43915.0	76.68	F
43955.0	74.30	G
43990.0	81.68	H
44030.0	65.76	I
44065.0	31.56	J
44100.0	20.35	K
44140.0	19.79	L
44185.0	14.88	M
44245.0	12.69	N
47710.0	11.82	O
47740.0	18.30	P
47785.0	10.72	Q
47825.0	11.82	R
47940.0	10.60	S
48190.0	14.97	T
87540.0	14.81	U
87620.0	12.79	V
87695.0	18.15	W
87745.0	19.76	X
87775.0	17.42	Y
87825.0	18.87	Z
87855.0	14.21	A2
87895.0	20.18	B2
87985.0	10.90	C2
88050.0	16.53	D2
88135.0	13.59	E2
88215.0	14.63	F2
88275.0	14.17	G2
88355.0	12.03	H2

Figure 5.25 – Native MS of CASQ1 WT with no added Ca^{2+} using the Q Exactive™ Plus instrument

A CASQ1 WT sample was buffer exchanged into 200 mM ammonium acetate and native mass spectrometry was performed using the Q Exactive™ Plus mass spectrometer. The Y axis shows the percentage intensity of each peak identified, where the predominant peak is normalised to 100%. The X axis shows the mass in Da and the masses of the resolved peaks are shown beneath the mass spectrum.

Species with masses corresponding to dimeric CASQ1 were identified (species U-H2), supporting previous observations of the elution of non-monomeric CASQ1 species during SEC (Figure 5.18). Sample heterogeneity meant that the accurate determination of the number of Ca^{2+} ions bound to dimer species was not possible, since the monomeric form of each dimer species was not known; however, the sequential addition of ~80 Da (potentially corresponding to 2 Ca^{2+} ions) was observed between species U and V, V and W, C2 and D2, D2 and E2 and G2 and H2. A single increase in mass by 40 Da was observed between species A2 and B2. Whilst the ability to determine the number of Ca^{2+} ions bound to each dimer species was limited, these data suggested that CASQ1-CASQ1 interactions could be maintained in the gas phase. As such, further experiments were performed to investigate whether a difference in the polymerisation capacity of each CASQ1 protein could be detected by MS. All of the CASQ1 proteins with and without 1 mM Ca^{2+} were submitted for analysis by native MS. Sample heterogeneity meant that the identity of each species was ambiguous, hence general trends in the data have been presented here. The possible identities of each species are speculated in Appendix D.

As expected, in the absence of added Ca^{2+}, CASQ1 WT existed in a predominantly monomeric form (Figure 5.26). The most abundant mass was 43728 Da with two additional species corresponding to monomers of 43890 Da and 43972 Da identified. Masses corresponding to dimeric CASQ1 were also identified ranging from 87488 Da to 87936 Da. Consistent with the well-established function of CASQ1, CASQ1 WT showed Ca^{2+} dependent polymerisation following addition of 1 mM Ca^{2+}, with dimeric (88200 Da) and higher order species identified. A peak corresponding to tetrameric CASQ1 (~175000 Da) was identified; however, a mass was not assigned due to the broadness of the peaks that prevented mass determination by the software used for analysis (Dr Rachel George, pers. comms.). The presence of a species at 132 kDa was unexpected, since CASQ1 forms back-to-back dimers that interact to form front-to-front tetramers. The presence of this seemingly trimeric species could reflect a limitation in the maintenance of CASQ1 polymers into the gas phase.

In the absence of Ca^{2+}, the CASQ1 p.I138T sample contained masses comparable to wild-type (Figure 5.26). Again, these were predominantly monomeric (43990 Da and 44182 Da) with a proportion of dimeric CASQ1s (88190 Da). In contrast to CASQ1 WT, no species larger than dimeric CASQ1 were identified in the CASQ1 p.I138T following 1 mM Ca^{2+} addition (44252 Da, 88148 Da and 88166 Da). In the absence of added Ca^{2+}, CASQ1 p.F186Y existed primarily as a monomer (43830 Da and 43986 Da) (Figure 5.27). Whilst a mass was not assigned, it appeared that dimeric species were present; however, the broadness of the peaks precluded mass determination (Dr Rachel George, pers. comms.). Similarly to CASQ1 p.I138T, p.F186Y did not appear to polymerise in response to 1 mM Ca^{2+} with only monomeric species identified (44172 Da and 44474 Da). For CASQ1 p.E364K, only monomeric species were identified in the absence of Ca^{2+} (43724 Da, 43906 Da and 43962 Da); however, Ca^{2+} dependent polymerisation occurred in a manner similar to that observed for CASQ1 WT (Figure 5.27), with species corresponding to tetrameric CASQ1 identified (175970 Da). Sample heterogeneity and a plethora of CASQ1-Ca^{2+} stoichiometries meant the determination of the number of Ca^{2+} ions bound to each species was not possible. Nonetheless, qualitatively, these data suggest that CASQ1 p.I138T and CASQ1 p.F186Y have impaired polymerisation capacities at 1 mM Ca^{2+} compared to CASQ1 WT and CASQ1 p.E364K, which is in agreement with data obtained from MST measurements.

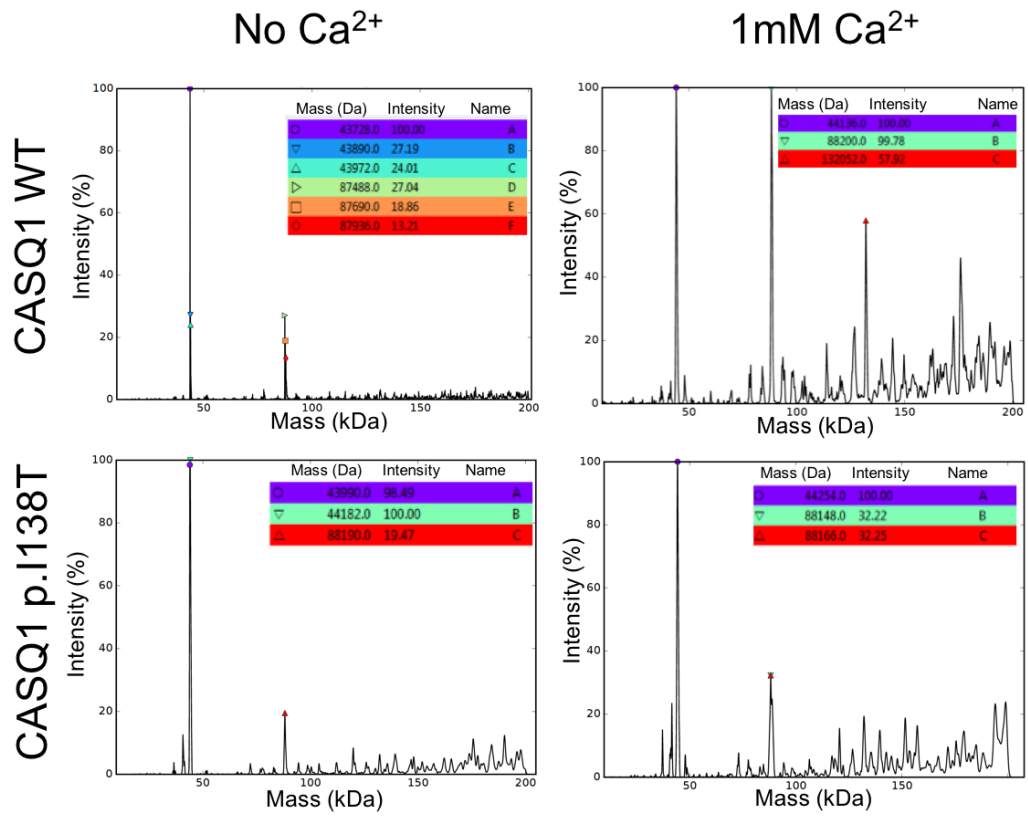

Figure 5.26 – Native MS of CASQ1 WT and CASQ1 p.I138T in the absence and presence of 1 mM Ca^{2+}

CASQ1 samples were buffer exchanged into 200 mM ammonium acetate (no added Ca^{2+}) or 200 mM ammonium acetate with 1 mM calcium acetate and native mass spectrometry was performed using the Q Exactive™ Plus mass spectrometer. The predominant peak is normalised to 100%. Masses of the resolved peaks are shown to the right of the mass spectra in Da.

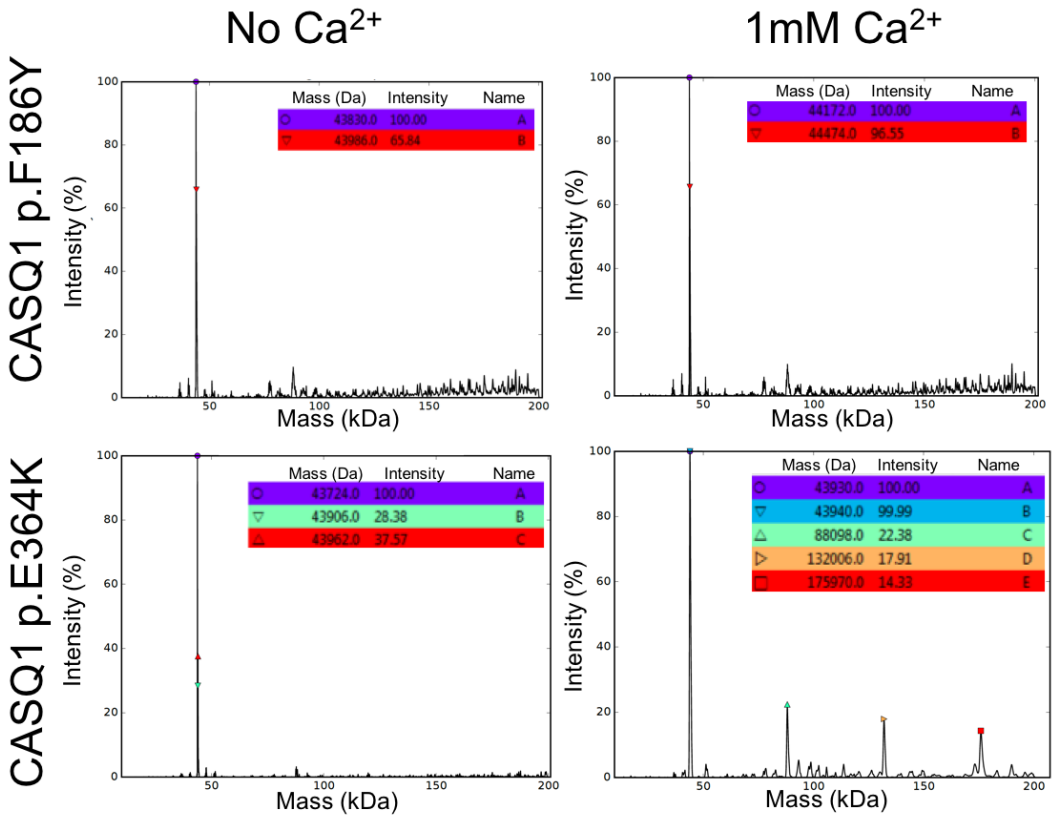

Figure 5.27 – Native MS of CASQ1 p.F186Y and p.E364K in the absence and presence of 1 mM Ca^{2+}

CASQ1 samples were buffer exchanged into 200 mM ammonium acetate (no added Ca^{2+}) or 200 mM ammonium acetate with 1 mM calcium acetate and native mass spectrometry was performed using the Q Exactive™ Plus mass spectrometer. The predominant peak is normalised to 100% intensity. Masses of the resolved peaks are shown to the right of the mass spectra in Da.

5.2.11 Dynamic light scattering in the absence and presence of Ca^{2+}

Since native MS takes place in the gas phase and the data obtained suggested limitations in the preservation of CASQ1-CASQ1 interactions, DLS was used to further explore the effect of Ca^{2+} on the polymerisation properties of CASQ1 WT and the variant CASQ1 proteins in solution. Due to usage limitations of the DLS instrument, a single Ca^{2+} concentration was selected to determine whether there were differences in the size of polymers produced by CASQ1 variants compared to CASQ1 WT. Ca^{2+} at 10 mM was selected since CASQ1 WT polymerisation has previously been shown to plateau at this concentration (Lewis et al., 2015). The CASQ1 p.I138T and CASQ1 p.E364K samples appeared to aggregate prior to the experiment with only species with higher

hydrodynamic radii (Rh) (>100 nm) present in both the 0 mM Ca^{2+} and 10 mM Ca^{2+} samples (data not shown). Light scattering data for CASQ1 WT and CASQ1 p.F186Y was analysed by the method of regularisation due to the anticipated polydispersity of samples (Hassan et al., 2015).

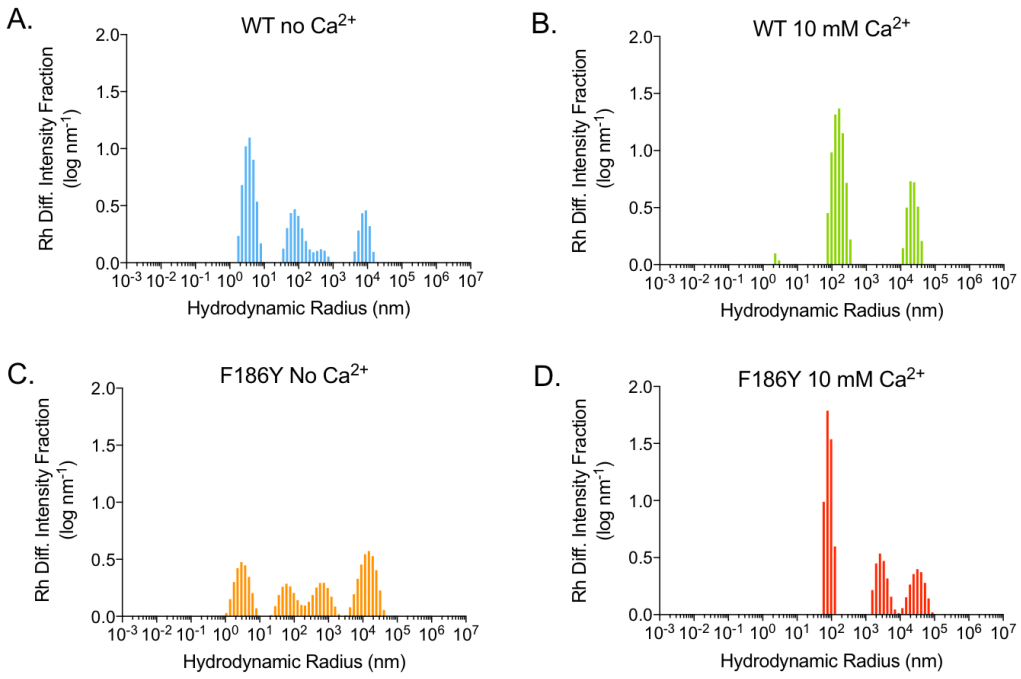

Figure 5.28 – DLS regularisation plots of CASQ1 WT and CASQ1 p.F186Y with and without 10 mM Ca^{2+}

DLS was performed for CASQ1 WT and CASQ1 p.F186Y in the absence of added Ca^{2+} (panel A and C, respectively) and in the presence of 10 mM Ca^{2+} (panel B and D, respectively). Data were analysed using ASTRA® 6.0.3 software. Regularisation graphs were plotted using Prism 7 (GraphPad), where the X axis shows the Rh differential intensity fraction (log nm^{-1}) i.e. the relative intensity of each Rh species and the Y axis shows the Rh in nm. Values are derived from a single experiment.

For the both CASQ1 WT and CASQ1 p.F186Y, four peaks were apparent in the absence of added Ca^{2+} (Figure 5.28; panel A and panel B); however the second and third peaks (from left to right) were merged due to high sample dispersity that precluded resolution into distinct peaks. As such, peaks 2 and 3 are collectively referred to as peak 2 here onwards. Rh values are reported as the species with the highest relative intensity within the peak. In the CASQ1 WT sample, peak 1 had an Rh of 3.76 nm. The two major species within peak 1, of near equal relative intensity, had Rh values of 2.92 nm and 3.76 nm. In

the presence of 300 mM KCl, at which these DLS assays were performed, CASQ1 monomers should be fully folded, as previously determined by circular dichroism (Sanchez et al., 2012). The estimated Rh for a folded globular protein of 43.8 kDa is 2.97 nm (determined using the hydrodynamic radius calculator available at fluidics.com/resources/hydrodynamic-radius-converter). Indeed, the globular protein ovalbumin (44 kDa) has an Rh of 3.05 nm, determined by gel filtration (Erickson, 2009). The estimated Rh for a folded globular protein of 87.6 kDa (i.e. dimeric CASQ1) is 3.81 nm. As such, the two most intense species at 2.92 nm and 3.76 nm appeared to correspond to CASQ1 monomers and dimers, respectively.

The Rh values of the second and third peaks in the CASQ1 WT sample were 260 nm and 9075 nm, respectively. Since the estimation of Rh from the Mw assumes a globular structure, and CASQ1 polymers form linear structures, the Mw of these larger species could not be determined accurately. For the CASQ1 p.F186Y sample, in the absence of added Ca^{2+}, peaks 1, 2 and 3 had Rh values of 2.92 nm, 405 nm and 14,988 nm, respectively. The proportion of peak 1 in the CASQ1 p.F186Y sample was decreased compared to CASQ1 WT, potentially reflecting an increased tendency of CASQ1 p.F186Y to aggregate. Indeed, CASQ1 p.F186Y peaks 2 and 3 were comprised of larger Rh species than the corresponding peaks for CASQ1 WT.

As expected, in the presence of 10 mM Ca^{2+}, the peak corresponding to monomeric/dimeric CASQ1 virtually disappeared in both the CASQ1 WT and CASQ1 p.F186Y sample (Figure 5.28; panel B and panel D). CASQ1 WT appeared to contain a minor proportion of monomeric species, with a distinct peak corresponding to 2.3 nm (peak 1). Peak 2 in the CASQ1 WT sample represented the major peak which had an Rh value of 163 nm and peak 3 had an Rh value of 19250 nm. The peak corresponding to monomeric CASQ1 identified in the CASQ1 WT sample was entirely absent from the CASQ1 p.F186Y sample. The first peak identified in the CASQ1 p.F186Y sample had an Rh of 77 nm (cf. 163 for the corresponding peak in CASQ1 WT). The second and third peaks identified in the p.F186Y sample were merged due to insufficient resolution of the polydisperse sample. As such, these peaks are collectively referred to as peak 2 here onwards, of which the Rh value was 18,881 nm. It appears that peak 3 in the CASQ1 sample corresponds to peak

2 in the CASQ1 p.F186Y sample and due to reduced resolution compared to CASQ1 p.F186Y, only a single peak was apparent.

It should be noted that the amount of light scattered increases with Mw (Hassan et al., 2015). As such, the relative proportions of higher Rh species in all samples are over-estimated. Nonetheless, the major species in the CASQ1 p.F186Y sample (peak 1) had a substantially smaller Rh value than the corresponding peak in the CASQ1 WT sample (peak 2), suggesting that CASQ1 p.F186Y could have a reduced capacity for Ca^{2+} dependent polymerisation, in agreement with data obtained from MST (Figure 5.23) and native MS (Figure 5.27).

5.3 Discussion

The data presented in this chapter are in support of an implication of CASQ1 in the MH and EHI phenotype. In agreement with reports in the literature, Casq1 null C2C12 myoblasts had an increased sensitivity to caffeine and appear to have reductions in the pool of releasable SR Ca^{2+} compared to wild-type C2C12 cells (Dainese et al., 2009; Paolini et al., 2011). Furthermore, CASQ1 variants identified in MHS/EHI individuals, CASQ1 p.I138T and p.F186Y, showed a reduced polymerisation and likely Ca^{2+} binding capacity compared to CASQ1 WT and CASQ1 p.E364K, validating the variants for future characterisation following expression in the Casq1 knockout C2C12 cells.

5.3.1 Mechanisms for the increased sensitivity to caffeine in Casq1 null C2C12 cells

All three of the CASQ1 knockout cell lines showed an increased sensitivity to caffeine, with significantly different EC_{50} values, compared to wild-type polyclonal C2C12 cells, which has been reported for mouse Casq1 null myoblasts and myofibres previously (Dainese et al., 2009). Increased caffeine sensitivity may result from an alleviation of the negative regulation of the RYR1 in the absence of Casq1 (Protasi et al., 2009). The polymerisation capacity of Casq1 could act to relay conformational signals to the RYR1 via its interactions with triadin and junctin (Györke et al., 2004). In the absence of such conformational signals communicated by Casq1, the RYR1 could become dysregulated, resulting in increased Ca^{2+} release. Increased Ca^{2+} levels may enhance ROS/RNS production that contribute to the MH/EHI phenotype (Paolini et al., 2015). It has also been reported previously that Casq1 null myotubes have increased resting Ca^{2+} levels (Dainese et al., 2009). Increased baseline fluorescence was observed in the C2C12 Casq1 knockout cells (data not shown); however, since this could be attributed to increased Fluo-8 AM loading in these cell lines, no conclusions can be made about the resting Ca^{2+} status of the C2C12 Casq1 null myotubes generated here without the use of a ratiometric Ca^{2+} indicator such as Fura-2 AM (Tong et al., 1999a). Since the SR provides a limited pool of Ca^{2+}, and Ca^{2+} leak from the SR would be rectified by the Na^{2+}/Ca^{2+} exchanger embedded in the sarcolemma, it has been

suggested that increased resting Ca^{2+} must be maintained by extracellular Ca^{2+} entry (Calderón et al., 2014). Indeed, CASQ1 knockdown has been shown to increase SOCE in mouse myofibres (Zhao et al., 2010), which has been postulated as a mechanism by which the rise in Ca^{2+} in MH is maintained (Duke et al., 2010).

The C2C12 Casq1 knockout cell lines 3B9 and 8E10 showed a modest, yet significant, reduction in the amplitude of fluorescence signal following caffeine stimulation compared to wild-type C2C12 cells, suggesting a reduced pool of SR Ca^{2+} stores. Indeed, this has been reported in Casq1 null mouse myotubes and Casq1 null mouse myofibres previously (Dainese et al., 2009; Paolini et al., 2007). Interestingly, a significant reduction in signal amplitude was not observed in cell line 7E5. Furthermore, cell line 7E5 consistently responded differently to cell lines 3B9 and 8E10 throughout the caffeine dose response experiments. The normalised increase in fluorescence signal in cell line 7E5 following caffeine perfusion was similar to wild-type cells until 10 mM caffeine perfusion at which cell line 7E5 responded maximally. One possibility for the apparent differential response in cell line 7E5 is the rescue of the Casq1 null phenotype by Casq2, the cardiac isoform of Casq which is also expressed in slow-twitch skeletal muscle fibres (Paolini et al., 2011). C2C12 cells have been shown to form predominantly fast twitch fibres based on MHC isoform expression (Brown et al., 2012); however, increases in slow twitch fibres have been observed in C2C12 cells following a range of treatments including Ca^{2+} ionophore treatment (Meissner et al., 2000), betaine supplementation (Du et al., 2018) and arginine supplementation (Chen et al., 2018). Increases in the proportion of slow twitch fibre types has been associated a range of pathways including upregulation of nuclear factor of activated T cell (NFATc1) that, in turn, downregulates MyoD expression (Du et al., 2018; Ehlers et al., 2014). Alternatively, arginine supplementation is thought to promote the transformation from fast to slow twitch fibres via the Sirt1/AMPK pathway (Chen et al., 2018). Slow to fast fibre type transitions in C2C12 cells have been observed in the presence of high glucose (25 mM) – the glucose concentration at which C2C12 cells were cultured in this project as recommended by the supplier, ATCC (www. https://www.lgcstandards-

atcc.org/). Interestingly, western blotting of the MHC in cell line 7E5 revealed an additional high Mw band that may correspond to an additional type 1, slow twitch, MHC isoform, potentially suggesting a preferential formation of slow twitch myotubes in cell line 7E5. Indeed, SDS-PAGE using 8% acrylamide gels has previously resulted in the successful resolution of MHC isoforms (Toniolo et al., 2005); however, all MHC species were detected within the 200 kDa region and the additional band observed here appeared to migrate corresponding to a molecular weight of ~150 kDa. As such, the identity of this additional band is unclear and could also represent degradation products or non-specific binding Nonetheless, if myotubes derived from the 7E5 cell line comprised predominantly slow twitch fibres, it is possible that Casq2 acted to rescue the function of ablated Casq1, at least at caffeine concentrations <10 mM. Indeed, Casq1 ablation in mice has been shown to have a lesser effect in slow twitch soleus fibres due to the abundance of Casq2 compared to fast twitch extensor digitorum longus fibres (Paolini et al., 2011). Despite the results presented here and a wealth of literature detailing the detrimental effect of Casq1 ablation in mouse myotubes and myofibres (Dainese et al., 2009; Tomasi et al., 2012; Paolini et al., 2015), siRNA-mediated Casq1/Casq2 knockdown in C2C12 myotubes has previously shown that Casq2 knockdown, but not Casq1 knockdown, resulted in reduced SR Ca^{2+} and reduced Ca^{2+} release following RYR1 agonist stimulation. The reasons for this finding are unclear but could be due to low levels of Casq1 expression in the knockdown cells that still contributed functional effects. Nonetheless, these data emphasise the incomplete understanding of the roles of calsequestrin isoforms in mouse skeletal muscle. Investigation of Casq2 protein levels in C2C12 myotubes generated from protocols used in this project and in the Casq1 knockout cell lines would provide further insight into the differential response of cell line 7E5.

Alternatively, since the western blot to confirm Casq1 knockout showed a reduction in the loading control for cell line 7E5 and chromosome 1 (where the *Casq1* gene lays) has four copies, it could be possible that Casq1 is not completely knocked out in this cell line and either 1 or 2 copies of it remain that precluded detection by western blot due to deceased loading of the sample.

This interpretation is complicated by the fact that no wild-type alleles were identified during sequencing of cell line 7E5. In fact, a seemingly diploid Sanger sequencing chromatogram was produced. In theory, if cell line 7E5 had at least one copy of wild-type *Casq1*, this would appear on the Sanger sequencing chromatogram as an overlapping trace in addition to the two sequences already identified. One possible explanation for seemingly diploid Sanger sequencing chromatogram is that the cell from which cell line 7E5 was derived could represent a rare subpopulation within the polyclonal C2C12 cell line that has 2 copies of chromosome 1 and was not identified by karyotyping. Indeed, karyotyping was performed on 20 individual cells that, whilst may represent the majority of the population, could have missed more rare subpopulations. An alternative could be that the two indels identified are present on at least one chromosome, since data presented here and in previous chapters has shown that the same indels are identified multiple times and in different cell lines, likely as a result of MMEJ (Bae et al., 2014). Whilst deep sequencing is becoming the gold-standard method to determine the consequences of genome editing, a more cost-effective method to investigate chromosome copy number or *Casq1* copy number in cell line 7E5 would be karyotyping or quantitative PCR (qPCR). Finally, it is possible that, for reasons unknown, PCR of the regions surrounding the Cas9 cut site preferentially amplified the two alleles detected, meaning that Sanger sequencing lacked the sensitivity to identify the remaining alleles.

5.3.2 Evaluation of the CRISPR-Cas9 gene-editing process for the production of Casq1 knockout C2C12 cells

The gRNAs designed for use in this chapter were of high quality with gRNA selected for use having just 6 predicted off-target sites. Unlike gRNA design for HDR, the only locational restriction of the gRNA was targeting of exon 1 of the Casq1 gene, with the aim of generating a severely truncated, non-functional protein that would be degraded by cellular mechanisms (Heck et al., 2010). Edited cell lines occurred at a frequency of 25%, with 8 out of the 32 lines screened showing some form of editing event; however, since some of these cell lines did not form myotubes, and differentiation into myotubes is

required to confirm a lack of Casq1 protein, the efficiency of producing knockout cell lines cannot be reported. Nonetheless, out of the 3 cell lines that formed myotubes comparable to wild-type polyclonal C2C12 cells, all of them showed Casq1 ablation by western blotting (although cell line 7E5 had reduced sample loading, the implications of which have been discussed in 5.3.1). The observed gene-editing efficiency of 25% was higher than that predicted by the T7 assay. Indeed, the estimation of gene-editing efficiency relies on four factors; i) that the range of mutations introduced into each allele are diverse enough to avoid re-annealing of identical strands, ii) that the strands of DNA are completely denatured prior to random re-annealing, iii) that strands do randomly re-anneal and iv) that T7I cleaves all mismatches between strands. Deviation from the above presumptions can result in an under-estimated gene-editing efficiency (Guschin *et al*., 2010). Furthermore, 2D densitometry is inherently subjective, requiring the manual assignment of peaks and could lead to inconsistencies in predicted gene-editing efficiencies. As mentioned in Chapter 4, the near-tetraploid genome of C2C12 cells complicated the determination of gene-editing events on each allele. Indeed, only 3 editing events were detected in cell lines 3B9 and 8E10 despite repeated attempts at TA cloning. Ultimately, deep sequencing of the region surrounding the Cas9 cut site would provide a comprehensive understanding of the gene-editing events on each allele. Overall, the CRISPR-Cas9 gene-editing process for the generation of Casq1 knockout C2C12 cells was largely efficient and achieved encouraging gene-editing efficiencies, validating the use of the tool for further knockout studies of genes potentially implicated in MH.

5.3.3 Impact of CASQ1 variants on Ca^{2+} binding and polymerisation

The *in-vitro* data presented in this chapter highlighted the complex Ca^{2+} binding and self-association events exhibited by CASQ1. MST was initially explored as a means to investigate the effect of the CASQ1 variants on the Ca^{2+} binding capacity of CASQ1. MST relies on the phenomenon by which molecules move in a directed manner in temperature gradients and fluorescent labelling of proteins enables their detection (Jerabek-Willemsen et al., 2011). Variations in

the hydrodynamic radius, charge or conformation result in altered movement of molecules that in turn, alter the fluorescence signal of the molecules. As such, in a simple binding system whereby there is a 1:1 stoichiometry of binding partners, a concentration gradient of the ligand incubated with protein of interest results in a sigmoidal binding curve from which binding constants can be derived. In contrast, CASQ1 monomers can bind up to 50-80 molecules of Ca^{2+} and these binding events are comprised of low and high affinity interactions (MacLennan and Wong 1971; Park et al., 2003; Sanchez et al., 2012). Furthermore, CASQ1 polymerises with increasing Ca^{2+}. As a result, a multiphasic binding curve was generated by MST that is likely to reflect not only Ca^{2+} binding but also CASQ1 self-association. The first binding event in CASQ1 WT appeared to occur at 100 µM Ca^{2+}, which is consistent with previous reports alterations in the conformation of CASQ1 monomers at this concentration (Park et al., 2003), the emergence of small proportions of higher order CASQ1 species, determined by cross-linking of CASQ1 polymers followed by SDS-PAGE (Wei et al., 2006), and increases in the turbidity of CASQ1 solutions (as a measure of aggregation) (Beard and Dulhunty, 2015). Further changes in the fluorescence signal were detected at ~1 mM Ca^{2+}, which is consistent with reports of a steep increase in Ca^{2+} binding of CASQ1 at 1 mM Ca^{2+}, determined by atomic absorption spectroscopy. Compared to CASQ1 WT, CASQ1 p.I138T and p.F186Y appeared to show a considerable reduction in the alteration of fluorescence signal, suggesting a Ca^{2+} binding or polymerisation defect induced by these variants. Whilst the signal from CASQ1 p.E364K differed from CASQ1 WT between 200 µM and 400 µM Ca^{2+}, this variant also showed an unstable baseline that could reflect experimental noise. Overall, the CASQ1 p.E364K variant showed a magnitude in the change in fluorescence comparable to CASQ1 WT.

A combination of native and denatured MS was used in an attempt to detect the number of Ca^{2+} ions bound to CASQ1. Data interpretation was complicated by sample heterogeneity and ultimately, the identity of each mass identified was ambiguous. Despite this, CASQ1 p.I138T and CASQ1 p.F186Y failed to produce tetrameric structures at 1 mM Ca^{2+} that were observed in CASQ1 WT and CASQ1 p.E364K. The presence of a 132 kDa species (trimeric CASQ1) in

the CASQ1 WT and CASQ1 p.E364K samples suggested a potential limitation in the maintenance of CASQ1 polymers in the gas phase, perhaps due to the absence of an aqueous environment that permits the stabilisation of hydrophobic interactions. Indeed, as CASQ1 polymerises, its structure becomes increasingly dependent on hydrophobic contacts (Kumar et al., 2013). Since results from MST indicated that CASQ1 WT behaved in a manner comparable to reports in the literature, it is unlikely that the 132 kDa species reflects aberrant polymerisation in the CASQ1 WT protein produced.

An additional possibility for the presence of trimeric species is that the +258 Da and +178 Da N-terminal 6His-tag modifications (Appendix D) affected N-terminal arm exchange required for the stabilisation of front-to-front dimer interactions that were ultimately destabilised and not maintained into the gas phase. Since the denatured intact analysis indicated that these modified species were present in considerably smaller proportions than the desired CASQ1 protein (and were present in roughly equal amounts across each CASQ1 protein), this was not a major concern for other experiments. The N-terminal 6His-tag was selected due to its small size and neutral charge at pH 7.5 (the pH at which CASQ1 assays were performed in the literature and consequently in this study). As such, 6His-tags tend not to affect protein structure and function (Kimple et al., 2013). Furthermore, the decision to locate the 6His-tag at the N-terminus was due to the dependence of the C-terminal tail for Ca^{2+} binding and polymerisation (Beard and Dulhunty, 2015). Indeed, CASQ1 WT appeared to polymerise in a manner comparable to previous reports (Wei et al., 2006). Nonetheless, 6His-tag cleavage should be considered for future work.

DLS is inherently suited to monodisperse systems (i.e. samples containing proteins of a single Mw) since it cannot accurately distinguish between molecules <3-5-fold different in size (Kaszuba et al., 2007). By its very nature, CASQ1 is heterogenous and this increased the complexity of DLS data interpretation (Hassan et al., 2015). Whilst aggregates were present in both CASQ1 WT and CASQ1 p.F186Y in the absence of Ca^{2+}, the proportion of

these aggregates compared to monomeric/dimeric CASQ1 was increased in p.F186Y. Furthermore, despite the increased aggregates in the absence of Ca^{2+}, the Rh values of each peak generated following incubation with 10 mM Ca^{2+} were smaller in p.F186Y compared to CASQ1 WT. This is in support of a reduction in the polymerisation capacity of CASQ1 p.F186Y previously observed by MST and MS. For future investigations, an optimised experimental design for DLS would include the incubation of CASQ1 proteins with a Ca^{2+} titration and the optimisation of protein concentration, since the movement of molecules by Brownian motion in DLS is dependent on concentration as well as size (Stetefeld et al., 2016). In summary, the preliminary *in-vitro* data generated from CASQ1 heterologous expression, purification and downstream *in-vitro* assays suggests impaired polymerisation and consequently Ca^{2+} binding in CASQ1 p.F186Y and CASQ1 p.I138T.

In the absence of Ca^{2+}, the CASQ1 proteins produced here contained a proportion of dimeric CASQ1, as determined my native MS and DLS. Cross-linking of CASQ1 samples has previously shown small proportions of dimeric CASQ1 at low Ca^{2+} concentrations (100 nM) but samples without added Ca^{2+} were not shown (Wei et al., 2006). Sanchez et al., (2012) showed by SEC and multi-angle light scattering (SEC-MALS) that in the absence of added Ca^{2+}, CASQ1 exists as a monomer. The differences observed between our results and those obtained elsewhere could be from differences in sample preparation that meant CASQ1 was able to remain bound to more Ca^{2+} throughout the purification process performed within this project. Dialysis of CASQ1 WT against 1 mM EGTA did not alter the masses of monomeric species identified by native MS that were speculated to result from Ca^{2+} binding, although the effect of 1 mM EGTA on dimeric species was not investigated. It may be worthwhile for future experiments to determine whether EGTA dialysis reduces dimeric CASQ1 populations.

5.3.4 A potential role of CASQ1 p.I138T and p.F186Y in MH/EHI

Alterations in the polymerisation of CASQ1 variants have previously been shown to cause disease in human muscle fibres (Barone et al., 2017; Lewis et

al., 2015). Whilst investigation of the effect of the CASQ1 p.I138T and CASQ1 p.F186Y variants on Ca^{2+} release within a cellular system is required, it is reasonable to speculate that impaired CASQ1 polymerisation could alter RYR1 regulation, resulting in the dysregulated Ca^{2+} release that underlies MH and potentially EHI. Whether the CASQ1 p.I138T variant acts to influence the MH phenotype by a major gene effect or, whether it potentiates an MH response in the presence of additional genes is unclear. The individual in which the CASQ1 p.I138T variant was identified did not harbour any variants in the *RYR1* or *CACNA1S* genes. As such, if these variants acted to potentiate an MH response, this must occur in combination with variants identified in genes yet unassociated with MH.

The underlying pathophysiology of EHI has not been fully elucidated; however, Ca^{2+} dysregulation that leads to mitochondrial dysfunction is thought to be implicated (Sagui et al., 2015; Dainese et al., 2009; Lopez et al., 2018; Yang et al., 2006). An analysis of genetic variants associated with EHI conducted by our group suggests that variants in multiple genes could cause or contribute to the EHI response, accounting for the variability in clinical phenotypes (unpublished data). The role of CASQ1 in RYR1 regulation and SOCE could present mechanisms by which the CASQ1 p.F186Y variant may contribute to the EHI phenotype.

Neither CASQ1 p.I138T or p.F186Y have been identified as residues associated with Ca^{2+} coordination, nor do they appear to be located within the front-to-front or back-to-back dimer interfaces (Sanchez et al., 2012; Park et al., 2003). *In-silico* analysis did reveal that the residues are highly conserved and suggested that they could have a structural role. Ultimately, structural interrogation of the CASQ1 p.I138T and p.F186Y proteins would be required to determine the mechanism by which the variants appear to affect polymerisation.

5.3.5 Future directions

5.3.5.1 Lentiviral transduction of CASQ1 knockout cell lines and functional analysis

The characterisation of edited lines was prioritised over screening of the entire monoclonal cell bank that had been processed for cryostorage. As such, there remains a pool of 52 monoclonal lines that require screening for editing events. Given that 25% of the 32 lines screened appeared to have undergone gene-editing, it is possible that up to ~20 Casq1 knockout cell lines have been generated in this project that provide an ample pool for further investigation of the role of CASQ1 in MH. One of the primary downstream uses of the Casq1 knockout C2C12 cells generated here is their transduction with lentiviral vectors encoding human CASQ1 WT and CASQ1 p.I138T, CASQ1 p.F186Y and CASQ1 p.E364K. Following the generation of stable, polyclonal cells (polyclonal cells would be used to eliminate the effects of random lentiviral integration), Ca^{2+} imaging would be performed to investigate the functional effect of the variants by determining whether the cell lines have altered sensitives to caffeine. Other areas that would be interesting to explore are whether the CASQ1 variants affect SOCE, via manganese quench assays (Pan et al., 2018), and the investigation of whether resting Ca^{2+} levels differ between cells expressing CASQ1 WT or the variant CASQ1s, via the use of ratiometric Ca^{2+} indicator, Fura-2 AM.

In addition to the work presented within this thesis, three pLenti-based (addgene plasmid #17448; a gift from Eric Campeau and Paul Kaufman) vectors have been constructed that encode CASQ1 WT, CASQ1 p.I138T, CASQ1 p.F186Y and CASQ1 p.E364K. Briefly, restriction digest cloning was used to replace the GFP sequence within pLenti-CMV-GFP-Hygromycin with the CASQ1 coding sequences. GFP was removed since it would interfere with fluorescence Ca^{2+} imaging using Ca^{2+} indicators that are excited at and emit at ~480-490 nm and ~510-520 nm, respectively. Generation of these data would provide corroboration, or would challenge, the *in-vitro* data presented in this

chapter. Ultimately, this would provide a more comprehensive analysis of the effects of the CASQ1 p.I138T, p.F186Y and p.E364K variants and better elucidate the potential for a role in MH/EHI. At the time of these experiments, despite the generation of Casq1 null mouse models, an immortalised Casq1 null mouse cell line was not available for use. In recent months, the Leeds MH unit has made significant progress in the immortalisation of primary mouse myoblasts by stable transduction with CDK4 (Xiaochen Liu, pers. comms.). The generation of consistent results between the immortalised Casq1 null myoblasts and Casq1 knockout C2C12 cells would provide increased confidence of the results observed and would validate the use of the fast growing and relatively easy to culture C2C12 cell line. Whilst the underlying theme of previous chapters has been a drive to progress from the cloning and heterologous expression of *RYR1* variant cDNAs in cell lines void of the gene of interest, the *CASQ1* coding sequence is ~1 kb (cf. ~15 kb for the *RYR1* gene). As such, *CASQ1* is considerably more amenable to cloning and this approach exploits the efficiency of knockout generation by CRISPR-Cas9 genome editing, whilst overcoming the efficiency limitations associated with HDR by CRISPR-Cas9 genome editing.

5.3.5.2 Further *in-vitro* investigations

Techniques that would enable the determination of Ca^{2+} binding kinetics were limited within the Biomolecular Interactions Facility in the Astbury Centre for Structural Molecular Biology, where this work was performed, primarily due to the complex binding events observed for CASQ1 in the presence of Ca^{2+}. A commonly used method to investigate binding affinities is isothermal titration calorimetry (ITC; Duff et al., 2011). This technique was not selected for use since it requires large sample consumption and most importantly, was unlikely to produce a quantitative read out for Ca^{2+} binding. ITC measures heat transfer that occurs during binding to produce binding curves and dissociation constants; however, the binding of CASQ1 monomers to form dimeric species and higher order structures would undoubtedly result in heat transfer, precluding the direct measurement of Ca^{2+} binding. A technique that may enable the determination of Ca^{2+} binding, at least at the monomeric level, would be surface plasmon resonance (SPR; Tang et al., 2010). SPR requires

the immobilisation of protein and subsequent incubation with a titration of the ligand, measuring alterations in reflected light that occur following binding. Immobilisation would likely hinder the ability of CASQ1 monomers to form dimeric structures and beyond; as such, this could enable a comparison of the Ca^{2+} binding capacity of CASQ1 monomers. Nonetheless, it is important to consider that some dimeric portions of CASQ1 were identified in samples without added Ca^{2+} which could affect the interpretation of data if certain proteins contained greater proportions of higher order structures in the absence of Ca^{2+}. As mentioned previously, it may be useful to investigate whether EGTA 'stripping' of CASQ1 would reduce dimeric structures that appear to have bound Ca^{2+} during the purification process.

Further methods to investigate CASQ1 polymerisation include SEC-MALS (Sanchez et al., 2012) which, in contrast to DLS, enables the clear resolution between species by gel filtration prior to light scattering; however, SEC columns will limit the size of CASQ1 polymers that can be analysed since larger species would clog the column. A turbidity assay, which measures absorbance at 350 nm (as a measure of protein aggregation), would provide insight into the polymerisation capacities of the CASQ1 variants compared to CASQ1 WT at increasing Ca^{2+} concentrations; however, no information about the mass of the polymers produced is obtained (Lewis et al., 2015).

Chapter 6 - General discussion

This thesis has provided the first report of the introduction of MH-associated VUS into a myoblast cell line by CRISPR-Cas9 genome editing, identifying key achievements and areas for future development of the process that will accelerate variant characterisation. Furthermore, multiple Casq1 null C2C12 cell lines were developed in a highly efficient manner that corroborated previous observations in Casq1 null mouse myotubes and fibres (Dainese et al., 2009). These Casq1 null cell lines provide immortalised lines into which CASQ1 variants can be introduced using lentiviral vectors for Ca^{2+} imaging in response to RYR1 agonists and for the investigations of alternative Ca^{2+} influx pathways such as SOCE. CASQ1 variants, p.I138T and CASQ1 p.F186Y, were shown to have impaired Ca^{2+} dependent polymerisation that ultimately, would affect the amount of Ca^{2+} bound and stored. These data provide further insight into the pathological mechanisms underlying MH and EHI and have validated these variants for further characterisation in the cellular systems generated within this project. Overall, this work provides a substantial contribution to the MH field and contributes to our fundamental understanding of the complex Ca^{2+} handling mechanisms in skeletal muscle.

6.1 Is CRISPR-Cas9 for MH-associated *RYR1* variant characterisation feasible?

The primary aim of this thesis was to develop a novel CRISPR-Cas9 genome editing pipeline for the introduction of MH-associated VUS into a myoblast cell line and explore the feasibility of this strategy for MH variant characterisation. Indeed, for the first time in the MH field, CRISPR-Cas9 was utilisied to introduce two MH-associated VUS into a myoblast cell line, namely the p.D3986E and p.S1728F variants into C2C12 cells. Variant characterisation methods without the need for cloning the large 15 kb RYR1 gene have been long sought after within the MH field and have so far amounted to isolation of patient myoblast or blood samples for Ca^{2+} imaging in response to RYR1 agonists. Variable genetic background between patient samples means that large numbers of unrelated samples are required to determine that an

observed effect can be attributed to a variant question. Since the majority of MH-associated *RYR1* variants are unique to single families, this method of characterisation is not possible for a vast proportion of MH cases (Miller et al., 2018). Furthermore, inconsistencies between techniques are widely reported (Merritt et al., 2017; Ducreux et al., 2006). The work presented here has provided proof of principle for the introduction of MH-associated VUS into a myoblast cell line, avoiding the laborious procedure for cloning of the 15 kb *RYR1* gene. This work undoubtedly provides the foundation for the future of MH variant characterisation. Whilst the complex mutational patterns in the resultant cell lines precluded determination of the functional effect of the p.D3986E variant in C2C12 myotubes, they have provided support for the proposed role of SDSA in the integration of single stranded HDR templates (Paix et al., 2017). The elucidation of the mechanisms that allow for strand incorporation are essential to strategy optimisation such as repair template design (Boel et al., 2018).

The selection of *RYR1* variants for characterisation in this project assumed a major gene mechanism of pathogenicity, whereby a single variant could act to determine MH susceptibility. *RYR1* variants were required to be rare and identified in multiple families. This strategy enabled the prioritisation of variants for characterisation and validation the CRISPR-Cas9 pipeline; however, a growing body of evidence suggests a role for modifier variants in MH. Indeed, the p.D3986E variant, despite high levels of conservation, a high C-score and enrichment in MHS individuals, has previously been shown not to result in reduced sensitivity to caffeine (Merritt et al., 2017). Whilst this could reflect limitations of the HEK293 functional characterisation system, it could also reflect the requirement of additional, potentially more common variants, that together potentiate the MH phenotype. This modifier variant theory could explain high levels of discordance observed in MH (Miller et al., 2018). The impact of the development of a CRISPR-Cas9 genome editing characterisation pipeline goes beyond the introduction of single variants into C2C12 cells for functional characterisation. To date, the power to investigate the theory of modifier variants has been limited. Indeed, by current methods, this would require the site directed mutagenesis and transfection of multiple *RYR1*

vectors. This is laborious and random integration means that more copies of one than the other could be inserted at unknown locations that could complicate data interpretation. Co-transfection of cells with multiple gRNAs and HDR templates (or, the sequential transfection) would enable the introduction of multiple variant combinations into the same cell line, enabling the study of potential modifiers. Whilst the near-tetraploid genome of C2C12 cells would complicate the study of modifiers, recent advances in the Leeds MH Unit in immortalising primary mouse cells would enable the study of modifiers in a diploid background. This strategy has recently been used to investigate the effect of modifier variants in childhood-onset cardiomyopathy (Gifford et al., 2019). Three rare variants in the *MKL2*, *MYH7*, and *NKX2-5* genes were identified in an infant with left ventricular noncompaction (LVNC). The asymptomatic father harboured the *MYH7* variant and the *MKL2* variant. Mice homozygous for the *MYH7* variant died at day 9 or 10, whereas mice homozygous for either the *MKL2* or *NKX2-5* variants (the latter of which was inherited from the unaffected mother) demonstrated only minor ventricular alterations. Mice heterozygous for all three variants recapitulated the LVNC phenotype, elucidating the role of modifier variants in the disorder. A study with a similar aim characterised a childhood-onset cardiomyopathy associated variant in the *PBX3* gene in zebrafish, which was found to enhance the phenotype caused by the loss of a known causative gene, *HAND2* (Farr et al., 2018). Another interesting avenue for exploration using CRISPR-Cas9 genome editing is the correction of MH-associated VUS to a ‘wild-type’ state for the study of causality and proof-of-concept for the future of gene therapy. Indeed, such advances have been made for the correction of Duchenne Muscular Dystrophy (DMD) mutations by adeno-associated virus delivery into DMD mouse models that enabled a significant improvement in the phenotype (Nelson et al., 2016).

CRISPR-Cas9 genome editing is, despite a wealth of achievements, still in its infancy. Rapid developments in the technology are likely to guide further use of the technique for the introduction of MH-associated VUS. Recent developments in cytidine deaminase base editors fused to catalytically inactive Cas9 were explored as a method for MH-associated VUS characterisation

(Komor et al., 2016; Banno et al., 2018). In general, MH-associated VUS were not amenable to editing in this way in murine cells, with the exception of the the p.R3366H variant. Whilst this presents an avenue for investigation of the p.R3366H variant, this method does not provide ample opportunity for characterisation of a range MH-associated VUS in murine cells and is unlikely to provide a comprehensive means for variant characterisation in human cells. The use of alternative Cas proteins, namely Cpf1 (derived from *Prevotella* and *Franscisella* 1), allows for diversification since it utilises an alternative PAM sequence and reductions in off-target activity have been reported (Moon et al., 2018). Furthermore, where possible, single-strand inducing Cas9 nickases can be utilised for increased on-target specificity (Ran et al., 2013b).

In conclusion, CRISPR-Cas9 remains an attractive and feasible method for the characterisation of MH-associated VUS. The progress presented in this thesis provides a foundation for future development and has highlighted key areas for optimisation that will enable the determination of the functional significance of desired variants, the investigation of modifier variants and proof-of-principle editing of variants back to a 'wild-type' state. This work will accelerate the development of a DNA-level diagnostic approach to MH.

6.2 Future work for CRISPR-Cas9 mediated introduction of *RYR1* variants

The primary area to explore for future use of CRISPR-Cas9 in the characterisation of MH-associated VUS is the suppression of NHEJ, potentially using Ligase IV inhibitors, to reduce the incorporation of undesired editing events in the resultant cell lines (Maruyama et al., 2015). In addition, it has been shown that HDR template incorporation can occur following the introduction of single stranded DNA breaks, such as those induced by Cas9 nickase, and this can reduce NHEJ events, presenting another area for future consideration (Liu et al., 2019). Indeed, undesired editing events presented a major limitation in obtaining cell lines that would enable functional characterisation of the p.D3986E and p.S1728F variants due to the unknown

effect of the undesired indels. In addition, whilst the mouse RYR1 protein and human RYR1 proteins share homology at 96% and mouse models are widely used to investigate the underlying pathophysiology of MH-associated *RYR1* variants (Chelu et al., 2006; Yang et al., 2006; Lopez et al., 2018), it is important to consider that effects observed in a murine context may not entirely reflect that in a human context. Ultimately, variant characterisation in a human cell line provides an optimal strategy. Further optimisation of the CRISPR-Cas9 process in human myoblasts is required, potentially by implementing strategies that circumvent the use of FACS. As mentioned, one of the major advantages of the CRISPR-Cas9 genome editing technique is its amenability to investigating the effect of modifier variants. Ultimately, this would provide unprecedented insight into the mechanisms underlying MH susceptibility.

6.3 Could variants in the *CASQ1* gene influence the MH and EHI phenotypes?

The secondary aim of this thesis was to generate a Casq1 knockout C2C12 cell line that would i) enable the determination of whether the effect of Casq1 ablation in C2C12 myotubes is consistent with reports in existing Casq1 null models and ii) enable the re-introduction of *CASQ1* variants using lentiviral vectors encoding variant cDNAs. Furthermore, the third aim of this thesis was to perform preliminary investigations into the effects of two *CASQ1* variants, p.I138T and p.F186Y, on the polymerisation and Ca^{2+} binding capacities of the CASQ1 protein. Casq1 null C2C12 cells showed increased sensitivity to caffeine and reduced SR Ca^{2+}, consistent with previous findings in Casq1 null mouse myotubes and fibres (Dainese et al., 2009). Furthermore, the finding that polymerisation was impaired in both the CASQ1 p.I138T and p.F186Y variants suggests that these variants could, at least, act to potentiate an MH/EHI response. Indeed, despite these variants showing similarities in the effects on Ca^{2+} dependent polymerisation, the individuals in which the variants were detected had different phenotypes determined by IVCT i.e. MHSh for p.I138T vs. MHN for p.F186Y. It is therefore likely that the presence of variants in other genes act in parallel to determine the observed phenotype. Since the

dynamic polymerisation of CASQ1 is thought to enable regulation of the RYR1, reduced polymerisation of CASQ1 could perturb normal gating of the channel, resulting in increased activity and Ca^{2+} release observed in MH and possibly EHI. Alternatively, a CASQ1 variant that results in diminished Ca^{2+} dependent polymerisation has been shown to increase SOCE in patients with tubular aggregate myopathy (Barone et al., 2017). SOCE has previously been hypothesised to allow for the sustained Ca^{2+} release observed in MH (Duke et al., 2010). Since ~25% of MH cases could be attributed to defects in genes other than the *RYR1* and *CACNA1S*, the elucidation of the role of variants in other genes further facilitates the development of a DNA-level approach to MH diagnosis and contributes to our understanding of the fundamental mechanisms underlying these complex disorders. The hypothesis of multiple genes acting to confer susceptibility to MH and EHI provides an explanation for the range of clinical severities observed.

Whilst variants in the *CASQ1* gene are certainly a promising candidate for a role in MH/EHI, the CASQ1 p.I138T and p.F186Y variants selected for use in this project have been identified in single individuals within Leeds MH Unit referrals (although, the presence of the p.I138T variant in family members of the individual in which the variant was identified remains to be determined). In total, 5 CASQ1 variants have been identified in referalls to the Leeds MH Unit (one of which is the common p.M87T variant). Of course, these variants require functional characterisation; however, their prevalence suggests that they do not represent a major mechanism by which susceptibility MH/EHI is determined in the UK population. Nonetheless, the findings presented in this thesis provide further substantiation of the role of multiple gene products in conferring susceptibility.

6.4 Future work for the investigation of *CASQ1* variants in MH

The Casq1 null C2C12 cells provide an immortalised system for the study of the effects of variants identified in the *CASQ1* gene. Based on the finding that

CASQ1 p.I138T and p.F186Y proteins appear to have impaired polymerisation, a primary area for exploration is whether these variants alter sensitivity to caffeine compared to the CASQ1 WT in myotubes. The determination of the effect of these variants in myotubes will provide further information about how they may contribute to the MH/EHI phenotypes. Indeed, in addition to the determination of caffeine sensitivity, resting Ca^{2+} levels can be determined by the use of ratiometric Ca^{2+} indictors such as Fura-2 AM and manganese quench assays would provide insight into whether these variants affect SOCE. Lentiviral vectors encoding the cDNAs for *CASQ1* WT and the three variants selected for investigation in this project have been generated to allow for the stable transduction of Casq1 null C2C12 cells. Lentiviral vectors have previously been used for the expression of MH-associated $Ca_V1.1$ p.R174W variant channels into dysgenic myoblasts for functional characterisation (Eltit et al., 2012), the delivery and stable expression of the full-length dystrophin gene (~15 kb) expression in myoblasts for DMD therapy (Counsell et al., 2017), and the delivery of short hairpin RNAs (shRNAs) to investigate the roles of genes involved in differentiation (Shu et al., 2009).

Since the outset of this project, the CASQ1 p.Y140F c. 418A>T (MAF 0.006; gnomAD) variant has been identified one MHShc individual and one EHI/MHSh individual. Interestingly, both of these individuals also harboured a variant in the *RYR1* gene of unknown significance in MH. The first variant, identified in the EHI individual was the relatively common RYR1 p.S1342G variant (MAF 0.02; ExAC). This variant has previously been associated with MH and exertional rhabdomyolysis and has been identified in another EHI individual and two MH families referred to the MH unit, each in the presence of an additional uncharacterised RYR1 variant (Levano et al.,2009; Sambuughin et al., 2009). The MHShc individual in which the CASQ1 p.F140Y variant was identified in also harboured the RYR1 p.P4496L (no MAF available) variant that has not been detected in any other individuals referred to the Leeds MH Unit. As such, the investigation of the role of the CASQ1 p.Y140F variant would be an interesting avenue for future characterisation, potentially using CRISPR-Cas9 genome editing as a tool for the investigation of a modifier effect resulting from the combination of *CASQ1* and *RYR1* variants identified.

The *in-vitro* studies performed for the investigation of the effect of CASQ1 p.I138T and p.F186Y were complicated by the inherent size heterogeneity of the CASQ1 protein and the complex self-association and Ca^{2+} binding events it undergoes. Structural analysis of the variant proteins by X-ray crystallography would elucidate the mechanism by which polymerisation is impaired.

6.5 Final summary

To summarise, significant progress has been presented in the development of the CRISPR-Cas9 genome editing technique for the characterisation of MH associated VUS in C2C12 cells. This was achieved by both the insertion of specific *RYR1* variants and the generation of a *Casq1* null C2C12 cell line. The work presented here has provided insight into the potential role of variants in the *CASQ1* gene in MH and EHI. Improvements in variant characterisation as a result of the progress made in this project will facilitate the elucidation of the complex genetic factors that underly MH and accelerate the establishment of a DNA-level diagnostic pipeline for MH. The transition to a whole-exome sequencing approach being explored by the Leeds MH Unit for variant detection offers increased scope for the detection of genetic variants in MHS/EHI individuals. Ultimately, a DNA-level pipeline for MH diagnosis would alleviate the need for the invasive IVCT procedure and would realise a personalised medicines approach to anaesthesia.

References

Addgene [Accessed August 2019]. Available at: www.addgene.org

Adeokun, A. M., West, S. P., Ellis, F. R., Halsall, P. J., Hopkins, P. M., Foroughmand, A. M.,Curran, J. L. (1997). The G1021A substitution in the RYR1 gene does not cosegregate with malignant hyperthermia susceptibility in a British pedigree. American Journal of Human Genetics, 60(4), 833–841.

Adzhubei, I. A., Schmidt, S., Peshkin, L., Ramensky, V. E., Gerasimova, A., Bork, P., Sunyaev, S. R. (2010). A method and server for predicting damaging missense mutations. Nat Methods, 7(4), 248-249. [Acessed August 2019] Available from: http://genetics.bwh.harvard.edu/pph2/

Al-Qusairi, L., & Laporte, J. (2011). T-tubule biogenesis and triad formation in skeletal muscle and implication in human diseases. Skeletal Muscle, 1(1), 26.

Alberts, B. J., A Lewis, J Raff, M Roberts, K Walter, P. (2008). Molecular biology of the cell. New York: Garland Science.

Alderton W.K., Cooper C.E., Knowles R.G. (2001) Nitric oxide synthases: structure, function and inhibition. Biochem J. 357(Pt 3):593-615.

Almagor, L., Chomsky-Hecht, O., Ben-Mocha, A., Hendin-Barak, D., Dascal, N., & Hirsch, J. A. (2012). The role of a voltage-dependent Ca2+ channel intracellular linker: a structure-function analysis. J Neurosci, 32(22), 7602-7613.

Alwan, R., Bruel, A. L., Da Silva, A., Blanquet, V., & Bouhouche, K. (2017). An siRNA-based screen in C2C12 myoblasts identifies novel genes involved in myogenic differentiation. Exp Cell Res, 359(1), 145-153.

Anderson, E. M., Haupt, A., Schiel, J. A., Chou, E., Machado, H. B., Strezoska, Ž., Smith, A. (2015). Systematic analysis of CRISPR-Cas9 mismatch tolerance reveals low levels of off-target activity. J Biotechnol, 211, 56-65.

Andronache, Z., Ursu, D., Lehnert, S., Freichel, M., Flockerzi, V., & Melzer, W. (2007). The auxiliary subunit gamma 1 of the skeletal muscle L-type Ca2+ channel is an endogenous Ca2+ antagonist. Proc Natl Acad Sci U S A, 104(45), 17885-17890.

Angermüller, C., Biegert, A. & Söding, J. (2012) Discriminative modelling of context-specific amino acid substitution probabilities. Bioinformatics, 28(24), 3240-7.

Angermüller, C., Biegert, A., & Söding, J. (2012). Discriminative modelling of context-specific amino acid substitution probabilities. Bioinformatics, 28(24), 3240-3247.

Ashkenazy, H., Abadi, S., Martz, E., Chay, O., Mayrose, I., Pupko, T., & Ben-Tal, N. (2016). ConSurf 2016: an improved methodology to estimate and visualize evolutionary conservation in macromolecules. Nucleic Acids Res, 44(W1), W344-350.

Ashkenazy, H., Erez, E., Martz, E., Pupko, T., & Ben-Tal, N. (2010). ConSurf 2010: calculating evolutionary conservation in sequence and structure of proteins and nucleic acids. Nucleic Acids Res, 38, W529-533.

Ata, H., Ekstrom, T. L., Martínez-Gálvez, G., Mann, C. M., Dvornikov, A. V., Schaefbauer, K. J., Ekker, S. C. (2018). Robust activation of microhomology-mediated end joining for precision gene editing applications. PLoS Genet, 14(9), e1007652.

ATCC [Accessed August 2019]. Available at: https://www.lgcstandards-atcc.org/.

Bae, S., Kweon, J., Kim, H. S., & Kim, J. S. (2014). Microhomology-based choice of Cas9 nuclease target sites. Nat Methods, 11(7), 705-706.

Bailey, A. G. & Bloch, E. C. (1987) Malignant hyperthermia in a three-month-old American Indian infant. Anesth Analg, 66(10), 1043-5.

Balci, B., & Dinçer, P. (2009). Efficient transfection of mouse-derived C2C12 myoblasts using a matrigel basement membrane matrix. Biotechnol J, 4(7), 1042-1045.

Bannister, R. A., Pessah, I. N., & Beam, K. G. (2009). The skeletal L-type Ca(2+) current is a major contributor to excitation- coupled Ca(2+) entry. J Gen Physiol, 133(1), 79-91.

Banno, S., Nishida, K., Arazoe, T., Mitsunobu, H., & Kondo, A. (2018). Deaminase-mediated multiplex genome editing in Escherichia coli. Nat Microbiol, 3(4), 423-429.

Barone, V., Del Re, V., Gamberucci, A., Polverino, V., Galli, L., Rossi, D., Costanzi, E., Toniolo, L., Berti, G., Malandrini, A., Ricci, G., Siciliano, G., Vattemi, G., Tomelleri, G., Pierantozzi, E., Spinozzi, S., Volpi, N., Fulceri, R., Battistutta, R., Reggiani, C. & Sorrentino, V. (2017) Identification and characterization of three novel mutations in the CASQ1 gene in four patients with tubular aggregate myopathy. Hum Mutat, 38(12), 1761-1773.

Beard N. A., Sakowska M. M., Dulhunty A. F., and Laver D. R. (2002) Calsequestrin is an inhibitor of skeletal muscle ryanodine receptor calcium release channels. Biophys. J. 82:310–320.

Beard, N. A., & Dulhunty, A. F. (2015). C-terminal residues of skeletal muscle calsequestrin are essential for calcium binding and for skeletal ryanodine receptor inhibition. Skelet Muscle, 5, 6.

Beard, N. A., Laver D. R., and Dulhunty A. F. (2004) Calsequestrin and the calcium release channel of skeletal and cardiac muscle. Prog. Biophys. Mol. Biol. 155:33–69.

Behere, S. P. & Weindling, S. N. (2016) Catecholaminergic polymorphic ventricular tachycardia: An exciting new era. Ann Pediatr Cardiol, 9(2), 137-46.

Berezin, C., Glaser, F., Rosenberg, J., Paz, I., Pupko, T., Fariselli, P., Ben-Tal, N. (2004). ConSeq: the identification of functionally and structurally

important residues in protein sequences. Bioinformatics, 20(8), 1322-1324.

Biral, D., Volpe, P., Damiani, E., & Margreth, A. (1992). Coexistence of two calsequestrin isoforms in rabbit slow-twitch skeletal muscle fibers. FEBS Lett, 299(2), 175-178.

Bjorksten, A. R., Gillies, R. L., Hockey, B. M., & Du Sart, D. (2016). Sequencing of genes involved in the movement of calcium across human skeletal muscle sarcoplasmic reticulum: continuing the search for genes associated with malignant hyperthermia. Anaesth Intensive Care, 44(6), 762-768.

Blau, H. M., Chiu, C. P., & Webster, C. (1983). Cytoplasmic activation of human nuclear genes in stable heterocaryons. Cell, 32(4), 1171-1180.

Boel, A., De Saffel, H., Steyaert, W., Callewaert, B., De Paepe, A., Coucke, P. J., & Willaert, A. (2018). CRISPR/Cas9-mediated homology-directed repair by ssODNs in zebrafish induces complex mutational patterns resulting from genomic integration of repair-template fragments. Dis Model Mech, 11(10).

Bogdanove A.J. and Voytas D.F. (2011) TAL effectors: customizable proteins for DNA targeting. Science. 333(6051):1843-6.

Bolotin A., Quinquis B., Sorokin A., Ehrlich S.D. (2005) Clustered regularly interspaced short palindrome repeats (CRISPRs) have spacers of extrachromosomal origin. Microbiology. 151(Pt 8):2551-61.

Boncompagni S , Rossi AE , Micaroni M , Hamilton SL , Dirksen RT , Franzini-Armstrong C & Protasi F (2009) Characterization and temporal development of cores in a mouse model of malignant hyperthermia . Proc Natl Acad Sci U S A 106 , 21996 – 22001.

Boncompagni S., Thomas M., Lopez J.R., Allen P.D., Yuan Q., Kranias E.G., Franzini-Armstrong C., Perez C.F. (2012). Triadin/Junctin double null mouse reveals a differential role for Triadin and Junctin in anchoring CASQ to the jSR and regulating Ca(2+) homeostasis. PLoS One. 7(7):e39962.

Brandom B.W. and Larach M.G. (2002) The North American MH Registry. Anesthesiology 96:A1199

Brinkmeier H, Krämer J, Krämer R, Iaizzo PA, Baur C, Lehmann-Horn F, Rüdel R. (1999) Malignant hyperthermia causing Gly2435Arg mutation of the ryanodine receptor facilitates ryanodine-induced calcium release in myotubes. Br J Anaesth. 83(6):855-61.

Britt, B. A., Endrenyi, L., Peters, P. L., Kwong, F. H., & Kadijevic, L. (1976). Screening of malignant hyperthermia susceptible families by creatine phosphokinase measurement and other clinical investigations. Can Anaesth Soc J, 23(3), 263-284.

Brookes PS, Darley-Usmar VM. (2004). Role of calcium and superoxide dismutase in sensitizing mitochondria to peroxynitrite-induced permeability transition. Am J Physiol 286: H39–H46.

Brouns, S.J.J., Jore, M.M., Lundgren, M., Westra, E.R., Slijkhuis, R.J.H., Snijders, A.P.L., Dickman, M.J., Makarova, K.S., Koonin, E.V., and van der Oost, J. (2008). Small CRISPR RNAs guide antiviral defense in prokaryotes. Science 321, 960–964.

Brown, D. M., Parr, T., & Brameld, J. M. (2012). Myosin heavy chain mRNA isoforms are expressed in two distinct cohorts during C2C12 myogenesis J Muscle Res Cell Motil. 32(6):383-90

Calderón, J. C., Bolaños, P., & Caputo, C. (2014). The excitation-contraction coupling mechanism in skeletal muscle. Biophys Rev, 6(1), 133-160.

Capacchione JF[1], Muldoon SM. (2009) The relationship between exertional heat illness, exertional rhabdomyolysis, and malignant hyperthermia. Anesth Analg. 2009 Oct;109(4):1065-9.

Carpenter, D., Robinson, R. L., Quinnell, R. J., Ringrose, C., Hogg, M., Casson, F., Hopkins, P. M. (2009). Genetic variation in RYR1 and malignant hyperthermia phenotypes. Br J Anaesth, 103(4), 538-548.

Catterall W.A. (2011) Voltage-Gated Calcium Channels. Cold Spring Harb Perspect Biol. 3(8): a003947.

Catteruccia, M., Fattori, F., Codemo, V., Ruggiero, L., Maggi, L., Tasca, G., D'Amico, A. (2013). Centronuclear myopathy related to dynamin 2 mutations: clinical, morphological, muscle imaging and genetic features of an Italian cohort. Neuromuscul Disord, 23(3), 229-238.

Celniker, G., Nimrod, G., Ashkenazy, H., Glaser, F., Martz, E., Mayrose, I., Ben-Tal, N. (2013). ConSurf: Using Evolutionary Data to Raise Testable Hypotheses about Protein Function. Israel Journal of Chemistry, 53(3-4), 199-206.

Chang, L., Daly, C., Miller, D. M., Allen, P. D., Boyle, J. P., Hopkins, P. M., & Shaw, M. A. (2019). Permeabilised skeletal muscle reveals mitochondrial deficiency in malignant hyperthermia-susceptible individuals. Br J Anaesth, 122(5), 613-621.

Chelu, M. G., Goonasekera, S. A., Durham, W. J., Tang, W., Lueck, J. D., Riehl, J., Hamilton, S. L. (2006). Heat- and anesthesia-induced malignant hyperthermia in an RyR1 knock-in mouse. FASEB J, 20(2), 329-330.

Chen, X., Guo, Y., Jia, G., Liu, G., Zhao, H. & Huang, Z. (2018) Arginine promotes skeletal muscle fiber type transformation from fast-twitch to slow-twitch via Sirt1/AMPK pathway. J Nutr Biochem, 61, 155-162.

Cherednichenko, G., Ward, C. W., Feng, W., Cabrales, E., Michaelson, L., Samso, M., Pessah, I. N. (2008). Enhanced excitation-coupled calcium entry in myotubes expressing malignant hyperthermia mutation R163C is attenuated by dantrolene. Mol Pharmacol, 73(4), 1203-1212.

Choi, R. H., Koenig, X., & Launikonis, B. S. (2017). Dantrolene requires Mg(2+) to arrest malignant hyperthermia. Proc Natl Acad Sci U S A, 114(18), 4811-4815.

Chowdhury SR, binti Ismail A, Chee SC, bin Laupa MS, binti Jaffri F, Saberi

SE, Idrus RB. (2015) One-step purification of human skeletal muscle myoblasts and subsequent expansion using laminin-coated surface. Tissue Eng. Part C Meth. 21(11):1135–1142.

Chu, V. T., Weber, T., Wefers, B., Wurst, W., Sander, S., Rajewsky, K. & Kühn, R. (2015) Increasing the efficiency of homology-directed repair for CRISPR-Cas9-induced precise gene editing in mammalian cells. Nat Biotechnol, 33(5), 543-8.

Clegg, C. H., Linkhart, T. A., Olwin, B. B., & Hauschka, S. D. (1987). Growth factor control of skeletal muscle differentiation: commitment to terminal differentiation occurs in G1 phase and is repressed by fibroblast growth factor. J Cell Biol, 105(2), 949-956.

Cong L., Ran F. A., Cox D., Lin S., Barretto R., Habib N., Hsu P. D., Wu X., Jiang W., Marraffini L. A., et al. (2013). Multiplex genome engineering using CRISPR/Cas systems. Science 339, 819–823

Cooper, G. (2000). The Cell: a Molecular Approach. Sunderland, MA, USA: Sinauer Associates.

Counsell, J. R., Asgarian, Z., Meng, J., Ferrer, V., Vink, C. A., Howe, S. J., Waddington S.N., Thrasher A.J., Muntoni F., Morgan J.E., Danos O.,(2017). Lentiviral vectors can be used for full-length dystrophin gene therapy. Sci Rep, 7, 44775.

Cui, Y., Tae, H. S., Norris, N. C., Karunasekara, Y., Pouliquin, P., Board, P. G.,Casarotto, M. G. (2009). A dihydropyridine receptor alpha1s loop region critical for skeletal muscle contraction is intrinsically unstructured and binds to a SPRY domain of the type 1 ryanodine receptor. Int J Biochem Cell Biol, 41(3), 677-686.

D'Adamo, M. C., Sforna, L., Visentin, S., Grottesi, A., Servettini, L., Guglielmi, L., Macchioni, L., Saredi, S., Curcio, M., De Nuccio, C., Hasan, S., Corazzi, L., Franciolini, F., Mora, M., Catacuzzeno, L. & Pessia, M. (2016) A Calsequestrin-1 Mutation Associated with a Skeletal Muscle Disease Alters Sarcoplasmic Ca2+ Release. PLoS One, 11(5), e0155516.

Dainese, M., Quarta, M., Lyfenko, A. D., Paolini, C., Canato, M., Reggiani, C.,Protasi, F. (2009). Anesthetic- and heat-induced sudden death in calsequestrin-1-knockout mice. FASEB J, 23(6), 1710-1720.

Darbellay, B., Arnaudeau, S., Bader, C. R., Konig, S., & Bernheim, L. (2011). STIM1L is a new actin-binding splice variant involved in fast repetitive Ca2+ release. J Cell Biol, 194(2), 335-346.

Das A.M. and Harris D.A. (1990) Regulation of the mitochondrial ATP synthase in intact rat cardiomyocytes. Biochem J. 266(2):355–361.

Dastidar, S., Ardui, S., Singh, K., Majumdar, D., Nair, N., Fu, Y., VandenDriessche, T. (2018). Efficient CRISPR/Cas9-mediated editing of trinucleotide repeat expansion in myotonic dystrophy patient-derived iPS and myogenic cells. Nucleic Acids Res, 46(16), 8275-8298.

Davies, K. E., & Nowak, K. J. (2006). Molecular mechanisms of muscular

dystrophies: old and new players. Nat Rev Mol Cell Biol, 7(10), 762-773.

Davis, A. J., & Chen, D. J. (2013). DNA double strand break repair via non-homologous end-joining. Transl Cancer Res, 2(3), 130-143.

Deltcheva, E., Chylinski, K., Sharma, C.M., Gonzales, K., Chao, Y., Pirzada, Z.A., Eckert, M.R., Vogel, J., and Charpentier, E. (2011). CRISPR RNA maturation by trans-encoded small RNA and host factor RNase III. Nature 471, 602–607.

Denborough, M., & Lovell, R. (1960). Anaesthetics deaths in family. Lancet, ii. Deufel T., R. Sudbrak, Y. Feist, B. Rübsam, I. Du Chesne, K.-L. Schäfer, N. Roewer, T. Grimm, F. Lehmann-Horn, E. J. Hartung, and C. R. Müller (1995) Discordance, in a Malignant Hyperthermia Pedigree, between in Vitro Contracture-Test Phenotypes and Haplotypes for the MHS1 Region on Chromosome 19q12–13.2, Comprising the C1840T Transition in the RYR1 Gene. Am J Hum Genet. 56(6): 1334–1342.

des Georges, A., Clarke, O. B., Zalk, R., Yuan, Q., Condon, K. J., Grassucci, R. A., Frank, J. (2016). Structural Basis for Gating and Activation of RyR1. Cell, 167(1), 145-157.e117.

Dewari, P. S., Southgate, B., Mccarten, K., Monogarov, G., O'Duibhir, E., Quinn, N., Pollard, S. M. (2018). An efficient and scalable pipeline for epitope tagging in mammalian stem cells using Cas9 ribonucleoprotein. Elife, 7.

Diaz-Sylvester, P. L., Porta, M., & Copello, J. A. (2008). Halothane modulation of skeletal muscle ryanodine receptors: dependence on Ca2+, Mg2+, and ATP. Am J Physiol Cell Physiol, 294(4), C1103-1112.

Dodds, E., Dunckley, M. G., Naujoks, K., Michaelis, U., & Dickson, G. (1998). Lipofection of cultured mouse muscle cells: a direct comparison of Lipofectamine and DOSPER. Gene Ther, 5(4), 542-551.

Du, J., Shen, L., Zhang, P., Tan, Z., Cheng, X., Luo, J., Zhu, L. (2018). The regulation of skeletal muscle fiber-type composition by betaine is associated with NFATc1/MyoD. J Mol Med (Berl), 96(7), 685-700.

Ducreux, S., Zorzato, F., Ferreiro, A., Jungbluth, H., Muntoni, F., Monnier, N., Treves, S. (2006). Functional properties of ryanodine receptors carrying three amino acid substitutions identified in patients affected by multi-minicore disease and central core disease, expressed in immortalized lymphocytes. Biochem J, 395(2), 259-266.

Duff, M. R., Grubbs, J. & Howell, E. E. (2011) Isothermal titration calorimetry for measuring macromolecule-ligand affinity. J Vis Exp(55).

Duke, A. M., Hopkins, P. M., Calaghan, S. C., Halsall, J. P., & Steele, D. S. (2010). Store-operated Ca2+ entry in malignant hyperthermia-susceptible human skeletal muscle. J Biol Chem, 285(33), 25645-25653.

Durham, W. J., Aracena-Parks, P., Long, C., Rossi, A. E., Goonasekera, S. A.,

Boncompagni, S., … Hamilton, S. L. (2008). RyR1 S-Nitrosylation Underlies Environmental Heat Stroke and Sudden Death in Y522S RyR1 Knockin Mice. Cell. 133(1), 53–65.

Edstrom L., and Kugelberg e., (1968) Histochemical composition, distribution of fibres and fatiguability of single motor units. Anterior tibial muscle of the rat. J Neurol. Neurosurg. Psychiatry. 31(5):424-433

Efremov, R. G., Leitner, A., Aebersold, R., & Raunser, S. (2015). Architecture and conformational switch mechanism of the ryanodine receptor. Nature, 517(7532), 39-43.

Ehlers, M. L., Celona, B., & Black, B. L. (2014). NFATc1 controls skeletal muscle fiber type and is a negative regulator of MyoD activity. Cell Rep, 8(6), 1639-1648.

Ehrlich, K. C., Paterson, H. L., Lacey, M., & Ehrlich, M. (2016). DNA Hypomethylation in Intragenic and Intergenic Enhancer Chromatin of Muscle-Specific Genes Usually Correlates with their Expression. Yale J Biol Med, 89(4), 441-455.

Ellis, K. O., & Bryant, S. H. (1972). Excitation-contraction uncoupling in skeletal muscle by dantrolene sodium. Naunyn Schmiedebergs Arch Pharmacol, 274(1), 107-109.

Eltit J.M., Feng W., Lopez J.R., Padilla I.T., Pessah I.N., Molinski T.F., Fruen B.R., Allen P.D. and Perez C.F. (2010) Ablation of skeletal muscle triadin impairs FKBP12/RyR1 channel interactions essential for maintaining resting cytoplasmic Ca2+. J Biol Chem. 285(49):38453-62.

Eltit, J. M., Bannister, R. A., Moua, O., Altamirano, F., Hopkins, P. M., Pessah, I. N., Allen, P. D. (2012). Malignant hyperthermia susceptibility arising from altered resting coupling between the skeletal muscle L-type Ca2+ channel and the type 1 ryanodine receptor. Proc Natl Acad Sci U S A, 109(20), 7923-7928.

Eltit, J. M., Ding, X., Pessah, I. N., Allen, P. D. & Lopez, J. R. (2013) Nonspecific sarcolemmal cation channels are critical for the pathogenesis of malignant hyperthermia. FASEB J, 27(3), 991-1000.

Emerson, C. P., & Beckner, S. K. (1975). Activation of myosin synthesis in fusing and mononucleated myoblasts. J Mol Biol, 93(4), 431-447.

Erickson, H. P. (2009). Size and shape of protein molecules at the nanometer level determined by sedimentation, gel filtration, and electron microscopy. Biol Proced Online, 11, 32-51.

ESP, N. G. E. S. P. Exome Variant Server. NHLBI GO Exome Sequencing Project (ESP). [Accessed August 2019]. Available at: http://evs.gs.washington.edu/EVS/

Fagerlund, T. H., Ording, H., Bendixen, D., Islander, G., Ranklev Twetman, E. & Berg, K. (1997). Discordance between malignant hyperthermia susceptibility and RYR1 mutation C1840T in two Scandinavian MH families exhibiting this mutation. Clin Genet, 52, 416-21.

Faggioni M., Kryshtal D.O., Knollmann B.C. (2012) Calsequestrin mutations

and catecholaminergic polymorphic ventricular tachycardia. Pediatr. Cardiol. 33(6):959-67.

Farr, G. H., Imani, K., Pouv, D., & Maves, L. (2018). Functional testing of a human PBX3 variant in zebrafish reveals a potential modifier role in congenital heart defects. Dis Model Mech, 11(10).

Feng W, Barrientos GC, Cherednichenko G, Yang T, Padilla IT, Truong K, Allen PD, Lopez JR, Pessah IN. (2011) Functional and biochemical properties of ryanodine receptor type 1 channels from heterozygous R163C malignant hyperthermia-susceptible mice. Mol Pharmacol. 2011 Mar;79(3):420-31.

Fill, M., Coronado, R., Mickelson, J. R., Vilven, J., Ma, J. J., Jacobson, B. A., and Louis, C. F. (1990) Biophys. J. 57 471–475

Fischer, U., Ludwig, N., Raslan, A., Meier, C., and Meese, E. (2016). Gene amplification during myogenic differentiation. Oncotarget, 7(6), 6864-6877.

Fiszer, D., Shaw, M. A., Fisher, N. A., Carr, I. M., Gupta, P. K., Watkins, E. J., Hopkins, P. M. (2015). Next-generation Sequencing of RYR1 and CACNA1S in Malignant Hyperthermia and Exertional Heat Illness. Anesthesiology, 122(5), 1033-1046.

Franzini-Armstrong C. (1970) Studies of the triad. J Cell Biol. 47:488–499.

Frontera, W. R., & Ochala, J. (2015). Skeletal muscle: a brief review of structure and function. Calcif Tissue Int, 96(3), 183-195.

Fu, Y., Foden, J. A., Khayter, C., Maeder, M. L., Reyon, D., Joung, J. K., & Sander, J. D. (2013). High-frequency off-target mutagenesis induced by CRISPR-Cas nucleases in human cells. Nat Biotechnol, 31(9), 822-826.

Fujii J., Otsu, K., Zorzato, F., De Leon, S., Khanna, V. K., Weiler, J. E., O'Brien, P. J. and Maclennan, D. H. (1991). Identification of a mutation in porcine ryanodine receptor associated with malignant hyperthermia. Science, 253, 448-51.

Gach, M. P., Cherednichenko, G., Haarmann, C., Lopez, J. R., Beam, K. G., Pessah, I. N., Franzini-Armstrong, C. & Allen, P. D. (2008) Alpha2delta1 dihydropyridine receptor subunit is a critical element for excitation-coupled calcium entry but not for formation of tetrads in skeletal myotubes. Biophys J, 94(8), 3023-34.

Garibaldi, M., Rendu, J., Brocard, J., Lacene, E., Fauré, J., Brochier, G., Romero, N. B. (2019). 'Dusty core disease' (DuCD): expanding morphological spectrum of RYR1 recessive myopathies. Acta Neuropathol Commun, 7(1), 3.

Gasiunas, G., Barrangou, R., Horvath, P., and Siksnys, V. (2012). Cas9-crRNA ribonucleoprotein complex mediates specific DNA cleavage for adaptive immunity in bacteria. Proc. Natl. Acad. Sci. USA 109, E2579–E2586.

Ge, X., Zhang, Y., Park, S., Cong, X., Gerrard, D. E., & Jiang, H. (2014). Stac3

inhibits myoblast differentiation into myotubes. PLoS One, 9(4), e95926.

Geoghegan, K. F., Dixon, H. B., Rosner, P. J., Hoth, L. R., Lanzetti, A. J., Borzilleri, K. A., Stroh, J. G. (1999). Spontaneous alpha-N-6-phosphogluconoylation of a "His tag" in Escherichia coli: the cause of extra mass of 258 or 178 Da in fusion proteins. Anal Biochem, 267(1), 169-184.

Gibson D.G., Young L., Chuang R.Y., Venter J.C., Hutchison C.A., Smith H.O. (2009) Enzymatic assembly of DNA molecules up to several hundred kilobases. *Nat Methods*. 6:343–5.

Gifford, C. A., Ranade, S. S., Samarakoon, R., Salunga, H. T., de Soysa, T. Y., Huang, Y., Srivastava, D. (2019). Oligogenic inheritance of a human heart disease involving a genetic modifier. Science, 364(6443), 865-870.

Gincel D., Zaid H., Shoshan-Barmatz V. (2001) Calcium binding and translocation by the voltage-dependent anion channel: a possible regulatory mechanism in mitochondrial function. Biochem J. 358(Pt 1):147-55.

Girard, T., Cavagna, D., Padovan, E., Spagnoli, G., Urwyler, A., Zorzato, F., and Treves, S. (2001). B-lymphocytes from malignant hyperthermia-susceptible patients have an increased sensitivity to skeletal muscle ryanodine receptor activators. J Biol Chem, 276(51), 48077-48082.

Giulivi C, Ross-Inta C, Omanska-Klusek A, Napoli E, Sakaguchi D, Barrientos G, Allen PD, Pessah IN. (2011) Basal bioenergetic abnormalities in skeletal muscle from ryanodine receptor malignant hyperthermia-susceptible R163C knock-in mice. J Biol Chem. 286(1):99-113.

Gonsalves, S. G. (2014). The Classification And Functional Characterization Of RYR1 Sequence Variants Associated With Malignant Hyperthermia Susceptibility Identified Through Exome Sequencing. Ph.D. Thesis. Uniformed Services University of the Health Sciences, Bethesda , MD, USA.

Görlach, A., Bertram, K., Hudecova, S. & Krizanova, O. (2015) Calcium and ROS: A mutual interplay. Redox Biol, 6, 260-271.

Graceffa, P., Jancsó, A., & Mabuchi, K. (1992a). Modification of acidic residues normalizes sodium dodecyl sulfate-polyacrylamide gel electrophoresis of caldesmon and other proteins that migrate anomalously. Arch Biochem Biophys, 297(1), 46-51.

Graceffa, P., Jancsó, A., & Mabuchi, K. (1992b). Modification of acidic residues normalizes sodium dodecyl sulfate-polyacrylamide gel electrophoresis of caldesmon and other proteins that migrate anomalously. Arch Biochem Biophys, 297(1), 46-51.

Group, T. E. M. H. Diagnostic Mutations. [Accessed August 2019]. Available at: https://www.emhg.org/diagnostic-mutations

Guo, Q., Mintier, G., Ma-Edmonds, M., Storton, D., Wang, X., Xiao, X., Feder,

J. N. (2018a). 'Cold shock' increases the frequency of homology directed repair gene editing in induced pluripotent stem cells. Sci Rep, 8(1), 2080.

Guo, T., Feng, Y. L., Xiao, J. J., Liu, Q., Sun, X. N., Xiang, J. F., Xie, A. Y. (2018b). Harnessing accurate non-homologous end joining for efficient precise deletion in CRISPR/Cas9-mediated genome editing. Genome Biol, 19(1), 170.

Gupta P.K. and Hopkins P.M. (2017) Diagnosis and management of malignant hyperthermia. BJA Education, BJA Education, Volume 17, Issue 7, Pages 249–254

Gupta R.M. and Musunuru K.J. (2014) Expanding the genetic editing tool kit: ZFNs, TALENs, and CRISPR-Cas9. Clin Invest.124(10):4154-61.

Guschin, D. Y., Waite, A. J., Katibah, G. E., Miller, J. C., Holmes, M. C. & Rebar, E. J. (2010) A rapid and general assay for monitoring endogenous gene modification. Methods Mol Biol, 649, 247-56.

Györke I.,Hester N., Jones L.R., Györke S. (2004) The role of calsequestrin, triadin, and junctin in conferring cardiac ryanodine receptor responsiveness to luminal calcium. Biophys. J. 86:2121–2128.

Haarmann CS, Dulhunty AF, Laver DR. (2005) Regulation of skeletal ryanodine receptors by dihydropyridine receptor II-III loop C-region peptides: relief of Mg2+ inhibition. Biochem J. 387(Pt 2):429-36.

Haeussler, M., Schönig, K., Eckert, H., Eschstruth, A., Mianné, J., Renaud, J. B., Concordet, J. P. (2016). Evaluation of off-target and on-target scoring algorithms and integration into the guide RNA selection tool CRISPOR. Genome Biol, 17(1), 148.

Halliday, N. J. (2003) Malignant hyperthermia. J Craniofac Surg, 14(5), 800-2.

Hamilton S.L. and Reid M.B. (2000) RyR1 modulation by oxidation and calmodulin. Antioxid Redox Signal. 2(1):41-5.

Hardeman, E. C., Minty, A., Benton-Vosman, P., Kedes, L., & Blau, H. M. (1988). In vivo system for characterizing clonal variation and tissue-specific gene regulatory factors based on function. J Cell Biol, 106(4), 1027-1034.

Hassan, P. A., Rana, S., & Verma, G. (2015). Making sense of Brownian motion: colloid characterization by dynamic light scattering. Langmuir, 31(1), 3-12.

Hayflick, L. and Moorhead, P.S. (1961) The Serial Cultivation of Human Diploid Cell Strains. Experimental Cell Research 25; 585–621.

Heck, J. W., Cheung, S. K., & Hampton, R. Y. (2010). Cytoplasmic protein quality control degradation mediated by parallel actions of the E3 ubiquitin ligases Ubr1 and San1. Proc Natl Acad Sci U S A, 107(3), 1106-1111.

Herzenberg L.A. and Sweet, R.G. (1976) Fluorescence-activated cell sorting. Scientific American, 234, 108-117.

Hilber K, Galler S, Gohlsch B & Pette D (1999). Kinetic properties of myosin

heavy chain isoforms in single fibers from human skeletal muscle. FEBS Lett 455, 267–270.

Holkers, M., Maggio, I., Liu, J., Janssen, J. M., Miselli, F., Mussolino, C., Recchia, A., Cathomen, T. & Gonçalves, M. A. (2013) Differential integrity of TALE nuclease genes following adenoviral and lentiviral vector gene transfer into human cells. Nucleic Acids Res, 41(5), e63.

Hopkins PM, Ellis FR, Halsall PJ. (1991) Evidence for related myopathies in exertional heat stroke and malignant hyperthermia. Lancet. 1991 Dec 14;338(8781):1491-2.

Hopkins, P. M. (2006). skeletal muscle physiology. Continuing Education in Anaesthesia Critical Care & Pain, 6, 1-6.

Hopkins, P. M. (2007). Is there a link between malignant hyperthermia and exertional heat illness? Br J Sports Med, 41(5), 283-284; discussion 284.

Hopkins, P. M., Ruffert, H., Snoeck, M. M., Girard, T., Glahn, K. P., Ellis, F. R., Urwyler, A. (2015). European Malignant Hyperthermia Group guidelines for investigation of malignant hyperthermia susceptibility. Br J Anaesth, 115(4), 531-539.

Horstick, E. J., Linsley, J. W., Dowling, J. J., Hauser, M. A., McDonald, K. K., Ashley-Koch, A., Kuwada, J. Y. (2013). Stac3 is a component of the excitation-contraction coupling machinery and mutated in Native American myopathy. Nat Commun, 4, 1952.

Hsu P.D., Scott D.A., Weinstein J.A., Ran F.A., Konermann S., Agarwala V., Li Y., Fine E.J., Wu X., Shalem O., Cradick T.J., Marraffini L.A., Bao G., Zhang F. (2013) DNA targeting specificity of RNA-guided Cas9 nucleases. Nat Biotechnol. 31(9):827-32.

Hu, H., Wang, Z., Wei, R., Fan, G., Wang, Q., Zhang, K., & Yin, C. C. (2015). The molecular architecture of dihydropyrindine receptor/L-type Ca2+ channel complex. Sci Rep, 5, 8370.

Hui, L., DelMonte, T., & Ranade, K. (2008). Genotyping using the TaqMan assay. Curr Protoc Hum Genet, Chapter 2, Unit 2.10.

Iles, D. E., Segers, B., Heytens, L., Sengers, R. C. & Wieringa, B. (1992) High resolution physical mapping of four microsatellite repeat markers near the RYR1 locus on chromosome 19q13.1 and apparent exclusion of the MHS locus from this region in two malignant hyperthermia susceptible families. Genomics, 14, 749-54.

Ioannidis, N. M., Rothstein, J. H., Pejaver, V., Middha, S., McDonnell, S. K., Baheti, S., Sieh, W. (2016). REVEL: An Ensemble Method for Predicting the Pathogenicity of Rare Missense Variants. Am J Hum Genet, 99(4), 877-885.

Jackson, M. F., Hoversten, K. E., Powers, J. M., Trobridge, G. D., & Rodgers, B. D. (2013). Genetic manipulation of myoblasts and a novel primary myosatellite cell culture system: comparing and optimizing approaches. FEBS J, 280(3), 827-839.

Jansen, R., Embden, J.D.A.V., Gaastra, W., and Schouls, L.M. (2002). Identification of genes that are associated with DNA repeats in prokaryotes. Mol. Microbiol. 43, 1565–1575.

Jerabek-Willemsen, M., Wienken, C. J., Braun, D., Baaske, P., & Duhr, S. (2011). Molecular interaction studies using microscale thermophoresis. Assay Drug Dev Technol, 9(4), 342-353.

Jiang, D., Chen, W., Xiao, J., Wang, R., Kong, H., Jones, P. P., Chen, S. R. (2008). Reduced threshold for luminal Ca2+ activation of RyR1 underlies a causal mechanism of porcine malignant hyperthermia. J Biol Chem, 283(30), 20813-20820.

Jinek, M., Chylinski, K., Fonfara, I., Hauer, M., Doudna, J.A., and Charpentier, E. (2012). A programmable dual-RNA-guided DNA endonuclease in adaptive bacterial immunity. Science 337, 816–821.

Kalow W Britt BA Terreau ME Haist C. (1970) Metabolic error of muscle metabolism after recovery from malignant hyperthermia. Lancet 2: 895–8

Karczewski , K., Francioli , L., Tiao , G., Cummings , B., Alföldi , J., Wang , Q., Wang , A. (2019). Variation across 141,456 human exomes and genomes reveals the spectrum of loss-of-function intolerance across human protein-coding genes. bioRxiv, In press.

Kaszuba, M., Connah, M. T., McNeil-Watson, F. K., & Nobbmann, U. (2007). Resolving Concentrated Particle Size Mixtures Using Dynamic Light Scattering. Particle & Particle Systems Characterization, 24(3), 159-162.

Katoh, K., & Standley, D. M. (2013). MAFFT multiple sequence alignment software version 7: improvements in performance and usability. Mol Biol Evol, 30(4), 772-780.

Katoh, K., Misawa, K., Kuma, K., & Miyata, T. (2002). MAFFT: a novel method for rapid multiple sequence alignment based on fast Fourier transform. Nucleic Acids Res, 30(14), 3059-3066.

Kawasaki, T. & Kasai, M. (1994) Regulation of calcium channel in sarcoplasmic reticulum by calsequestrin. Biochem Biophys Res Commun, 199(3), 1120-7.

Kim Y.G., and Chandrasegaran S. (1994) Chimeric restriction endonuclease. Proc Natl Acad Sci U S A; 91(3):883–887.

Kim, D. C. (2012). Malignant hyperthermia. Korean J Anesthesiol, 63(5), 391-401.

Kim, K. M., Rana, A., & Park, C. Y. (2019). Orai1 inhibitor STIM2β regulates myogenesis by controlling SOCE dependent transcriptional factors. Sci Rep, 9(1), 10794.

Kimple, M. E., Brill, A. L., & Pasker, R. L. (2013). Overview of affinity tags for protein purification. Curr Protoc Protein Sci, 73, Unit 9.9.

Kircher, M., Witten, D. M., Jain, P., O'Roak, B. J., Cooper, G. M., & Shendure, J. (2014). A general framework for estimating the relative pathogenicity

of human genetic variants. Nat Genet, 46(3), 310-315.

Kirichok Y., Krapivinsky G., Clapham D.E. (2004) The mitochondrial calcium uniporter is a highly selective ion channel. Nature. 427:360–364.

Klug, A., and Rhodes, D. (1987). Zinc Fingers: A Novel Protein Fold for Nucleic Acid Recognition. Cold Spring Harb. Symp. Quant. Biol. 52, 473–482.

Komor, A. C., Kim, Y. B., Packer, M. S., Zuris, J. A., & Liu, D. R. (2016). Programmable editing of a target base in genomic DNA without double-stranded DNA cleavage. Nature, 533(7603), 420-424.

Konigsberg, I. R. (1971). Diffusion-mediated control of myoblast fusion. Dev Biol, 26(1), 133-152.

Kraeva, N., Heytens, L., Jungbluth, H., Treves, S., Voermans, N., Kamsteeg, E., Riazi, S. (2015). Compound RYR1 heterozygosity resulting in a complex phenotype of malignant hyperthermia susceptibility and a core myopathy. Neuromuscul Disord, 25(7), 567-576.

Kraeva, N., Zvaritch, E., Frodis, W., Sizova, O., Kraev, A., MacLennan, D. H., & Riazi, S. (2013). CASQ1 gene is an unlikely candidate for malignant hyperthermia susceptibility in the North American population. Anesthesiology, 118(2), 344-349.

Kreiss, P., Cameron, B., Rangara, R., Mailhe, P., Aguerre-Charriol, O., Airiau, M., Scherman, D., Crouzet, J. & Pitard, B. (1999). Plasmid DNA size does not affect the physicochemical properties of lipoplexes but modulates gene transfer efficiency. Nucleic Acids Res, 27, 3792-8.

Kumar, A., Chakravarty, H., Bal, N. C., Balaraju, T., Jena, N., Misra, G., Sharon, A. (2013). Identification of calcium binding sites on calsequestrin 1 and their implications for polymerization. Mol Biosyst, 9(7), 1949-1957.

Kurebayashi N. and Ogawa Y. (2001) Depletion of Ca2+ in the sarcoplasmic reticulum stimulates Ca2+ entry into mouse skeletal muscle fibres. J Physiol. 15;533(Pt 1):185-99.

Labuhn, M., Adams, F. F., Ng, M., Knoess, S., Schambach, A., Charpentier, E. M. and Heckl, D. (2017). Refined sgRNA efficacy prediction improves large- and small-scale CRISPR–Cas9 applications. Nucleic Acids Research. 16;46(3):1375-1385.

Lai, F. A., Anderson, K., Rousseau, E., Liu, Q. Y. & Meissner, G. (1988) Evidence for a Ca2+ channel within the ryanodine receptor complex from cardiac sarcoplasmic reticulum. Biochem Biophys Res Commun, 151(1), 441-9.

Laitinen, P. J., Swan, H. & Kontula, K. (2003) Molecular genetics of exercise-induced polymorphic ventricular tachycardia: identification of three novel cardiac ryanodine receptor mutations and two common calsequestrin 2 amino-acid polymorphisms. Eur J Hum Genet, 11(11), 888-91.

Lattanzi, A., Duguez, S., Moiani, A., Izmiryan, A., Barbon, E., Martin, S.,

Bovolenta, M. (2017). Correction of the Exon 2 Duplication in DMD Myoblasts by a Single CRISPR/Cas9 System. Mol Ther Nucleic Acids, 7, 11-19.

Lau, K., & Van Petegem, F. (2014). Crystal structures of wild type and disease mutant forms of the ryanodine receptor SPRY2 domain. Nat Commun, 5, 5397.

Launikonis, B. S., Barnes, M. and Stephenson, D. G. (2003) Identification of the coupling between skeletal muscle store-operated Ca2+ entry and the inositol trisphosphate receptor. Proc. Natl. Acad. Sci. USA 100, 2941–2944

Launikonis, B. S., Murphy, R. M. & Edwards, J. N. (2010) Toward the roles of store-operated Ca2+ entry in skeletal muscle. Pflugers Arch, 460(5), 813-23.

Laver D.R., O'Neill E.R. and Lamb G.D. (2004) Luminal Ca^{2+}–regulated Mg^{2+} Inhibition of Skeletal RyRs Reconstituted as Isolated Channels or Coupled Clusters. J Gen Physiol. 124(6): 741–758

Laver, D. R., Owen, V. J., Junankar, P. R., Taske, N. L., Dulhunty, A. F. & Lamb, G. D. (1997) Reduced inhibitory effect of Mg2+ on ryanodine receptor-Ca2+ release channels in malignant hyperthermia. Biophys J, 73(4), 1913-24.

Lavorato M, Gupta PK, Hopkins PM, Franzini-Armstrong C. (2016) Skeletal Muscle Microalterations in Patients Carrying Malignant Hyperthermia-Related Mutations of the e-c Coupling Machinery. Eur J Transl Myol. 26(4):6105.

Lebendiker, M., & Danieli, T. (2014). Production of prone-to-aggregate proteins. FEBS Lett, 588(2), 236-246.

Lee, E. H., Cherednichenko, G., Pessah, I. N., & Allen, P. D. (2006). Functional coupling between TRPC3 and RyR1 regulates the expressions of key triadic proteins. J Biol Chem, 281(15), 10042-10048.

Lek, M., Karczewski, K. J., Minikel, E. V., Samocha, K. E., Banks, E., Fennell, T., Consortium, E. A. (2016). Analysis of protein-coding genetic variation in 60,706 humans. Nature, 536(7616), 285-291.

Levano, S., Vukcevic, M., Singer, M., Matter, A., Treves, S., Urwyler, A., & Girard, T. (2009). Increasing the number of diagnostic mutations in malignant hyperthermia. Hum Mutat, 30(4), 590-598.

Levitt, R. C., Olckers, A., Meyers, S., Fletcher, J. E., Rosenberg, H., Isaacs, H. & Meyers, D. A. (1992). Evidence for the localization of a malignant hyperthermia susceptibility locus (MHS2) to human chromosome 17q. Genomics, 14, 562-6.

Lewis, K. M., Ronish, L. A., Ríos, E., & Kang, C. (2015). Characterization of Two Human Skeletal Calsequestrin Mutants Implicated in Malignant Hyperthermia and Vacuolar Aggregate Myopathy. J Biol Chem, 290(48), 28665-28674.

Li, K., Wang, G., Andersen, T., Zhou, P., & Pu, W. T. (2014). Optimization of genome engineering approaches with the CRISPR/Cas9 system. PLoS One, 9(8), e105779.

Lieber, M. R. (2008). The mechanism of human nonhomologous DNA end joining. J Biol Chem, 283(1), 1-5.

Litman, R. S., & Rosenberg, H. (2005). Malignant hyperthermia: update on susceptibility testing. Jama, 293(23), 2918-2924.

Liu, M., Rehman, S., Tang, X., Gu, K., Fan, Q., Chen, D. & Ma, W. (2018) Methodologies for Improving HDR Efficiency. Front Genet, 9, 691.

Lodish, H. B., A Zipursky, SL. (2000). Molecular Cell Biology (4th edition ed.). New York: W. H. Freeman.

Long, C., McAnally, J. R., Shelton, J. M., Mireault, A. A., Bassel-Duby, R. & Olson, E. N. (2014) Prevention of muscular dystrophy in mice by CRISPR/Cas9-mediated editing of germline DNA. Science, 345(6201), 1184-1188.

Lopez J.R., Kaura V., Diggle C.P., Hopkins P.M., Allen P.D. (2018) Malignant hyperthermia, environmental heat stress, and intracellular calcium dysregulation in a mouse model expressing the p.G2435R variant of RYR1. Br J Anaesth. 2018 Oct;121(4):953-961.

Lopez, J. R., Allen, P., Alamo, L., Ryan, J. F., Jones, D. E., & Sreter, F. (1987). Dantrolene prevents the malignant hyperthermic syndrome by reducing free intracellular calcium concentration in skeletal muscle of susceptible swine. Cell Calcium, 8(5), 385-396.

López, J. R., Linares, N., Pessah, I. N., & Allen, P. D. (2005). Enhanced response to caffeine and 4-chloro-m-cresol in malignant hyperthermia-susceptible muscle is related in part to chronically elevated resting [Ca2+]i. Am J Physiol Cell Physiol, 288(3), C606-612.

Lyfenko and Dirksen (2008) Differential dependence of store-operated and excitation-coupled Ca2+ entry in skeletal muscle on STIM1 and Orai1. J Physiol. 15; 586(Pt 20): 4815–4824.

Lynch, P. J., Tong, J., Lehane, M., Mallet, A., Giblin, L., Heffron, J. J., Vaughan, P., Zafra, G., MacLennan, D. H. & McCarthy, T. V. (1999). A mutation in the transmembrane/luminal domain of the ryanodine receptor is associated with abnormal Ca2+ release channel function and severe central core disease. Proc Natl Acad Sci U S A, 96, 4164-9.

MacLennan D.H. and Chen S.R. (2009) Store overload-induced Ca2+ release as a triggering mechanism for CPVT and MH episodes caused by mutations in RYR and CASQ genes. J Physiol. 587(Pt 13):3113-5.

MacLennan DH, Duff C, Zorzato F, Fujii J, Phillips M, Korneluk RG, Frodis W, Britt BA, Worton RG. (1990) Ryanodine receptor gene is a candidate for predisposition to malignant hyperthermia. Nature. 343(6258):559-61.

MacLennan D.H. and Wong P.T. (1971) Isolation of a calcium sequestering

protein from sarcoplasmic reticulum. Proc Natl Acad Sci U S A 68, 1231–1235

Mamchaoui, K., Trollet, C., Bigot, A., Negroni, E., Chaouch, S., Wolff, A., Mouly, V. (2011). Immortalized pathological human myoblasts: towards a universal tool for the study of neuromuscular disorders. Skelet Muscle, 1, 34.

Mammedov T.G., Pienaar E., Whitney S.E., TerMaat J.R., Carvill G., Goliath R., Subramanian A. and Viljoen H.J. (2008) A Fundamental Study of the PCR Amplification of GC-Rich DNA Templates. Comput Biol Chem. 32(6): 452–457.

Martindale J.L. and Holbrook N.J. (2002) Cellular response to oxidative stress: signaling for suicide and survival. J Cell Physiol. 192(1):1-15.

Marty, M. T., Baldwin, A. J., Marklund, E. G., Hochberg, G. K., Benesch, J. L., & Robinson, C. V. (2015). Bayesian deconvolution of mass and ion mobility spectra: from binary interactions to polydisperse ensembles. Anal Chem, 87(8), 4370-4376.

Maruyama, T., Dougan, S. K., Truttmann, M. C., Bilate, A. M., Ingram, J. R., & Ploegh, H. L. (2015). Increasing the efficiency of precise genome editing with CRISPR-Cas9 by inhibition of nonhomologous end joining. Nat Biotechnol, 33(5), 538-542.

Mason, D. M., Weber, C. R., Parola, C., Meng, S. M., Greiff, V., Kelton, W. J., & Reddy, S. T. (2018). High-throughput antibody engineering in mammalian cells by CRISPR/Cas9-mediated homology-directed mutagenesis. Nucleic Acids Res, 46(14), 7436-7449.

McCarthy T.V., Quane K.A. and Lynch P.J. (2000). Ryanodine receptor mutations in malignant hyperthermia and central core disease. Hum Mutat. 15:410–7

Meissner, G., Darling E.,, and Eveleth J., (1986) Kinetics of rapid Ca^{2+} release by sarcoplasmic reticulum. Effects of Ca^{2+}, Mg^{2+}, and adenine nucleotides. Biochemistry.25:236–244

Meissner, J. D., Gros, G., Scheibe, R. J., Scholz, M., & Kubis, H. P. (2001). Calcineurin regulates slow myosin, but not fast myosin or metabolic enzymes, during fast-to-slow transformation in rabbit skeletal muscle cell culture. J Physiol, 533(Pt 1), 215-226.

Meissner, J. D., Kubis, H. P., Scheibe, R. J. & Gros, G. (2000) Reversible Ca2+-induced fast-to-slow transition in primary skeletal muscle culture cells at the mRNA level. J Physiol, 523 Pt 1, 19-28.

Merlie, J. P., & Gros, F. (1976). In vitro myogenesis. Expression of muscle specific function in the absence of cell fusion. Exp Cell Res, 97(2), 406-412.

Merritt A, Booms P, Shaw MA, Miller DM, Daly C, Bilmen JG, Stowell KM, Allen PD, Steele DS, Hopkins PM (2017) Assessing the pathogenicity of RYR1 variants in malignant hyperthermia. Br J Anaesth. 118(4):533-

543
Michelucci A, Paolini C, Boncompagni S, Canato M, Reggiani C, Protasi F. (2017) Strenuous exercise triggers a life-threatening response in mice susceptible to malignant hyperthermia. FASEB J. (8):3649-3662.
Migita T., Mukaida K., Kawamoto M., Kobayashi M., and Yuge O. (2007) Fulminant-type malignant hyperthermia in Japan: cumulative analysis of 383 cases. J Anesth. 21(2):285-288.
Miller, D. M., Daly, C., Aboelsaod, E. M., Gardner, L., Hobson, S. J., Riasat, K., Hopkins, P. M. (2018). Genetic epidemiology of malignant hyperthermia in the UK. Br J Anaesth, 121(4), 944-952.
Min, Y. L., Li, H., Rodriguez-Caycedo, C., Mireault, A. A., Huang, J., Shelton, J. M., Olson, E. N. (2019). CRISPR-Cas9 corrects Duchenne muscular dystrophy exon 44 deletion mutations in mice and human cells. Sci Adv, 5(3), eaav4324.
Mizunoya, W., Wakamatsu, J., Tatsumi, R., & Ikeuchi, Y. (2008). Protocol for high-resolution separation of rodent myosin heavy chain isoforms in a mini-gel electrophoresis system. Anal Biochem, 377(1), 111-113.
Mojica, F.J.M., Diez-Villasen or, C., Garcia-Martinez, J., and Soria, E. (2005). Intervening sequences of regularly spaced prokaryotic repeats derive from foreign genetic elements. J. Mol. Evol. 60, 174–182.
Mojica, F.J.M., Juez, G., and Rodrı´guez-Valera, F. (1993). Transcription at different salinities of Haloferax mediterranei sequences adjacent to partially modified PstI sites. Mol. Microbiol. 9, 613–621.
Monnier, N., Kozak-Ribbens, G., Krivosic-Horber, R., Nivoche, Y., Qi, D., Kraev, N., Lunardi, J. (2005). Correlations between genotype and pharmacological, histological, functional, and clinical phenotypes in malignant hyperthermia susceptibility. Hum Mutat, 26(5), 413-425.
Monnier, N., Krivosic-Horber, R., Payen, J. F., Kozak-Ribbens, G., Nivoche, Y., Adnet, P., Reyford, H. & Lunardi, J. (2002). Presence of two different genetic traits in malignant hyperthermia families: implication for genetic analysis, diagnosis, and incidence of malignant hyperthermia susceptibility. Anesthesiology, 97, 1067-74
Moon, S. B., Lee, J. M., Kang, J. G., Lee, N.-E., Ha, D.-I., Kim, D. Y., Kim, Y.-S. (2018). Highly efficient genome editing by CRISPR-Cpf1 using CRISPR RNA with a uridinylate-rich 3′-overhang. Nature Communicationsvolume, 9.
Mosca B, Delbono O, Laura Messi M, Bergamelli L, Wang ZM, Vukcevic M, Lopez R, Treves S, Nishi M, Takeshima H, Paolini C, Martini M, Rispoli G, Protasi F, Zorzato F (2013): Enhanced dihydropyridine receptor calcium channel activity restores muscle strength in JP45/CASQ1 double knockout mice. Nat Commun 4:1541.
Muldoon, S., Deuster, P., Brandom, B. & Bunger, R. (2004) Is there a link between malignant hyperthermia and exertional heat illness? Exerc Sport Sci Rev, 32(4), 174-9.

Nakai, J., Dirksen, R. T., Nguyen, H. T., Pessah, I. N., Beam, K. G. and Allen, P. D. (1996). Enhanced dihydropyridine receptor channel activity in the presence of ryanodine receptor. Nature, 380, 72-5.

Needham, D. (1926). Red and white muscles. Physiol Rev 6, 1-27.

Nelson, B. R., Wu, F., Liu, Y., Anderson, D. M., McAnally, J., Lin, W., Olson, E. N. (2013). Skeletal muscle-specific T-tubule protein STAC3 mediates voltage-induced Ca2+ release and contractility. Proc Natl Acad Sci U S A, 110(29), 11881-11886.

Nelson, C. E., Hakim, C. H., Ousterout, D. G., Thakore, P. I., Moreb, E. A., Castellanos Rivera, R. M., Gersbach, C. A. (2016). In vivo genome editing improves muscle function in a mouse model of Duchenne muscular dystrophy. Science, 351(6271), 403-407.

Ng, P. C., & Henikoff, S. (2003). SIFT: Predicting amino acid changes that affect protein function. Nucleic Acids Res, 31(13), 3812-3814.

Nishimasu H, Ran FA, Hsu PD, Konermann S, Shehata SI, Dohmae N, Ishitani R, Zhang F, Nureki O (2014) Crystal structure of Cas9 in complex with guide RNA and target DNA. Cell 156: 935–949

Nyegaard, M., Overgaard, M. T., Søndergaard, M. T., Vranas, M., Behr, E. R., Hildebrandt, L. L., Lund, J., Hedley, P. L., Camm, A. J., Wettrell, G., Fosdal, I., Christiansen, M. & Børglum, A. D. (2012) Mutations in calmodulin cause ventricular tachycardia and sudden cardiac death. Am J Hum Genet, 91(4), 703-12.

O'Reilly FM, Robert M, Jona I, Szegedi C, Albrieux M, Geib S, De Waard M, Villaz M, Ronjat M. (2002) FKBP12 modulation of the binding of the skeletal ryanodine receptor onto the II-III loop of the dihydropyridine receptor. Biophys J. 2002 Jan;82(1 Pt 1):145-55.

Ording H Brancadoro V Cozzolino S et al (1997). In vitro contracture test for diagnosis of malignant hyperthermia following the protocol of the European MH Group: results of testing patients surviving fulminant MH and unrelated low-risk subjects. Acta Anaesthesiol Scand 41: 955–66

Ording, H. (1985) Incidence of malignant hyperthermia in Denmark. Anesth Analg, 64(7), 700-4.

Ousterout, D. G., Kabadi, A. M., Thakore, P. I., Majoros, W. H., Reddy, T. E., & Gersbach, C. A. (2015). Multiplex CRISPR/Cas9-based genome editing for correction of dystrophin mutations that cause Duchenne muscular dystrophy. Nat Commun, 6, 6244.

Paix, A., Folkmann, A., Goldman, D. H., Kulaga, H., Grzelak, M. J., Rasoloson, D., Seydoux, G. (2017a). Precision genome editing using synthesis-dependent repair of Cas9-induced DNA breaks. Proc Natl Acad Sci U S A, 114(50), E10745-E10754.

Pan, Z., Choi, S., & Luo, Y. (2018). Mn 2+ Quenching Assay for Store-Operated Calcium Entry. Methods Mol Biol, 1843, 55-62.

Paolini, C., Quarta, M., D'Onofrio, L., Reggiani, C., & Protasi, F. (2011). Differential effect of calsequestrin ablation on structure and function of

fast and slow skeletal muscle fibers. J Biomed Biotechnol, 2011, 634075.

Paolini, C., Quarta, M., Nori, A., Boncompagni, S., Canato, M., Volpe, P., Protasi, F. (2007). Reorganized stores and impaired calcium handling in skeletal muscle of mice lacking calsequestrin-1. J Physiol, 583(Pt 2), 767-784.

Paolini, C., Quarta, M., Wei-LaPierre, L., Michelucci, A., Nori, A., Reggiani, C., Protasi, F. (2015). Oxidative stress, mitochondrial damage, and cores in muscle from calsequestrin-1 knockout mice. Skelet Muscle, 5, 10.

Paquet, D., Kwart, D., Chen, A., Sproul, A., Jacob, S., Teo, S., Tessier-Lavigne, M. (2016a). Efficient introduction of specific homozygous and heterozygous mutations using CRISPR/Cas9. Nature, 533(7601), 125-129.

Paredes, R. M., Etzler, J. C., Watts, L. T., Zheng, W., & Lechleiter, J. D. (2008). Chemical calcium indicators. Methods, 46(3), 143-151.

Park, H., Wu, S., Dunker, A. K., & Kang, C. (2003). Polymerization of calsequestrin. Implications for Ca2+ regulation. J Biol Chem, 278(18), 16176-16182.

Park, M. Y., Park, W. J., & Kim, D. H. (1998). Expression of excitation-contraction coupling proteins during muscle differentiation. Mol Cells, 8(5), 513-517.

Paul-Pletzer, K., Palnitkar, S. S., Jimenez, L. S., Morimoto, H., & Parness, J. (2001). The skeletal muscle ryanodine receptor identified as a molecular target of [3H]azidodantrolene by photoaffinity labeling. Biochemistry, 40(2), 531-542.

Peng, R., Lin, G., & Li, J. (2016). Potential pitfalls of CRISPR/Cas9-mediated genome editing. FEBS J, 283(7), 1218-1231.

Periasamy, M., & Kalyanasundaram, A. (2007). SERCA pump isoforms: their role in calcium transport and disease. Muscle Nerve, 35(4), 430-442.

Peter J.B., Barnard J.R., Edgerton R.V, Gillespie C.A. and Stempel K.E. (1972) Metabolic profiles of three fiber types of skeletal muscle in guinea pigs and rabbits. Biochemistry. 197211142627-2633

Polster A, Nelson BR, Olson EN, Beam KG. (2016) Stac3 has a direct role in skeletal muscle-type excitation-contraction coupling that is disrupted by a myopathy-causing mutation. Proc Natl Acad Sci U S A; 113(39):10986-91.

Popp, M. W., & Maquat, L. E. (2016). Leveraging Rules of Nonsense-Mediated mRNA Decay for Genome Engineering and Personalized Medicine. Cell, 165(6), 1319-1322. Protasi, F., Paolini, C., & Dainese, M. (2009). Calsequestrin-1: a new candidate gene for malignant hyperthermia and exertional/environmental heat stroke. J Physiol, 587(Pt 13), 3095-3100.

Protasi F, Paolini C, Dainese M. (2009) Calsequestrin-1: a new candidate gene for malignant hyperthermia and exertional/environmental heat stroke. J Physiol. 2009 Jul 1;587(Pt 13):3095-100.

Rada, H. (2017). OPPF Standard Protocols Cloning and Expression Screening

(pp. 26).

Ran, F. A., Hsu, P. D., Lin, C. Y., Gootenberg, J. S., Konermann, S., Trevino, A. E., Zhang, F. (2013b). Double nicking by RNA-guided CRISPR Cas9 for enhanced genome editing specificity. Cell, 154(6), 1380-1389.

Ran, F. A., Hsu, P. D., Wright, J., Agarwala, V., Scott, D. A., & Zhang, F. (2013a). Genome engineering using the CRISPR-Cas9 system. Nat Protoc, 8(11), 2281-2308.

Rezniczek, G. A., Winter, L., Walko, G., & Wiche, G. (2016). Functional and Genetic Analysis of Plectin in Skin and Muscle. Methods Enzymol, 569, 235-259.

Richards S, Aziz N, Bale S, Bick D, Das S, Gastier-Foster J, Grody WW, Hegde M, Lyon E, Spector E, Voelkerding K, Rehm HL; ACMG Laboratory Quality Assurance Committee. (2015) Standards and guidelines for the interpretation of sequence variants: a joint consensus recommendation of the American College of Medical Genetics and Genomics and the Association for Molecular Pathology. Genet Med. 17(5):405-24

Rios E. and Brum G. (1987) Involvement of dihydropyridine receptors in excitation-contraction coupling in skeletal muscle. Nature. 19-25;325(6106):717-20.

Robinson RL, Brooks C, Brown SL, Ellis FR, Halsall PJ, Quinnell RJ, Shaw MA, Hopkins PM. (2002) RYR1 mutations causing central core disease are associated with more severe malignant hyperthermia in vitro contracture test phenotypes. Hum Mutat. 20(2):88-97.

Robinson RL, Curran JL, Ellis FR, Halsall PJ, Hall WJ, Hopkins PM, Iles DE, West SP, Shaw MA. (2000) Multiple interacting gene products may influence susceptibility to malignant hyperthermia. Ann Hum Genet. Jul;64(Pt 4):307-20.

Robinson, R. L., Monnier, N., Wolz, W., Jung, M., Reis, A., Nuernberg, G., Curran, J. L., Monsieurs, K., Stieglitz, P., Heytens, L., Fricker, R., van Broeckhoven, C., Deufel, T., Hopkins, P. M., Lunardi, J. & Mueller, C. R. (1997) A genome wide search for susceptibility loci in three European malignant hyperthermia pedigrees. Hum Mol Genet, 6(6), 953-61.

Robinson, R., Carpenter, D., Shaw, M. A., Halsall, J., & Hopkins, P. (2006). Mutations in RYR1 in malignant hyperthermia and central core disease. Hum Mutat, 27(10), 977-989.

Röckl, K. S., Hirshman, M. F., Brandauer, J., Fujii, N., Witters, L. A., & Goodyear, L. J. (2007). Skeletal muscle adaptation to exercise training: AMP-activated protein kinase mediates muscle fiber type shift. Diabetes, 56(8), 2062-2069.

Roos, J., DiGregorio, P. J., Yeromin, A. V., Ohlsen, K., Lioudyno, M., Zhang, S., Stauderman, K. A. (2005). STIM1, an essential and conserved component of store-operated Ca2+ channel function. J Cell Biol,

169(3), 435-445.
Rosenberg, H., Pollock, N., Schiemann, A., Bulger, T., & Stowell, K. (2015). Malignant hyperthermia: a review. Orphanet J Rare Dis, 10, 93.
Rossi, A. E., & Dirksen, R. T. (2006). Sarcoplasmic reticulum: the dynamic calcium governor of muscle. Muscle Nerve, 33(6), 715-731.
Rossi, D., Vezzani, B., Galli, L., Paolini, C., Toniolo, L., Pierantozzi, E., Spinozzi, S., Barone, V., Pegoraro, E., Bello, L., Cenacchi, G., Vattemi, G., Tomelleri, G., Ricci, G., Siciliano, G., Protasi, F., Reggiani, C. & Sorrentino, V. (2014) A mutation in the CASQ1 gene causes a vacuolar myopathy with accumulation of sarcoplasmic reticulum protein aggregates. Hum Mutat, 35(10), 1163-70.
Royer, L., & Rios, E. (2009). Deconstructing calsequestrin. Complex buffering in the calcium store of skeletal muscle. J Physiol, 587(Pt 13), 3101-3111.
Ruebsam, B., Schoemig, P., & Wappler, F. (1993). Das Auftreten der C1840T-Mutation des
Ryanodinrezeptorgens in Maligne Hyperthermie Familien. Anaesthesist, 42, 846.
Rueffert H, Kraus H, Olthoff D, Deutrich C, Froster UG. (2001) Identification of a novel mutation in the ryanodine receptor gene (RYR1) in patients with malignant hyperthermia. Hum Mutat.(3):238.
Sagui, E., Montigon, C., Abriat, A., Jouvion, A., Duron-Martinaud, S., Canini, F., Brosset, C. (2015). Is there a link between exertional heat stroke and susceptibility to malignant hyperthermia? PLoS One, 10(8), e0135496.
Sambuughin, N., Capacchione, J., Blokhin, A., Bayarsaikhan, M., Bina, S., & Muldoon, S. (2009). The ryanodine receptor type 1 gene variants in African American men with exertional rhabdomyolysis and malignant hyperthermia susceptibility. Clin Genet, 76(6), 564-568.
Samso M., Shen X., Allen P.D. (2006). Structural characterization of the RyR1-FKBP12 interaction. J Mol Biol. 3;356(4):917-27.
Samso, M. (2015). 3D Structure of the Dihydropyridine Receptor of Skeletal Muscle. Eur J Transl Myol, 25(1), 4840.
Samsó, M. (2017) A guide to the 3D structure of the ryanodine receptor type 1 by cryoEM. Protein Sci, 26(1), 52-68.
Sanchez, E. J., Lewis, K. M., Danna, B. R., & Kang, C. (2012). High-capacity Ca2+ binding of human skeletal calsequestrin. J Biol Chem, 287(14), 11592-11601.
Sandow A. Excitation-contraction coupling in muscular response. Yale J Biol Med. 1952;XXV:176–201
Scherer, S., & Cold Spring Harbor Laboratory. Press. (2008). A short guide to the human genome. Cold Spring Harbor, N.Y.: Cold Spring Harbor Laboratory Press.
Schiaffino, S., & Reggiani, C. (2011). Fiber types in mammalian skeletal muscles. Physiol Rev, 91(4), 1447-1531.

Schiaffino, S., Gorza, L., Sartore, S., Saggin, L., Ausoni, S., Vianello, M., Gundersen, K. & Lømo, T. (1989) Three myosin heavy chain isoforms in type 2 skeletal muscle fibres. J Muscle Res Cell Motil, 10(3), 197-205.

Schiemann, A. H., & Stowell, K. M. (2016). Comparison of pathogenicity prediction tools on missense variants in RYR1 and CACNA1S associated with malignant hyperthermia. Br J Anaesth, 117(1), 124-128.

Schredelseker J, Di Biase V, Obermair GJ, Felder ET, Flucher BE, Franzini-Armstrong C, Grabner M. (2005) The beta 1a subunit is essential for the assembly of dihydropyridine-receptor arrays in skeletal muscle. Proc Natl Acad Sci U S A. 102(47):17219-24.

Scott W., Stevens J., Binder-Macleod S.A. (2001) Human skeletal muscle fiber type classifications. Phys Ther. 81(11):1810-6.

Sei, Y., Brandom, B. W., Bina, S., Hosoi, E., Gallagher, K. L., Wyre, H. W., Pudimat, P. A., Holman, S. J., Venzon, D. J., Daly, J. W. & Muldoon, S. (2002) Patients with malignant hyperthermia demonstrate an altered calcium control mechanism in B lymphocytes. Anesthesiology, 97(5), 1052-8.

Shahini, A., Choudhury, D., Asmani, M., Zhao, R., Lei, P., & Andreadis, S. T. (2018). NANOG restores the impaired myogenic differentiation potential of skeletal myoblasts after multiple population doublings. Stem Cell Res, 26, 55-66.

Sharples, A. P., Al-Shanti, N., Lewis, M. P., & Stewart, C. E. (2011). Reduction of myoblast differentiation following multiple population doublings in mouse C2 C12 cells: a model to investigate ageing? J Cell Biochem, 112(12), 3773-3785.

Shay, J. W., & Wright, W. E. (2000). Hayflick, his limit, and cellular ageing. Nat Rev Mol Cell Biol, 1(1), 72-76.

Shu, L., & Houghton, P. J. (2009). The mTORC2 complex regulates terminal differentiation of C2C12 myoblasts. Mol Cell Biol, 29(17), 4691-4700.

Sim, N. L., Kumar, P., Hu, J., Henikoff, S., Schneider, G., & Ng, P. C. (2012). SIFT web server: predicting effects of amino acid substitutions on proteins. Nucleic Acids Res, 40(Web Server issue), W452-457.

Singapore, B. I. i. SIFT-Sorting intolerant from tolerant. [Accessed August 2019]. Available at: https://sift.bii.a-star.edu.sg/

Smerdu V, Karsch-Mizrachi I, Campione M, Leinwand L, Schiaffino S. (1994) Type IIx myosin heavy chain transcripts are expressed in type IIb fibers of human skeletal muscle. Am J Physiol. 267(6 Pt 1):C1723-8.

Stathopulos, P. B., Li, G. Y., Plevin, M. J., Ames, J. B., & Ikura, M. (2006). Stored Ca2+ depletion-induced oligomerization of stromal interaction molecule 1 (STIM1) via the EF-SAM region: An initiation mechanism for capacitive Ca2+ entry. J Biol Chem, 281(47), 35855-35862.

Steele DS, Duke AM. (2007) Defective Mg2+ regulation of RyR1 as a causal

factor in malignant hyperthermia. Arch Biochem Biophys. 458(1):57-64.
Stemmer, M., Thumberger, T., Del Sol Keyer, M., Wittbrodt, J., & Mateo, J. L. (2015). CCTop: An Intuitive, Flexible and Reliable CRISPR/Cas9 Target Prediction Tool. PLoS One, 10(4), e0124633.
Stemmer, M., Thumberger, T., Del Sol Keyer, M., Wittbrodt, J., & Mateo, J. L. (2017). Correction: CCTop: An Intuitive, Flexible and Reliable CRISPR/Cas9 Target Prediction Tool. PLoS One, 12(4), e0176619.
Stetefeld, J., McKenna, S. A., & Patel, T. R. (2016). Dynamic light scattering: a practical guide and applications in biomedical sciences. Biophys Rev, 8(4), 409-427.
Stiber J., Hawkins A., Zhang Z.S., Wang S., Burch J., Graham V., Ward C.C., Seth M., Finch E., Malouf N., Williams R.S., Eu J.P., Rosenberg P. (2008) STIM1 signalling controls store-operated calcium entry required for development and contractile function in skeletal muscle. Cell Biol. 10(6):688-97.
Storti, R. V., Horovitch, S. J., Scott, M. P., Rich, A., & Pardue, M. L. (1978). Myogenesis in primary cell cultures from Drosophila melanogaster: protein synthesis and actin heterogeneity during development. Cell, 13(4), 589-598.
Strazis K.P and Fox A.W. (1993) Malignant hyperthermia: a review of published cases. Anesth. Analg. 77(2):297-304
Stuart, C. A., Stone, W. L., Howell, M. E., Brannon, M. F., Hall, H. K., Gibson, A. L., & Stone, M. H. (2016). Myosin content of individual human muscle fibers isolated by laser capture microdissection. Am J Physiol Cell Physiol, 310(5), C381-389.
Sun J., Steenbergen C., and Murphy E. (2006) S-Nitrosylation: NO-Related Redox Signalling to Protect Against Oxidative Stress. Antioxid Redox Signal. 8(9-10): 1693–1705.
Suzek, B. E., Wang, Y., Huang, H., McGarvey, P. B., Wu, C. H., & Consortium, U. (2015). UniRef clusters: a comprehensive and scalable alternative for improving sequence similarity searches. Bioinformatics, 31(6), 926-932.
Tanabe T, Beam KG, Powell JA, Numa S. (1988) Restoration of excitation-contraction coupling and slow calcium current in dysgenic muscle by dihydropyridine receptor complementary DNA. Nature 336(6195):134–139.
Tang, Y., Zeng, X., & Liang, J. (2010). Surface Plasmon Resonance: An Introduction to a Surface Spectroscopy Technique. J Chem Educ, 87(7), 742-746.
Thomas J, Crowhurst T. (2013) Exertional heat stroke, rhabdomyolysis and susceptibility to malignant hyperthermia. Intern Med J. 2013 Sep;43(9):1035-8
Thompson SJ, Riazi S, Kraeva N, Noseworthy MD, Rayner TE, Schneiderman JE, Cifra B, Wells GD. (2017) Skeletal Muscle Metabolic Dysfunction in

Patients With Malignant Hyperthermia Susceptibility. Anesth Analg. 125(2):434-441.

Tobin JR, Jason DR, Challa VR, Nelson TE, Sambuughin N. Malignant hyperthermia and apparent heat stroke. JAMA. 2001;286(2):168–169.

Tomasi, M., Canato, M., Paolini, C., Dainese, M., Reggiani, C., Volpe, P.,. Nori, A. (2012). Calsequestrin (CASQ1) rescues function and structure of calcium release units in skeletal muscles of CASQ1-null mice. Am J Physiol Cell Physiol, 302(3), C575-586.

Tong, J., Du, G. G., Chen, S. R. & Maclennan, D. H. (1999a). HEK-293 cells possess a carbachol- and thapsigargin-sensitive intracellular Ca2+ store that is responsive to stop-flow medium changes and insensitive to caffeine and ryanodine. Biochem J, 343 Pt 1, 39-44.

Tong, J., McCarthy, T. V. & MacLennan, D. H. (1999b) Measurement of resting cytosolic Ca2+ concentrations and Ca2+ store size in HEK-293 cells transfected with malignant hyperthermia or central core disease mutant Ca2+ release channels. J Biol Chem, 274(2), 693-702.

Tong, J., Oyamada, H., Demaurex, N., Grinstein, S., McCarthy, T. V., and MacLennan, D. H. (1997) J. Biol. Chem. 272 26332–26339

Toniolo, L., Maccatrozzo, L., Patruno, M., Caliaro, F., Mascarello, F., & Reggiani, C. (2005). Expression of eight distinct MHC isoforms in bovine striated muscles: evidence for MHC-2B presence only in extraocular muscles. J Exp Biol, 208(Pt 22), 4243-4253.

Tsai, S. Q., Zheng, Z., Nguyen, N. T., Liebers, M., Topkar, V. V., Thapar, V., Joung, J. K. (2015). GUIDE-seq enables genome-wide profiling of off-target cleavage by CRISPR-Cas nucleases. Nat Biotechnol, 33(2), 187-197.

Tukey, J. W. (1949). Comparing individual means in the analysis of variance. Biometrics, 5(2), 99-114.

Tung, C. C., Lobo, P. A., Kimlicka, L., & Van Petegem, F. (2010). The amino-terminal disease hotspot of ryanodine receptors forms a cytoplasmic vestibule. Nature, 468(7323), 585-588.

Van Agtmaal, E. L., André, L. M., Willemse, M., Cumming, S. A., van Kessel, I. D. G., van den Broek, W. J. A. A., Wieringa, B. (2017). CRISPR/Cas9-Induced (CTG·CAG) n Repeat Instability in the Myotonic Dystrophy Type 1 Locus: Implications for Therapeutic Genome Editing. Mol Ther, 25(1), 24-43.

Voss, A. A., Lango, J., Ernst-Russell, M., Morin, D., & Pessah, I. N. (2004). Identification of hyperreactive cysteines within ryanodine receptor type 1 by mass spectrometry. J Biol Chem, 279(33), 34514-34520.

Wang, C., Liu, W., Nie, Y., Qaher, M., Horton, H. E., Yue, F., Asakura, A. & Kuang, S. (2017) Loss of MyoD Promotes Fate Transdifferentiation of Myoblasts Into Brown Adipocytes. EBioMedicine, 16, 212-223.

Wang, L., Zhang, L., Li, S., Zheng, Y., Yan, X., Chen, M., Luo, D. (2015). Retrograde regulation of STIM1-Orai1 interaction and store-operated

Ca2+ entry by calsequestrin. Sci Rep, 5, 11349.

Wang, S., Trumble, W. R., Liao, H., Wesson, C. R., Dunker, A. K., & Kang, C. H. (1998). Crystal structure of calsequestrin from rabbit skeletal muscle sarcoplasmic reticulum. Nat Struct Biol, 5(6), 476-483.

Wang, Y., Li, X., Duan, H., Fulton, T. R., Eu, J. P. & Meissner, G. (2009) Altered stored calcium release in skeletal myotubes deficient of triadin and junctin. Cell Calcium, 45(1), 29-37.

Wehner M, Rueffert H, Koenig F, Neuhaus J, Olthoff D. (2006) Increased sensitivity to 4-chloro-m-cresol and caffeine in primary myotubes from malignant hyperthermia susceptible individuals carrying the ryanodine receptor 1 Thr2206Met (C6617T) mutation. Clin Genet. 62(2):135-46.

Wei L., Gallant E.M., Dulhunty A.F., Beard N.A. (2009). Junctin and triadin each activate skeletal ryanodine receptors but junctin alone mediates functional interactions with calsequestrin. Int J Biochem Cell Biol. 41(11): 2214–2224.

Wei, L., Varsányi, M., Dulhunty, A. F., & Beard, N. A. (2006). The conformation of calsequestrin determines its ability to regulate skeletal ryanodine receptors. Biophys J, 91(4), 1288-1301.

Weiss, N., & Ivanova, E. (2008). Does the voltage-gated calcium channel alpha2delta-1 subunit play a dual function in skeletal muscle? J Physiol, 586(8), 2035-2037.

Weiss, R. G., O'Connell, K. M., Flucher, B. E., Allen, P. D., Grabner, M., & Dirksen, R. T. (2004). Functional analysis of the R1086H malignant hyperthermia mutation in the DHPR reveals an unexpected influence of the III-IV loop on skeletal muscle EC coupling. Am J Physiol Cell Physiol, 287(4), C1094-1102.

Wingfield, P. T. (2017). N-Terminal Methionine Processing. Curr Protoc Protein Sci, 88, 6.14.11-16.14.13.

Wojtal, D., Kemaladewi, D. U., Malam, Z., Abdullah, S., Wong, T. W., Hyatt, E., Cohn, R. D. (2016). Spell Checking Nature: Versatility of CRISPR/Cas9 for Developing Treatments for Inherited Disorders. Am J Hum Genet, 98(1), 90-101.

Chapter 7 Wu J., Yan Z., Li Z., Qian X., Lu S., Dong M., Zhou Q. and Yan N. (2016) Structure of the voltage-gated calcium channel Ca(v)1.1 at 3.6 Å resolution. Nature. 8;537(7619):191-196.

Wu, M. M., Buchanan, J., Luik, R. M., & Lewis, R. S. (2006). Ca2+ store depletion causes STIM1 to accumulate in ER regions closely associated with the plasma membrane. J Cell Biol, 174(6), 803-813.

Wu, X., Kriz, A. J. & Sharp, P. A. (2014) Target specificity of the CRISPR-Cas9 system. Quant Biol, 2(2), 59-70.

Würtele, H., Little, K. C., & Chartrand, P. (2003). Illegitimate DNA integration in mammalian cells. Gene Ther, 10(21), 1791-1799.

Xu, L., Park, K. H., Zhao, L., Xu, J., El Refaey, M., Gao, Y., Zhu, H., Ma, J. &

Han, R. (2016) CRISPR-mediated Genome Editing Restores Dystrophin Expression and Function in mdx Mice. Mol Ther, 24(3), 564-9.

Xu, X., Gao, D., Wang, P., Chen, J., Ruan, J., Xu, J., & Xia, X. (2018). Efficient homology-directed gene editing by CRISPR/Cas9 in human stem and primary cells using tube electroporation. Sci Rep, 8(1), 11649.

Yaffe, D., & Saxel, O. (1977). Serial passaging and differentiation of myogenic cells isolated from dystrophic mouse muscle. Nature, 270(5639), 725-727.

Yan, Z., Bai, X., Yan, C., Wu, J., Li, Z., Xie, T., Yan, N. (2015). Structure of the rabbit ryanodine receptor RyR1 at near-atomic resolution. Nature, 517(7532), 50-55.

Yang, L., Guell, M., Byrne, S., Yang, J. L., De Los Angeles, A., Mali, P., Church, G. (2013). Optimization of scarless human stem cell genome editing. Nucleic Acids Res, 41(19), 9049-9061.

Yang, T., Allen, P. D., Pessah, I. N., & Lopez, J. R. (2007). Enhanced excitation-coupled calcium entry in myotubes is associated with expression of RyR1 malignant hyperthermia mutations. J Biol Chem, 282(52), 37471-37478.

Yang, T., Riehl, J., Esteve, E., Matthaei, K. I., Goth, S., Allen, P. D., Lopez, J. R. (2006). Pharmacologic and functional characterization of malignant hyperthermia in the R163C RyR1 knock-in mouse. Anesthesiology, 105(6), 1164-1175.

Yang, T., Ta, T. A., Pessah, I. N., & Allen, P. D. (2003). Functional defects in six ryanodine receptor isoform-1 (RyR1) mutations associated with malignant hyperthermia and their impact on skeletal excitation-contraction coupling. J Biol Chem, 278(28), 25722-25730.

Ye, J., Coulouris, G., Zaretskaya, I., Cutcutache, I., Rozen, S., & Madden, T. L. (2012). Primer-BLAST: a tool to design target-specific primers for polymerase chain reaction. BMC Bioinformatics, 13, 134.

Yoshida, N., Yoshida, S., Koishi, K., Masuda, K., & Nabeshima, Y. (1998). Cell heterogeneity upon myogenic differentiation: down-regulation of MyoD and Myf-5 generates 'reserve cells'. J Cell Sci, 111 (Pt 6), 769-779.

Young, C. S., Hicks, M. R., Ermolova, N. V., Nakano, H., Jan, M., Younesi, S., Pyle, A. D. (2016). A Single CRISPR-Cas9 Deletion Strategy that Targets the Majority of DMD Patients Restores Dystrophin Function in hiPSC-Derived Muscle Cells. Cell Stem Cell, 18(4), 533-540.

Yuan, Y., Shi, X. E., Liu, Y. G., & Yang, G. S. (2011). FoxO1 regulates muscle fiber-type specification and inhibits calcineurin signaling during C2C12 myoblast differentiation. Mol Cell Biochem, 348(1-2), 77-87.

Yuchi, Z., Yuen, S. M., Lau, K., Underhill, A. Q., Cornea, R. L., Fessenden, J. D., & Van Petegem, F. (2015). Crystal structures of ryanodine receptor SPRY1 and tandem-repeat domains reveal a critical FKBP12 binding determinant. Nat Commun, 6, 7947.

Zalk, R., Clarke, O. B., des Georges, A., Grassucci, R. A., Reiken, S., Mancia, F., Marks, A. R. (2015). Structure of a mammalian ryanodine receptor. Nature, 517(7532), 44-49.

Zhang N., Heruth D., Wu W., Zhang L.Q., Nsumu M.N., Shortt K., Li K., Jiang X., Wang B., Friesen C., Li D.Y. and Ye S.Q. (2019) Functional characterization of SLC26A3 c.392C>G (p.P131R) mutation in intestinal barrier function using CRISPR/CAS9-created cell models. Cell Biosci. 9: 40.

Zhang Z., Yang X., Meng L., Liu F., Shen C. andYang W. (2009) Enhanced amplification of GC-rich DNA with two organic reagents. Biotechniques. 47(3):775-9.

Zhang, X. H., Tee, L. Y., Wang, X. G., Huang, Q. S., & Yang, S. H. (2015). Off-target Effects in CRISPR/Cas9-mediated Genome Engineering. Mol Ther Nucleic Acids, 4, e264.

Zhao, X., Min, C. K., Ko, J. K., Parness, J., Kim, D. H., Weisleder, N., & Ma, J. (2010). Increased store-operated Ca2+ entry in skeletal muscle with reduced calsequestrin-1 expression. Biophys J, 99(5), 1556-1564.

Zhu, C. H., Mouly, V., Cooper, R. N., Mamchaoui, K., Bigot, A., Shay, J. W., Wright, W. E. (2007). Cellular senescence in human myoblasts is overcome by human telomerase reverse transcriptase and cyclin-dependent kinase 4: consequences in aging muscle and therapeutic strategies for muscular dystrophies. Aging Cell, 6(4), 515-523.

Appendix A – Ryr1 p.D3986E off-target site Sanger sequencing chromatograms

Zmiz 8G6

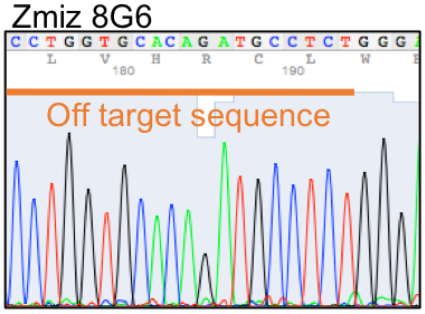

Zmiz 2G7

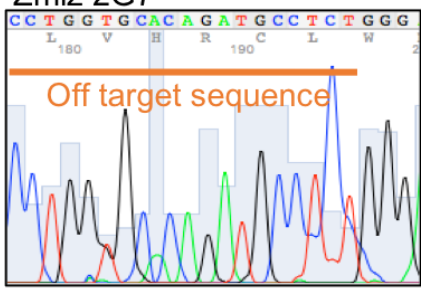

Zmiz 1C5

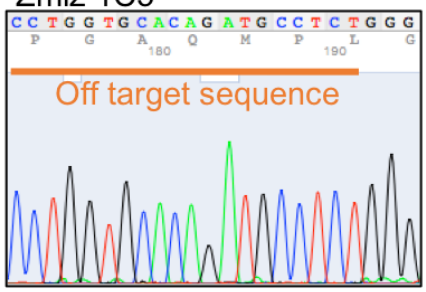

Zmiz 1E6

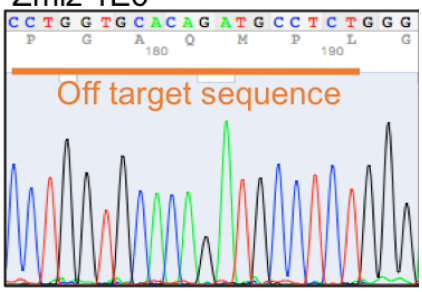

Zmiz 10G5

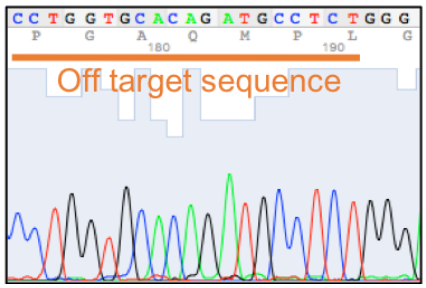

Appendix A continued (1)

Optn 1C5

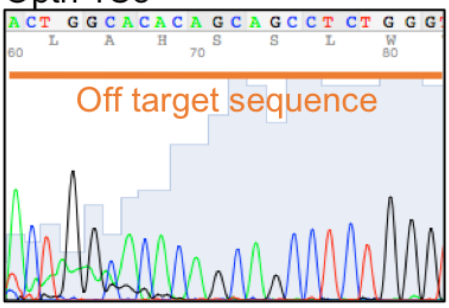

Optn 1E6

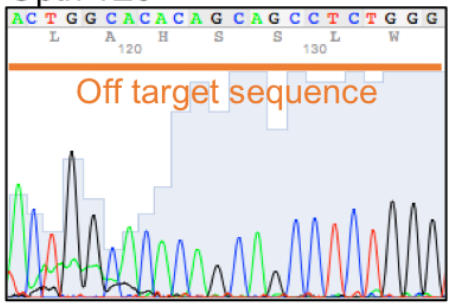

Optn 8G6

Optn 10G5

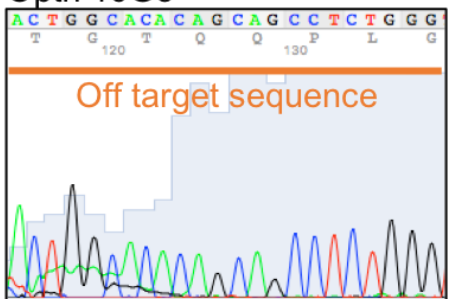

Ptpn 1c5

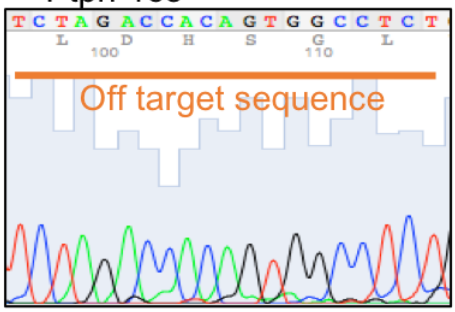

Ptpn 14 2G7

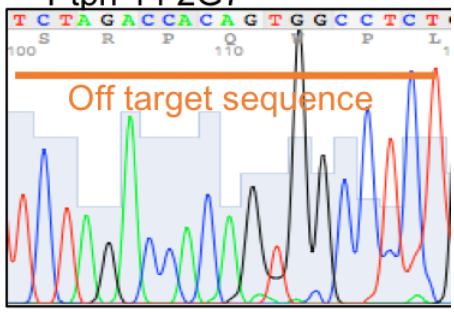

Ptpn 10G5

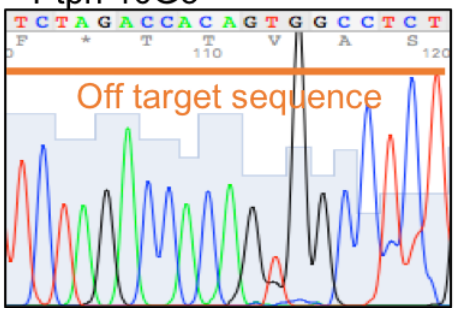

Ptpn 8G6

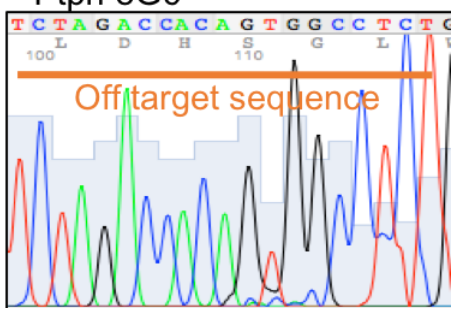

Appendix A continued (2)

Bcat 1C5

Bcat 1E6

Bcat 8G6

Bcat 10G5

Bcat 2G7

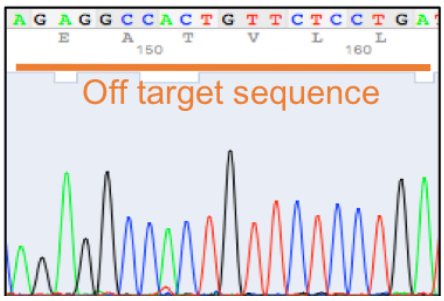

Appendix A continued (3)

Nrros 1E6

Nrros 2G7

Nrros 10G5

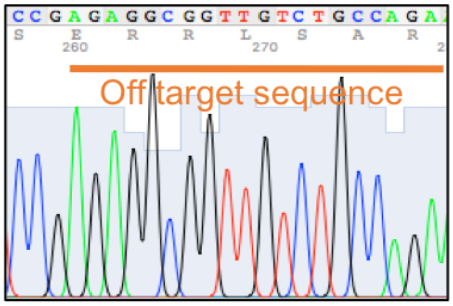

Nrros 1C5

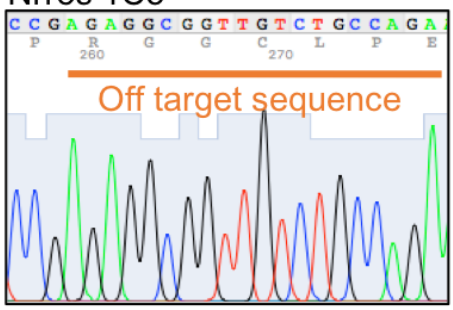

Nrros 8G6

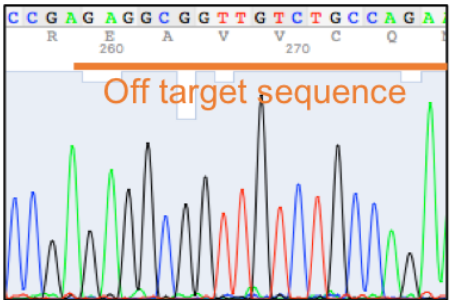

Appendix A continued (4)

Gm23796-Gm23831 1C5

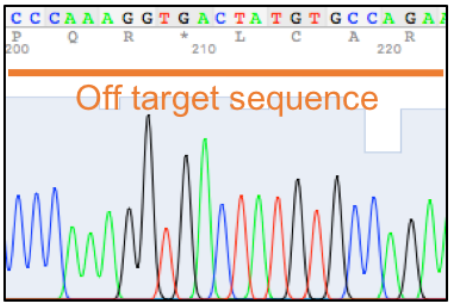

Gm23796-Gm23831 1E6

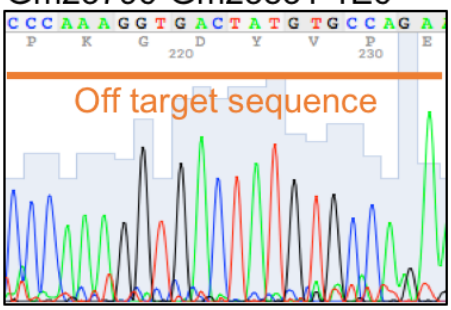

Gm23796-Gm23831 2G7

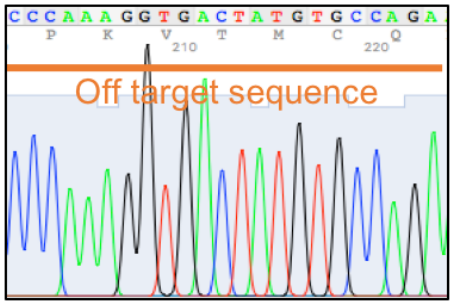

Gm23796-Gm23831 8G6

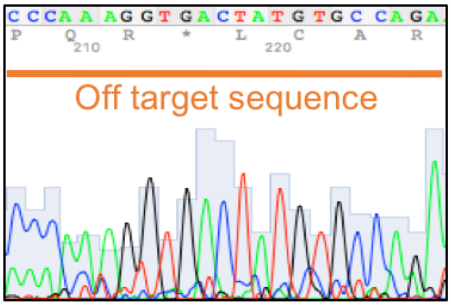

Gm23796-Gm23831 10G5

Appendix A continued (5)

Pabpc6-qk 1C5

Pabpc6-qk 1E6

Pabpc6-qk 2G7

Pabpc6-qk 8G6

Pabpc6-qk 10G5

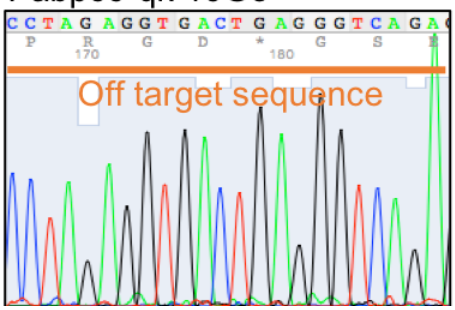

Appendix A continued (6)

Nkx6-2 1C5

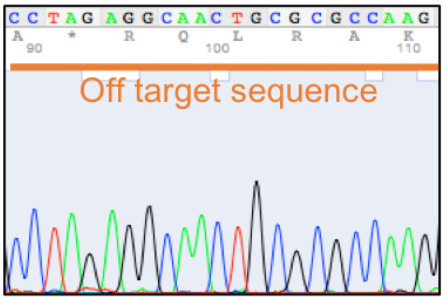

Nkx6-2 1E6

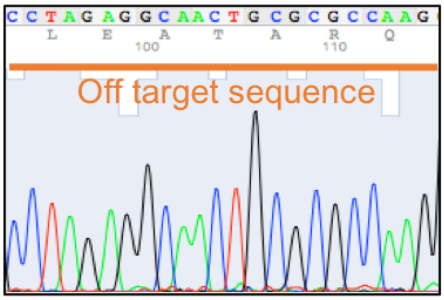

Nkx6-2 2G7

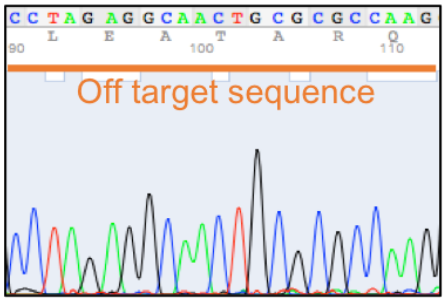

Nkx6-2 8G6

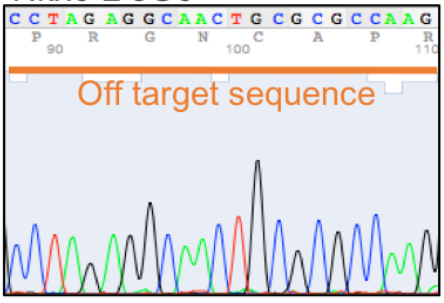

Nkx6-2 10G5

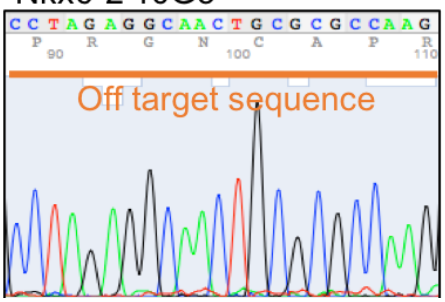

Appendix A continued (7)

Med23 1E6

Med23 8G6

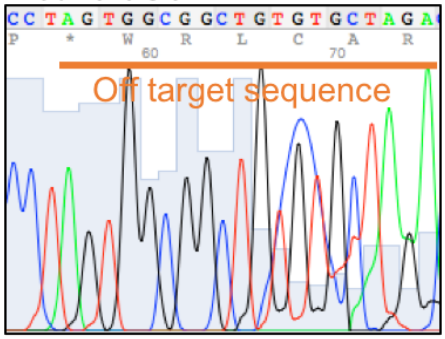

Med23 10G5

Med23 2G7

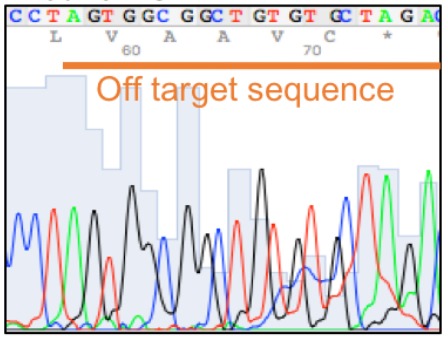

Med23 1C5

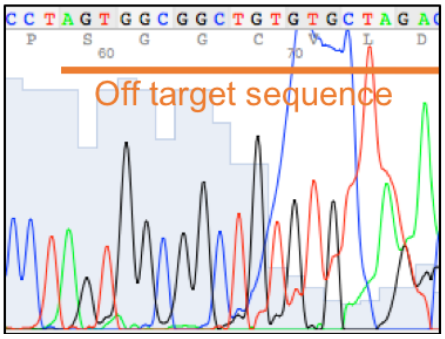

Appendix A continued (8)

Gm4889-Dusp4 1E6

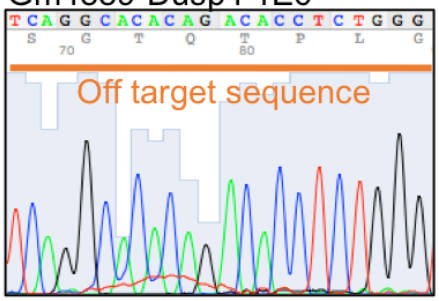

Gm4889-Dusp4 1C5

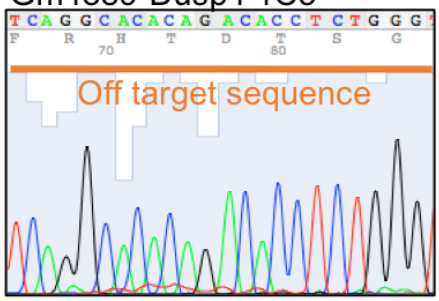

Gm4889-Dusp4 2G7

Gm4889-Dusp4 8G6

Gm4889-Dusp4 10G5

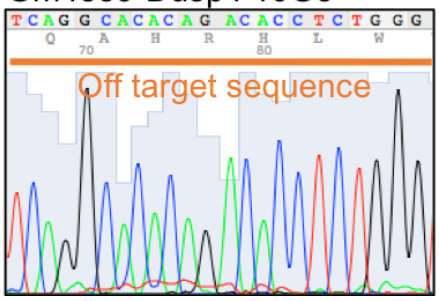

6030407O03Rik 1C5

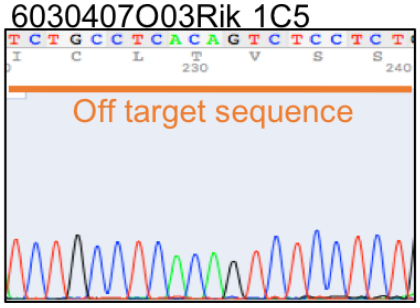

6030407O03Rik 1E6

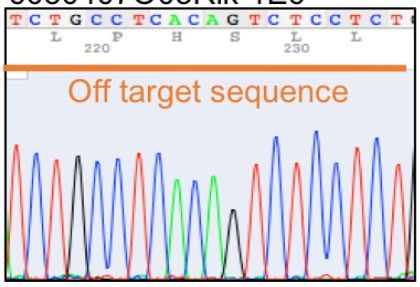

6030407O03Rik 10G5

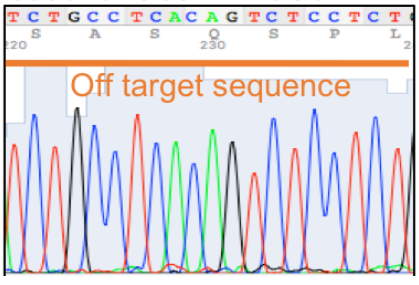

6030407O03Rik 8G6

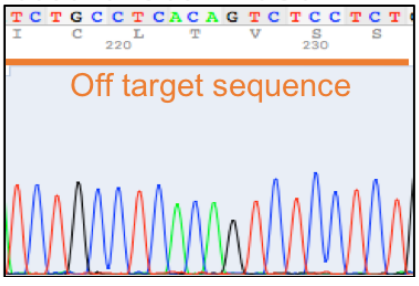

Appendix A continued (9)

Rreb1 1C5

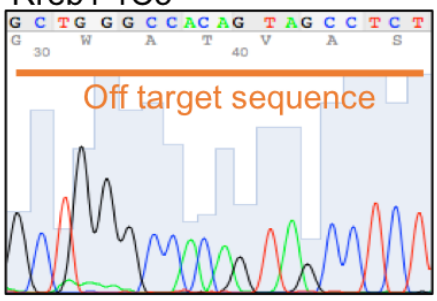

Rreb1 2G7

Rreb1 8G6

Rreb1 1E6

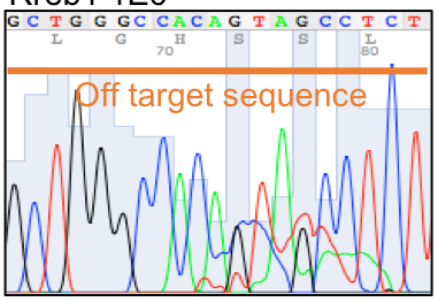

Rreb1 10G5

Rreb1 1E6

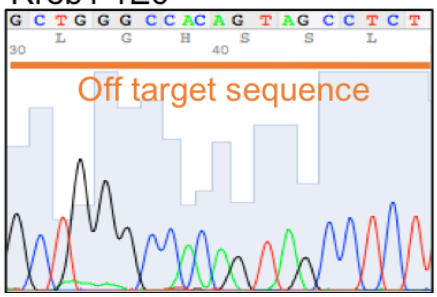

Appendix B – Ryr1 p.S1728F off-target site Sanger sequencing chromatograms

Zhx2 6B4

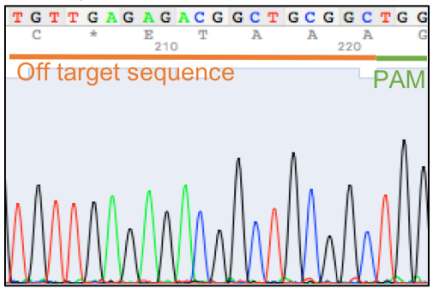

Zhx2 6F12

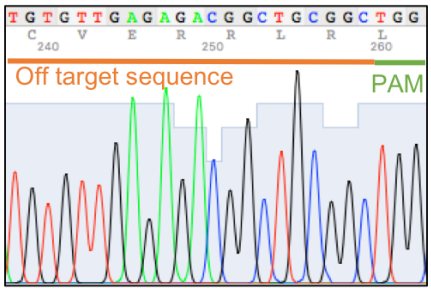

Cenph 6B4

Cenph 6F12

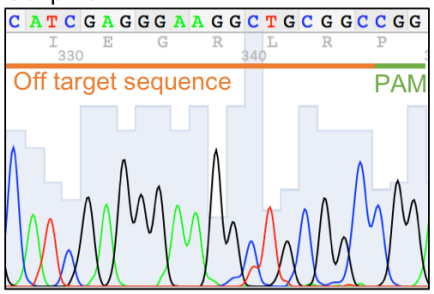

2310022B05Rik 6B4

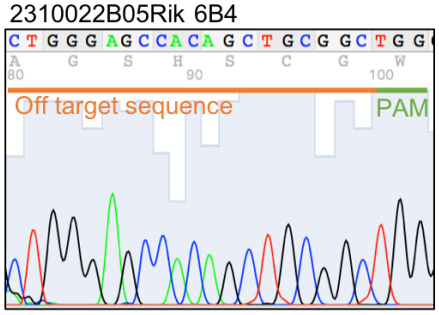

2310022B05Rik 6F12

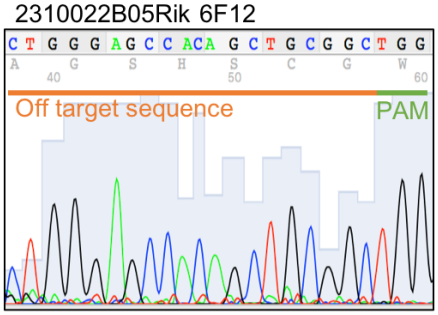

Adcy1 6B4

Adcy1 6F12

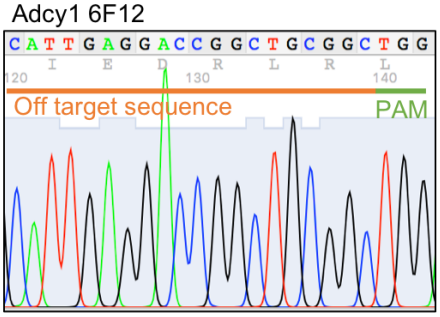

Dusp26 6B4

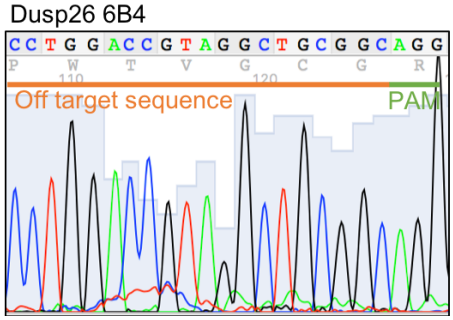

Dusp26 6F12

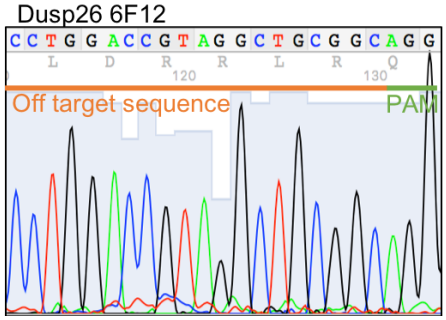

Appendix B continued (1)

GM5464 6B4

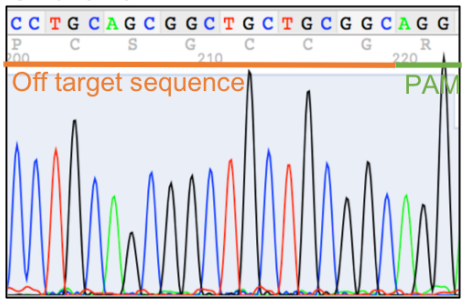

GM5464 6F12

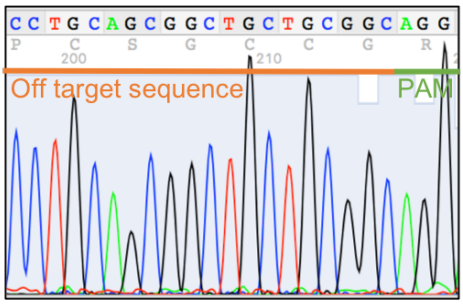

Tnfrsf25 6B4

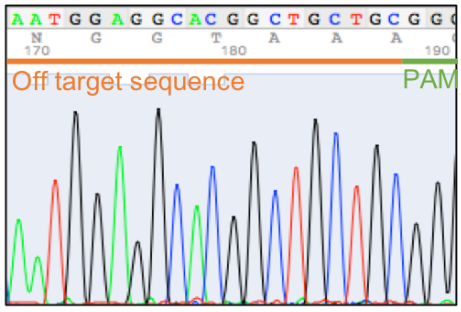

Tnfrsf25 6F12

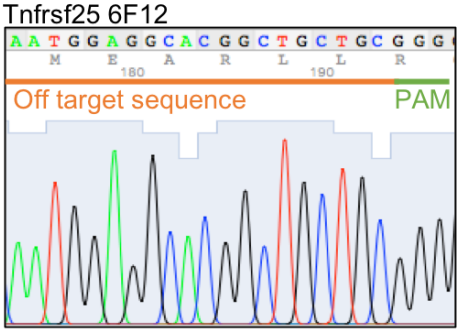

GM12604-Mllt3 6B4

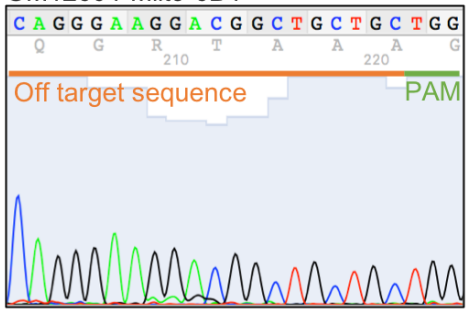

GM12604-Mllt3 6F12

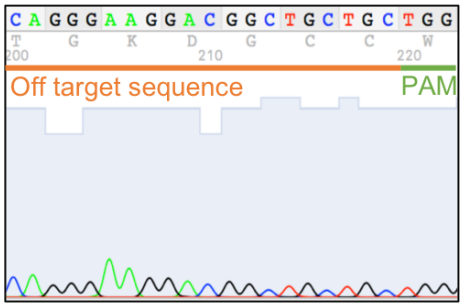

GM25665-GM24469 6B4

GM25665-GM24469 6F12

Scara5 6B4

Scara5 6F12

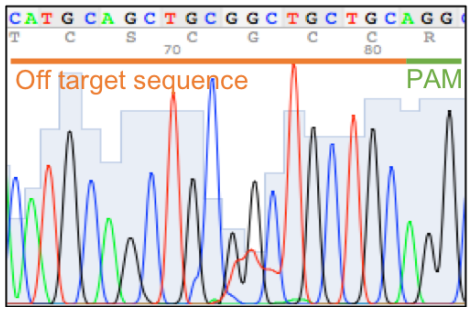

Appendix B continued (2)

A930001A20Rik-GM9733 6B4

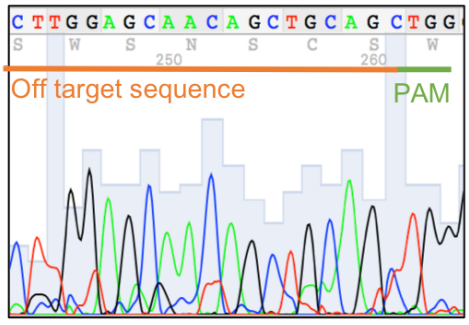

A930001A20Rik-GM9733 6F12

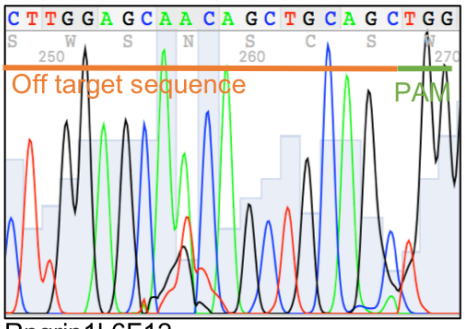

Rpgrip1l 6B4

Rpgrip1l 6F12

Hmcn2 6B4

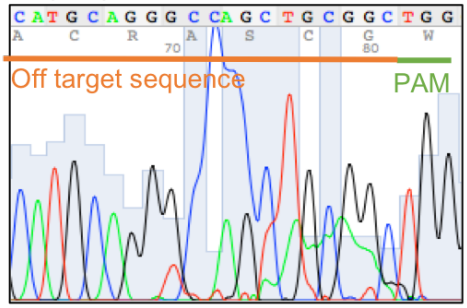

Hmcn2 6F12

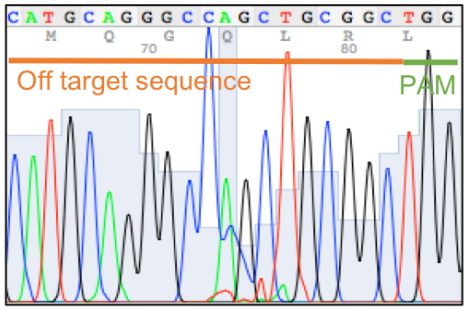

Aqp9-Aldh1a2 6B4

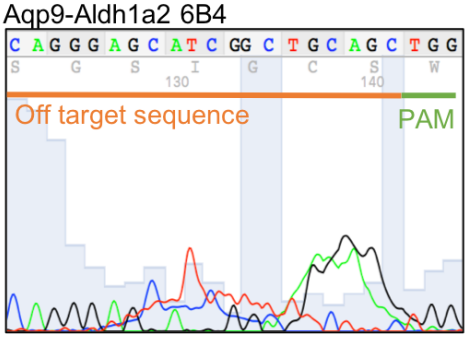

Aqp9-Aldh1a2 6F12

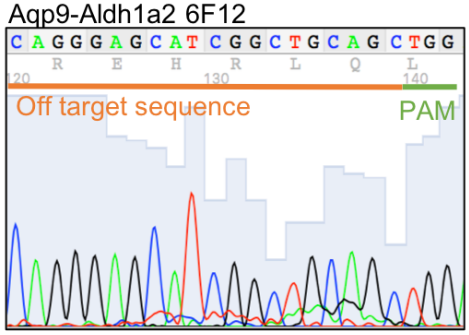

Gm23892-Gm25382 6B4

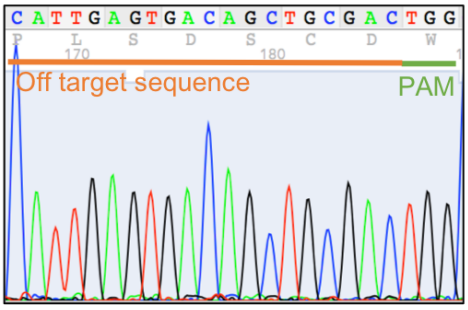

Gm23892-Gm25382 6F12

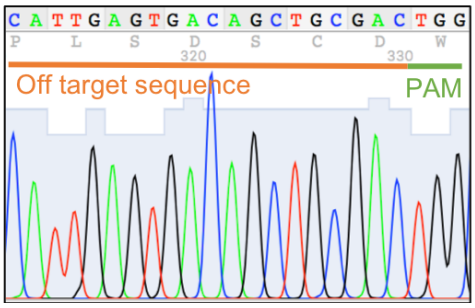

Appendix C – Casq1 off-target site Sanger sequencing chromatograms

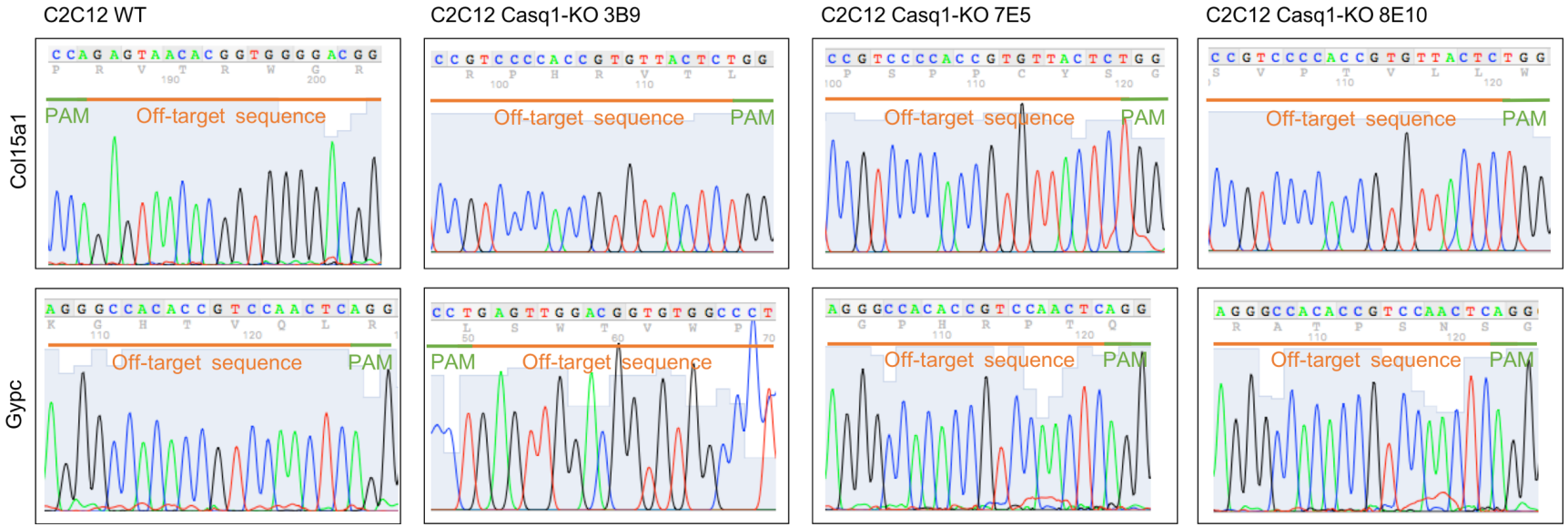

Appendix C continued (1)

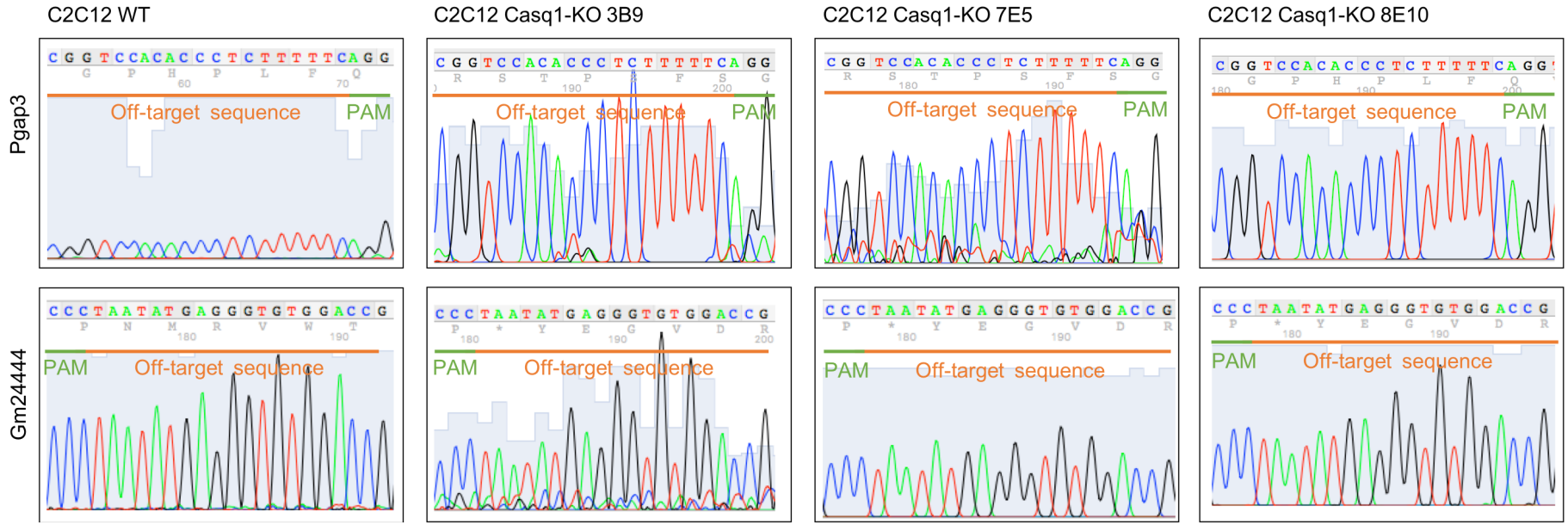

Appendix C continued (2)

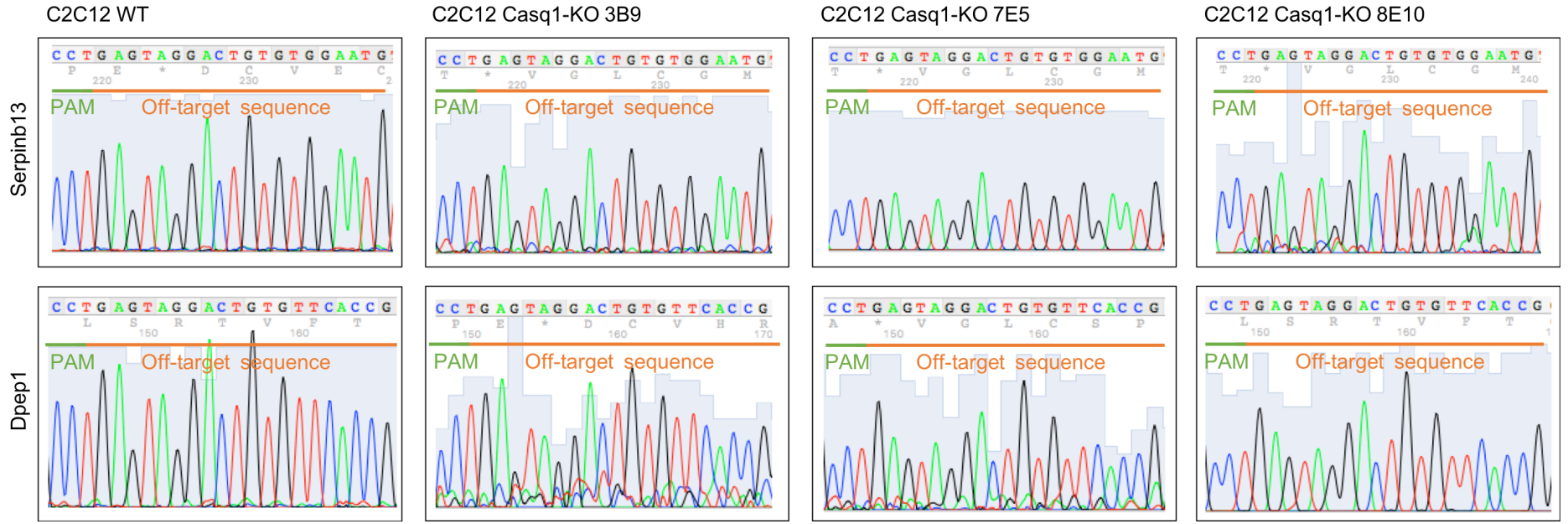

Appendix D – Putative identities of CASQ1 species identified by denatured and native mass spectrometry

Table S1 - Summary of the modifications identified on CASQ1 proteins by denatured intact mass spectrometry

Species have been assigned arbitrary species numbers to allow for ease of comparison. Italicised values indicate those that do not show an exact Mw match to the proposed adduct but when error is taken into account, they could represent exact matches. Brackets indicate the Mw difference between the variant CASQ1 proteins compared to CASQ1 WT in DaMST to investigate Ca^{2+} binding to CASQ1

Species	WT	I138T (-12)	F186Y (+16)	E364K (-1)	Modification
1	43679.6992		43695.1992		Unknown modification/contaminant
2	43697.36±0.62	43685.21±0.68	43713.49±0.71	43696.57±0.69	CASQ1 -132 Da = loss of N terminal methionine
3	43713.3984	43700.6992	43728.14±0.8	43711.38±0.62	2 + 16 Da = oxidation
4				43722.66±3.24	Unknown modification/contaminant
5	*43733.53±2.33*		43745.1.5±0.9	43728.01±2.18	2 + 32 Da = 2 oxidations
6				43742.6992	3 + 32 Da = 2 oxidations
7	43813.1992	43800.500	43828.8984	43811.6016	Unknown modification/contaminant
8	43875.61±1.17	43863.57±1.08	43891.0000±0.90	43874.90±2.16	2 + 178.8 Da = His-tag modification
9			43908.5000	43890.1016	8 + 16 Da = oxidation
10			43922.8984		8 + 32 = 2 oxidations
11	43955.89±1.38	43943.61±0.61	43971.25±1.32	43954.72±1.21	2 + 258.2 Da = His-tag modification
12			*44005.8984*	*43985.0000*	*11 + 31-33 Da = 2 oxidations*
13	44010.8008				Unknown modification/contaminant
14		44121.0000		44134.3984	Unknown modification
15				44212.3008	Unknown modification/contaminant

Appendix D continued (1)

*Addition of a 258 Da α-6-N-phosphogluconyl group to the His-tag occurs via the activity of 6-phosphoglucono-1,5-lactone which is produced from the dehydrogenation of glucose-6-phosphate. Subsequent dephosphorylation of the α-6-N-phosphogluconyl group yields a 178 Da α-6-N-gluconyl adduct (Geoghegan et al., 1999).

Appendix D continued (2)

Possible identities of species identified by native mass spectrometry using the Q Exactive™ Plus mass spectrometer

For CASQ1 WT, the predominant species (species A) was 43728 Da (Figure 5.26). This was ~80 Da smaller than the predominant species identified in the previous native analysis (species C, 43810 Da), suggesting a single Ca^{2+} ion could be bound to species A. Species B (43890) was 80 Da larger than the predominant species identified in the previous analysis (species C, 43810 Da) and consequently, 160 Da larger than species A identified in this analysis, suggesting 5 bound Ca^{2+} ions. Species C identified in this analysis (43972 Da) was ~80 Da larger than species B, suggesting 7 Ca^{2+} ions were bound to species C. Three dimeric species were also identified in this second native analysis (Figure 5.26) without added Ca^{2+}. An alternative interpretation of these data for the monomeric forms of CASQ1 WT would be that species A identified in both native analyses (Figure 5.25 and Figure 5.26), at 39 Da and 32 Da larger than WT CASQ1 minus the N terminal methionine, respectively, represent a species with 2 oxidations. Furthermore, differences of 80 Da could reflect the 80 Da difference between the +178 Da 6His-tag modification and the +258 6His-tag modification identified in the denatured analysis. When 1 mM Ca^{2+} was added, the monomeric species (species A) was 44136 Da, which is 440 Da larger than CASQ1 WT minus the N terminal methionine, suggesting 11 Ca^{2+} ions were bound. Alternatively, if this species represents CASQ1 minus the N terminal methionine with 2 oxidation events, this could reflect 10 bound Ca^{2+} ions. Assuming that the dimeric species identified was derived from the CASQ1 WT protein minus the N terminal methionine, a mass of 88200 Da indicates 20 bound Ca^{2+} ions. For CASQ1 p.I138T, in the absence of Ca^{2+}, the predominant species was 44182 Da (species B; Figure 5.26), which is ~497 Da larger than CASQ1 p.I138T without the N terminal methionine. This 497 Da difference does not correspond to a number divisible by 40 (the mass of a Ca^{2+} ion). It may be possible that this species represents the CASQ1 p.I138T protein with an oxidation event (+16 Da), leaving a difference compared to p.I138T minus the N terminal methionine of ~480 Da, or 12 Ca^{2+} ions. Alternatively, this species could represent CASQ1 p.I138T with the +258 Da 6His-tag modification, leaving a difference of ~240 Da, or 6 Ca^{2+} ions. The

identity of species A (43990 Da) is also unclear, which is 192 Da smaller than species B. This could reflect 200 Da (5 Ca^{2+} ions) or, if species B contains 2 additional oxidation events (+32), this would indicate 4 bound Ca^{2+} ions to species B. Alternatively, the difference between species A and the mass of p.I138T minus N terminal methionine is 305 Da, which again is not divisible by 40 Da. This mass could reflect the CASQ1 p.I138T protein with the +32 Da double oxidation event, leaving a difference of 273 Da (280 Da would represent 7 Ca^{2+} ions). In the presence of 1 mM Ca^{2+}, the predominant species was 44254 Da (species A) which is 569 Da larger than CASQ1 p.I138T minus the N terminal methionine. A total of 560 Da would correspond to 14 Ca^{2+} ions. Subtraction of all of the other masses of the modifications identified in the CASQ1 p.I138T denatured sample from 44254 Da did not yield any values that were divisible by 40 Da. The second and third species identified (species B and species C, respectively) represented dimeric CASQ1 p.I138T at 88148 Da and 88166 Da. As described previously, the identities of dimeric species can be speculated; however, it is not possible to conclusively determine their composition. Species B may correspond to a CASQ1 p.I138T minus the N terminal methionine protein bound to the CASQ1 p.I138T minus the N terminal methionine with a single oxidation event. This would correspond to the dimer being bound 19 Ca^{2+} ions. Species C was 18 Da larger than species B, potentially reflecting an additional oxidation event (+16). For CASQ1 p.F186Y, in the absence of added Ca^{2+}, the predominant species (species A) was 43830 Da which was 117 Da larger than the CASQ1 p.F186Y protein minus the N terminal methionine residue (43713 Da) which could reflect 3 bound Ca^{2+} ions. The second species identified (species B) was 43986 Da which was 273 Da larger than CASQ1 p.F186Y protein minus the N terminal methionine residue, which could reflect 7 bound Ca^{2+} ions (280 Da). An alternative to this is that the species B 43986 Da mass could reflect a previously undetected species containing the +258 Da 6His-tag modification in addition to a single oxidation event (+16 Da). The addition of 1 mM Ca^{2+} did not appear to induce the formation higher order CASQ1 species, with only monomers and dimers detected. The predominant species (species A) was 44172 Da, which is 459 Da larger than the CASQ1 p.F186Y protein minus the N terminal methionine. Whilst this value is not divisible by 40 Da, it could reflect the CASQ1 p.F186Y

protein minus the N terminal signal peptide in addition to an oxidation event (+16) and 11 Ca^{2+} ions (+440 Da). Alternatively, this value could also correspond to the CASQ1 p.F186Y protein minus the N terminal methionine with the +258 Da 6His-tag modification, in addition to 5 Ca^{2+} ions (+200 Da) or the +178 Da 6His-tag modification in addition to 3 Ca^{2+} ions. The second species identified in the presence of 1 mM Ca^{2+} was 44474 Da. This was 761 Da larger than the CASQ1 p.F186Y protein minus the N terminal methionine, which could correspond to 19 bound Ca^{2+} ions. Finally, for CASQ1 p.E364K, in the absence of Ca^{2+}, the predominant species was 43724 Da, which was 28 Da larger than the CASQ1 p.E364K protein without the N terminal methionine residue. This mass could correspond to the CASQ1 p.E364K protein without the N terminal methionine residue in addition to 2 oxidation events (+32 Da). The second species identified was 43906 Da, which was 210 Da larger than the the CASQ1 p.E364K protein without the N terminal methionine residue. This 210 Da difference could reflect the +178 Da 6His-tag modification in addition to 2 oxidation events (+32 Da). CASQ1 p.E364K appeared to polymerise in a manner similar to CASQ1 WT, with the presence of CASQ1 species up to tetrameric level following the addition of 1 mM Ca^{2+}. The predominant species (species A) detected in the presence of 1 mM Ca^{2+} was 43930 Da, which was 234 Da larger than the CASQ1 p.E364K protein without the N terminal methionine residue. This 234 Da difference could reflect the CASQ1 p.E364K protein without the N terminal methionine residue with 2 oxidation events (+32 Da) and 5 bound Ca^{2+} ions (+200 Da). The second most prominent species identified, species B, was 43940 Da which was 244 Da larger than CASQ1 p.E364K protein without the N terminal methionine residue. The 244 Da difference could reflect 6 bound Ca^{2+} ions. The dimeric species (species C) identified was 88098 Da which was 706 Da larger than the mass of two CASQ1 p.E364K proteins without the N terminal methionine residue. This 706 Da difference could reflect 4 oxidation events (+64 Da).